Experimental Investigation and Multi-scale Modeling of Strain Localization, Shear Banding and Fracture in Precipitation Hardened Aluminum alloys

by

Waqas Muhammad

A thesis

presented to the University of Waterloo

in fulfillment of the

thesis requirement for the degree of

Doctor of Philosophy

in

Mechanical and Mechatronics Engineering

Waterloo, Ontario, Canada, 2019

Examining Committee Membership

The following served on the Examining Committee for this thesis. The decision of the Examining Committee is by majority vote.

Supervisor(s)	Dr. Kaan Inal NSERC/General Motors Industrial Research Chair Professor, University of Waterloo
External Examiner	Dr. Sean R. Agnew Professor, University of Virginia
Internal Member	Dr. Mary Wells Professor, University of Waterloo Dean of Engineering, University of Guelph
Internal Member	Dr. Grzegorz Glinka Professor, University of Waterloo
Internal-external Member	Dr. Hassan Baaj Professor, Civil Eng., University of Waterloo

Author's Declaration

This thesis consists of material all of which I authored or co-authored: see 'Statement of Contributions' included in the thesis. This is a true copy of the thesis, including any required final revisions, as accepted by my examiners.

I understand that my thesis may be made electronically available to the public.

Statement of Contributions

The following co-authors have contributed to the current work as outlined below:

Professor Kaan Inal supervised this PhD thesis.

Dr. Jidong Kang (Scientist, CanmetMATERIALS, Natural Resources of Canada, Hamilton, ON) provided mentorship and co-supervision on the experimental work of this thesis.

Dr. Raja K. Mishra (R&D Center, General Motors, MI, USA) provided mentorship and access to GM facility to conduct EBSD measurements of the microstructure.

Dr. Abhijit P. Brahme (Research Associate, University of Waterloo) provided mentorship, guidance, converted EBSD measurements to develop synthetic 3D microstructures for simulations and assisted the authors with editing parts of the work.

Dr. Jürgen Hirsch, Dr. Olaf Engler and Dr. Henk-Jan Brinkman (Scientists, Hydro Aluminium Rolled Products GmbH, Germany) provided guidance on microstructure and texture analysis, provided raw material for research and mechanical test data of alloy AA8079.

Dr. Babak Shalchi-Amirkhiz (Scientist, CanmetMATERIALS, Natural Resources of Canada, Hamilton, ON) helped and provided guidance in TEM analysis.

Dr. Rama Sabat (Postdoctoral Fellow, University of Waterloo) helped in development of the failure model for age-hardenable aluminum alloys and Dr. Usman Ali (Postdoctoral Fellow, University of Waterloo) helped with laser profilometry measurements.

The balance of work is my own.

Abstract

Finite element (FE) simulations are widely used in automotive design processes to model the forming and crashworthiness behavior of structural materials. Comprehensive material characterization and the availability of suitable constitutive models are prerequisites for accurate modeling of these operations. Numerical modeling of formability and crashworthiness is complex as it involves large deformations, instability, ruptures, damage propagation, and fracture. The effectiveness of computer-aided engineering (CAE) based design and performance evaluations significantly depends on the ability of numerical models to predict the material work hardening behavior, flow localization and fracture.

This thesis presents a combined experimental and numerical study to explore microstructure property relationships involving strain localization, shear banding and fracture in precipitation hardened aluminum alloys. More specifically, the AA6xxx series aluminum alloys are of key interest for automotive applications, requiring good formability, hemmability and crash energy absorption characteristics. The goal of this work is to enhance the existing experimental understanding and modeling capabilities with respect to strain localization, shear banding and fracture in AA6xxx series precipitation hardened aluminum alloys, through development and coupling of multiscale modeling frameworks with advanced constitutive models for material work hardening and failure.

In these regards, a crystal plasticity based constitutive hardening model is developed to account for the intragranular backstresses that arise from the formation of deformation induced dislocation substructure in precipitation hardened aluminum alloys. Based on thorough experimental investigation, it is learned that the substructure starts as pinned dislocation tangles with some regions having relatively high dislocation content while others being virtually dislocation free. With persistent deformation the substructure evolves into a well defined equiaxed cell/subgrain structure with majority of dislocations being trapped at the subgrain cell wall boundaries. The substructure induces intragranular backstresses due to blockage of dislocation passage leading to the experimentally observed Bauschinger effect at the macroscopic scale. The proposed hardening model accounts for these induced stresses and successfully predicts the experimentally measured flow behavior during cyclic simple shear and cyclic TCT and CTC loadings of AA6063. More importantly, the new backstress hardening model successfully reproduces the experimentally observed Bauschinger effect upon loading reversal. It is further shown that the crystallographic texture evolves significantly during cyclic simple shear deformation and the model successfully predicts the experimentally observed texture evolution. The study reveals that for proper prediction of flow behavior and the experimentally observed Bauschinger effect in precipitation hardened aluminum alloys, a physically motivated model that can account for the induced internal stresses, must be employed to describe material hardening on a polycrystalline level.

Next, a multiscale modeling approach is developed where a macro-scale component level simulation is performed using conventional phenomenological plasticity and the boundary

conditions of the region of interest are extracted and applied to the crystal plasticity based finite element model to account for the relevant microstructural physics. The proposed approach is successfully validated by simulating wrap-bending deformation of AA6063 and by comparing the observed texture evolution, slip band formation within grains, through thickness strain localization and the development of surface roughness with corresponding experimental data. The proposed approach enhances existing modeling capabilities for better predictability of material response under complex loading paths.

After developing the multiscale framework, a new constitutive approach is developed to predict failure by extending the existing nano-void theory of ductile failure to precipitation hardened aluminum alloys by accounting for the effects of precipitation induced dislocation substructure on point defect generation. A new evolution law for the effective obstacle strength associated with substructure evolution is incorporated into the formulation. The proposed failure criterion is successfully validated against experimental data and its versatility is demonstrated by coupling the failure criterion with stress-strain data generated through crystal plasticity simulations, to predict failure strain for arbitrary loading – stress triaxiality conditions.

Next, a comprehensive experimental investigation is performed to study the relationship between microstructure, plastic deformation and fracture behavior of precipitation hardened aluminum alloy AA6016 during bending. It is shown that the bendability of AA6016 alloy is limited by the formation of severe surface undulations and surface cracking, which are associated with the heterogenous nature of slip concentrating into coarse slip bands and intense shear banding originating from surface low cusps in the form of mutually orthogonal transgranular bands. Micro-cracks originate from low cusp regions along the outer tensile surface and propagate along the intensely sheared planes within shear bands. Results show that grains with S texture component are prone to shear banding and failure during bending and the contrary is true for Cube oriented grains. It is observed that intergranular micro-void nucleation and crack propagation is favored in areas with high grain boundary misorientations and intense slip band impingements along boundaries, perhaps due to the reduction in local cohesive strength of such boundaries.

Finally, the developed multiscale modeling approach in conjunction with the newly developed hardening and failure models for age-hardenable aluminum alloys are applied to predict the experimentally observed shear banding and fracture behavior of AA6016 during bending. The simulated results successfully predict the experimentally observed shear banding and the predominant transgranular fracture behavior. It is shown that the advancing crack tip alternates from a less critical localization condition to a more critical one, as it requires lesser energy for the creation of new fracture surfaces while still sustaining the imposed plastic deformation. It is observed that Copper, Brass and Cube texture components show good resistance to shear banding and are therefore characterized as high bendability components, whereas the contrary is true for the S texture component. Lastly, the coupled numerical framework, presented herein, provides an excellent tool for CAE, virtual material characterization and analysis of microstructure-property relationships.

Acknowledgements

First and foremost, I would like to express my sincere gratitude to my supervisor, Professor Kaan Inal, whose expertise, understanding, patience and excellent supervision added considerably to my graduate experience. I would like to thank him for encouraging my research and for providing me this valuable opportunity to grow as a research scientist. Apart from his academic and technical support, I would like to thank him for his motivation, moral support, kindness and generosity throughout the entire process; without him this thesis would not have been completed. I would also like to express my deepest appreciation for the one of a kind opportunity that I was granted, to be a visiting research fellow at CanmetMATERIALS, Natural Resources Canada, Hamilton, and General Motors – Canadian Technical Center, Oshawa, throughout the duration of my PhD. Thank you very much from the bottom of my heart.

I would also like to express my special thanks to Dr. Jidong Kang from CanmetMATERIALS, Natural Resources Canada, in Hamilton, Ontario, for his co-supervision, mentorship and many helpful and long discussions on the experimental aspect of my thesis. He raised many precious points in our discussions, and I hope that I have managed to address several of them here. I would like to thank him for his motivation, moral support, kindness and great supervision. At this point I would also like to sincerely thank Dr. Jian Li, Dr. Babak Shalchi-Amirkhiz, Ms. Renata Zavadil, Ms. Catherine Bibby and Mr. Jie Liang from CanmetMATERIALS, Natural Resources Canada for their friendship, support and guidance.

A very special thanks goes out to Dr. Raja K. Mishra from General Motors R&D center in Warren, MI for his mentorship, technical expertise and helpful discussions. I would like to thank him for providing me with a unique opportunity to visit the General Motors R&D center in Warren, MI several times to conduct EBSD texture measurements.

A special thanks also goes out to Dr. Jürgen Hirsch and Dr. Olaf Engler (Scientists, Hydro Aluminium Rolled Products GmbH, Germany) for their support and guidance.

I would like to take the time and offer my deepest appreciation and gratitude to Dr. Abhijit Brahme for his mentorship, motivation, encouragement, great friendship and countless helpful discussions on my thesis. I could not have done this without you. Thank you very much Sir!

I would also like to thank my office mates and friends Dr. Usman Ali, Dr. Rama K. Sabat and Talal Ali Paracha for the good times and several helpful discussions. I also thank all my colleagues at the University of Waterloo for their support throughout the entire process.

Most importantly, I would like to offer my profound and eternal gratitude to my beloved parents and siblings for all the sacrifices that you've made on my behalf. Your prayers for me was what sustained me thus far.

This work was supported by Natural Sciences and Engineering Research Council of Canada (NSERC) under grant no. APCPJ 441668-12, the Engineering Research Council - Industrial Research Chair (NSERC-IRC) under grant no. IRCPJ-503185-2016, CanmetMATERIALS, Natural Resources Canada, General Motors of Canada, Hydro Aluminium Rolled Products GmbH, Germany, Ontario Graduate Scholarship (OGS), President's Graduate Scholarship of Waterloo, UW Graduate Scholarship of Waterloo, Alan Plumtree Graduate Scholarship of Waterloo and Faculty of Engineering Graduate Scholarship of Waterloo.

Dedication

"I dedicate this thesis to my beloved parents. You are truly a blessing from God"

Table of Contents

List of Figures

List of Tables

List of Abbreviations

AA	aluminum alloy
BCC	body centre cubic
BF	bright field
BSE	backscatter electrons
CA	cellular automata
CAE	computer aided engineering
CDM	continuum damage mechanics
CI	confidence index
CPFEM	crystal plasticity finite element method
CSL	coincidence site lattice
CTC	compression-tension-compression
DDD	discrete dislocation dynamics
DIC	digital image correlation
EBSD	electron backscatter diffraction
ED	extrusion direction
EDM	electrical discharge machining
EDS	energy dispersive spectroscopy
EFG	element free galerkin
EPSC	elasto-plastic self-consistent
FCC	face centre cubic
FE	finite element
FRF	forward-reverse-forward
GBDF	grain boundary ductile fracture
GND	geometrically necessary dislocations
HAADF	high-angle annular dark-field
HAGB	high angle grain boundary
HCP	hexagonal close packed
IPF	inverse pole figure
KAM	kernel average misorientation
LAGB	low angle grain boundary
ND	normal direction
ODF	orientation distribution function
PFZ	precipitate free zone
RD	rolling direction
RVE	representative volume element
SE	secondary electrons
SEM	scanning electron microscopy
SFE	stacking fault energy
SPH	smoothed particle hydrodynamics
SRC	short-range clustering
SSSS	supersaturated solid solution
STEM	scanning transmission electron microscopy
TCT	tension-compression-tension
TD	transverse direction
TEM	transmission electron microscopy
UMAT	user-defined material model
VPSC	visco-plastic self-consistent
XFEM	extended finite element method

Chapter 1: Introduction

1.1 Motivation

The automotive industry is one of the largest industries in the world, with approximately over 20 million new vehicles sold last year in North America alone [1]. It is a very competitive industry and thus requires continuous research and product development. Recently, there has been a resurgence of research interest in aluminum alloys mainly due to the ever-increasing demand for vehicle light weighing, driven by a need to lower fuel consumption and reduce harmful carbon emissions. Aluminum alloys have proven to be very attractive candidates for automotive applications due to their relatively high strength to weight ratio and excellent corrosion resistance properties as compared to steel.

Advancements in alloy design and processing over the past few decades have led to the development of a wide range of aluminum alloys suitable for many different automotive applications. Aluminum alloys are categorized into several groups based on certain material's characteristics such as its ability to respond to thermal and mechanical treatment and the primary alloying elements added to the aluminum alloy. Wrought aluminum alloys are classified into eight different series (i.e. AA1xxx to AA8xxx) based on their main alloying elements (see Figure 1-1). The AA2xxx, AA6xxx and AA7xxx series aluminum alloys are heat treatable alloys and therefore can be strengthened via precipitation hardening heat treatment. Some of the AA8xxx series aluminum alloys such as the Al-Li alloys are also heat treatable. Aluminum alloys are used in a wide range of automotive applications. For example, AA1xxx series alloys are used for manufacturing heat shields, AA3xxx series alloys are used for manufacturing heat exchangers, and AA5xxx series alloys are used for making chassis, wheels and inner body panels due to their excellent bending and torsion stiffness.

The heat treatable (i.e. precipitation – age hardening) aluminum alloys are of special interest to automotive manufacturers due to their high strength vs. ductility compared to non-heat treatable alloys. These alloys are used in manufacturing outer body panels, where high strength, dynamic dent resistance and high surface quality are required, and bumper and crush rails, where good strength and shock absorption are needed. The precipitation hardening AA6xxx series Al-Mg-Si alloys are currently used for the outer panels in a number of vehicle models such as Audi A8 andA2, Ford's Lincoln LS, and General Motor's GMC Yukon and Chevrolet Suburban [2]. Aluminum alloy AA6111 has been widely used by North American auto manufacturers for skin panel applications due to their good formability and high strengthening potential [2]. The AA6xxx series aluminum alloys also have excellent extrudability and weldability and are therefore used to make crush rails that are installed in the front-end of the vehicle to absorb impact energy during crash. More recently, the AA6xxx series alloys have also been considered for aerospace applications. For example, currently AA6013 is being used on Boeing 777 and AA6065 is being

used for fuselage applications on some aircrafts [2]. Apart from the AA6xxx series alloys, the AA7xxx series precipitation hardening aluminum alloys are widely used for aerospace applications. For instance, AA7075 is heavily used in manufacturing aeroplanes fuselage skins, wing box, flight control surfaces, engine supports and main frames [3]. Due to their wide range of applications, there has been a strong research and industrial interest for better understanding the processing-material behavior-performance relationship in precipitation hardening aluminum alloys.

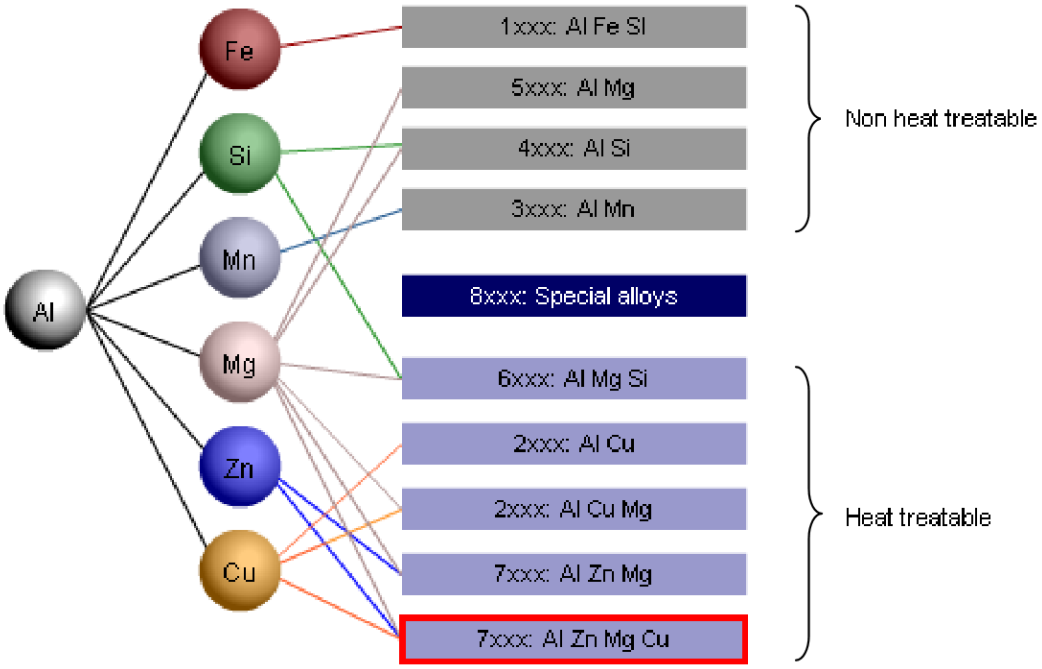

Figure 1-1: Classification of wrought aluminum alloys [4]**.**

Owing to a constant increase in the number of vehicles on the road and strict government safety regulations, the automakers are called upon to increase the levels of safety protection in their vehicles and reduce the number of injuries that occur in accidents. The most direct approach is experimental testing on components level or full-scale vehicles, which is obviously very expensive. CAE based numerical modeling has therefore become a powerful tool for crashworthiness and structural optimization. Figure 1-2 shows result of a finite element simulation of a frontal impact between two vehicles. Simulations of such full-scale vehicle models are also computationally very expensive and time consuming. Furthermore, numerical modeling of crash simulations is complex because it involves large deformations, instability, ruptures, damage propagation, fracture and other nonlinear events related to structures and materials. The effectiveness of CAE based crash performance assessments significantly depends on the ability of numerical models to predict the actual material hardening behavior, flow localization and fracture.

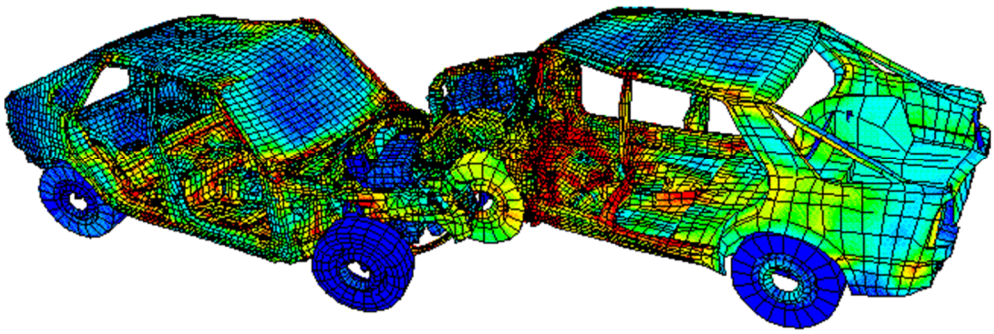

Figure 1-2: CAE based simulation for assessing vehicle's crash performance [5].

1.2 Scope and Objectives

The work hardening behavior of AA6xxx series precipitation hardening aluminum alloys is rather complex due to the additional hardening mechanisms associated with precipitation strengthening and formation of deformation induced dislocation microstructures. Studies have shown that these alloys tend to develop cellular dislocation substructures that are characterized by three-dimensional tangles of dislocations that serve as "cell walls" and less dense internal regions (cell interiors) [6–9]. It is shown that the presence of such dislocation microstructure induces intragranular backstresses due to blockage of dislocation passage leading to the experimentally observed Bauschinger effect at the macroscopic scale [10–13]. Furthermore, as of now, flow localization, damage and fracture phenomena are not well understood for precipitation hardening aluminum alloys. In addition, physically motivated hardening and fracture models, which can represent the underlying microstructural physics relevant to these alloys, are also not well developed. Therefore, majority of vehicle components are over-designed because the existing material models are unable to predict failure – fracture accurately and hence, large safety margins are incorporated into the design by automotive manufacturers. In this regard, the availability of accurate hardening and fracture models is essential for optimizing the impact performance and formability of designed parts.

In addition, the ability to numerically predict component performance relies on understanding fundamental physical mechanisms governing material behavior and robust modeling capabilities that represent all relevant microstructural phenomena. Such modeling approaches can be computationally very expensive. An alternative approach is to use multi-scale material modeling technique (see Figure 1-3) by linking macroscale modeling which is rather computationally efficient with microscale modeling that can represent all relevant microstructural physics, to arrive at a reasonable compromise between accuracy and efficiency. In the current research, a multi-scale modeling approach has been developed that links macroscale finite element modeling with

microscale crystal plasticity based finite element modeling to analyze flow localization and fracture in precipitation hardening aluminum alloys.

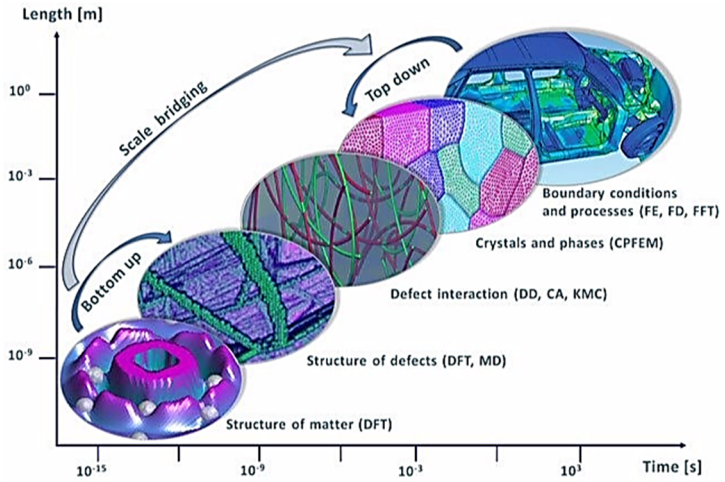

Figure 1-3: Schematic representation of a multi-scale material modeling approach [14].

The major goal of this research is to study the localization, damage and fracture behavior of AA6xxx series aluminum alloys through experiments, with emphasis on developing physically motivated crystal plasticity-based hardening and fracture models applicable to precipitation hardening aluminum alloys. The main objectives of this research are as follows

- Develop physical understanding of the hardening and fracture behavior of AA6xxx series precipitation hardening aluminum alloys through experimentations.
- Develop a slip level hardening model for precipitation hardening aluminum alloys incorporating the relevant microstructural aspects.
- Develop a physics-based fracture/failure criterion for precipitation hardening aluminum alloys with direct physical inputs from experiments.
- Develop a multiscale modeling approach and verify the predictive capability of proposed models by simulating flow localization and fracture in precipitation hardening alloys under different stain path such as bending.

1.3 Thesis Outline

The thesis consists of eleven chapters. The first chapter presents the introduction and describes the motivation, scope and objectives of this research.

Chapter two presents the general background knowledge related to microstructural aspects of materials such as crystal structures, dislocations, crystallographic slip, deformation induced dislocation microstructures, texture and grain boundaries. The chapter also provides a brief background of precipitation hardening in aluminum alloys including the heat treatment process, the microstructural changes and the strengthening mechanisms. In addition, a brief overview of

the crystal plasticity theory, the numerical approaches of modeling fracture and experimental characterization techniques (i.e. SEM, TEM, EBSD, DIC) is also provided in this chapter.

Chapter three presents a literature review of the fracture behavior of aluminum alloys and the proposed failure models. The section also provides a literature review of the existing crystal plasticity based hardening models.

Chapter four provides an overview of the research plan to achieve the thesis objectives.

Chapters five through ten are accepted and submitted publications presenting studies that have been conducted to meet the overall goal and objectives of this research. These chapters are the published / submitted version of the manuscripts, i.e., other than formatting, no modifications have been made to the papers.

Chapter five develops a new crystal plasticity based backstress hardening model for AA6xxx series alloys, which employs experimentally measured microstructure to incorporate the effects of intragranular backstresses due to the formation of deformation and precipitation induced cellular dislocation substructure. The hardening model is validated against experimentally measured data for complex cyclic loading paths such as large strain cyclic simple shear and cyclic tension-compression tests. The chapter presents a detailed experimental investigation of texture and dislocation substructure evolution during cyclic simple shear deformation of an extruded precipitation hardened aluminum alloy AA6063.

Chapter six develops a multi-scale modeling framework and applies the new backstress hardening model to study the evolution of microstructure and the development of surface roughness (which is a precursor to fracture) during bending of an extruded precipitation hardened aluminum alloy AA6063. The chapter also presents a detailed experimental and numerical study with emphasis on investigating correlations between heterogeneous plastic deformation, strain localization, the accompanying texture evolution and the development of surface topography effects during bending of AA6063.

Chapter seven presents the development and validation of a failure criterion for precipitation hardened aluminum alloys. The proposed failure model is employed to predict failure strains for extruded and rolled AA6xxx alloys along different strain paths.

Chapter eight presents a comprehensive experimental study to analyze the bendability and fracture behavior of age-hardenable aluminum alloy AA6016. The study also presents experimental investigation of bendability enhancement of alloy AA6106 through thermomechanical roll-bonding. The focus of the experimental study is to characterize the bendability and to investigate correlations between microstructure, the nature of plastic deformation, slip distribution, texture evolution, strain localization, surface topography development, macro-crack initiation and propagation during wrap bending.

Chapter nine presents a detailed crystal plasticity finite element based numerical study that couples the multiscale modeling framework and the developed hardening and fracture models to study the sequence of microstructural events leading to final fracture and the relationship between crystallographic texture, shear band development, micro-crack initiation and propagation during wrap bending of monolithic AA6016 and cladded AA606X aluminum alloys.

Chapter ten presents novel experimental findings related to the occurrence of deformation banding in a precipitation hardened aluminum alloy during simple shear deformation. The results presented in this chapter form basis for the future work.

Lastly, chapter eleven summarizes the thesis with conclusions of the contributions and presents some opportunities for future work.

Chapter 2: Background

This section provides a brief introduction and background information on the topics covered in this document. Firstly, an overview of some of the important microstructural aspects has been provided, followed by a brief overview of the precipitation hardening heat treatment process and its effects on the microstructure of aluminum alloys have been discussed. Next, a brief background on the different fracture mechanisms observed in metals has been provided. Lastly, an overview of the different numerical modeling methods and experimental characterization techniques has been provided.

2.1 Microstructural Aspects

A brief overview of important material microstructure related aspects (such as crystal structure, dislocations, crystallographic slip, deformation induced microstructures, texture, misorientations, and grain boundaries) has been provided in this section.

2.1.1 Crystal Structure

Metals are crystalline materials comprising of one or many small crystals of atoms exhibiting long-range periodicity. This long-range periodicity is described by the crystal structure. The crystal structure is characterized by the arrangement of atoms in to a regular, repeatable lattice with unit cell being the smallest possible subdivision of the crystal structure. Some of the commonly observed crystal structures of engineering materials are shown in Figure 2-1. Aluminum and its alloys have an FCC crystal structure where the atoms are located at the four outer corners of the unit cell and at all of the centers of the cube faces.

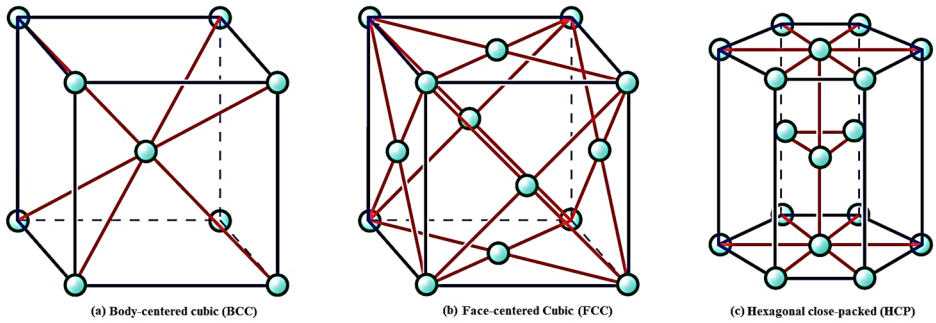

Figure 2-1: Crystal structure showing (a) body centered-cubic (ex. Ferritic steels, Potassium, and Molybdenum etc.) (b) face centered cubic (ex. Aluminum, Copper, Brass, and Nickel etc.) and (c) hexagonal closed-packed lattice (ex. Magnesium, Titanium, and Zirconium etc.).

2.1.2 Dislocations and Slip

Dislocations are line imperfections in an otherwise perfect crystal lattice. In other words, dislocation in a crystalline material is a microstructural defect which disrupts the perfect periodic arrangement of atoms in the material. Dislocations are usually introduced into a crystal during

solidification of the material or by means of permanent - plastic deformation [15]. In 1930's, the existence of dislocations was first inferred based on discrepancies between the theoretical and experimental results of the applied shear stress required to initiate plastic deformation in a single crystal [16]. In 1934, Orowan, Polanyi and Taylor independently were able to account for this discrepancy by the presence of dislocations [16].

There are two main types of dislocations: the edge dislocation and the screw dislocation. The edge dislocation can be illustrated by partly slicing through a perfect crystal and inserting an extra half plane of atoms. The bottom edge of the extra half plane is an edge dislocation (Figure 2-2(a)). The Burgers vector of an edge dislocation is normal to the line of the dislocation. The screw dislocation can be illustrated by partly cutting through a perfect crystal and then skewing the crystal by one atom spacing as shown in Figure 2-2(b). The Burgers vector of a screw dislocation is parallel to the line of the dislocation. Generally, the dislocations can have a mixed edge and screw character and are called mixed dislocations. These dislocations have both edge and screw components, with a transition region between the two components (Figure 2-2(c)).

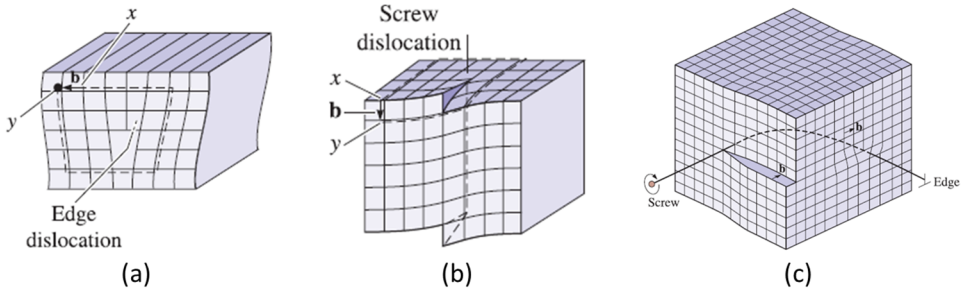

Figure 2-2: Illustration of (a) an edge dislocation (b) a screw dislocation and (c) a mixed dislocation in a crystal [15].

Dislocations play a fundamental role during plastic deformation of metals. There are two basic types of dislocation motion: dislocation glide or dislocation climb. Dislocation glide refers to the movement of dislocation within the plane which contains both its line and Burgers vector. Dislocation climb happens when a dislocation moves out of the glide surface, normal to the Burgers vector. This glide and climb motion of many dislocations results in slip and the cumulative effect of slip of numerous dislocations is plastic deformation [17].

Slip in metals tends to occur along the closed-packed directions within the closed-packed planes. For an FCC crystal structure, this corresponds to the <1 1 0> directions within the [1 1 1] slip plane. There are four unique [1 1 1] planes and three <1 1 0> directions per plane resulting in 12 unique slip systems for an FCC material. A characteristic applied stress is required for slip to occur. For example, if a unidirectional force *F* is applied to a cylinder made up of a single crystal (see Fig), in order for the dislocation to move in its slip system, a resolved shear stress acting in the slip direction must be produced by the applied force. This resolved shear stress is given by the following relationship known as the Schmid law:

$$\tau_r = \frac{F}{A_0} cos\lambda cos\phi \tag{2-1}$$

Thus, slip occurs when the resolved shear stress τ_r equals the critical resolved shear stress τ_{crss}, which is the shear stress required for slip to occur and is a material dependent parameter.

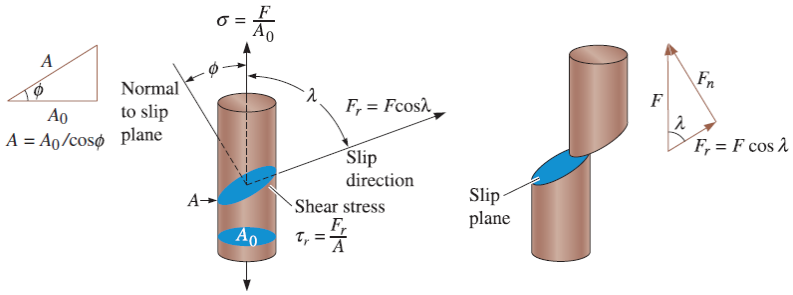

Figure 2-3: The concept of the resolved shear stress on a slip plane also known as Schmid law [15].

2.1.3 Deformation-Induced Dislocation Microstructure

Metals exhibit the formation of deformation induced dislocation microstructures. These microstructures tend to form dislocation cells or nets that are characterized by three-dimensional tangles of dislocations that serve as "cell walls" and less dense internal regions (cell interiors) [6, 9, 18]. Several transmission electron microscopy (TEM) studies have shown the existence of these dislocation microstructures in face centered cubic (FCC) metals and alloys if the applied strain is large enough [19–21]. Figure 2-4 shows the formation of dislocation substructure in polycrystalline copper under cyclic tension-compression. The presence of such dislocation microstructure induces intragranular backstresses (stress incompatibilities) due to blockage of dislocation passage leading to the experimentally observed Bauschinger effect at the macroscopic scale. The deformation induced dislocation microstructure is important for the current work as its formation influences the observed mechanical behavior of the material.

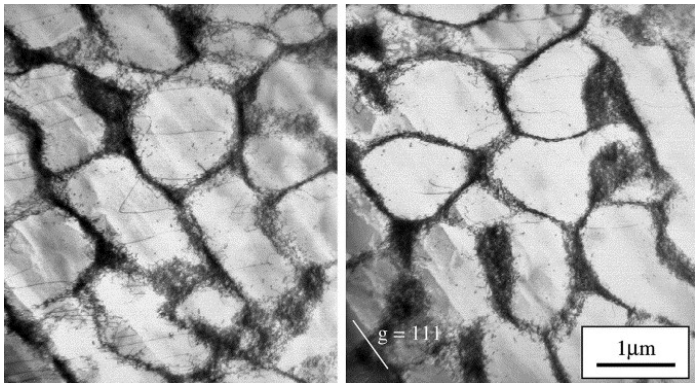

Figure 2-4: Dislocation substructure after fully reversed tension–compression of polycrystalline copper [22].

2.1.4 Texture & Misorientations

Many common engineering materials such as metals, ceramics and some plastics have a polycrystalline structure composed of a multitude of individual crystallites. The so-called term 'texture' represents the preferred crystallographic orientation of the crystallites within the polycrystalline aggregate. Since many of the properties of the crystals are directionally dependent, the texture plays an important role in defining the properties of a polycrystalline material [23].

To represent a crystallographic orientation, three independent parameters are needed to specify the orientation of the crystal with respect to a fixed reference frame, usually the sample frame. These three parameters are known as Euler angles (ϕ_1, Φ, ϕ_2), which are used to describe rotations from the sample frame coordinate axis to the crystal coordinate axis. The texture of a material is commonly illustrated by the use of pole figures, inverse pole figures and orientation distribution functions (ODF).

Most polycrystalline materials develop strong textures due to prior deformation processing such as cold working. The texture of a material can be represented in terms of frequently occurring texture components. Some of the important texture components that occur frequently in cold rolled FCC metals are presented in Table 2-1 along with the Euler angles [24].

Table 2-1: Common Texture components in FCC Metals.

Component	Euler angles ($\boldsymbol{\phi_1, \Phi, \phi_2}$)
Cube	(0,0,0)
Copper	(0,35,45)
S	(64.93,74.50,33.69)
Goss	(0,45,0)
Brass	(35,45,0)

When analyzing texture of a material, the term misorientation refers to the difference between the orientations of two neighbouring crystals. Given two crystals A and B, the misorientation between these crystals is the crystal rotation required to bring the crystal lattice of A in coincidence with the crystal lattice of B. Misorientations among crystals are of significance as they are directly linked with the creation of sub-grains, grains and grain boundaries.

2.1.5 Grain Boundaries

The microstructure of crystalline materials such as metals, consists of many grains. A grain represents the portion of the material within which the orientation of the crystallites is nearly identical. The orientation of the crystal structure can be different for each adjoining grain and the grain boundary that separates the individual grains is comprised of a narrow zone known as the grain boundary zone. Figure 2-5(a) shows a schematic view of three grains with different orientations being separated by a grain boundary and Figure 2-5(b) shows a micrograph of grains and grain boundaries in a stainless steel sample.

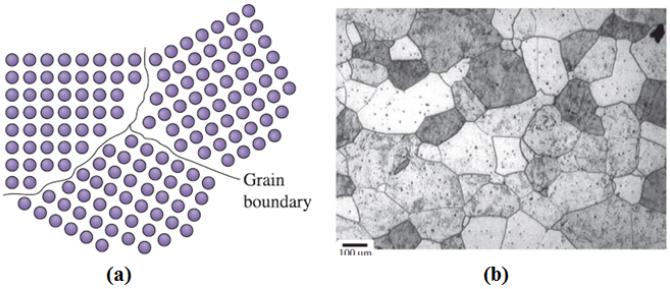

Figure 2-5: (a) Schematic representation of grains and grain boundary. (b) Grains and grain boundaries in stainless steel [15].

Since a grain boundary is the interference between two grains, it can be sufficiently described by the misorientation between the two grains. In the present work, the grain boundary zones are identified using misorientation description of grain boundaries. A grain boundary can be further classified into low angle grain boundary (LAGB) or a high angle grain boundary (HAGB) based on the disorientation (θ) between the two grains. The cut-off angle for this classification is ~ 10º to 15º. In present work, any boundary with a disorientation higher 15º is classified as a high angle grain boundary. The small angle grain boundary is produced by an array of dislocations causing a small misorientation between the lattices on either side of the boundary as shown in Figure 2-6.

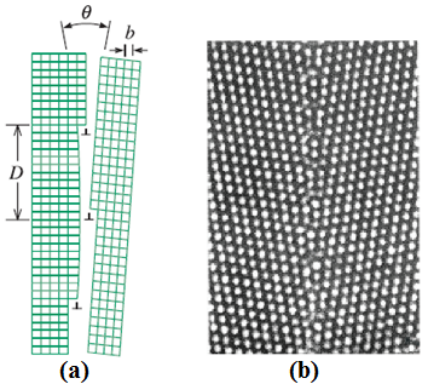

Figure 2-6: (a) Schematic of a small angle grain boundary. (b) A TEM image of a small angle grain boundary in aluminum [15].

Grain boundaries are surface defects and play a vital role in defining the strength of the material as explained by the Hall-Petch effect. Grain boundaries present obstacles for dislocation movement and slip transmission across grains and therefore controlling the strain hardening behavior of the material. Fracture behavior in many alloys, especially, some precipitation hardened aluminum alloys is also linked with the strength of those grain boundaries, with weaker boundaries leading to an intergranular fracture.

2.2 Precipitation Hardening in Aluminum Alloys

Precipitation hardening aluminum alloys (also known as heat treatable or age hardening aluminum alloys) have been widely used in aircraft and automotive industries due to their good workability

and high strength-to-weight ratio [25, 26]. The mechanical properties of these alloys are strongly dependent on the microstructure obtained after the precipitation hardening heat treatment. Strength in such alloys is mainly dependent on the formation of nano-sized finely dispersed precipitates within the aluminum matrix [27–30]. A carefully conducted age hardening heat treatment would avoid the formation of precipitation free zones (PFZ) and grain boundary precipitates and will tend to maximize the precipitation of nano-sized finely dispersed precipitates which are essential to strengthening [31–34].

2.2.1 Brief History

The history of precipitation hardening is dated back to early 20th century. In 1906, A. Wilm discovered that the strength of a rapidly quenched Al-Cu-Mg alloy increased while it was left at room temperature [35]. Since the alloy hardened with age, the observed phenomenon was called 'age hardening'. In 1919, Mercia and co-workers observed similar increase in hardness of an Al-Cu alloy after quenching [36]. The authors proposed that the increase in hardness after quenching is related to copper atoms precipitating out as particles from the supersaturated solid solution. It was not until 1938, when Guinier and Preston, in pioneering independent research using X-ray scattering, found evidence of clustering of atoms in aged aluminum alloys, since termed Guinier-Preston (GP) zones [37, 38]. However, the first direct observation of GP zones using transmission electron microscopy was performed in 1950's, justifying the presence of small precipitate particles and hence the name 'precipitation hardening' was adopted [39].

2.2.2 The Heat Treatment Process

Precipitation or age hardening is a heat treatment technique used to enhance mechanical properties (i.e. strength, hardness, ductility) of metallic alloys through precipitation of finely dispersed particles. The heat treatment consists of three main stages (i.e. solution heat treatment, quenching and aging) as shown in Figure 2-7.

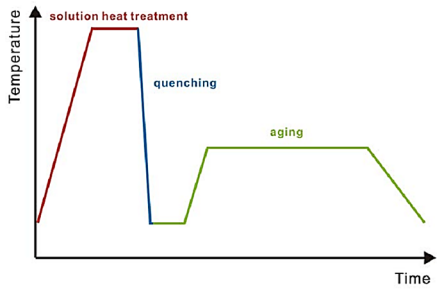

Figure 2-7: Stages of precipitation hardening heat treatment [4].

During the solution heat treatment stage, the alloy is heated above the solvus temperature and held at this temperature for some duration. The purpose of solution heat treatment is to obtain a single phase solid solution. In addition, depending on solutionizing temperature, a great amount of thermal vacancies may also be generated in this stage [40]. The quenching process involves rapid cooling of the heated solid solution to a low temperature to achieve a supersaturated solid solution.

At this stage, the supersaturated solid solution is thermodynamically unstable and may contain a high concentration of quenched-in vacancies. The quenching process is followed by an aging heat treatment which involves heating the alloy at a relatively low temperature below the solvus for considerable time duration. The aim of aging heat treatment is to precipitate finely dispersed nano-sized particles from the supersaturated solid solution.

2.2.3 Microstructural Changes - Phase Transformations

Upon aging, the thermodynamically unstable supersaturated solid solution (SSSS) usually goes through a series of transformations before reaching an equilibrium state. The typically observed transformation stages for a 2000 series Al-Cu alloy are as follows [41]:

$$SSSS \rightarrow Clustering\ and\ GP\ I\ zones \rightarrow \theta''(GP\ II\ zones) \rightarrow \theta' \rightarrow \theta\ (Al_2Cu) \qquad \textbf{(2-2)}$$

The GP I zones are the early nano-sized coherent precipitates to form due to clustering of solute atoms on specific planes within the parent matrix and are responsible for a large increase in strength of the material. θ'' is a quasi-coherent intermediate phase also known as GP II zones. These precipitates are larger in size than the initially formed GP I zones and are responsible for peak strengthening. Upon further aging, the formation of a large size semi-coherent θ' phase leads to a reduction in coherency strain and overall strength of the alloy. Over aging (i.e. aging for a sufficiently longer time) leads to the formation of the incoherent equilibrium θ phase. At this point, the precipitates may have grown up to several microns in size. The formation of the equilibrium θ phase have detrimental effects on mechanical properties (i.e. strength and hardness) of the alloy. The transmission electron micrographs in Figure 2-8 show presence of GP zones, θ'', θ' and θ in an Al-Cu alloy under different aging conditions.

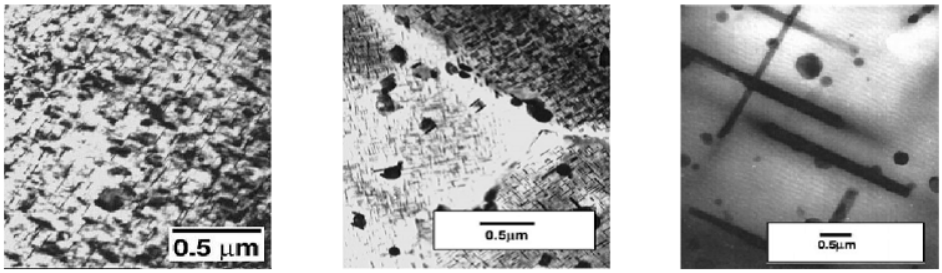

(a) (b) (c)

Figure 2-8: TEM Micrographs of precipitates in Al-Cu, (a) Cu rich GP zones and θ'' after aging for 6 hours at 180°C, (b) θ' precipitates after aging for 2 hours at 200°C and (c) θ precipitates after aging for 45 minutes at 450°C in Al-4%Cu alloys [4]**.**

Other alloys such as the 6xxx series Al-Mg-Si alloys typically follow the following precipitation sequence [42]:

$$SSSS \rightarrow Si\ and\ Mg\ clusters \rightarrow GP\ I\ zones \rightarrow \beta''(GP\ II) \rightarrow \beta' \rightarrow \beta\ (Mg_2Si) \qquad \textbf{(2-3)}$$

The Al-Zn-Mg-Cu based alloys such as AA7075 exhibit the following typical precipitation sequence [43]:

$$SSSS \rightarrow GP\ zones \rightarrow \eta' \rightarrow \eta\ \{Mg(Cu, Zn_2)\} \quad \textbf{(2-4)}$$

The current work is focused on the fracture behavior of 6xxx series precipitation hardening aluminum alloys.

2.2.4 Strengthening Mechanisms

On an atomic scale, plastic deformation is by the glide of dislocations along certain crystallographic planes of the face-centered cubic (fcc) crystal. Strengthening by precipitation hardening is obtained by increasing the resistance to dislocation glide by introducing finely dispersed precipitate particles within the parent matrix. The strengthening mechanisms (i.e. dislocation-precipitate interactions) could be one of the following kind [4]:

1) Resistance to dislocation motion due to particle induced coherency strain filed

The precipitation of coherent precipitates such as GP zones results in a high strain field in the surrounding regions. As a consequence, a passing dislocation would require a much higher shear stress to be able to pass through the distorted region [16], as shown in Figure 2-9.

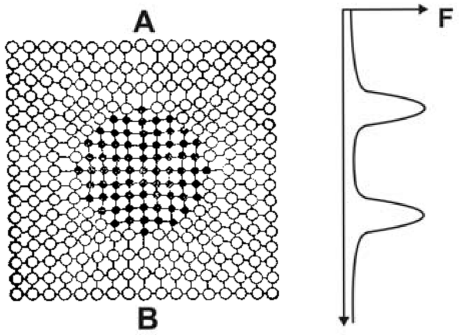

Figure 2-9: Lattice distortion caused by coherent GP zones and precipitates [4]**.**

2) Dislocations shearing through particles

Moving dislocations can shear through coherent particles as shown in Figure 2-10. The process of shearing requires extra energy leading to an increase in the material strength.

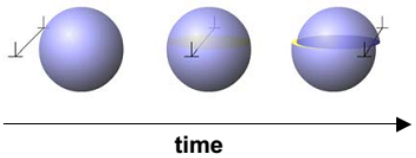

Figure 2-10: Schematic of a dislocation shearing through a particle [4]**.**

3) Dislocations bowing around particles

If it is not possible for a dislocation to shear through a precipitate (i.e. incoherent or large precipitate) than it will tend to bypass the particle by a bowing mechanism known as Orowan looping mechanism (Figure 2-11). Strengthening in this case is associated with the Orowan looping process [16].

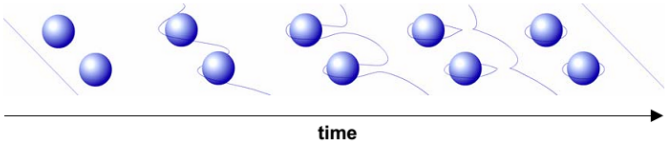

Figure 2-11: The Orowan looping process of a dislocation around particles [4].

However, at very large particle sizes, the average resistance to dislocation glide again decreases. This is because at a large particle spacing, the gliding dislocations can bypass the particles. Maximum strengthening is achieved by precipitates of an optimal radius as shown in Figure 2-12. The dislocation-precipitate interaction is important for the present study as it defines the distribution of slip within the matrix for precipitation hardening alloys and the eventual fracture behavior [44].

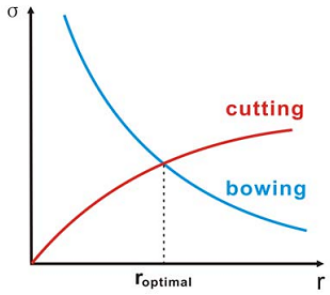

Figure 2-12: Optimal radius for maximum strengthening [4].

2.3 Fracture Mechanisms in Metals

Metals are routinely subjected to large plastic deformations through various metal forming operations to permanently shape them into a final product. However, due to inherent material heterogeneity, metals sometimes will fail or fracture prematurely. Three of the most common fracture mechanisms observed in metals are: ductile fracture, cleavage fracture and intergranular fracture as shown schematically in Figure 2-13. Ductile fracture usually results from the nucleation, growth and the coalescence of microscopic voids. Transgranular-cleavage fracture on the other hand involves failure of material along specific crystallographic planes and is usually associated with brittle materials and lastly intergranular fracture occurs when separation along grain boundaries is the preferred fracture path in the material [45].

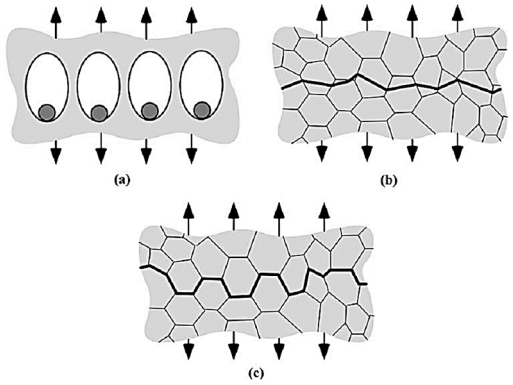

Figure 2-13: Three common modes of fracture in metals (a) ductile fracture, (b) transgranular-cleavage fracture, (c) intergranular fracture [45].

2.4 Numerical Modeling

A brief overview of the numerical modeling methods is presented in this section.

2.4.1 Crystal Plasticity Formulation

The crystal plasticity formulation is based on Schmid's law which provides a relationship between the applied stress and the resolved shear stress on a slip system. Schmid's law serves as a yield criterion for single crystals and a crystal yields or undergoes plastic deformation, when the resolved shear stress on any of its slip systems reaches the critical resolved shear stress.

In crystal plasticity framework, the total deformation of a crystallite is taken to be a function of two different physical mechanisms: crystallographic slip due to dislocation motion on the active slip systems and elastic lattice distortion. The deformation gradient **F** can be written as

$$F = F^{*}F^{p} \tag{2-5}$$

Where $\mathbf{F}^{*}$denotes elastic stretching and rigid body rotation of the crystal lattice and $\mathbf{F}^{p}$represents the deformation solely due to plastic shearing on crystallographic slip systems (**s**, **m**) where **s** is the unit slip direction and **m** is the unit slip plane normal. Furthermore, the rate of change of $\mathbf{F}^{p}$ is related to the slip rate $\dot{\gamma}^{(\alpha)}$ of the αth slip system by

$$\dot{F}^{p}.F^{p-1} = \sum_{\alpha} \dot{\gamma}^{(\alpha)}\ s^{(\alpha)}m^{(\alpha)} \tag{2-6}$$

Where the sum ranges over all activated slip systems. The unit vectors $\mathbf{s}^{(\alpha)}$ and $\mathbf{m}^{(\alpha)}$ represents the unit slip direction and the unit slip normal in the reference configuration. These vectors are defined in the deformed state as follows:

$$s^{*(\alpha)} = F^{*}.\ s^{(\alpha)}\ , \qquad m^{*(\alpha)} = m^{(\alpha)}.F^{*\,-1} \tag{2-7}$$

The velocity gradient for the current deformation state can be defined as:

$$L = \dot{F} . F^{-1} = D + W \tag{2-8}$$

Where the symmetric part **D** represents the strain-rate and the anti-symmetric part **W** represents the spin. The strain-rate tensor **D** can be decomposed into elastic and plastic strain-rate (i.e. $\mathbf{D}^*$ and $\mathbf{D}^{\mathbf{p}}$ respectively) whereas the spin tensor **W** can be decomposed into elastic and plastic spin (i.e. $\mathbf{W}^*$ and $\mathbf{W}^{\mathbf{p}}$ respectively) as shown below

$$D = D^* + D^p, \quad W = W^* + W^p \tag{2-9}$$

After some tensorial manipulation, the plastic strain-rate and plastic spin tensor can be written as:

$$D^p = \sum_{\alpha} D^{(\alpha)} \dot{\gamma}^{(\alpha)} , \quad W^p = \sum_{\alpha} W^{(\alpha)} \dot{\gamma}^{(\alpha)} \tag{2-10}$$

Where for the αth slip system, the symmetric ($\mathbf{D}^{(\boldsymbol{\alpha})}$) and the anti-symmetric tensors ($\mathbf{W}^{(\boldsymbol{\alpha})}$) are defined as follows:

$$D^{(\alpha)} = \frac{1}{2} (s^{*(\alpha)} \otimes m^{*(\alpha)} + m^{*(\alpha)} \otimes s^{*(\alpha)}) \tag{2-11}$$

and

$$W^{(\alpha)} = \frac{1}{2} (s^{*(\alpha)} \otimes m^{*(\alpha)} - m^{*(\alpha)} \otimes s^{*(\alpha)}) \tag{2-12}$$

The relationship between the elastic strain rate of the lattice, $\mathbf{D}^*$, and the Jaumann rate of Kirchhoff stress is as follows:

$$\overset{\nabla}{\tau}* = \dot{\tau} - W^*\tau + \tau W^* = \mathcal{L}D^* \tag{2-13}$$

Where $\overset{\nabla}{\boldsymbol{\tau}}*$ represents the Jaumann rate of Kirchhoff stress and $\boldsymbol{\mathcal{L}}$ represents the elastic stiffness tensor. The above relationship can be expressed in terms of the Jaumann rate of Cauchy stress $\overset{\nabla}{\boldsymbol{\sigma}}$ by introducing a tensor $\mathbf{R}^{(\boldsymbol{\alpha})}$ as follows:

$$R^{(\alpha)} = \mathcal{L}D^{(\alpha)} + W^{(\alpha)}\sigma - \sigma W^{(\alpha)} \tag{2-14}$$

Using Eq. (2-9) through Eq. (2-14), the constitutive equation can be written in terms of the Jaumann rate of Cauchy stress $\overset{\nabla}{\boldsymbol{\sigma}}$ as follows:

$$\overset{\nabla}{\sigma} = \mathcal{L}D - \dot{\sigma}^0 - \sigma\, trD \tag{2-15}$$

Where $\dot{\boldsymbol{\sigma}}^{\mathbf{0}}$ represents a visco-plastic type stress rate and is defined as

$$\dot{\sigma}^{0} = \sum_{\alpha} \mathrm{R}^{(\alpha)}\, \dot{\gamma}^{(\alpha)} \tag{2-16}$$

The resolved shear stress $\tau^{(\alpha)}$ on slip system α is related to the Cauchy stress σ through the following relationship:

$$\tau^{(\alpha)} = \mathrm{D}^{(\alpha)} . \sigma \tag{2-17}$$

The slip rate $\dot{\gamma}^{(\alpha)}$ of the αth slip system in a rate dependent crystalline solid is determined by the corresponding resolved shear stress as

$$\dot{\gamma}^{(\alpha)} = \dot{a}^{(\alpha)} f^{(\alpha)} \left(\frac{\tau^{(\alpha)}}{g^{(\alpha)}} \right) \tag{2-18}$$

where the constant $\dot{a}^{(\alpha)}$ represents the reference strain rate on the αth slip system, $f^{(\alpha)}$ is a general function describing the dependence of strain (slip) rate on shear stress $\tau^{(\alpha)}$. By defining $f^{(\alpha)}$ as a power law expression, the expression for slip rate can be re-written as:

$$\dot{\gamma}^{(\alpha)} = \dot{a}^{(\alpha)} sgn\, \tau^{(\alpha)} \left| \frac{\tau^{(\alpha)}}{g^{(\alpha)}} \right|^{1/m} \tag{2-19}$$

Where m is the strain rate sensitivity index. The function $g^{(\alpha)}$ characterizes the current strength (strain hardening) of the αth slip system. In other words, the single crystal work hardening is characterized by the evolution of strengths $g^{(\alpha)}$according to the following incremental relationship:

$$\dot{g}^{(\alpha)} = \sum_{\beta} h_{\alpha\beta}\, \dot{\gamma}^{(\beta)} \tag{2-20}$$

Where $h_{\alpha\beta}$ is the hardening rate on slip system α due to shearing on slip system β. In other words, the matrix $[h_{\alpha\beta}]$ represents a set of instantaneous hardening moduli that relate the rate of hardening on each αth slip system to the plastic slip-rate on all β systems.

One of the most important parameters in the constitutive modeling of single crystals are the components of the hardening matrix $[h_{\alpha\beta}]$. Every element of $[h_{\alpha\beta}]$ depends on the deformation history. The hardening moduli are chosen to incorporate the effects of slips on all systems on the active hardening of each system (i.e. the diagonal components $h_{\alpha\alpha}$) and on the latent hardening of each system (i.e. the off-diagonal components $h_{\alpha\beta}$). The tensor $h_{\alpha\beta}$ can be written as

$$h_{\alpha\beta} = q_{\alpha\beta} h_{\beta} \qquad \text{(no sum on } \beta) \tag{2-21}$$

where h_β represents a single crystal hardening rate and the matrix $\boldsymbol{q_{\alpha\beta}}$ represents the latent hardening behavior of the crystallite. For FCC crystals with 12 slip systems, the form of $\boldsymbol{q_{\alpha\beta}}$ is shown below where the constant q represents the ratio of latent hardening rate to self hardening rate and **A** is a 3 x 3 unity matrix.

$$q_{\alpha\beta} = \begin{bmatrix} A & qA & qA & qA \\ qA & A & qA & qA \\ qA & qA & A & qA \\ qA & qA & qA & A \end{bmatrix} \tag{2-22}$$

In the above, slip systems {1, 2, 3} are coplanar, as are systems {4, 5, 6}, {7, 8, 9}, and {10, 11, 12}. Thus, the ratio of the latent hardening rate to the self-hardening rate for coplanar systems are taken as unity. Several analytical representations of the hardening rate h_β have been reported in the literature and will be discussed in a later section.

2.4.2 Numerical Modeling of Fracture

The numerical modeling techniques that are used to model fracture (i.e. crack initiation & propagation) are reviewed in this section. The techniques include conventional finite element method (FEM) with element erosion or cohesive zone modeling, the extended finite element method (XFEM), meshfree methods and peridynamics. These modeling techniques are already existent in literature and are well developed and they will be used as a tool for modeling fracture in the present work. The aim of this section is to familiarize the reader with some of these modeling methods without focusing much on their inner workings as it is out of the scope of the present work.

2.4.2.1 Finite Element Method (FEM)

Finite element method is based on discretization of a structure or geometry into domains which are defined by nodes that describe the elements. A field quantity such as displacement is approximated using polynomial interpolation over each domain while minimizing the total energy. FEM has been the most widely used numerical procedure in the field of solid and structural mechanics. At its core, the numerical procedure seeks a solution to the stress equilibrium equation

$$\sigma_{ij,j} + \rho f_i = \rho \ddot{x}_i \tag{2-23}$$

satisfying the traction and displacement boundary conditions

$$\begin{aligned} \sigma_{ij} n_i &= t_i(t) \\ x_i(X_\alpha, t) &= D_i(t) \end{aligned} \tag{2-24}$$

where σ is the Cauchy stress, ρ is the material density, f is the body force, t is the traction and $\ddot{x}$ is the acceleration. Using divergence theorem and applying boundary conditions leads to the weak form of the equilibrium equation

$$\delta\pi = \int_v \rho\ddot{x}_i\delta x_i dv + \int_v \sigma_{ij}\delta x_{i,j} dv - \int_v \rho f_i \delta x_i dv - \int_b t_i \delta x_i ds = 0 \qquad \textbf{(2-25)}$$

After superimposing a mesh of finite elements interconnected at nodal points and by making use of shape functions, the above relationship is rewritten as

$$\sum_{m=1}^{n}\{\int_v \rho \boldsymbol{N}^T \boldsymbol{N}\boldsymbol{a} dv + \int_v \boldsymbol{B}^T\boldsymbol{\sigma}\, dv - \int_v \rho \boldsymbol{N}^T \boldsymbol{b} dv - \int_b \boldsymbol{N}^T \boldsymbol{t} ds\} = 0 \qquad \textbf{(2-26)}$$

where $\boldsymbol{N}$ is the interpolation matrix, $\boldsymbol{\sigma}$ is the stress vector, $\boldsymbol{B}$ is the displacement matrix, $\boldsymbol{a}$ is the nodal acceleration vector, $\boldsymbol{b}$ is the body force load vector and $\boldsymbol{t}$ is the applied traction load. The system of equations is numerically solved to find nodal displacements.

The simplest method to model fracture is through element erosion in conjunction with FEM. In this method, element erosion or deletion occurs when an element satisfies a predefined failure criteria. The failed element is unloaded and is removed from the mesh and further calculations. This is a very basic approach and failure response is dependent on model attributes such as mesh refinement, element formulation and the number of integration points being employed.

Another approach to model fracture is through cohesive zone modeling (CZM) in conjunction with FEM. The cohesive elements are used to model cohesive interfaces between standard elements (see Figure 2-14) and the delamination of these cohesive interfaces is used to model fracture. In Figure 2-14, a cohesive layer is placed between the faces of two elements defined by nodes n_1, n_2, n_3, n_4 and nodes m_1, m_2, m_3, m_4. The separation of the cohesive layer is defined through a cohesive constitutive law. The cohesive interface behaves elastically up to a critical separation distance and peak stress after which damage initiates. The interface is damaged and fracture proceeds at a certain critical separation distance.

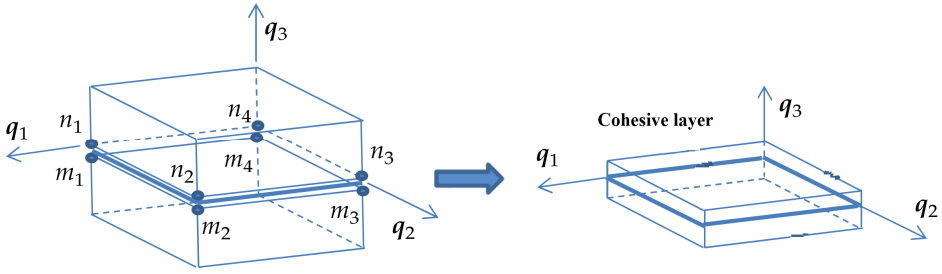

Figure 2-14: Cohesive zone modeling

The classical FEM approach is a powerful tool and is widely used to model solid mechanics problems but it has limitations in the analysis of certain problems such as modeling of fracture (crack initiation, crack propagation, branching) due to difficulties in treating discontinuities. The

classical FEM method is based on piecewise differentiable polynomial approximations and is not well suited to problems with discontinuous - singular solutions.

2.4.2.2 Extended Finite Element Method (XFEM)

The extended finite element method (XFEM) extends that classical FEM approach by enriching the finite element approximations to differential equations with discontinuous functions. The XFEM method was originally proposed by Belytschko and Black in 1999, to help alleviate shortcomings of the classical FEM approach and the method has been used since then to model the propagation of various discontinuities such as cracks, holes and inclusions [46].

The essential idea behind the XFEM method is to add discontinuous enrichment functions to the finite element approximation. The displacement using XFEM is approximated as

$$u(X,t) = \sum N_i(X)\ \{u_i(t) + H\big(f(X)\big)H(g(X,t))q_i\} \tag{2-27}$$

where $N_i(X)$ are the standard finite element shape functions and u_i and q_i are the regular and enriched nodal values respectively. The functions $H(f(X))$ and $H(g(X,t))$ are the discontinuous Heaviside jump functions used for enrichment.

The XFEM method has been extensively applied to model crack initiation and growth problems. However, the method is favorable in situations where the crack path is already known and can be represented explicitly. The XFEM approach also becomes cumbersome and computationally expensive with increasing number of cracks and crack branches.

2.4.2.3 Meshfree Methods (MMs)

As the name suggests, meshfree methods do not contain standard FE mesh and construct the approximation entirely in terms of nodes. Such methods permit reduced restriction in the discretization of the problem domain and are not susceptible to element distortion difficulties as observed in classical FEM. The meshfree methods offer a suitable alternative to model extremely large deformation, moving boundaries or discontinuities such as cracks. Most mesh free methods employ the moving least-squares approximation to construct the numerical discretization. Two of the most popular meshfree methods are the smoothed particle hydrodynamics (SPH) method [47] and the element-free galerkin (EFG) method [48].

In contrast to the classical FEM method, fracture in meshfree methods can occur naturally and there is no need to erode particles. Fracture will occur when particles move outside the domain of influence of neighboring particles [49–51]. A major drawback of meshfree methods is that they are computationally expensive due to the relatively complicated shape functions used for displacement approximations.

2.4.2.4 Peridynamics

The peridynamics approach is an alternate theory of continuum mechanics which is specifically oriented towards modeling cracks or discontinuities [52, 53]. In peridynamics, any point x within the body interacts directly with other points within a distance δ known as the 'horizon'. The material within the horizon of point x is called the 'family' of x, H_x. The vector between x and any point in its family is called a bond. The governing peridynamics equation can be written as

$$\rho\ddot{u}(x,t) = \int_{H_x} f(q,x)dV_q + b(x,t) \quad \textbf{(2-28)}$$

where $f(q,x)$ is the pairwise bond force density, q represents the force state at x, and $b(x,t)$ is the applied external force density. The bond forces are determined through corresponding material models which define bond force density as a function of bond strain. A bond breaks when its stretch exceeds a predefined critical value and when a bond breaks its load is shifted to its neighbors, leading to progressive failure. Damage or fracture is modeled through bond breakage.

2.4.3 Statistically Equivalent Microstructures

Statistically equivalent microstructures are required for 3D crystal plasticity finite element simulations performed in this work. M-Builder is one of the most advanced microstructure generation procedures developed by Rollet and co-workers [54, 55]. The procedure makes use of 2D EBSD scans of the material to obtain grain size, grain aspect ratio, orientation distribution, and misorientation distribution data. A volume of space is filled with ellipsoids of varying sizes using the experimentally measured grain morphology. A Cellular Automata (CA) procedure is used to generate a volume filled 3D grain microstructure. The grains are then assigned orientations, and the orientation distribution and misorientation distribution are calculated. A simulated annealing approach is used to adjust the assigned grain orientations until the calculated orientation and misorientation distributions within the generated microstructure match the experimental values obtained through EBSD scans. Shows an example of a 3D microstructure generated using M-builder.

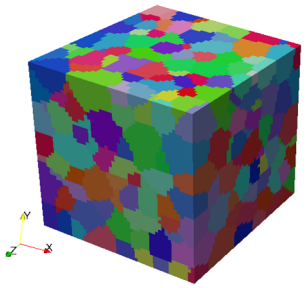

Figure 2-15: An example of a statistically equivalent microstructure.

2.5 Experimental Characterization Techniques

A brief overview of the experimental characterization techniques used in the present work is presented in this section. The techniques include scanning electron microscopy (SEM),

transmission electron microscopy (TEM), electron backscatter diffraction (EBSD) and digital image correlation (DIC).

2.5.1 Scanning Electron Microscopy (SEM)

Scanning electron microscopy is used to produce images of a specimen by scanning it with a focused beam of electrons. The images are produced due to interaction of electrons with atoms in the sample, generating various signals that contain information about the sample's surface topography and composition. Two of the most common SEM detection modes are secondary electrons (SE) detection and back-scattered electrons (BSE) detection. The SE method makes use of the secondary electrons emitted by atoms excited by the electron beam to form an image displaying topography of the surface. BSE method uses beam electrons that are reflected from deeper locations within the specimen and are therefore useful in providing information about the distribution of different elements within the sample. In the present work, SEM imaging is used to characterize the microstructure and fracture topology of precipitation hardening aluminum alloys.

2.5.1.1 Electron Backscatter Diffraction (EBSD)

Electron backscatter diffraction (EBSD) is a comparatively modern technique used in conjunction with a scanning electron microscope to obtain crystallographic information about the microstructure of a sample [56]. During EBSD analysis, a beam of electron is aimed at the point of interest on the sample surface which is tilted by approx. 70º from the horizontal (see Figure 2-16(a)) and the diffracted electrons form a pattern of kikuchi bands on the detector screen (Figure 2-16(b)). The kikuchi pattern is characteristic of the crystal structure and orientation in the sample region where it was generated. These patterns are compared to crystal structures within a database which allows the EBSD software to identify the crystallographic orientation of the lattice where the beam is positioned.

The EBSD method can provide a wealth of information about material microstructure (see Figure 2-16(c)) such as texture, grain size, grain morphology, grain boundary characterization and the different constituent phases. In the present work, EBSD method is used to characterize the initial microstructure, texture evolution and fracture behavior of the precipitation hardening aluminum alloys subjected to different loading conditions - strain paths.

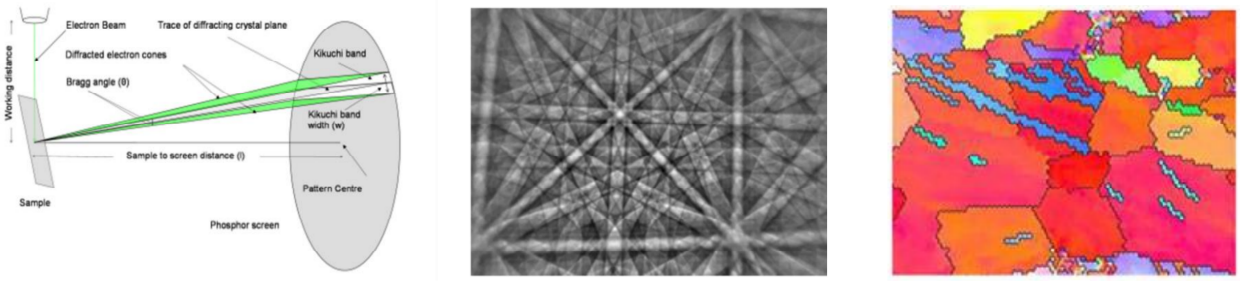

Figure 2-16: (a) Schematic of the EBSD technique. (b) The electron backscattered diffraction pattern or the kikuchi pattern. (c) An EBSD map showing microstructural state (i.e. grain size, grain orientation, deformation twinning) of an AZ31 magnesium alloy [57].

2.5.2 Transmission Electron Microscopy (TEM)

Transmission electron microscopy is used to produce images of a specimen by transmitting beam of electrons through an ultra-thin specimen. The images are produced from the interactions of the electrons transmitted through the specimen. The resolution of TEM imaging is to the order of a few Angstrom (10^{-10} m). In the present work, TEM imaging is used to study precipitates distribution within matrix, dislocation microstructure and grain boundary zones.

2.5.3 Digital Image Correlation (DIC)

Digital image correlation (DIC) is a 3D non-contact optical technique to measure surface strains during deformation. The technique can be applied from very small to large testing areas. A schematic of a DIC system is shown in Figure 2-17(a). Before testing, a random black-and-white speckle pattern is usually spray painted on the specimen surface and the DIC measurements are made from a set of snapshots collected automatically at a preset frame rate during the deformation process. The recorded images are later analyzed to generate full-field strain maps for each load step using the DIC software.

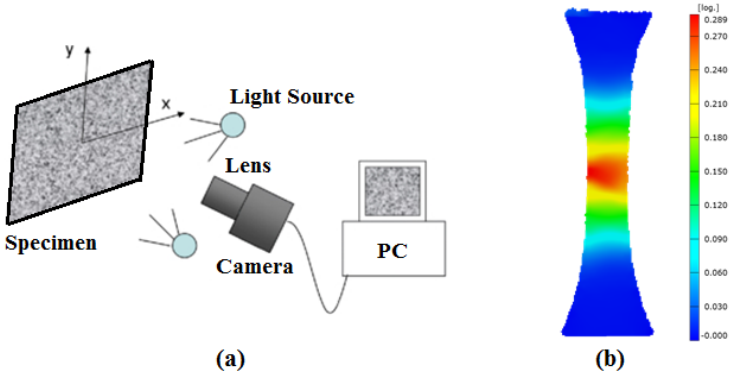

Figure 2-17: Schematic representation of a digital image correlation system. (c) Axial true strain contour map acquired during tensile testing of a magnesium alloy.

The DIC method is based on the use of facets (i.e. an area defined by pixels) to correlate distributions of grey scale values between the reference and destination states. The pixels of the

facet in the reference image are related to the deformed destination image using correlation mapping functions. The displacement fields associated with various points are converted into strains using deformation tensors. The DIC technique is extensively used in this project for strain mapping on specimen's surface during mechanical testing. The technique is used to obtain local failure strains which otherwise cannot be obtained using conventional strain measuring methods such as extensometers or strain gauges.

Chapter 3: Literature Review

3.1 Ductile Fracture in Aluminum alloys

Ductile fracture is one of the most common mechanisms of failure in aluminum alloys at room temperature. The ductile fracture is usually accompanied by a sequence of micro-macroscopic events. The most noteworthy are void nucleation, void growth, void coalescence and eventual fracture [58, 59]. The process of ductile fracture from initial void nucleation to final fracture is illustrated schematically in Figure 3-1. During metal forming processes, the presence of initial inclusions and second phase particles in the ductile matrix, offers sites where damage can nucleate in the form of micro-voids (Figure 3-1(a)-(b)). These micro-voids begin to grow around the particles by means of continued plastic deformation and induced stress triaxiality (Figure 3-1(c)). Upon further growth, the plastic strain tends to concentrate along a sheet of voids and local necking instabilities develop (Figure 3-1(d)-(e)). At a certain stage of plastic deformation, the neighbouring voids interact which triggers the process of void coalescence (Figure 3-1(f)) leading to the formation of macroscopic cracks and an eventual failure through ductile fracture. Even though the process of ductile fracture has been characterized into the three aforementioned stages (i.e. void nucleation, growth, coalescence), these mechanisms are interlinked and the actual process may also depend on many other important factors such as the morphology - distribution of precipitates and second phase particles, stress state, strain rate and temperature [60].

Due to the complexity of ductile fracture and the micro-mechanisms involved, an extensive amount of experimental as well as modeling research already exists in the literature that deals with ductile fracture of aluminum alloys. The current literature review will focus on the micro-mechanisms of ductile fracture in aluminum alloys at room temperature. The review will focus on the three aforementioned stages of damage-induced ductile fracture, i.e. void nucleation, growth and coalescence. Within each stage, an emphasis will be placed on the existing experimental observations and their link with the observed ductile fracture behavior. Furthermore, an emphasis will also be placed upon the various existing continuum based modeling techniques used to model damage evolution within each of the three aforementioned stages of ductile fracture

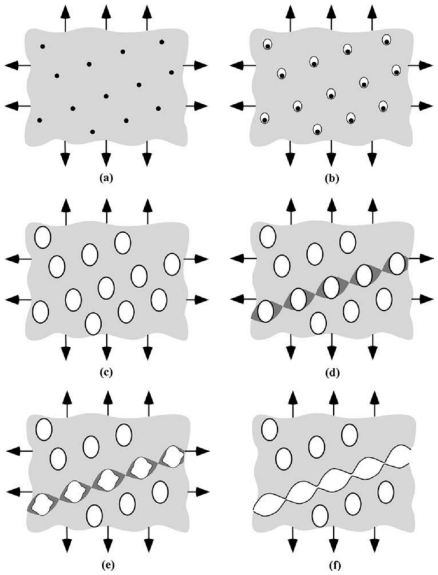

Figure 3-1: The process of ductile fracture in metals: (1) inclusion - second phase particles in the matrix, (b) void nucleation at inclusions, (c) void growth, (d) strain localization between voids, (e) necking between voids and (f) void coalescence and eventual fracture [45].

3.1.1 Void Nucleation

This stage of ductile fracture has been extensively studied in the literature. The nucleation of a void is usually not detected from the macroscopic mechanical response of materials and its definition usually depends on the scale at which the observations are being made [61]. Most of the observations made to date are on the microscale as the presence of a void can be observed with relative ease at a micro level.

3.1.1.1 Experimental Observations

Void nucleation is usually associated to the presence of second phase particles and inclusions within the grains and along the grain boundaries [62–65]. This kind of heterogeneous nucleation is common in engineering materials due to the presence of impurities and second phase particles. It has been reported that void nucleation usually occurs either by cracking of inclusion or by decohesion of the inclusion-matrix interface as shown in Figure 3-2.

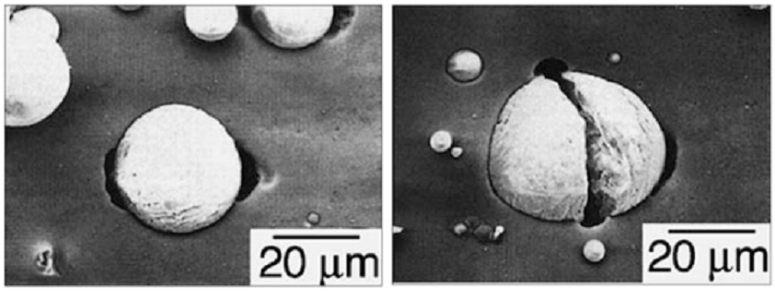

Figure 3-2: Particle-matrix decohesion (left) and cracking (right) in aluminum 6061 reinforced with alumina particles [66].

More recently, Lassance and co-workers have performed a series of microscopic observations on fractured tensile samples of direct-chill casts AA 6060 and AA 6005A aluminum alloys [67]. The authors have reported similar observations of particle cracking and decohesion at the particle-matrix interface. The authors concluded that the particles break into several fragments when their long-axis is aligned parallel to the main loading axis while particle-matrix interface separation occurs when the particle's long axis is orthogonal to the main loading direction (see Figure 3-3). Mrowka-Nowotnik has performed a study on the effects of intermetallics on fracture mechanism in extruded commercial AA 6082 aluminum alloy [68]. The author reported that void nucleation in the material is heterogeneous and most likely occurs by deboning of the particle matrix interfaces (Figure 3-4(a)). The author has also reported the occurrence of damage due to fracture of intermetallics particles (Figure 3-4(b)). Apart from these observations, Babout et al. suggested that the mechanical response of the matrix also has an effect on void nucleation [69]. As shown in Figure 3-5, the authors observed that a soft matrix favors particle decohesion while a reinforced matrix leads to particle cracking under similar testing conditions.

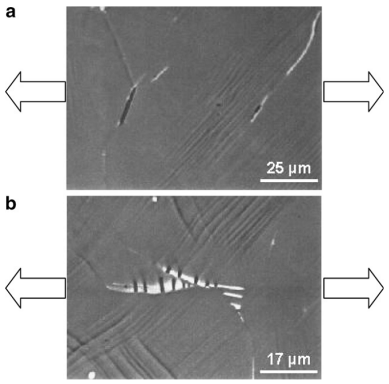

Figure 3-3: SEM micrographs taken during in situ tensile tests at room temperature on alloy AA 6060 (a) voids nucleated by interface decohesion and (b) voids nucleated by particle fragmentation [67].

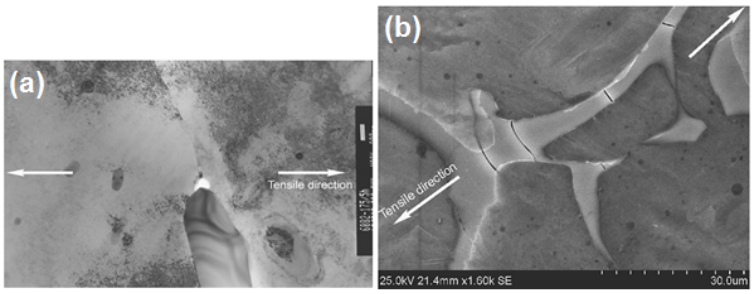

Figure 3-4: (a) TEM micrograph of AA 6082 after static tensile test. Void nucleation by decohesion at particle/matrix interface is presented and (b) SEM micrograph of AA6082 after static tensile test showing cracking of the intermetallic phase [68].

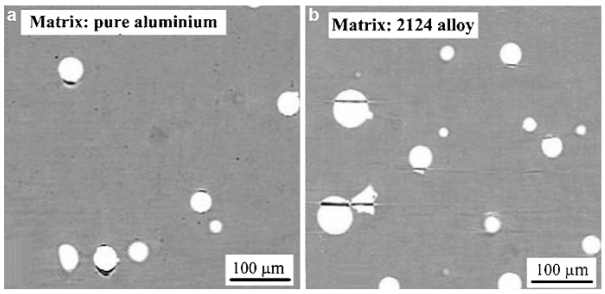

Figure 3-5: Reconstructed images of x-ray tomography during in-situ tensile test (a) pure aluminum matrix deformed by 27.5% (b) AA 2124-T6 matrix deformed by 9% [69].

It has been reported that nucleation of voids occurs at relatively lower strains for large irregularly shaped particles as they contain more internal surface defects and have a large interface area. Small particles tend to be equiaxed or spherical and favor interfacial decohesion due to the pile-up of dislocations at the particle-matrix interface [70]. Furthermore, unlike large particles, nucleation behavior at small particles is observed to be less sensitive to the loading direction [71]. In addition, it is observed that lower testing temperatures promote both particle cracking and debonding due to increased work hardening rate. However, an increase in temperature is envisaged as a decrease in matrix strength which may lead to a change from particle cracking to particle-matrix debonding [60].

There is also a significant debate in the literature on the nature of nucleation mechanisms (i.e. strain-controlled or stress-controlled). McClintock stated that the debonding of small particles is related to dislocation kinetics and hence nucleation could be considered strain-controlled [72]. Other researchers (i.e. Needleman and Shabrov) argued that process of nucleation could be considered as stress-controlled, since particle debonding and separation of interface is dependent on the hydrostatic stress [73]. In short, void nucleation is a complex and material dependent phenomenon which is rather difficult to be observed experimentally and is also quite challenging to be modelled numerically. However, there has been several attempts made to model void nucleation using a continuum-based approach. Some of the proposed models are discussed in the next section.

3.1.1.2 Void Nucleation Models

Various void nucleation models have been proposed in the literature. They are either based on dislocation-particle interactions (i.e. dislocation kinetics) [64] or on continuum mechanics [62, 74]. The dislocation theory based models are required for particles < 1µm in diameter [64].

One of the first and most widely used continuum based model is due to Argon et al. [62]. Argon et al. suggested that for particles over 1µm in equivalent diameter, the local strain hardening around the particle is comparatively similar to that in the matrix because the particle size is of the same order or greater than the mean dislocation spacing and hence, a continuum based approach could be adopted. The authors argued that the particle-matrix interfacial stress is approximately equal to

the sum of mean (hydrostatic) stress and the effective (Von Mises) stress. They proposed a critical stress condition for void nucleation by particle-matrix interface decohesion defined as:

$$\sigma_c = \sigma_e + \sigma_m \tag{3-1}$$

where σ_e is the effective Von Mises stress and σ_m is the mean (i.e. hydrostatic) stress within the matrix. According to the model proposed by Argon et al., the nucleation strain decreases with an increase in hydrostatic stress. In other words, void nucleation occurs more readily in tri-axial tensile stress field.

Brown and Stobbs also proposed a stress-based nucleation rule through relating the stress at the particle-matrix interface with dislocation density as follows [75]:

$$\sigma_n = \frac{\mu b \sqrt{\rho_d}}{2\pi} \tag{3-2}$$

where σ_n is the nucleation stress, μ is the shear modulus, ρ_d is the dislocation density and b is the burgers vector. The authors related dislocation density to the critical strain required to nucleate a particle of a given size and the interfacial stress. This enabled the authors to incorporate the effects of particle size in to their model while observing the fact that large particles tend to nucleate at comparatively smaller plastic strains.

Gurson suggested that nucleation can be expressed in terms of equivalent plastic strain [76]. Based on Gurson's results, Chu and Needleman postulated that the stress or strain required to nucleate a void follows a normal distribution [77]. The proposed strain-controlled nucleation model is expressed as:

$$\dot{f}_{\text{nucleation}} = \frac{f_{\text{n}}}{s_{\text{N}}\sqrt{2\pi}} \exp\left[-\frac{1}{2}\left(\frac{\bar{\varepsilon}^{\text{p}} - \varepsilon_{\text{N}}}{s_{\text{N}}}\right)^2\right] \dot{\bar{\varepsilon}}^{\text{p}} \tag{3-3}$$

where $\dot{f}_{nucleation}$ is the time rate of porosity contributed by void nucleation, $\bar{\epsilon}^p$ is the equivalent plastic strain, f_n is the volume fraction of void nucleating particles and ϵ_n and s_n are the average and standard deviation of the strain at which void nucleation occurs. f_n is usually determined from metallurgical analysis of the volume fraction of the second phase particles and inclusions in the material.

Many variations of the Chu and Needleman's model has been proposed in the literature [78–80]. However, the difficulty lies in the proper calibration of such models as the volume fraction of void nucleating particles and the nucleation rate depends on the type of material, its chemical composition and prior heat treatments etc. As such, these parameters are not easily quantifiable through experiments. Even though, there are many different variations of void nucleation models

currently available in the literature, most of these models only consider void nucleation by particle-matrix decohesion. Voids can also nucleate when particles crack. Similarly, some of the particles may already be damaged, cracked or deboned due to prior fabrication which may affect the subsequent process of void nucleation. Hence, further research is required to develop void nucleation models which are physically motivated, can be easily calibrated and are more representative of experimental observations.

3.1.2 Void Growth

Void growth is relatively the most understood stage of ductile fracture. Unlike void nucleation and coalescence that can occur suddenly, void growth is a comparatively stable phase of fracture process, and hence can be observed experimentally with relative ease. Once voids are nucleated, any further plastic deformation will lead to void growth usually in the direction of the applied load.

3.1.2.1 Experimental Observations

Experimental techniques such as in-situ tensile testing or interrupted examinations of longitudinal sections of tensile samples, have been used by many researchers to perform microscopic observations on void growth. Hancock and MacKenzie reported an important experimental observation about ductile fracture highlighting the fact that fracture strain decreases exponentially with increasing stress triaxiality [81]. It is also established that the increase in stress triaxiality is directly related to a significant increase in void growth rate. Geni and Kikuchi performed a series of sophisticated experiments using notched bar specimens and confirmed the occurrence of an exponential increase in void growth rate with increasing stress triaxiality [82].

Experimental observations performed on tensile specimens of an aluminum alloy have revealed that at large strains, voids within the center of neck region tend to grow both longitudinally and laterally while those outside the neck region show very little lateral growth [83]. The same study also revealed the formation of a quadrangular cavity within the necked region of the tensile specimens as a result of void growth and its interaction with shear bands (Figure 3-6).

The preceding experimental observations are based on two-dimensional analysis and therefore, cannot properly provide the volume, shape and three dimensional distribution of the voids within the matrix. However, over the past decade, the advent of in-situ 3D tomography techniques, have provided more thorough information about the 3D morphology of voids and their growth [69, 84, 85]. Figure 3-7 shows an example of a 3D tomography image obtained on an aluminum alloy containing ceramic particles. 3D tomography and other novel methods (i.e. 3D synchrotron methods) are being used in present day research by many researchers to provide new insights into the mechanisms of ductile fracture.

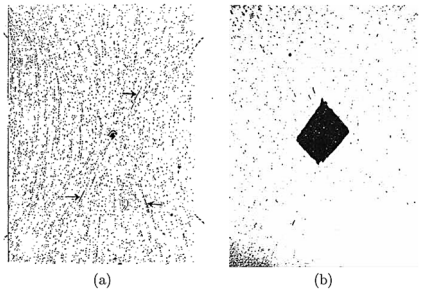

Figure 3-6: Section of necked region of aluminum crystals (a) showing cavity at intersection of shear bands at early stage of void growth and (b) formation of quadrangular cavity at a later stage of void growth [83].

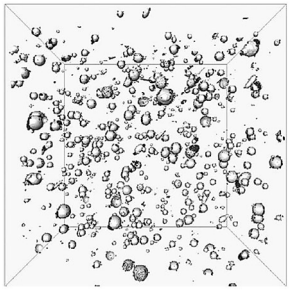

Figure 3-7: 3D X-ray tomography of an aluminum matrix containing spherical ceramic particles [85].

3.1.2.2 Void Growth Models

Void growth is a continuum-based deformation process and hence is relatively easier to model than void nucleation or coalescence. The early continuum based void growth models have been developed for initially cylindrical voids by McClintock [72] and spherical voids by Rice and Tracey [86]. McClintock analyzed a cylindrical void in an infinite work hardening matrix and expressed void growth as function of remote strain [72]. Rice and Tracey analyzed spherical void growth in an infinite perfectly plastic material and observed exponential increase of void growth with increasing hydrostatic stress [86]. A number of researchers modified the Rice and Tracey void growth model to better reflect the experimental observations [87, 88]. Huang modified the Rice and Tracey model to improve its response at lower stress triaxialities. The resulting void growth model is as follows [89]:

$$\dot{f}_{\text{growth}} = 1.28 \exp\left(\frac{3}{2}T\right)\dot{\bar{\varepsilon}}^{\text{p}} \quad \text{for } T > 1$$

$$\dot{f}_{\text{growth}} = 1.28 T^{\frac{1}{4}} \exp\left(\frac{3}{2}T\right)\dot{\bar{\varepsilon}}^{\text{p}} \quad \text{for } \frac{1}{3} \leq T \leq 1 \tag{3-4}$$

where $\dot{f}_{growth}$ represents the change in the volume fraction of voids and T represents the stress triaxiality, which is defined as the ratio of hydrostatic pressure, or mean stress, to the von Mises equivalent stress. It is important to mention here that the Rice and Tracy model is based on a

single void in an infinite medium and does not consider the interaction between voids and hence is a very simplified representation of actual void growth process in an engineering material.

One of the most famous and, in fact, the first coupled micromechanical model for deformation and void growth in a ductile material was proposed by Gurson [90]. The model is based on the simplified assumption of a ductile porous medium with an initial volume fraction of voids or porosity$f$. The porous medium obeys a standard Von Mises yield criterion and the associated flow rule. The proposed yield surface is defined as follows:

$$\phi = \frac{{\sigma_n}^2}{{\sigma_{ys}}^2} + 2f cosh \frac{3{\sigma_m}^2}{2{\sigma_{ys}}^2} - (1 - f^2) = 0 \quad \textbf{(3-5)}$$

where σ_n, σ_{ys}, σ_m are the Von Mises equivalent, yield and hydrostatic stresses respectively and f is the volume fraction of voids. One of the major drawbacks of the original Gurson model lies in the fact that void growth rate is found to be independent of porosity which is not in agreement with the experimental findings. Furthermore, the model is unable to represent coalescence and fracture. Since then, many other extensions of the Gurson model has been proposed. One noteworthy extension to the Gurson model is proposed by Tvergaard and Needleman [91]. The modified Gusron-Tvergaard-Needleman (GTN) yield surface is as follows:

$$\phi = \left(\frac{\Sigma_{\mathrm{eq}}}{R_{\mathrm{p}}}\right)^2 + 2q_1 f^* \cosh\left(\frac{3q_2}{2}\frac{\Sigma_{\mathrm{m}}}{R_{\mathrm{p}}}\right) - 1 - \left(q_1 f^*\right)^2 = 0 \quad \textbf{(3-6)}$$

In the GTN model, R_p represents the flow stress of the matrix material and q_1, q_2 and $f^*$are new parameters. The parameters q_1 and q_2 are introduced to more accurately describe the void growth rate whereas the parameter f^* can be considered as the effective porosity which is defined as:

$$f^* = \begin{cases} f & \text{if } f \le f_{\mathrm{c}} \\ f_{\mathrm{c}} + \left(\frac{1}{q_1} - f_{\mathrm{c}}\right)\frac{f - f_{\mathrm{c}}}{f_R - f_{\mathrm{c}}} & \text{if } f > f_{\mathrm{c}} \end{cases} \quad \textbf{(3-7)}$$

where f_c defines the critical volume fraction of voids for the onset of coalescence. When $f \le f_c$, the GTN model essentially behaves in a similar manner to that of the Gurson model. However, after the initiation of void coalescence (i.e. $f > f_c$), the void growth rate using the GTN model is accelerated to represent the sudden loss of load carrying capacity.

Several other extensions of the Gurson model such as the Rousselier model have been proposed [92]. More recently, void growth models with the introduction of Lode angle parameter have been proposed by many researchers [93–95]. However, the applicability, calibration and experimental validation of these models still remains a challenge to be addressed.

3.1.3 Void Coalescence

Void coalescence is perhaps the least understood of the three stages of ductile fracture. However, it is of utmost significance as it dictates the eventual failure and therefore ductility of the metal. Void coalescence phenomenon usually occurs rapidly and is associated with the sudden linkage of microvoids to form microcracks. Void coalescence behavior can depend on many different factors such as material hardening behavior, initial porosity, stress triaxiality, void size, shape and spacing.

3.1.3.1 Experimental Observations

There are two main modes of void coalescence reported in the literature. The first mode of void coalescence is due to inter-ligament necking between the voids as shown in Figure 3-8(a) [61]. During this mode of coalescence, voids tend to evolve toward a diamond shape. The second mode of void coalescence is due to inter-ligament shearing between large primary voids as shown in Figure 3-8(b) [96]. The fracture surface for failure due to ligament necking (Figure 3-9(a)[97]) exhibits a typical dimpled appearance while the fracture surface for failure due to ligament shearing (Figure 3-9(b) [97]) exhibits a smoother surface as most of the voids have been smeared out by the strong shear stress. Close examination of the fracture surfaces (in Figure 3-9) reveals the presence of multiple populations of void sizes (i.e. primary large voids and a secondary population of smaller voids). Such behavior has also been observed by many other researchers [96, 98, 99]. It is suggested that these smaller voids nucleate between the much larger primary voids and link up to assist in a rapid ligament collapse.

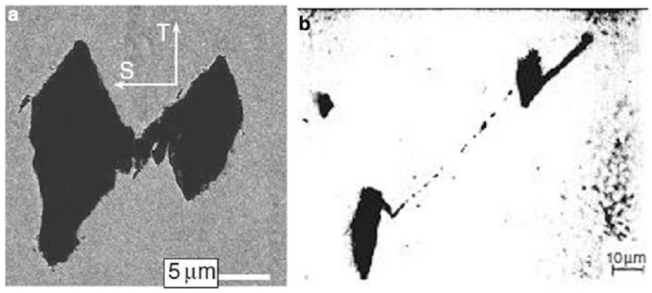

Figure 3-8: Void coalescence (a) due to inter ligament necking in plain carbon steel [61] and (b) coalescence due to inter ligament shearing [96].

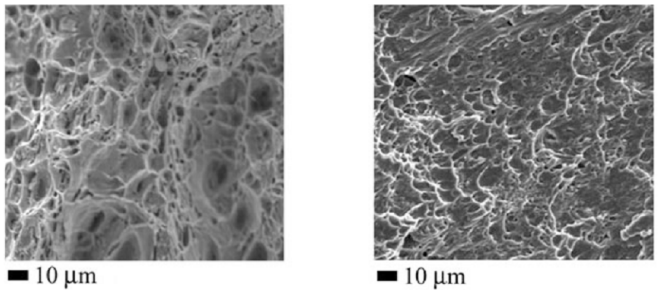

Figure 3-9: SEM fractography of Weldox 420 steel (a) failure due to ligament necking and (b) failure due to ligament shearing [97].

It is important to mention here, that even though the current literature review is aimed at ductile fracture in aluminum alloys, the above images corresponding to different grade of steels are reproduced for illustrative purposes.

A comprehensive study of void coalescence due to inter ligament necking and shearing in aluminum alloy AA 5052 sheets, has been performed by Weck and Wilkinson [100]. In the study, holes were laser drilled into the sheet in different arrangement of cavities as shown in Figure 3-10(a)-(c). Their results showed that the failure mode (i.e. inter ligament necking Figure 3-10(b) or shearing Figure 3-10(d)) is dependent on the arrangement of initial holes in the sheet. The study is significant as it shows the importance of void spacing, void orientation, constraining effects, materials yield and work hardening rate in correspondence with ductile fracture and shear localization.

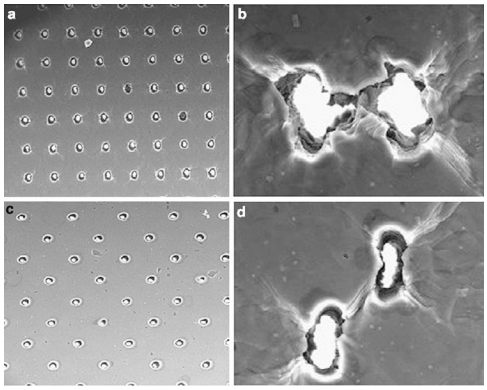

Figure 3-10: Micrograph illustrating the two main modes of void coalescence in laser drilled sheets of aluminum alloy AA 5052; (a) square array arrangement of drilled holes and (b) corresponding void coalescence by inter ligament necking and (c) holes oriented at 45° with respect to the vertical tensile axis and (d) corresponding void coalescence due to inter ligament shearing [100].

In general, void coalescence occurs due to a combination of inter ligament necking and shearing at low to moderate stress triaxialities. However, at high stress triaxialities, inter ligament necking plays a more significant role in failure due to void coalescence [97].

3.1.3.2 Void Coalescence Models

Most of the earliest models for void coalescence are based on the assumption that void coalescence starts once a critical geometric parameter has been reached. The critical geometric parameter could be the void radius, spacing or volume fraction of porosity [72, 101]. These types of criterion are easier to implement and may produce satisfactory results for a given material. However, a more general approach would require models to incorporate microstructural information related to void/ligament dimensions, morphology and inter ligament spacing etc.

One such model, incorporating void coalescence by inter ligament necking was proposed by Brown and Embury [102]. The authors proposed that the internal necking between voids could be

considered to initiate when it is possible for 45° micro-shear bands to connect two neighboring voids as shown schematically in Figure 3-11.

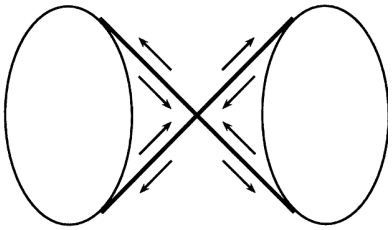

Figure 3-11: Schematic of the void coalescence model proposed by Brown and Embury [102].

Using the Brown and Embury's model, the strain to failure ε_f is defined as:

$$\varepsilon_f = ln(1 + \varepsilon_g + \varepsilon_n) = ln\left(\sqrt{\frac{\pi}{6V_f}} - \sqrt{\frac{2}{3}} + \varepsilon_n\right) \quad \textbf{(3-8)}$$

where ε_n is the strain to nucleate the void, ε_g is the strain to grow itto the critical size and V_f is the volume fraction of spherical voids. The Brown and Embury's model has been successfully employed by several researchers to model void coalescence failure by ligament necking in aluminum alloys [100, 103, 104]. On the contrary, it is worth mentioning that, no proper model for void coalescence by shearing (void sheeting) exists in the literature.

Based on the experimental observations of Brown and Embury for critical distance between voids at coalescence, Needleman and Tvergaard extended the Gurson's model of void growth to account for the final failure [105]. They incorporated a parameter accounting for the critical volume fraction of voids f_c and modified the Gurson's model when the actual volume fraction $f > f_c$ using a function f^*as follows:

$$f^* = \begin{cases} f, & \text{for} f \le f_c \\ f_c + K(f - f_c), & \text{for} f \ge f_c \end{cases} \quad \textbf{(3-9)}$$

where K is a constant known as acceleration factor.

Another well know model for void coalescence is proposed by Thomason by studying the transition to localisation for elastic-perfectly plastic solids using slip line solutions [70, 106]. The condition for the onset of void coalescence is defined as

$$\frac{1}{1 - f_2}\frac{1}{1 - \chi^2}\frac{\Sigma_n}{R_p} = \frac{2}{3}\left[\alpha\left(\frac{1 - \chi}{\chi\lambda}\right)^2 + 1.24\frac{1}{\chi^{1/2}}\right] \quad \textbf{(3-10)}$$

where $\Sigma_n$is the critical value of axial stress, Σ_z is the value at which void coalescence starts, f_2 is the volume fraction of secondary voids, the parameter α defines the hardening, λ defines the void shape and the paramter χ is used to define void spacing. The significance of Thomason model is much more than providing a criterion for void coalescence. The model also provides the evolution of axial stresses as a function of the change in void shape and spacing during the process of void coalescence. The Thomason model was later transformed into a yield surface to be implemented in to a constitutive model [81, 107].

3.1.4 Continuum Damage Approach

Continuum damage mechanics (CDM) has been widely used to model ductile fracture in aluminum alloys. The CDM approach allows one to describe the material's progressive deterioration (damage) by using damage as an internal state variable. The damage is modeled progressively within each stage of ductile fracture (i.e. void nucleation, void growth and void coalescence) through evolution of the internal state variables. The void nucleation, growth and coalescence models presented in the previous sections provide evolution equations for damage within each stage of ductile fracture. Recently, more complex flow potential formulations have been proposed in the literature to account for void volume fraction, void aspect ratio and void axis and particles distribution [108–113]. However, major challenges still remain in the parameter identification and proper calibration of the phenomenological evolution equations of these models due to the added complexity associated with a large set of calibration parameters.

3.2 Intergranular Fracture in Aluminum alloys

In contrast to the wealth of information on ductile fracture in literature, there exists a limited amount of experimental and modeling research on intergranular fracture in precipitation hardening aluminum alloys. The intergranular fracture in precipitation hardening aluminum alloys is also referred to as the grain boundary ductile fracture (GBDF) since the material behaves in a ductile manner but the crack path favors grain boundaries. This section is aimed to shed some light on the experimental observations related to the phenomenon of grain boundary ductile fracture in precipitation hardening aluminum alloys and the limited existent modeling efforts in the literature.

3.2.1 Experimental Observations

Three main mechanisms that have been linked to the occurrence of intergranular ductile fracture in precipitation hardening aluminum alloys. The first being the growth of microvoids at large grain boundary precipitates, the second being the localization of strain in the soft and comparatively solute-free grain boundaries, precipitation free zones (PFZ) and the third being the dislocation-precipitate interaction giving rise to inhomogeneous slip distributions that may apply large stress concentrations to the grain boundaries at the end of slip bands. The existing experimental evidences supporting the link of each mechanism to the occurrence of intergranular ductile fracture are discussed next.

The early work by Ryder and Smale in 1962, on commercial precipitation hardening aluminum alloys, has shown that the heterogeneously nucleated grain boundary precipitates in aluminum alloys served as initiation sites for microvoid formation and coalescence, leading to a ductile grain boundary fracture [114]. Similar observations have been made by several other researchers in which evidence of the presence of fine dimples on the fracture surface was linked with microvoid formation and coalescence at grain boundary precipitates [115–117]. An example of an Mg_2Si equilibrium precipitate nucleated at grain boundaries in aluminum alloy AA6260 is shown in Figure 3-12. An important study performed by Embury and Nes on commercial Al-Zn-Mg alloys showed that longer aging times and higher aging temperatures can both lead to coarser grain boundary precipitates, lowering the intrinsic fracture strength of the boundary [118]. Kirman and Burghard, in independent works, studied grain boundary fracture in various precipitation hardening aluminum alloys and the authors demonstrated that the spacing of the ductile grain boundary dimples on the fracture surface was similar to the spacing of precipitates on the grain boundaries prior to fracture [119, 120]. More recently, a study performed by Poole and co-workers, to evaluate the nature of the dislocation–precipitate interaction and its relationship to the mechanical properties for a commercial Al–Mg–Si–Cu alloy, reported the occurrence of grain boundary fracture in peak-aged condition. The authors suggested that the presence of grain boundary precipitates and formation of PFZs results in a reduction of the intrinsic fracture strength of the grain boundary and since the stress acting on the grain boundary is proportional to the far field applied stress which is a maximum at the peak strength, the peak-aged alloy failed along grain boundaries.

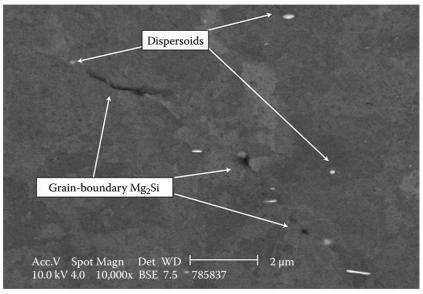

Figure 3-12: Mg_2Si precipitates at grain boundaries in AA6260 [121].

The initial work of Geisler in 1951 and by several other researchers thereafter, has suggested that grain boundary fracture in precipitation hardened aluminum alloys is linked with strain localization in the soft precipitate free zones adjacent to the grain boundaries [115, 116, 122]. Abe and co-workers have studied the mechanical properties of an Al-Zn-Mg alloy with various width of precipitate-free zones (Figure 3-13(a)) and the authors have reported that the plastic deformation has been found to occur preferentially in the PFZ, resulting in the pile up of dislocations at the PFZ-matrix boundary (see Figure 3-13 (b)). The author suggested that cracks may initiate in the PFZ, particularly at the interface of grain boundary precipitates since the dislocation density in the PFZ becomes extremely high (Figure 3-13(c)).

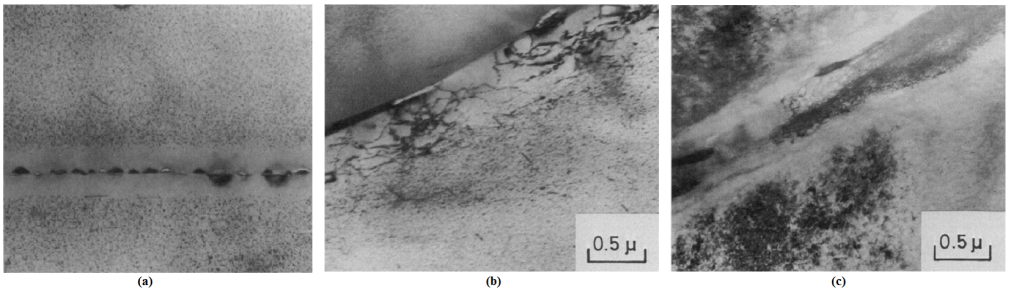

Figure 3-13: Precipitation free zone and grain boundary precipitates in an Al-Zn-Mg alloy. (b) Dislocations pile-up at the PFZ-matrix boundary. (c) Extremely high dislocation content close to fracture in a tensile test.

Lutjering and Gysler studied the role of PFZ in correlation with fracture strains in a commercial alloy 7475 [123]. The authors reported a significant decrease in tesnile fracure strains when the samples were tested in an orientation giving maximum opportunity for PFZ shear . The work by several other researchers also suggest that localized PFZ strain plays a detrimental role in that it can induce more GB void growth than would have occurred at a given sample strain in the absence of [118, 124]. However, the role of PFZ in the eventual final fracture process still remains an area of research, since the development of voids at grain boundary precipitates appear to be formed by stress concenrations even in the absence of a PFZ [125, 126].

In the early 1950's, based on his experimental work on dislocations and plastic flow, Mott suggested that stress concentration around piled-up dislocations at the end of a slip line may be adequate to initiate a crack [127]. Based on this preliminary investigation, Ryum studied grain boundary fracture in Al-Zn-Mg precipitation hardening alloys [128]. The auhtor reported the localization of slip into narrow slip bands, leading to stress concentrations along grain boundaries and resulting in intergranular fracture. Several other researchers have reported similar observations of surface slip steps on GB fracture surfaces in precipitation hardening alloys [123, 129, 130]. Evensen and co-workers studied intergrannular fracture in Al-Mg-Si precipitation hardening alloys using different aging heat treatments and the authors consistently observed the channeling of slip into coarse slip bands (see Figure 3-14) for under-aged and peak-aged conditions [44]. The authors suggested that prior to the condition of maximum precipitation hardening the role of the precipitate particles is not only to increase the yield strength but to promote the localization of slip in coarse slip bands, raising the stress concentration imposed on the grain boundaries, resulting in grain boundary decohesion.

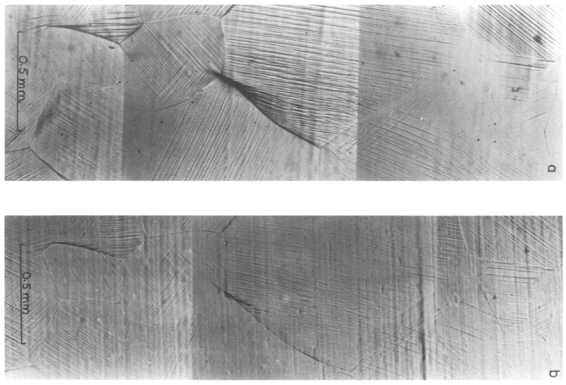

Figure 3-14: Optical micrographs showing coarse slip lines on specimens' surfaces after tensile straining[44].

A recent study by Poole and co-workers on the shearable – non-shearable transition in Al–Mg–Si–Cu precipitation hardening alloys suggested that the distribution of slip (which in turn is governed by the nature of precipitates-dislocations interaction) and the intrinsic fracture properties of the grain boundary are critical factors in controlling the intergranular fracture process [131]. Even though there has been several experimental studies performed to gain insights in to the phenomenon of grain boundary ductile fracture, the literature still lacks a systematic experimental approach to tackle such an issue.

3.2.2 Physical Models

In contrast to the several models available for ductile fracture, there are only a limited number of physical models proposed for grain boundary ductile fracture in precipitation hardening aluminum alloys. One of the earliest models was proposed by Stroh [132]. The model is based on the idea that the stress concentration around the piled-up dislocations at the end of a slip line is sufficient to initiate a crack. Stroh proposed a relationship to estimate this maximum stress as shown below

$$\sigma_{max} = \left(\frac{2}{\sqrt{3}}\right)\left(\frac{L}{r}\right)^{\frac{1}{2}}\sigma \qquad \textbf{(3-11)}$$

where σ is the applied stress, L the pile-up length and $2r$ the crack length. The pile-up length is dependent on the number of locked dislocations, the applied stress and material dependent parameters such as the Poisson's ratio and the modulus of rigidity. Embury and Nes proposed an empirical fracture model by linking the grain boundary shear strain γ_f with the area fraction of the grain boundary covered by precipitates A_f [118]. The authors suggested that for materials containing high area fraction of incoherent grain boundary precipitates and a PFZ of unspecified width, the voids around each particle will join up and the material will fracture when the grain boundary shear strain γ_f reaches a critical value, given by

$$\gamma_f \approx \left[\left(1/A_f\right)^{0.5} - 1\right]/2 \quad \textbf{(3-12)}$$

Evensen and co-workers studied the fracture behavior of Al-Mg-Si and suggested that intergranular fracture is controlled by a critical stress condition acting on the grain boundary [44]. The authors proposed a simple model for the stress acting on the grain boundary, σ_{GB} due to the intersection of a slip band with the grain boundary as follows

$$\sigma_{GB} = \sigma_{app} + (d/w)^{0.5}\left(\sigma_{app} - \sigma_0\right) \quad \textbf{(3-13)}$$

where σ_{app} is the far field applied stress, d is the length of the slip band, w is the width of the slip band and σ_0 is the resistance within the slip band due to precipitates. The intergranular failure would result when the grain boundary stress, σ_{GB} is equal to the intrinsic fracture strength of the boundary. The authors proposed the following relationship to estimate the fracture strength of the boundary

$$\sigma_F = \left(4\mu\gamma/k_f\right)(d)^{-0.5} \quad \textbf{(3-14)}$$

where d is the grain diameter, μ is the shear modulus, k_f is a measure of the difficulty of transmitted slip at the boundary and γ is a measure of the total work per unit area needed for continued crack growth. More recently, Pouillier and co-workers studied intergranular fracture in an aluminum alloy and the authors proposed a simplified stress based grain boundary failure criterion [133]. The authors suggested that a first approximation to the normal tractions σ_f needed to fracture a given grain boundary can be obtained by solving an Eshelby's inclusion problem where the failed grain boundary is a hard phase which behaves elastically. Using this assumption, the authors showed that the solution to the Eshelbian problem yields uniform stresses within the inclusion, and that the maximum principal stress σ_{xx} is given by

$$\sigma_{xx} = \Sigma_{xx} + k\left(\Sigma_{eq} - \sigma_y\right) \quad \textbf{(3-15)}$$

where Σ_{xx} is the average axial stress in the polycrystal at the moment the first grain boundary fails, σ_y is the material yield stress, Σ_{eq} is the average Mises stress in the inclusion and k is a function of the inclusion shape – equal to 1 for the spherical particle. The authors suggested that the value of σ_{xx} can be considered to be a first estimate of the critical grain boundary traction, σ_f, required to fracture a grain boundary. Even though, efforts have been made to develop fracture models for grain boundary ductile failure in precipitation hardening aluminum alloys, there still is a need for robust, accurate and physically motivated fracture models for these alloys.

3.3 Crystal Plasticity Hardening Models

Work hardening (also referred to as strain hardening) is a strengthening mechanism in metals. Work hardening results from a dramatic increase in the number of dislocation-dislocation and

dislocation-precipitates interactions reducing dislocation mobility. As a consequence, larger stresses must be applied to cause any additional plastic deformation, hence strengthening the material. Figure 3-15 shows the typical strain hardening response of single crystals. The shear stress - shear strain curve contains three distinct regions corresponding to three different stages of hardening during plastic deformation: Stage I, a region of easy glide; Stage II, a region of linear hardening; and Stage III, a region of parabolic hardening or dynamic recovery. A number of crystal plasticity hardening models have been proposed to predict the strain hardening behavior of metallic materials. A literature review on some of the existing hardening models is presented in the following subsections.

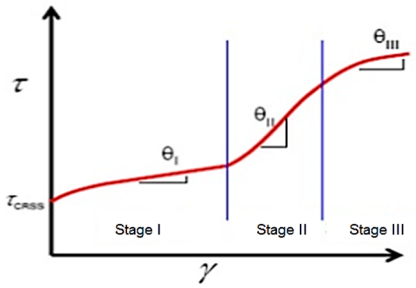

Figure 3-15: Schematic representation of shear stress-strain curve for single crystals

3.3.1 Phenomenological Hardening Models

Several phenomenological constitutive hardening laws have been proposed to date. These models use the critical resolved shear stress τ_c^α, as the state variable for each slip system α. The slip system shear rate $\dot{\gamma}^\alpha$, is then expressed as a function of the critical resolved shear stress τ_c^α and the resolved shear stress τ^α. The evolution of the critical resolved shear stress τ_c^α is further expressed in terms of some function $g^{(\alpha)}$ which characterizes the current strength (strain hardening) of the αth slip system. Using this framework, the earliest formulations were proposed by Rice et al. [134] and Peirce et al. [135, 136] for FCC single crystals where the kinetic law for single slip is written as:

$$\dot{\gamma}^{(\alpha)} = \dot{\gamma}_0 \, sgn\, \tau^{(\alpha)} \left| \frac{\tau^{(\alpha)}}{g^{(\alpha)}} \right|^{1/m} \tag{3-16}$$

where $\dot{\gamma}_0$ and m are material dependent parameters that represent the reference shear rate and the strain rate sensitivity index, respectively. Eq. (2-19) – Eq. (2-22) are reproduced here as Eq. (3-16) – Eq. (3-19) for clarity. The single crystal work hardening is characterized by the evolution of strengths $g^{(\alpha)}$according to the following incremental relationship:

$$\dot{g}^{(\alpha)} = \sum_{\beta} h_{\alpha\beta} \, \dot{\gamma}^{(\beta)} \tag{3-17}$$

where $h_{\alpha\beta}$ is the hardening rate on slip system α due to shearing on slip system β. In other words, the matrix $[h_{\alpha\beta}]$ represents a set of instantaneous hardening moduli that relate the rate of hardening on each αth slip system to the plastic slip-rate on all β systems.

One of the most important parameters in the constitutive modeling of single crystals are the components of the hardening matrix $[h_{\alpha\beta}]$. Every element of $[h_{\alpha\beta}]$ depends on the deformation history. The hardening moduli are chosen to incorporate the effects of slips on all systems on the active hardening of each system (i.e. the diagonal components $h_{\alpha\alpha}$) and on the latent hardening of each system (i.e. the off-diagonal components $h_{\alpha\beta}$). The tensor $h_{\alpha\beta}$ can be written as

$$h_{\alpha\beta} = q_{\alpha\beta} h_{\beta} \qquad \text{(no sum on } \beta) \tag{3-18}$$

Where h_{β} represents a single crystal hardening rate and the matrix $q_{\alpha\beta}$ represents the latent hardening behavior of the crystallite. The form of $q_{\alpha\beta}$ is shown below where the constant q represents the ratio of latent hardening rate to self hardening rate and A is a 3 x 3 matrix fully populated by ones.

$$q_{\alpha\beta} = \begin{bmatrix} A & qA & qA & qA \\ qA & A & qA & qA \\ qA & qA & A & qA \\ qA & qA & qA & A \end{bmatrix} \tag{3-19}$$

Several analytical representations of h_{β} have been reported in the literature [137–140]. For instance, Chang and Asaro [137] studied localized shearing in single crystals of aluminum alloys and proposed the following relation for the hardening rate.

$$h_{\beta} = h_s + (h_o - h_s) sech^2 \left\{ \left(\frac{h_o - h_s}{\tau_s - \tau_o} \right) \gamma^{\alpha} \right\} \tag{3-20}$$

where τ_s is the saturation value of shear stress, h_o and h_s represents the system's initial and asymptotic hardening rates.

The phenomenological strain hardening models are widely used in crystal plasticity simulations. However, their main drawback is the lack of their physical basis and such models cannot directly correlate back to microstructural aspects such as dislocation content.

3.3.2 Physics based Hardening Models

More recently, several physically based hardening models have been proposed for crystal plasticity framework. Unlike the phenomenological hardening models, these physics based hardening models rely on internal state variables, most notably dislocation density. These models are dependent on the evolution of dislocation densities to calculate the macroscopic flow stress response. Since dislocations lie at the core of plastic deformation, such models are able to correlate

the macroscopic deformation phenomena with the underlying microstructural aspects. Several dislocations based hardening models have been proposed [141–146]. Ma et al. recently developed and implemented a dislocation density based constitutive model for face-centred cubic crystals into a crystal plasticity finite element framework [144–146]. The approach assumes a homogeneous dislocation structure and tracks the evolution of the statistically stored and the geometrically necessary dislocation densities in order to consider strain gradients. However, calculation of strain gradients renders the model size sensitive and increases the difficulty for complex loading cases.

3.3.2.1 Saimoto-Van Houtte Constitutive Model

Saimoto and Van Houtte proposed an alternative and useful approach of including dislocation physics into a local crystal plasticity framework [147]. They proposed a constitutive relationship based on Taylor slip analysis to model the work hardening behavior of materials. The approach used by the authors is to equate the energy of dislocations, required to generate the imposed incremental strain, with the amount of energy stored as determined by the flow stress of the material. According to the model, the density of new dislocations that have been generated can be calculated by:

$$\Delta\rho^{create} = \frac{p\Delta\Upsilon}{C_1\tau^{\beta}b} = \frac{P\Delta\Upsilon}{\lambda b} \tag{3-21}$$

Where $\lambda = C_1\tau^{\beta}$ represents the mean slip distance and b is the burgers vector. The amount of stored energy can be calculated from the flow stress using Taylor's relationship:

$$\tau = \alpha\mu b\rho^{1/2} \tag{3-22}$$

where α is a parameter quantifying the strength of obstacles. In a similar manner, the retained dislocation density can be written as:

$$\Delta\rho^{retain} = \frac{2(2\tau d\tau)}{(\alpha\mu b)^2} \tag{3-23}$$

The possibility of dynamic annihilation during deformation has also been considered by introducing an annihilation factor A. By equating $\Delta\rho^{create}$ and $\Delta\rho^{retain}$ and further mathematical manipulations, the authors were able to obtain a constitutive relation between flow stress and strain in terms of the parameters related to the evolving microstructure that can be determined experimentally. The constitutive relationship is as follows:

$$\tau = \left[(2+\beta)(\alpha\mu b)^2\frac{1}{4b}\right]^{\frac{1}{(2+\beta)}}\gamma^{\frac{1}{(2+\beta)}}C_{P/A}\,\dot{\gamma}^{m} \tag{3-24}$$

by rearranging the above equation in terms of $\dot{\gamma}$, one can write:

$$\dot{\gamma} = \left(\left[(2+\beta)(\alpha \mu b)^2 \frac{1}{4b} \right]^{\frac{-1}{(2+\beta)}} \gamma^{\frac{-1}{(2+\beta)}} \frac{1}{C_{P/A}} \right)^{\frac{1}{m}} \tau^{\frac{1}{m}} \quad \textbf{(3-25)}$$

where $C_{P/A}$ can be written as:

$$C_{P/A} = C_f \left(\frac{P}{A} . \frac{1}{c_1} \right)^{\frac{1}{(2+\beta)}} \quad \textbf{(3-26)}$$

P, A, c_1 and β are material parameters and are obtained from the stress-strain curve following the procedure outlined by Saimoto and Van Houtte [147]. The model has been previously implemented into crystal plasticity framework by Brahme *et al*. [148] and the model shows excellent predictability of flow stress and forming limit strains at room temperature.

One of the objectives of the present work is to develop a crystal plasticity based hardening model for precipitation hardening aluminum alloys. It is hypothesized that the Saimoto-Van Houtte hardening model, described above, can provide an excellent foundation for development of a physics based hardening model for these alloys.

Chapter 4: Research Overview

4.1 Research Strategy

To address each of the major objectives, the research project has been divided into several parts as outlined next.

4.1.1 Physical understanding of the hardening and fracture behavior of AA6xxx series precipitation hardening aluminum alloys through experiments.

The experimental study in the current research is focused on characterizing the mechanical behavior of AA6xxx series precipitation hardening aluminum alloys under different strain paths. An emphasis is put on investigating correlations between microstructure and the observed hardening, flow localization and fracture behavior. Strain paths such as bending, cyclic shear and cyclic tension-compression are investigated as they are commonly observed in forming and crashworthiness applications. Furthermore, the physical understanding developed through experimentations and the accompanying experimental data is used to develop, calibrate and validate the proposed hardening and failure models. Characterization techniques such as optical microscopy, scanning electron microscopy, scanning transmission electron microscopy, electron backscatter diffraction, energy dispersive x-ray spectroscopy, 3D laser scanning profilometry and digital image correlation are used to facilitate experimental analysis.

4.1.2 Development of a slip level hardening model for precipitation hardening aluminum alloys.

The dislocation based hardening models discussed previously use dislocation densities as an internal state variable. Even though, dislocations are fundamental to plastic deformation, more essential parameters are required for a full characterization of the material microstructure, such as grain size and grain morphology. Furthermore, for precipitation hardening aluminum alloys, it is also vital to introduce physics that can account for the effects of precipitate – dislocation interactions and the formation of deformation induced dislocation microstructure. In this research, a backstress hardening model is developed to incorporate the relevant microstructural physics and is validated against experimental results.

4.1.3 Development of a physics-based fracture/failure criterion for precipitation hardening aluminum alloys.

The fracture behavior of the AA6xxx series precipitation hardening alloys is rather complex and can exhibit a predominant transgranular or intergranular crack propagation behavior, depending on the heat treatment and related microstructural aspects. However, in general, the fracture behavior is a mix of both transgranular and intergranular failure. In contrast to the several phenomenological models available for ductile fracture such as those for void nucleation, growth and coalescence, the physics-based models for failure are not well developed. In the current research, a physics-based failure criterion is developed for precipitation hardening aluminum

alloys. The model is based on the concept of point defects generation, nano-void accumulation and growth during deformation. The proposed model is implemented into crystal plasticity framework, where richness of the microstructure can be harnessed, and validated against experimental data.

4.1.4 Development and validation of a multiscale modeling approach by simulating flow localization and fracture in precipitation hardening alloys under different stain paths.

In this work, a multi-scale modeling approach is proposed to enhance existing modeling capabilities for better predictability of material response under complex loading paths. The proposed approach links component level or macroscale phenomenological modeling to micro level crystal plasticity modeling to predict microstructure dependent response such as strain localization, shear banding and fracture. The component or part level modeling is performed using classical phenomenological plasticity which is computationally less expensive and is the industrial norm. However, the drawback of using phenomenological plasticity lies in the inability to include the relevant microstructural physics that is significant for accurate predictions. To address this issue, boundary conditions for the region of interest are extracted from macroscale simulation and are applied to the crystal plasticity model which operates at a lower length scale. The usefulness of this approach lies in the ability to acquire and apply realistic boundary conditions to the microscale CPFEM RVE with a better representation of microstructural physics through crystal plasticity formulation. If required, the relevant information from microscale simulation is than fed back to component level for further analysis.

Figure 4-1 shows a schematic that represents the overall research strategy and further highlights the interaction between each research task or component.

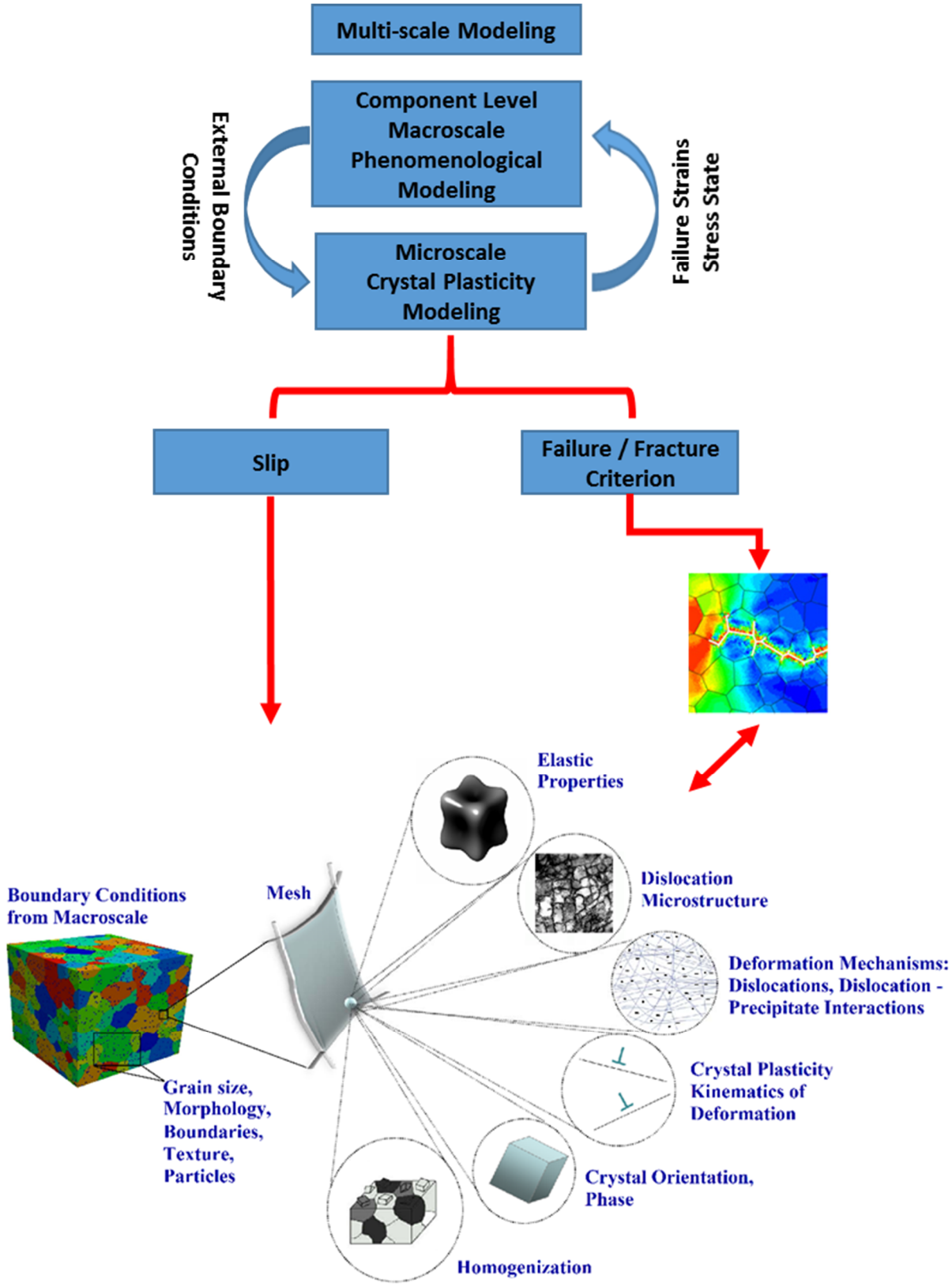

Figure 4-1: The overall research strategy

4.2 Summary of Contributions

The work completed to achieve the research objectives are presented in next six chapters. Each chapter is based on the following published or submitted manuscripts:

Chapter 5 **Muhammad, W**., Brahme, A. P., Kang, J., Mishra, R. K., & Inal, K. (2017). Experimental and numerical investigation of texture evolution and the effects of intragranular backstresses in aluminum alloys subjected to large strain cyclic deformation. International Journal of Plasticity, 93, 137-163. Doi: 10.1016/j.ijplas.2016.11.003

Chapter 6 **Muhammad, W**., Ali, U., Brahme, A., Kang, J., Mishra, R. K., & Inal, K. (2019). Experimental analyses and numerical modeling of texture evolution and the development of surface roughness during bending of an extruded aluminum alloy using a multiscale modeling framework. International Journal of Plasticity, 117, 93-121. Doi: 10.1016/j.ijplas.2017.09.013

Chapter 7 **Muhammad, W**., Brahme, A. P, Sabat, R. K., Mishra, R. K., & Inal, K. (2019). A criterion for ductile failure in age-hardenable aluminum alloys. Metallurgical and Materials Transactions A. Submitted.

Chapter 8 **Muhammad, W**., Kang, J., Brahme, A. P., Ali, U, Hirsch, J., Brinkman, H, Engler, O., Mishra, R. K., & Inal, K. (2019). Bendability enhancement of an age-hardenable aluminum alloy: Part I — relationship between microstructure, plastic deformation and fracture. Materials Science & Engineering A, 753, 179-191. Doi: 10.1016/j.msea.2019.03.053

Chapter 9 **Muhammad, W**., Brahme, A. P., Ali, U., Hirsch, J., Engler, O., Aretz, H., Kang, J., Mishra, R. K., & Inal, K. (2019). Bendability enhancement of an age-hardenable aluminum alloy: Part II — multiscale numerical modeling of shear banding and fracture. Materials Science & Engineering A, 754, 161-177. Doi: 10.1016/j.msea.2019.03.050

Chapter 10 **Muhammad, W**., Sabat, R. K., Brahme, A. P., Kang, J., Mishra, R. K., Shalchi-Amirkhiz, B., Hirsch, J., & Inal, K. (2019). Deformation banding in a precipitation hardened aluminum alloy during simple shear deformation. Scripta Materialia, 162, 300-305. Doi: 10.1016/j.scriptamat.2018.11.032

In addition to these publications, the research conducted herein also facilitated the following publications. However, these published works do not have a direct impact on the overall research objectives of this thesis and are referenced only as supporting work:

- **Muhammad, W**., Brahme, A., Kang, J., Mishra, R., & Inal, K. (2016). Large strain cyclic simple shear behavior of aluminum extrusions: an experimental and numerical study. In Light Metals 2016 (pp. 169-174). Springer.
  Doi: 10.1007/978-3-319-48251-4_29

- Kang, J., & **Muhammad, W**. (2016). Measurement of Plastic Strain Ratio Using Digital Image Correlation. ASTM Journal of Testing and Evaluation, 45(5), 1587-1600. Doi: 10.1520/JTE20160192
  To be included in updated ASTM standard.

- **Muhammad, W**., Kang, J., Mishra, R. K., & Inal, K. (2018). A Simple Approach to Performing Large Strain Cyclic Simple Shear Tests: Methodology and Experimental Results. ASTM Journal of Testing and Evaluation, 46(6), 2604-2615. Doi: 10.1520/JTE20170172
  To be included in updated ASTM standard.

- Ali, U., Odoh, D., **Muhammad, W**., Brahme, A., Mishra, R. K., Wells, M., & Inal, K. (2017). Experimental investigation and through process crystal plasticity-static recrystallization modeling of temperature and strain rate effects during hot compression of AA6063. Materials Science and Engineering: A, 700, 374-386.
  Doi: 10.1016/j.msea.2017.06.030

- Kohar, C. P., Bassani, J. L., Brahme, A., **Muhammad, W**., Mishra, R. K., & Inal, K. (2017). A new multi-scale framework to incorporate microstructure evolution in phenomenological plasticity: Theory, explicit finite element formulation, implementation and validation. International Journal of Plasticity, 1-35. In Press, Corrected Proof. Doi: 10.1016/j.ijplas.2017.08.006

Chapter 5: Development and Validation of Slip level Hardening Model for Precipitation Hardened Aluminum alloys

In this chapter, a new crystal plasticity based hardening model for AA6xxx series aluminum alloys is developed. The model employs experimentally measured microstructure to incorporate the effects of intragranular backstresses due to the formation of deformation and precipitation induced cellular dislocation substructure. A detailed experimental characterization of texture and dislocation substructure evolution during cyclic simple shear deformation of an extruded alloy AA6063–T6 is performed to understand its plastic deformation behavior. The proposed hardening model is successfully validated against experimentally measured data for complex cyclic loading paths such as large strain cyclic simple shear and cyclic tension-compression-tension (TCT) and compression-tension-compression (CTC) tests.

The chapter presents an accepted manuscript of an article published in International Journal of Plasticity.

International Journal of Plasticity 93 (2017): 137-163. Doi: 10.1016/j.ijplas.2016.11.003

Experimental and Numerical Investigation of Texture Evolution and the effects of Intragranular Backstresses in Aluminum alloys subjected to large strain Cyclic Deformation

International Journal of Plasticity 93 (2017): 137-163

Waqas Muhammad[1,2], Abhijit P. Brahme[1], Jidong Kang[2], Raja K. Mishra[3], Kaan Inal[1]

1 Department of Mechanical and Mechatronics Engineering, University of Waterloo, Waterloo, N2L 3G1, Canada

2 CanmetMATERIALS, 183 Longwood Road South, Hamilton, ON L8P 0A5, Canada

3 General Motors Research & Development Center, Warren, MI 48090, USA

Overview

Strain hardening in FCC metals and alloys can be accompanied by the formation of deformation induced dislocation microstructures. These microstructures tend to form dislocation cells or nets which are characterized by three-dimensional tangles of dislocations that serve as “cell walls” and less dense internal regions “cell interiors”. The presence of such dislocation microstructure induces intragranular backstresses due to blockage of dislocation passage leading to kinematic hardening at the macroscopic scale. The present work focuses on the effects of dislocation induced backstresses and the accompanying texture evolution on strain hardening behavior of AA 6063-T6 extruded aluminum alloy during cyclic forward-reverse-forward (FRF) simple shear deformation. The accompanying texture evolution is characterized using electron backscatter diffraction (EBSD) texture measurements. The development of the underlying dislocation substructure during the cyclic simple shear loading is determined using transmission electron microscopy (TEM). Furthermore, a new crystal plasticity backstress hardening model is proposed to incorporate the effects of intragranular backstresses due to the dislocation cells substructure. The hardening model is validated by comparing the numerically predicted results against the experimental cyclic simple shear flow response as well as texture evolution. An excellent agreement is found between the simulated and experimental results. In particular, the proposed model is able to predict the experimentally observed Bauschinger effect as well as the accompanying texture evolution during cyclic simple shear testing. The applicability of the proposed backstress hardening model is further validated by applying it to different cyclic strain paths (i.e. tension-compression-tension (TCT) and compression-tension-compression (CTC)) for different strain amplitudes. The numerically predicted results show good agreement to the corresponding experimental cyclic test results.

Keywords: cyclic loading; microstructures; crystal plasticity; dislocations; Bauschinger effect; finite elements

5.1 Introduction

Metals with medium to high stacking fault energies such as aluminum and copper exhibit the formation of deformation induced dislocation microstructures. These microstructures tend to form dislocation cells or nets that are characterized by three-dimensional tangles of dislocations that serve as "cell walls – hard phase" and less dense internal regions (cell interiors – soft phase) [6, 9, 18]. Several transmission electron microscopy (TEM) studies have shown the existence of these dislocation microstructures in face centered cubic (FCC) metals and alloys if the applied strain is large enough [149–152]. It has been shown that the presence of such dislocation microstructure induces intragranular backstresses due to blockage of dislocation passage leading to the experimentally observed Bauschinger effect at the macroscopic scale [7, 8, 10–12]. Furthermore, these backstresses are of opposite signs in the soft and hard phase and may result due to incompatibilities in dislocation motion as dislocations tend to glide much easily in the soft phase as compared to the hard phase [7, 153]. The term backstress was originally introduced by Nowick and Machlin [154] as the inner stress field of the lattice of stuck dislocations. The internal backstress has been widely used to explain the mechanical Bauschinger effect induced by dislocations [155]. Using TEM analysis, Hasegawa et al. [8] studied dislocation mechanisms responsible for the Bauschinger effect during stress reversal in polycrystalline aluminum. The authors correlated the observed Bauschinger effect and the decrease in hardening rate after loading reversal to the evolution of the dislocation microstructure in pure aluminum. In particular, the authors linked the decrease in hardening rate to the partial dissolution of dislocation cells after stress reversal**.** Levine et al. [156] examined heavily deformed Copper single crystals for the occurrence of dislocation microstructure and found their linkage to long range internal stresses. Zhu et al. [157] studied the influence of nano-scale grain boundaries (GB) on the mechanical behavior and Bauschinger's effect in copper during cyclic loading. The authors reported that the annihilation of dislocations or partial dislocations with opposite signs and the shrinkage/extension of associated stacking faults upon stress reversal are mainly responsible for Bauschinger's effect in the nano-copper systems. Kato et al. [158] investigated the development of backstresses in a 1 mm thick sheet of interstitial free (IF) steel was by tensile pre-straining and subsequent four-point bending. It is observed that the occurrence of back stress coincided with the development of dislocation cell structures, observed with transmission electron microscopy. Recently, Chen et al. [159] examined the role of misfit stress (i.e. intergranular internal stresses) in kinematic hardening under reversed straining of a Type 316H austenitic stainless steel using neutron diffraction combined with in situ deformation. The authors found that the origin of the kinematic hardening of Type 316H austenitic stainless steel arises from the misfit stress between grains.

Several methodologies have been proposed to incorporate the effects of backstresses in computational models. The most well-known ones are models based on inclusion problems. Using the inclusion based approach, one can take into account the dislocation microstructure geometry. These models consider either the soft phase as surrounded by the matrix or the soft phase as surrounded by an elastic wall and by the matrix [6, 160–162]. Generally, it is assumed that the cell walls are elastic whereas the soft cell interior as well as the matrix is elastoplastic. The backstresses

within the soft cell interiors are then calculated using Eshelby mechanics [163]. Most of these models are thermoelastic and use no plastic accommodation factor and it has been shown that these models tend to over predict the computed backstresses as the plastic deformation proceeds [160]. To counter this issue, Sauzay [7] proposed a simple two-phase localization rule for computing the intragranular backstresses while making use of an accommodation factor to prevent the over prediction of the computed backstresses. Brahme et al. [164] used the approach presented by Sauzay [7] to incorporate kinematic hardening into a crystal–plasticity-based model. However, these modelling approaches assume volume fraction of cell walls to be a constant during plastic deformation. In addition, the dislocation cell size is not accounted for in the formulation which may be important particularly if the cell size becomes comparable to the mean slip distance, then the cell structure may not be an effective barrier to dislocations movement anymore.

Several other models such as the Armstrong–Frederick type, nonlinear kinematic hardening models have been employed by Voyiadjis and Kattan [165], Khan and Cheng [166], McGinty and McDowell [167], Yoshida and Uemori [168], Goh et al. [169], Wollmershauser et al. [170], Wagoner et al. [171]. Such phenomenological modeling approaches are frequently applied to model the effects of backstresses including the Bauschinger effect [168, 172–176]. Recently, Bardel et al. [177] coupled the kinematic contribution of grain boundaries as well as precipitates with elastoplastic modelling to predict the multi-level cyclic loading behavior of 6061 aluminum alloy. However, majority of these approaches do not take into account the dislocation microstructure geometry. Even though, a lot of these models could be used to compute the value of backstress on a slip system but they are more phenomenological in nature and lack a physical base. Other approaches such as those proposed by Peeters et al. [178], Bayley et al. [179], Mughrabi [18], Kitayama et al. [180], and Wen et al. [181] make use of the geometrically necessary dislocation models to model backstress at slip system level. These more physical models based on dislocation densities are complicated and can have large number of fitting parameters (for example Peeters et al. [182]). Knezevic et al. [183] proposed a rate- and temperature-sensitive hardening law for hexagonal single crystals that accounts explicitly for the evolution of dislocation densities by including the effects of reverse dislocation motion and de-twinning on strain hardening and texture evolution. The model was implemented into a VPSC framework and was applied to simulate macroscopic behavior of polycrystalline beryllium during strain-path changes. Zecevic et al. [184] proposed a polycrystal plasticity constitutive law based on the elasto-plastic self consistent (EPSC) theory for prediction of cyclic tension-compression deformation of AA6022-T4. The crystallography based model integrates a dislocation based hardening model to account for slip system level backstresses to capture non-linear unloading and the Bauschinger effect. Recently, Zecevic et al. [185] proposed an elasto–plastic crystal plasticity model which integrates a hardening law based on statistically stored dislocation density, localized hardening due to geometrically necessary dislocations (GNDs), slip-system-level kinematic backstresses, and annihilation of dislocations. The proposed model is used to predict the hardening rates, non-linear unloading, and Bauschinger effect of DP 590 steel under cyclic tension–compression tests. Wen et al. [186] proposed an extension of the crystallographic-based hardening model (RGBV model)

to predict the macroscopic stress-strain response including the Bauschinger effect for rolled low carbon steel during cyclic shear.

Other approaches such as discrete dislocation dynamics (DDD) have been used for computing the long-range stress field induced by the dislocation microstructures [187, 188]. Zhou et al. [189] performed three-dimensional dislocation dynamics simulations using Cu (FCC) polycrystalline thin films and observed the occurrence of a significant Bauschinger effect during unloading. It is determined that the reverse motion of dislocation pile-ups and the collapse of misfit dislocations are responsible for the observed Bauschinger effect. Even though, DDD simulations can provide useful insight into the physical deformation mechanisms, they are rather time consuming and the results cannot be coupled easily with crystal plasticity finite element (CPFE) framework afterwards.

There has been efforts made-to-date to incorporate the effects of backstresses within CPFE framework. Yapici et al. [190] incorporated backstress into a viscoplastic self-consistent (VPSC) polycrystal model to study the stress–strain asymmetry under different strain paths. Kim et al. [191] used a simplified dislocation density model along with a representative volume element (RVE) approach to model Bauschinger effect in dual phase steels. More recently, Li et al. [155] used a texture-based representative volume element (TBRVE) crystal plasticity model with an Armstrong–Frederick nonlinear kinematic hardening rule to model the Bauschinger effect in rolled polycrystalline aluminum alloy 7075 under tension-compression cyclic loading. However, the accuracy of current crystal plasticity models depends on the hardening laws they employ (i.e. Asaro and Rice [192]; Peirce et al. [135]; Asaro and Needleman [193]). The majority of dislocation based hardening models as well as the other established hardening models, used in conjunction with crystal plasticity, do not include the contribution due to the formation of dislocation cell substructure within the microstructure.

The work hardening behavior of aluminum alloys at large strain is of special interest in the design and modeling of sheet metal forming processes. Material models commonly used for simulating these processes require stress-strain data of mechanical tests, such as uniaxial tension or simple shear tests. Shear tests are important as they avoid the early localization / necking that is observed in uniaxial tensile tests and therefore, can provide the constitutive behavior at large strains. Furthermore, characterization of large strain shear behavior is also important as it is usually observed in sheet metal forming applications, when sheet element moves through the tool radii from the flange area by the action of punch [194].

The purpose of the current work is twofold. Firstly, a comprehensive experimental investigation of the quasi-static, cyclic in-plane simple shear response of extruded AA6063-T6 at room temperature is presented. Cyclic forward-reverse-forward (FRF) simple shear tests are conducted along the extrusion direction introducing a new simplified testing procedure. The application of simple shear loading leads to a significant evolution of the crystallographic texture. Hence, electron backscatter diffraction texture (EBSD) measurements are performed to characterize the

evolution of texture during the cyclic simple shear deformation. Furthermore, transmission electron microscopy (TEM) analysis is also conducted to observe the development of the underlying dislocation microstructure during the cyclic simple shear loading. Secondly, a new crystal plasticity backstress hardening model is proposed that employs experimentally measured microstructure to incorporate the effects of intragranular backstresses due to the formation of dislocation cells structure with plastic deformation. The hardening law proposed in the present work is based on the Saimoto and Van Houtte (SV) constitutive relationship [147]. The newly proposed backstress hardening model extends the SV relationship by incorporating the backstress effect due to dislocation cell substructure, into the relationship. The new backstress hardening law is incorporated into an existing crystal plasticity finite element framework. To validate the proposed hardening model, the numerically predicted results are compared against the experimental cyclic simple shear flow response as well as texture evolution. The proposed backstress hardening model is further validated by applying it to different cyclic strain paths (i.e. tension-compression-tension (TCT) and compression-tension-compression (CTC)) for different strain amplitudes and the numerical results are compared against the corresponding experimental cyclic test results.

5.2 Material Characterization

5.2.1 Material

Commercially available aluminum alloy AA6063-T6 was used in the present study. The material was received as an extruded profile (see Figure 5-1) with a nominal extrusion wall thickness of 1.8 mm. The chemical composition of the alloy is given in Table 5-1. In order to characterize the mechanical behavior of the as-received material, quasi-static, room-temperature tensile tests were performed along the extrusion direction (ED) using standard ASTM-E8M specimens made from 11 different locations, as marked on the extrusion. The tensile behavior of the extruded material is found to be consistent across all 11 locations. Figure 5-2 shows the engineering stress – engineering strain curve for a specimen made from location 4 marked on the extrusion. It is observed that the as-received material has a yield strength of approx. 178 MPa and an ultimate tensile strength of approx. 208 MPa.

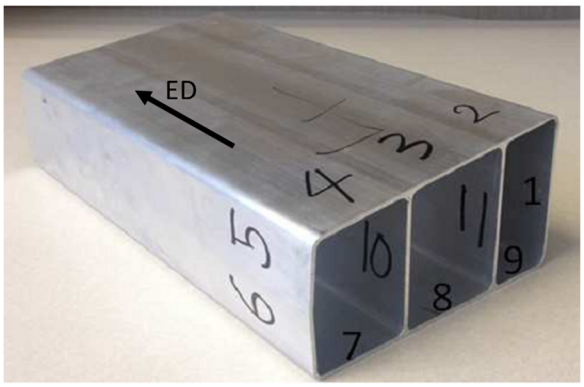

Figure 5-1: Extruded profile of the as-received AA6063-T6 material.

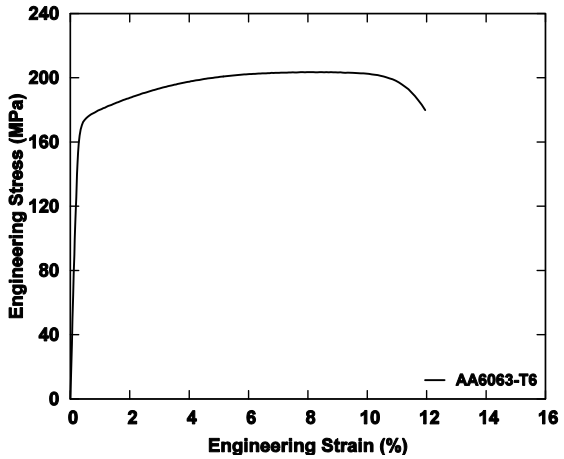

Figure 5-2: Engineering stress - engineering strain curve of the as-received material along the extrusion direction.

Table 5-1: Chemical composition (max. wt%) of as-received AA6063-T6 extruded material.

Material	Mg	Si	Fe	Mn	Cu	Ti	Al
AA6063	0.49	0.4	0.16	0.029	0.01	0.01	Bal.

EBSD texture measurements were performed to characterize the through thickness texture of the as-received material. The inverse pole figure (IPF) map corresponding to the through thickness microstructure of the as received material is shown in Figure 5-3. In Figure 5-3, the term 'ED' and 'ND' represent the extrusion and the through thickness directions, respectively. It is observed that the through thickness texture and grain size of the extruded material are different in the center as compared to in vicinity of the extrusion walls. This is rather expected as the material closer to the extrusion wall experiences a somewhat different deformation history and cooling rate as compared to the center of the extrusion. The average grain size of the material is approximately 63 μm. Furthermore, the <111> pole figure (see Figure 5-3) shows that the through thickness texture is predominantly Cube followed by a comparatively weaker Goss texture.

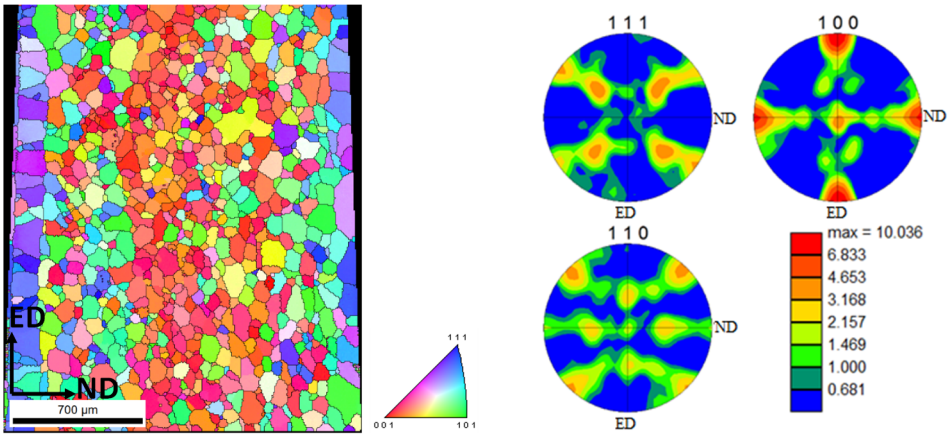

Figure 5-3: Through thickness texture of the as received extruded AA6063-T6 material.

5.2.2 Experimental Procedures

Displacement controlled forward-reverse-forward (FRF) simple shear experiments were carried out along the extrusion direction (ED) to characterize the in-plane cyclic simple shear response of the alloy. The term FRF stands for forward shearing followed by reverse shearing in the opposite direction and then subsequent forward shearing in the initial direction. FRF loading is applied to reverse the direction of applied shear and to study the accompanying microstructure and work hardening behavior. The shear sample geometry (ASTM B831-14) used in this study was originally proposed by Kang et al. [195] to characterize the planar simple shear behavior of AA5754 sheet material. However, the sample dimensions were modified to allow for cyclic planar simple shear testing and to prevent buckling of the shear sample upon loading reversal [196]. The proposed shear sample geometry is shown in Figure 5-4. The shear sample is 130 mm in length and is 38 mm wide. The length and width of the shear zone are 6.35 mm and 1.2 mm respectively. As proposed by Kang and Gong [197], a notch of 0.25 mm in the thickness direction was machined on each side of the specimen to ensure simple shear state within the shear zone. The shear tests were performed at room temperature using an MTS Landmark 370 Servo-hydraulic tensile machine with a load cell capacity of 100 KN and a constant cross-head speed of 1.0 mm/min. Each test was repeated three times to ensure repeatability and accuracy of experimental data.

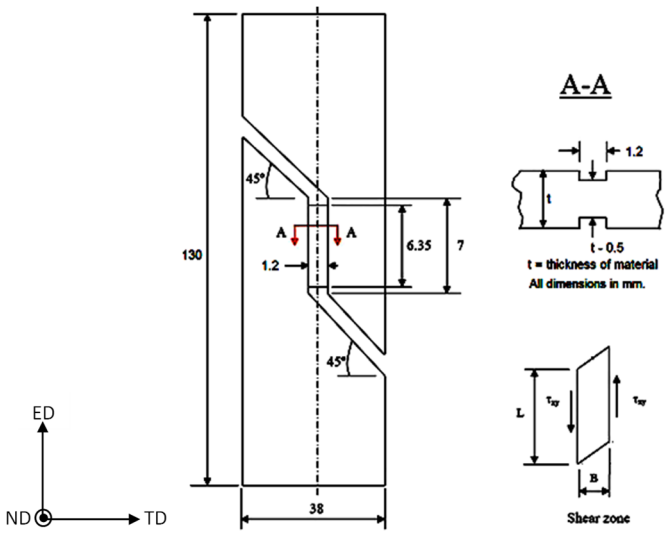

Figure 5-4: The proposed sample geometry for cyclic planar simple shear tests.

A commercially available digital image correlation (DIC) system "ARAMIS™" was used to capture surface strain evolution within the shear zone. Before testing, a random black-and-white speckle pattern was spray painted on the specimen surface within the shear zone and the DIC measurements were made from a set of snapshots collected automatically at a preset frame rate of 1 fps during the deformation process. The recorded images were analyzed to generate full-field strain maps for each load step using ARAMIS software and the shear strains were calculated from the measured shear angles [198]. For this purpose, the measured shear angles θ were averaged over the entire shear zone and then converted to shear strain γ, using the following relationship.

$$\gamma = \tan\theta \tag{5-1}$$

EBSD texture measurements were performed to characterize texture evolution at three different deformation stages during the cyclic shear tests: Stage (1) – fully forward in initial shearing, Stage (2) – subsequently fully reversed shearing in the opposite direction and Stage (3) – successively fully forward shearing in the initial direction. The EBSD measurements were made on the ED-TD plane (see Figure 5-4). For this purpose, the samples were cut from within the shear zone and were cold-mounted, grinded and polished using standard metallography techniques followed by ion-milling to achieve the desired surface finish. All texture measurements were made using a field-emission Nova NanoSEM™ equipped with a TSL EBSD camera. A step size of 0.5 µm was used for all EBSD measurements and the data was further processed using the TSL OIM™ software. The data is cleaned using neighbour CI correlation with single iteration to remove bad data points within the TSL software.

For each of the three aforementioned deformation stages, thin foils for transmission electron microscopy (TEM) were prepared from within the shear zone to view the samples in the ED-TD plane. The TEM samples were prepared by punching 3mm diameter disks with a Gatan puncher, followed by mechanical polishing of the disks to a thickness of approximately 80-90 µm. Dimpling

of the samples was done using 4-6 μm CBN paste with a felt wheel and finished using alumina suspension down to about 10 μm at sample's center. Sample's thinning to electron transparency was achieved by ion milling of the dimpled disks using a Gatan 691 PIPS with liquid nitrogen cooling until the perforation. The samples were analyzed at 200 keV using FEI's Tecnai Osiris TEM equipped with an X-FEG gun and ChemiSTEM energy dispersive X-ray (EDX) spectroscopy.

5.2.3 Experimental Results and Discussion

5.2.3.1 Flow Behavior

Figure 5-5 shows the shear stress – shear strain response of AA6063-T6 in forward shear up till fracture. The material yields at a shear stress of approximately 134 MPa and the maximum shear stress reached before failure is approximately 166 MPa. The material fails at a shear strain of approximately 50 %. Kang et al. [195] used a similar test setup to characterize simple shear behavior of AA5754 sheet material. The authors reported shear strains well in excess of 100 % before failure for AA5754.

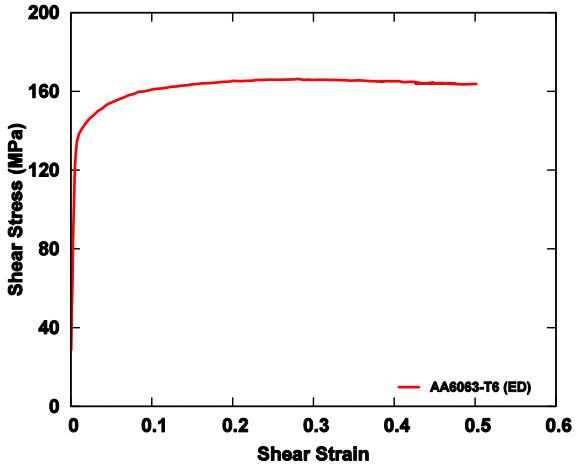

Figure 5-5: Shear stress vs. shear strain behavior of AA6063-T6.

The DIC strain mapping results for shear strains corresponding to initially fully forward, subsequently fully reverse and successively fully forward deformation stages, are shown in Figure 5-6. For clarity, these deformation stages are also marked as "(1)", "(2)" and "(3)" on the cyclic FRF shear stress-strain curve shown in Figure 5-7(a). EBSD and TEM samples were also made from the same deformation stages. It can be observed from the strain mapping results (see Figure 5-6) that the deformation within the shear zone is macroscopically homogeneous. It is noted that shear strains were calculated using the shear angles shown in Figure 5-6. The DIC maps show a small gradient of deformation outside the shear zone but its effects on the flow behavior are insignificant in the present study. Furthermore, Figure 5-7(a) shows that the flow behavior of the AA6063-T6 is fairly symmetric during cyclic planar simple shear deformation. However, for a more meaningful comparison of flow behavior during the initial forward, reverse and subsequent forward loadings, data shown in Figure 5-7(a) is replotted using the absolute values scale as shown

in Figure 5-7(b). It can be observed that the hardening rate during the initial forward simple shear loading is significantly higher than the subsequent reverse and forward loadings (see Figure 5-7(b)). However, the hardening rate during reverse loading is comparatively similar to that of subsequent forward loading. These differences in hardening rates may well be related with the development of the underlying dislocation microstructure as well as texture evolution with continuous plastic deformation. Furthermore, Figure 5-7(b) also shows the occurrence of a moderate Bauschinger effect as the yield stress during subsequent reverse loading is relatively lower than that during the initial forward loading.

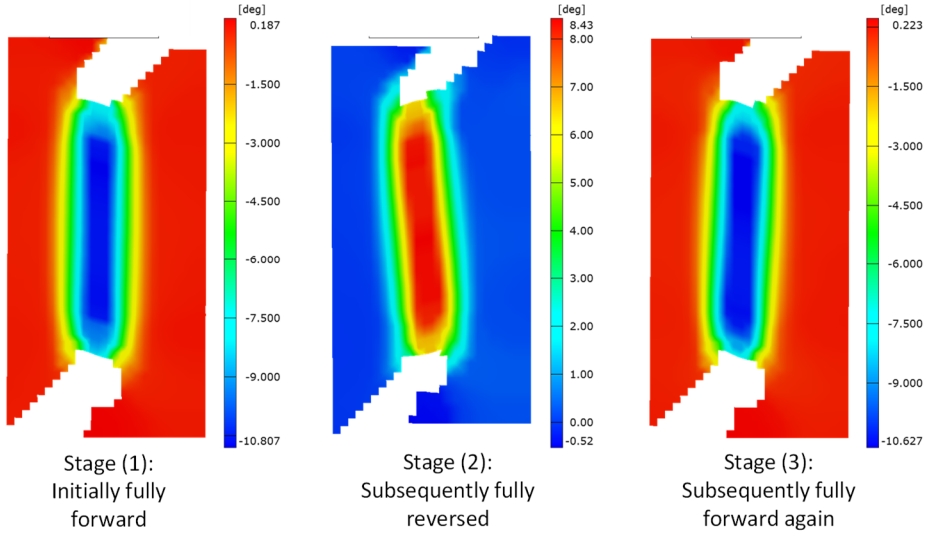

Figure 5-6: DIC strain maps showing shear strain distributions at different stages during the cyclic FRF deformation. Note that shear strains are represented as shear angles in the maps.

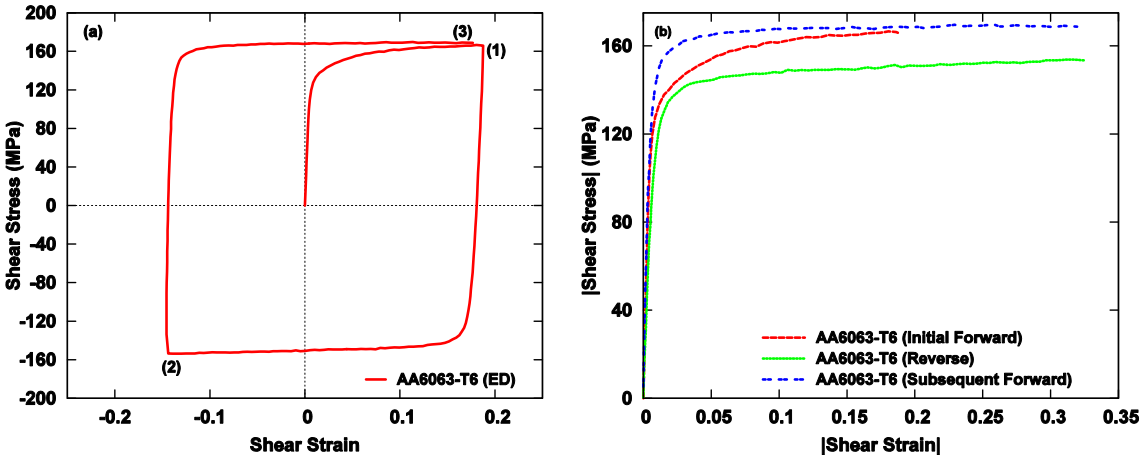

Figure 5-7: (a) Shear stress vs. shear strain response under cyclic (FRF) planar simple shear loading, (b) Absolute shear stress vs. absolute shear strain curve for initial forward, reverse and subsequent forward planar simple shear loadings in extrusion direction.

5.2.3.2 Texture Evolution

The initial texture as well as its evolution with the cyclic simple shear deformation is shown in Figure 5-8. As mentioned previously, the texture measurements were performed on region within the shear zone using the ED-TD plane (see Figure 5-4). Figure 5-8(a) shows that the starting texture within the gage section is primarily a cube texture followed by a comparatively weaker Goss texture. During the forward shear deformation, these texture components experience a clockwise rotation along the normal direction (ND) as shown in Figure 5-8(b) and Figure 5-8 (d). The texture components experience a counter clockwise rotation once the shearing direction is reversed from the initial forward direction as shown in Figure 5-8(c). Apart from the apparent rotation of texture components, one can also observe an overall weakening of the texture as the deformation proceeds from one stage to the next. This is apparent from the peak/max intensity values shown in Figure 5-8. Furthermore, it is to be noted that the Goss component of the texture weakens continuously as the deformation proceeds from Stage (1) to Stage (3). This can be observed from the <111> pole figures where the Goss peaks are disappearing with deformation from Stage (1) (see Figure 5-8(b)) to Stage (3) (see Figure 5-8(d)). This behavior was also observed by Rossiter et al. [199], where the authors performed 3D crystal plasticity finite element modelling of simple shear in AA5754 and found the Goss component of texture to be comparatively less stable than the cube component.

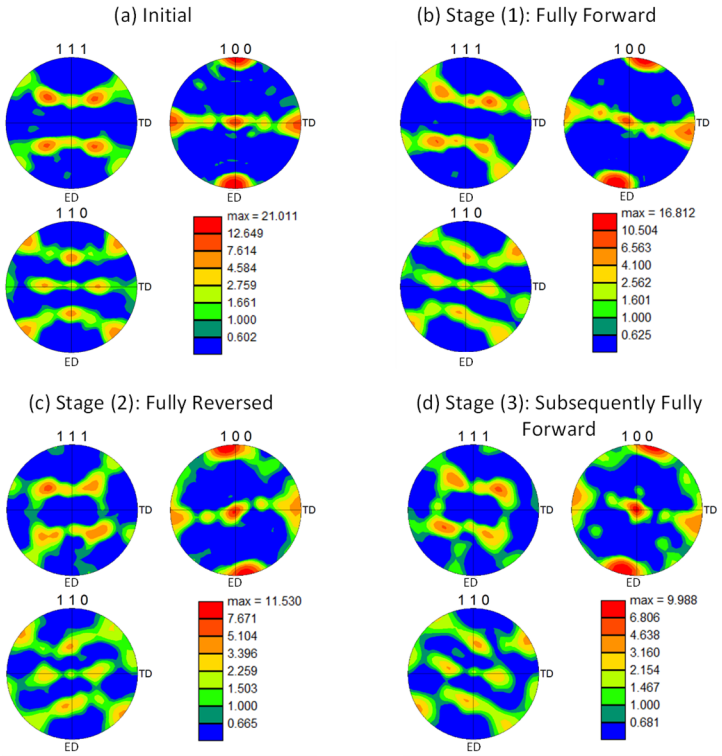

Figure 5-8: (a) Initial texture and texture (b) after fully forward loading, (c) after fully reversed loading in opposite direction, (d) after subsequent fully forward loading in initial direction.

5.2.3.3 Microstructure Evolution

Figure 5-9 shows the grain microstructure observed within the shear zone at the three different deformation stages. It is apparent that the original equiaxed grain structure is partly maintained even after Stage (3) of the shear deformation (Figure 5-9(c)). In Figure 5-9, one of the most important microstructure feature is the presence of a banded structure indicating localized deformation in slip and shear bands. Similar deformation features have been reported by many researchers for deformation processes such as equal channel angular extrusion and cyclic extrusion compression [200–202]. After initial forward shearing (see Figure 5-9(a)), one can see the presence of short microscopic bands within several grains and a large localized macroscopic band parallel to the loading (i.e. extrusion) direction. As the deformation proceeds further, several intersecting bands appear making their way through multiple grains. Furthermore, a comparison of Figure 5-9(a), (b) and (c) indicates that the number and size of shear bands have increased with increasing strain. In particular, after the deformation Stage (3) (Figure 5-9(c)), one can see the presence of multiple macroscopic deformation bands along the length of the shear zone and several intersecting bands making an approximate 90° angle to those large deformation bands.

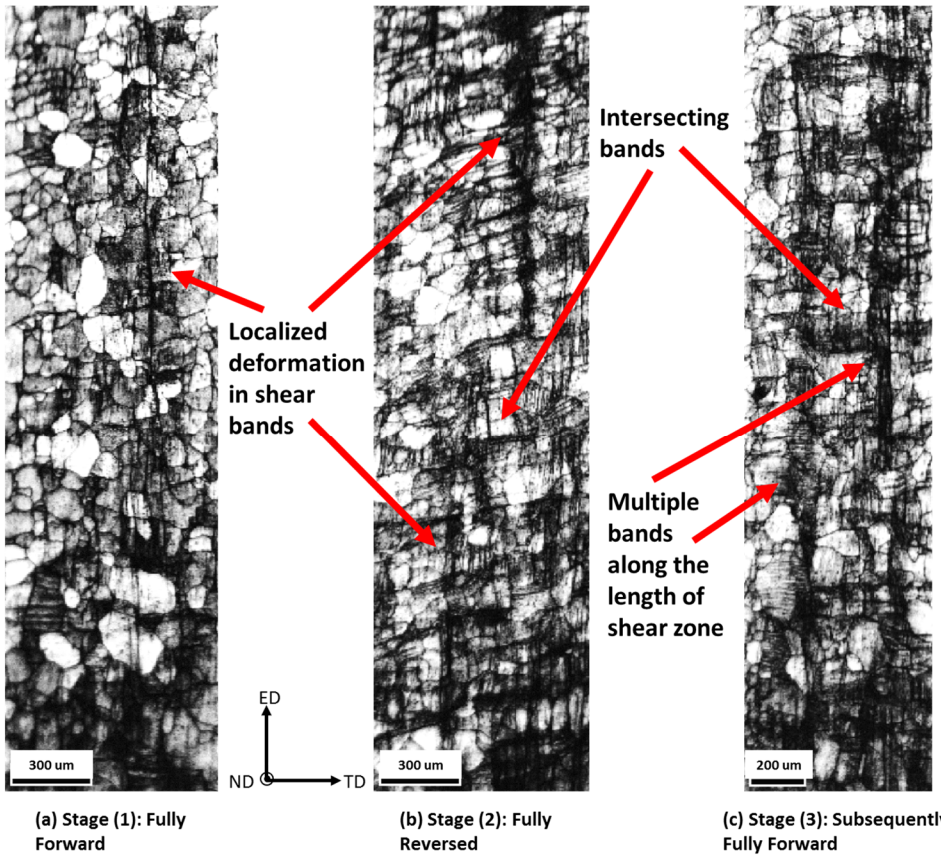

Figure 5-9: Microstructure within the shear zone at different deformation stages (a) fully forward shear, (b) fully reversed shear in opposite direction, (c) subsequent fully forward shear in initial direction.

From the dislocation microstructure after the initial forward shear deformation (i.e. Stage 1) (Figure 5-10), one can see the presence of micro shear bands with a specific orientation to the

loading axis (see in Figure 5-10(a) and (b)). These micro shear bands appear inside grains as previously observed in Figure 5-9(a). Inside these shear bands, many dislocations form chaotic networks. Figure 5-10(c) shows a zoomed-in view of the region encircled in red in Figure 5-10(b). One can mainly observe the tangling of dislocations with some regions with relatively high dislocation content while others being virtually dislocation free. As suggested by many researchers [203–205], these dislocations could move and interact with each other to form a cell wall structure with high dislocation content and cell interiors with a relatively low dislocation content. A tendency towards the formation of this dislocation cell structure is apparent in regions highlighted by arrows in Figure 5-10(c) and zoomed in Figure 5-10(d). The needle shape precipitates with their circular end-on views (as seen in Figure 5-10(d)) are typical of Al-Mg-Si based alloys [206] and are identified to be Mg_2Si precipitates. Figure 5-10(d) clearly shows the dislocations-to-dislocations and the dislocations-to-precipitates interaction leading to the development of regions with high dislocation content encompassing regions with relatively lower dislocation content. It is this dislocation-dislocation and dislocation-precipitate interaction which provides the obstacle strength during initial hardening as discussed later in the manuscript. However, at this point in deformation, the cell structure is still being developed.

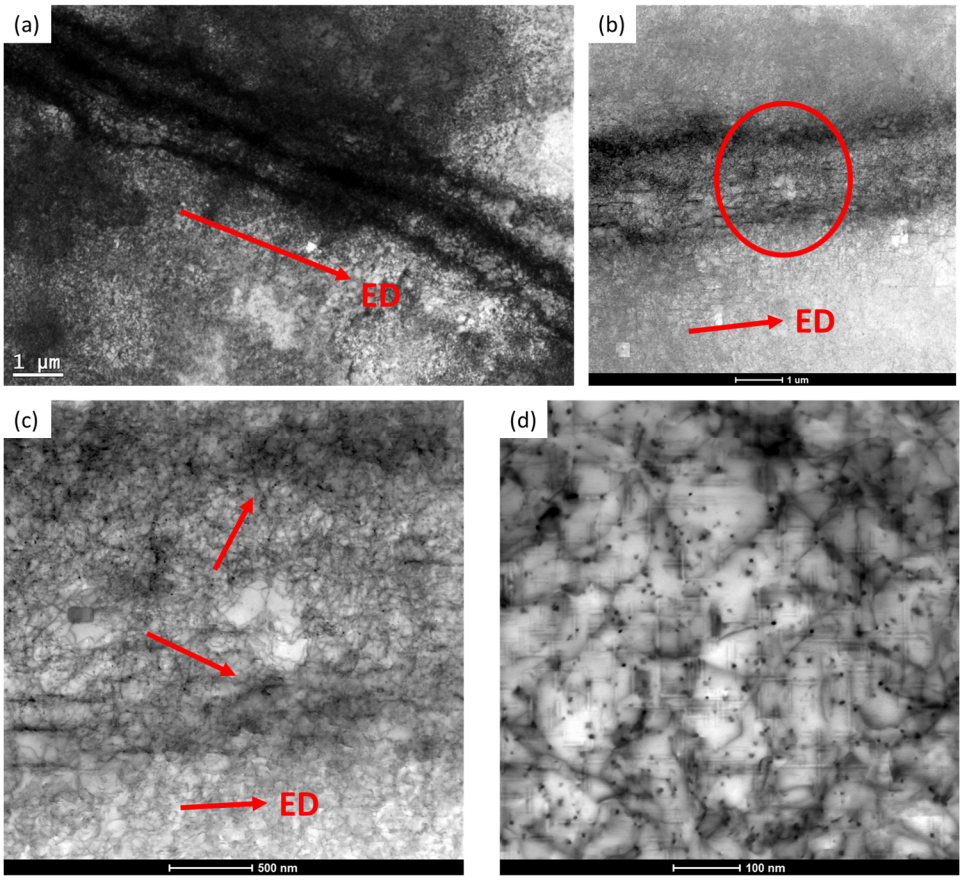

Figure 5-10: TEM images of microstructure evolution after the initial forward deformation at Stage 1.

The dislocation microstructure after the subsequent reverse shear deformation at Stage (2) is shown in Figure 5-11(a) and (b). At this stage, there are regions in the microstructure which have gradually evolved into a cell/subgrain structure with dimensions of 0.3 µm to 0.5 µm in size. The dislocation network inside the subgrain cells is more ordered. The microstructure after subsequent forward shear deformation at Stage (3) (see Figure 5-11(c)) still consists of cells/subgrains structure. However, the subgrain cell size at Stage (3) is comparatively smaller than that of the previous deformation Stage (2). This is apparent from a visual comparison of Figure 5-11(b) and (c). Furthermore, most of the dislocations are trapped at the subgrain cell boundaries (shown by arrows in Figure 5-11(e) and (f)) indicating the presence of high internal stresses [201, 207, 208]. Some of the subgrain boundaries are characterized as well formed, sharp boundaries as shown in Figure 5-12. In addition to this, the misorientations between the subgrains have also increased as shown by the presence of distinct spots in selected area diffraction patterns shown in Figure 5-13. These diffraction pattern measurements correspond to the subgrains marked in Figure 5-12. The subgrains appear more equiaxed, more misoriented with an approximate size of 0.2 µm to 0.4 µm.

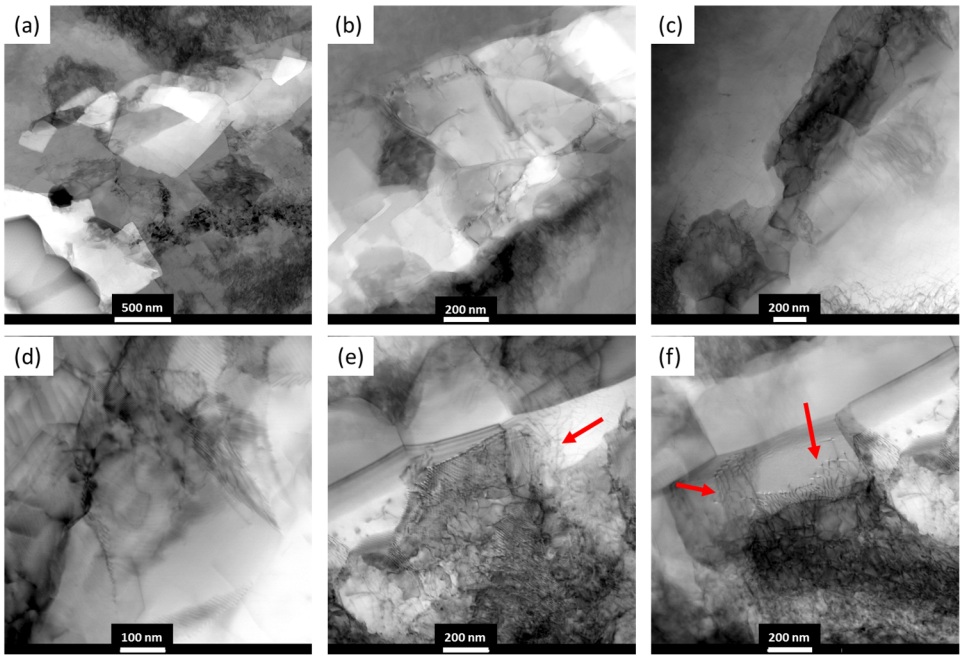

Figure 5-11: TEM images of microstructure (a)(b) after subsequent reverse shear deformation at Stage 2 and (c)(d)(e)(f) after subsequent forward shear deformation at Stage 3.

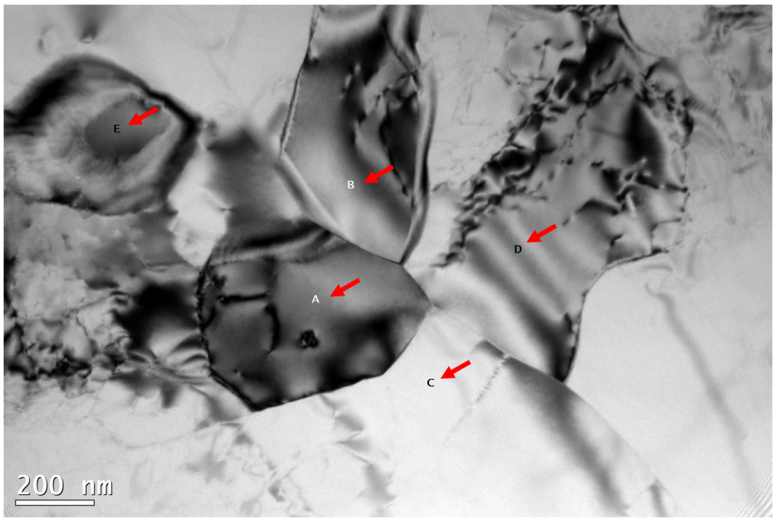

Figure 5-12: TEM image of microstructure after subsequent forward deformation at Stage 3, showing well formed, sharp subgrain boundaries.

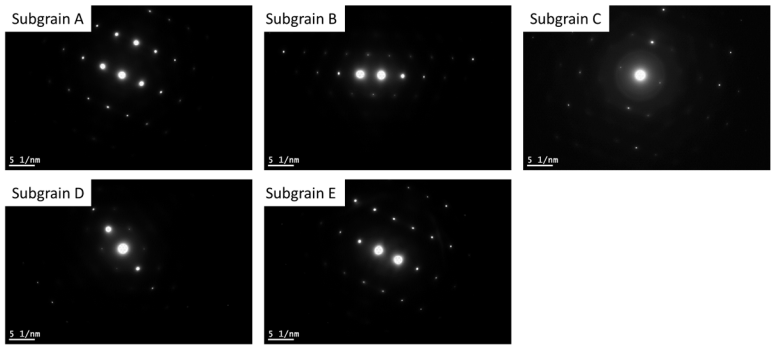

Figure 5-13: Selected area diffraction patterns corresponding to subgrains A, B, C, D and E marked in Figure 5-12.

As mentioned previously, the dislocation cell walls or subgrain cell boundaries may act as barriers for dislocation motion and therefore induce internal stresses due to blockage of dislocation passage (see Figure 5-11(e) and (f)) [6, 7, 201, 207, 208] leading to the experimentally observed Bauschinger effect at the macroscopic scale [8, 10–12]. The next section of the manuscript will present the proposed hardening model to account for the effects of intragranular backstresses due to the formation of dislocation microstructure. The proposed hardening model will be implemented within a crystal plasticity finite element (CPFEM) framework and validated against experimental flow stresses and texture evolution data for large strain cyclic simple shear.

5.3 Constitutive Modelling

5.3.1 Modeling Framework

The polycrystal modeling framework proposed by Asaro and Needleman [193] is used in the present work. The details of the model can be found in Wu et al. [209]and Inal et al. [210]. However, for completeness, the main ideas of the model are summarized below:

The total deformation of a crystallite is based on two distinct physical mechanisms: crystallographic slip due to dislocation motion on the active slip systems and elastic lattice distortion. Following this, the deformation gradient is divided into an elastic and a plastic part: elastic part accounting for rigid body rotation and plastic part due to slip on specific slip systems. The rate sensitive constitutive behavior of each crystal is specified by the following equation

$$\overset{\nabla}{\boldsymbol{\sigma}} = LD - \dot{\sigma}^{0} - \sigma \mathbf{tr} D \tag{5-2}$$

where $\overset{\nabla}{\sigma}$ is the Jaumann rate of Cauchy stress, L is the elastic moduli tensor, D is the strain rate tensor and $\dot{\sigma}^{0}$ is the visco-plastic stress rate which depends on the slip rates of the slip systems. In Eq. (5-2), the term **tr***D* is the trace (i.e. the first invariant) of the 2nd order strain rate tensor. The governing equation used to calculate the slip rates for the slip systems is as follows

$$\dot{\gamma}_{(\alpha)} = sign\, \tau_{(\alpha)} \left| \frac{\tau_{(\alpha)}}{g'_{(\alpha)}} \right|^{\frac{1}{m}} \tag{5-3}$$

where $\tau_{(\alpha)}$ is the resolved shear stress on the slip system α, $g'_{(\alpha)}$ is the slip system hardening and m is the strain rate sensitivity index. The term $g'_{(\alpha)}$ is the new hardening model proposed in this work to account for backstresses due to the formation of dislocation cells in the microstructure.

5.3.2 Backstress Hardening Model

As shown in the previous section, strain hardening in FCC metals and alloys can be accompanied by the formation of deformation induced dislocation microstructures. The microstructure is subdivided into dense dislocation walls forming cell blocks as shown schematically in Figure 5-14. The cell walls are regions of high dislocation content whereas the cell interiors are relatively dislocation free. This cell structure may induce internal stresses due to blockage of dislocations. The magnitude of internal stresses does not remain constant and depends on the size and volume fraction of dislocation cell walls [6, 202]. Furthermore, at increasing strains, the cell structure gradually evolves into an equiaxed cell/subgrain structure [201, 202, 207].

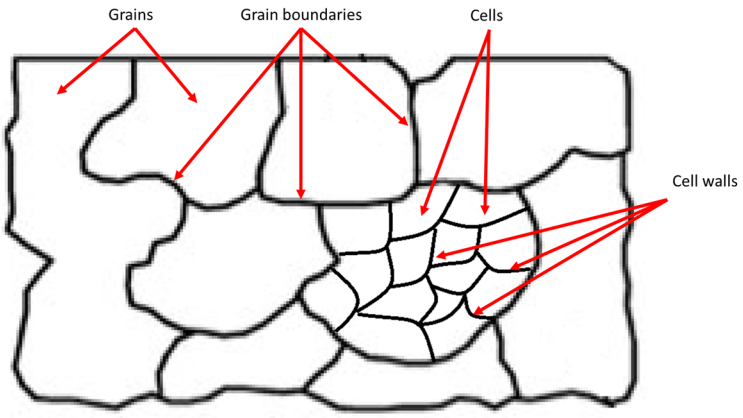

Figure 5-14: Schematic of a polycrystalline material showing the formation of dislocation cells within the microstructure.

Based on the aforementioned experimental observations, the dislocation cells are modeled as spheres with a cell radius R and cell wall thickness t as shown schematically in Figure 5-15. As the cells are assumed to be spherical (i.e. equiaxed), the volume of a single cell V_{cell} is given by

$$V_{cell} = \frac{4}{3}\pi R^3 \tag{5-4}$$

and similarly, the volume of the cell wall V_{wall} is given by

$$V_{wall} = 4\,\pi R^2 t \tag{5-5}$$

One can also estimate the total number of cells N_{cells} and the total volume of cell walls V_{wall}^{total} as follows

$$N_{cells} = \frac{V}{V_{cell}} \tag{5-6}$$

$$V_{wall}^{total} = N_{cells}\, V_{wall} \tag{5-7}$$

where V in Eq. (5-6) is the volume of the microstructure. From Eq. (5-3) – Eq. (5-7), the volume fraction of cell walls f_w at any given time can be simplified as follows

$$f_w = \frac{V_{wall}^{total}}{V} = 3\frac{t}{R} \tag{5-8}$$

Based on the previous work of Holt [211] , $R \propto \rho^{-\frac{1}{2}}$ where R is the radius of a cell and ρ is the dislocation density and the proportionality constant is ≈ 16 [212, 213]. Using these results, the volume fraction of cell walls f_w can be re-written as follows

$$f_w = \frac{3t}{16}\rho^{\frac{1}{2}} \tag{5-9}$$

Based on the assumptions that the cell wall (i.e. the hard phase) due to its high dislocation content is elastic whereas the soft interior phase is elastoplastic and assuming that the two phase cell is embedded in an infinite matrix, the backstress due to dislocation cells τ_b is given by [7, 164]

$$\tau_b = \left(\frac{f_w}{1-f_w}\right)\mu(1-\chi_E)\gamma \tag{5-10}$$

where μ is the elastic shear modulus, γ is the shear on the slip system and χ_E is the factor from Eshelby's [163] analysis of spherical inclusion given by

$$\chi_E = \left(\frac{2}{15}\right)\left(\frac{4-5\nu}{1-\nu}\right) \tag{5-11}$$

In Eq. (5-11), ν is the Poisson's ratio of the material. By substituting (5-9) in Eq. (5-10) and retaining the leading term in f_w, one can re-write the backstress τ_b as follows

$$\tau_b = 3Ct\mu(1-\chi_E)\gamma\rho^{\frac{1}{2}} \tag{5-12}$$

Note that the exclusion of the rest of the terms in the expansion of $\left(\frac{f_w}{1-f_w}\right)$ leads to an error of less than a few percent and are therefore ignored. The constant C in Eq. (5-12) is a material parameter.

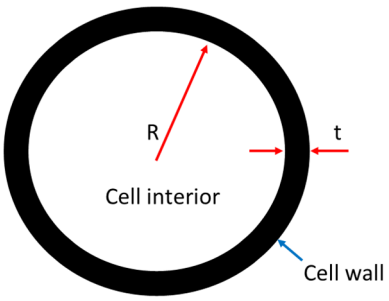

Figure 5-15: Schematic of a dislocation cell where *R* represents the radius and *t* is the cell wall thickness.

Saimoto and Van Houtte [147] proposed a constitutive relationship between flow stress and strain by equating the amount of new dislocations generated with those that has been retained while considering the possibility of dynamic annihilation during deformation. The amount of new dislocations generated can be calculated using the following relationship

$$\Delta\rho^{create} = \frac{P\Delta\gamma}{\lambda b} \tag{5-13}$$

where λ is the mean slip distance, b is the burgers vector and P is a variable parameter less than 1 and typically 0.2 [147]. The amount of retained energy can be calculated from the flow-forward stress as follows [11]

$$\tau_f = \alpha\mu b\rho^{\frac{1}{2}} \tag{5-14}$$

where α is a parameter related to the strength of obstacles. Using the relationships in Eq. (5-13) and Eq. (5-14) and accounting for the possibility of dynamic annihilation during deformation by introducing an annihilation factor A, Saimoto and Van Houtte [147] proposed a constitutive relationship in terms of parameters which are related to evolving microstructure and can be determined by experimental investigations. The Saimoto and Van Houtte [147] (SV) constitutive relationship between the flow stress and strain rate is as follows

$$\tau = \left[(2+\beta)(\alpha\mu b)^2 \frac{1}{4b}\right]^{\frac{1}{(2+\beta)}} \gamma^{\frac{1}{(2+\beta)}} C_{(P/A)}\, \dot{\gamma}^m \tag{5-15}$$

where the term $C_{(P/A)}$ is given by

$$C_{(P/A)} = C_f \left(\frac{P}{A}\frac{1}{C_1}\right)^{\frac{1}{(2+\beta)}} \tag{5-16}$$

In Eq. (5-15) and Eq. (5-16), the parameter α is related to the strength of obstacles, μ is the shear modulus, b is the burgers vector and m is the strain rate sensitivity index. The terms P, A, C_1, C_f and β are material dependent parameters and are obtained from stress strain curve using the procedure outlined in Saimoto and Van Houtte [147] and Brahme et al. [148].

In materials which exhibit dislocation cells formation, the total flow stress in the cell interiors can be expressed as follows

$$\tau = \tau_f + \tau_b \tag{5-17}$$

where τ_f is the forward stress or stress due to forest dislocations given by Eq. (5-14) and τ_b is the effective backstress due to dislocation cells, derived earlier in Eq. (5-12). By substituting Eq. (5-12) and Eq. (5-14) in Eq. (5-17), one can obtain

$$\tau = \alpha'\mu b\rho^{\frac{1}{2}} \tag{5-18}$$

where α' is given by

$$\alpha' = \alpha + \frac{3Ct}{b}(1-\chi_E)\gamma \tag{5-19}$$

In Eq. (5-19), the first term is a constant related to the obstacle strength of a forest dislocation and the second term can be viewed as the obstacle strength of a dislocation cell and evolves with accumulated shear. The constitutive relationship in Eq. (5-15) can be updated to incorporate the effects of dislocation cells by replacing the term α in Eq. (5-15) with α' as follows

$$\tau = \left[(2 + \beta)(\alpha'\mu b)^2 \frac{1}{4b}\right]^{\frac{1}{(2+\beta)}} \gamma^{\frac{1}{(2+\beta)}} C_{(P/A)}\, \dot{\gamma}^m \tag{5-20}$$

where α' is given by Eq. (5-19). The above constitutive relationship can be rearranged in terms of $\dot{\gamma}$ as follows

$$\dot{\gamma} = \left(\left[(2 + \beta)(\alpha'\mu b)^2 \frac{1}{4b}\right]^{\frac{-1}{(2+\beta)}} \gamma^{\frac{-1}{(2+\beta)}} \frac{1}{C_{(P/A)}}\right)^{\frac{1}{m}} \tau^{\frac{1}{m}} \tag{5-21}$$

Eq. (5-21) can be rewritten so that the relationship between flow stress and strain rate has a similar form as that of Eq. (5-3) as follows

$$\dot{\gamma} = sign\,\tau \left|\frac{\tau}{g'}\right|^{\frac{1}{m}} \qquad where \tag{5-22}$$

$$g' = \left[(2 + \beta)(\alpha'\mu b)^2 \frac{1}{4b}\gamma\right]^{\frac{1}{(2+\beta)}} C_{(P/A)} \tag{5-23}$$

The term g' is the proposed hardening model to account for the intragranular backstresses which arise from the formation of dislocation cell structure in the microstructure. The hardening model is incorporated within the Asaro and Needleman [193] polycrystal modeling framework outlined in the previous section.

5.4 Numerical Analysis

5.4.1 Problem Formulation

In the previous section, a backstress hardening model is proposed which can account for internal stresses attributed to the formation of dislocation cell/subgrain microstructure. These dislocation microstructures induce backstresses leading to the experimentally observed Bauschinger effect at the macroscopic scale [8, 10–12]. In this section, the new backstress hardening model is applied to cyclic simple shear deformation. The cyclic simple shear tests were chosen, as one can avoid the necking phenomenon and therefore reach higher strains along with substantial texture evolution.

The backstress hardening model is incorporated into the preceding polycrystal modeling framework (see Section 5.3.1) embedded within a 2D finite element framework [164, 210, 214]. A finite element procedure based on a Lagrangian formulation of the field equations using convected coordinates has been used in the present analysis [210]. Using this formulation, if $\boldsymbol{g}_i$ represent the base vectors in the undeformed configuration corresponding to the convected coordinates x_i, the deformed base vectors are $\boldsymbol{G}_i = \boldsymbol{F}\boldsymbol{g}_i$, where $\boldsymbol{F}$ is the deformation gradient. The initial, undeformed configuration of the body with volume V and surface S is used as a reference. In the absence of body forces, the equilibrium equations for quasistatic deformations are expressed through the virtual work condition

$$\int_V \tau^{ij}\delta\eta_{ij}dV = \int_S T^i\delta u_i dS \qquad \textbf{(5-24)}$$

for arbitrary variations of the displacement components u_i and corresponding variations of the components η_{ij} of the Lagrangian strain tensor. In Eq. (5-24), τ^{ij} are the components on the undeformed basis of the second Piola-Kirchhoff tensor and T^i are the corresponding traction vectors.

In the linear incremental problem, the current state of approximate equilibrium is supposed to be known at time t.The equations for the field quantity rates are determined by applying the Taylor series expansion about time to Eq. (5-24) as follows

$$\Delta t\int_V \left(\dot{\tau}^{ij}\delta\eta_{ij} + \tau^{ij}\dot{u}_{k,i}\delta u_{k,j}\right)dV = \Delta t\int_S \dot{T}^i\delta u_i dS - \left[\int_V \tau^{ij}\delta\eta_{ij}dV - \int_S T^i\delta u_i dS\right] \qquad \textbf{(5-25)}$$

The last term on the right in Eq. (5-25) serves as an equilibrium correction to prevent any drift away from the true equilibrium path during the incremental procedure [210].

The elements used in the simulations are similar to those described by Wu et al. [215]. In the numerical analyses, quadrilateral elements, each consisting of four linear velocity triangular sub-elements are employed. These elements are modified to incorporate a higher order integration scheme [210, 214]. Using this integration scheme and the ‘‘crossed triangle’’ configuration of the elements, different material properties (i.e., Euler angles) can be mapped efficiently to a single element. Therefore, fewer elements are needed to model grain–grain and/or grain–particle interactions. The experimentally observed grain morphologies are exactly implemented into the finite element analyses by incorporating EBSD maps in the numerical simulations. The initial texture of AA6063-T6 is given in Figure 5-8(a) and the corresponding EBSD map is shown in Figure 5-16 below. The EBSD map of 286 grains has been incorporated to a finite element mesh using 60,000 elements. Each pixel in the EBSD map is represented by an element in the FE mesh. Each element in the mesh has a dimension of 5 μm x 5 μm. The typical dislocation cells have a size of less than a micron (as shown in Figure 5-11) and each element has multiple dislocation cells in it. The FE mesh is then subjected to forward-reverse-forward simple shear loading along

the ED and the resulting flow stresses and texture evolution are compared against the experimental data. The finite element framework includes certain parallel computing algorithms so that simulations can be performed with models containing a sufficiently large numbers of elements. Details regarding the parallelization method can be found in Inal et al. [214]and Inal et al. [210].

Figure 5-16: EBSD map of the input microstructure grain colors represent the crystallographic orientations.

5.4.2 Results and Discussion

Using the numerical model proposed in Section 5.3.2 in conjunction with the crystal plasticity finite element setup, the parameters for the new backstress model are calibrated using the experimental flow stress data presented in Figure 5-5. Figure 5-17 shows the simulated shear stress - shear strain curve obtained after calibrating the model parameters to the experimental forward shear data. The calibrated fitting shows an excellent match to the experimental data. The calibrated model parameters are given in Table 5-2. The backstress coefficient C in Eq. (5-12) is tuned along with material parameters in the crystal plasticity hardening model during calibration. A detailed calibration procedure to obtain material parameters of the model from the experimental stress-strain curve is outlined in Saimoto and Van Houtte [147] and Brahme et al. [148]. In Table 5-2, the parameter σ_0 is a yield parameter which defines $\tau = (\sigma - \sigma_0)/M$, where M is the Taylor factor. The superscripts *II* and *III* in Table 5-2, refer to material parameters corresponding to Stage II and Stage III hardening respectively. The microstructural parameters P/A and β are determined from the actual true stress–true strain curve. The Saimoto and Van Houtte [147] relationship is based on Taylor slip analysis where the parameter P (in Table 5-2) is effectively the ratio of the newly created perimeter length of the slip patch to its area, and A (in Table 5-2) is the annihilation factor invoked to assess the amount of dislocation length which dynamically annihilates. The terms C_1 and β relates the mean slip distance λ to τ as $\lambda = C_1\tau^{\beta}$. In Table 5-2, C_f is a material parameter which assures the continuity of the flow curve during transition from Stage II to Stage III hardening. The reader is referred to Saimoto [216], Saimoto and Van Houtte [147] and Saimoto et al. [217] for further information on the Saimoto-Van Houtte relationship. The parameter t in Table 5-2 represents the wall thickness of a dislocation cell and is approximated from TEM analysis. Furthermore, the backstress parameter C in Table 5-2, accounts for the proportionality constant introduced in Eq. (5-9) and it also accounts for any discrepancies in the measured dislocation cell wall thicknesses from TEM analysis as well as the cell wall volume fraction. In Table 5-2, the parameters C_{11}, C_{12} and C_{44} are the elastic constants used in numerical simulations.

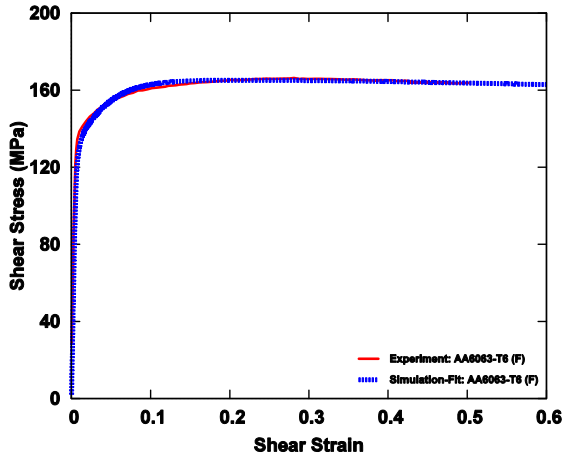

Figure 5-17: Hardening model fit to the experimental forward shear data for AA6063-T6.

Table 5-2: Material parameters for the backstress model used in simulations

Crystal Plasticity Model Hardening Parameters								Backstress Parameters		Elastic Constants (GPa)		
$\sigma_0\ (MPa)$	P/A	β^{II}	β^{III}	$C_1^{II}(\mu m)$	$C_1^{III}(nm$	C_f^{II}	C_f^{III}	C	$t\ (nm)$	C_{11}	C_{12}	C_{44}
65	0.0744	0	0.25	0.1623	2.478	2.6	1.2	0.15	7.0	104.2	51.4	26.3

Figure 5-18 compares the simulated results of cyclic simple shear with the experimental data. The "without backstress" results in the figure are computed by solely using the Saimoto and Van Houtte relationship (given in Eq. (5-15)) without including backstress implementation. It is observed that without backstress, the polycrystal model is able to predict the shear stress – shear strain response during initial forward shearing. However, once the loading is reversed, the model is no longer able to account for the early yielding (i.e. Bauschinger) phenomenon during reverse loading and the simulation results start to differ from thereafter. It is important to note that no matter how one would calibrate the original Saimoto and Van Houtte hardening model (or any existing hardening model such as Asaro and Needleman model, power law model) which does not account for internal backstresses, it will not be able to predict this early yielding phenomenon as it is not a mere hardening change as shown in Figure 5-19, which shows the comparison of the experimental and simulated flow behavior for the initial forward, reverse and subsequent forward loadings plotted using absolute scale along with the respective hardening rates. This is due to the nature of the Bauschinger effect which is characterized by a reduction of the yield strength upon reversal of loading or change in loading path [8]. Since most of the crystal plasticity models would have the same critical value of resolved shear to initiate plastic flow and if there is no other way to keep track of the internal stress they would predict similar values for yielding on load reversal. On the other hand, simulation results with the newly proposed backstress model show an excellent conformity to the experimental data (see Figure 5-18). Bauschinger effect is attributed to

obstruction of dislocation motion by obstacles (i.e. cell walls) which impedes further forward loading but on load reversal help the plastic flow without the need to create additional dislocations leading to a softer response during reverse yielding. It is noted that, the new backstress hardening model is able to reproduce the experimentally observed Bauschinger effect once the loading is reversed. As noted in the formulation (Section 5.3.2), the model does not employ dislocation cells in the microstructure (due to their size being smaller than the element size) but incorporates their effect through the backstress term (τ_b). Also as noted in Eq. (5-12) $\tau_b \propto \gamma$, initially τ_b is small and grows with straining. For plastic flow to occur, in the model, the applied stress τ has to overcome the resultant backstress as shown in Figure 5-20 and has to be greater than the critical resolved shear stress (τ_{CRSS}). During the initial forward yielding, since τ_b is zero, the applied stress τ has to only overcome τ_{CRSS}. During subsequent reverse yielding, τ_b which is in the opposite direction of the applied stress $\tau_f^{Forward}$, is now in the same direction of $\tau_f^{Reverse}$. Thus plastic slip is easier and allows for an early yielding as the critical resolved shear stress is reached much earlier.

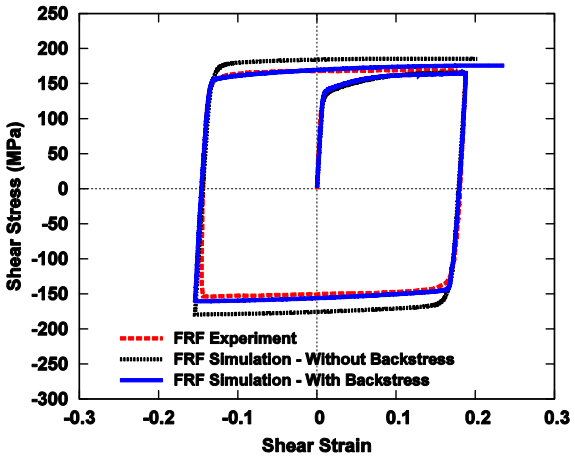

Figure 5-18: Comparison between simulated cyclic simple shear response and experimental data for extruded AA6063-T6

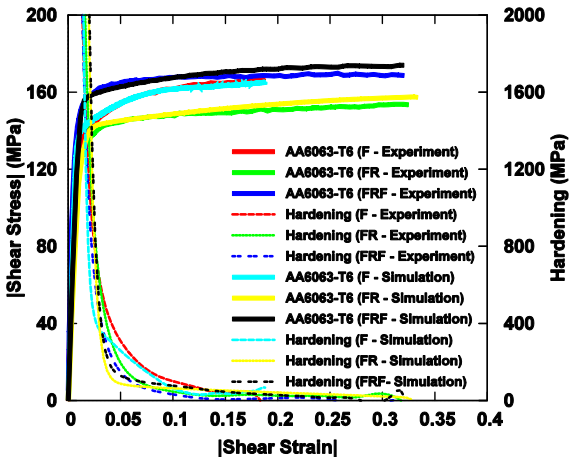

Figure 5-19: Absolute shear stress vs. absolute shear strain curves with corresponding hardening rates plotted on the y2 axis for initial forward shear, subsequent reverse shear and subsequent forward shear loadings.

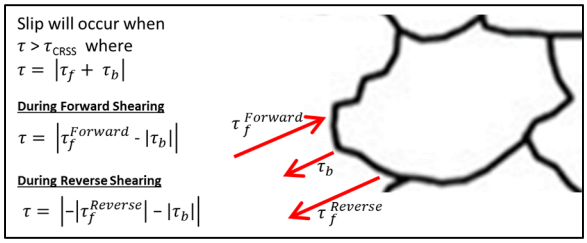

Figure 5-20: Schematic showing resolved shear stress during forward shearing versus reverse shearing.

It can be observed from Figure 5-19 that the hardening rate during initial forward shearing is comparatively much higher than that during the subsequent reverse and forward shear deformations. The higher hardening rate is associated with the development of dislocation substructure during initial forward shearing as shown in Figure 5-10. However, during the subsequent reverse and forward loadings the dislocation substructure seems to have settled into clear dislocation cells (as shown in Figure 5-11) which is also reflected by the relatively similar hardening rates during subsequent reverse and forward loadings (see Figure 5-19). It is also noted that during the subsequent forward loading after previous reverse shearing, the major apparent change in the microstructure is the decrease in the dislocation cell size (i.e. radius) as shown in Figure 5-11(c). As the cell radius R decreases, it leads to an increase in the volume fraction of cell walls f_w since $f_w \propto \frac{1}{R}$ (see Eq. (5-8)). Hence, a much higher forward stress τ_f is required to overcome the increase obstacles to dislocation movement presented by the cell walls and as a result the yield stress during subsequent forward loading is comparatively higher.

It is also worth mentioning that the backstress within the model evolves with plastic deformation as given by Eq. (5-19). It should be noted that the evolution of backstress τ_b is directly related to the term α' as shown in Eq. (5-12) and Eq. (5-19). As mentioned previously, the term α' (see Eq. (5-19)) consists of a constant α, which is the obstacle strength of a forest dislocation (taken to be 0.4 [216]) and a second evolving term which represents the obstacle strength of a dislocation cell. Figure 5-21 shows the evolution of the backstress term α' after the initial forward, fully reversed and subsequently fully forward simple shear loadings. In Figure 5-21, the contour of $\alpha'$are superimposed over the initial undeformed mesh. The term α' starts increasing with plastic deformation and at the end of the initial forward deformation (Figure 5-21(a)), the maximum value of α' is 0.49. The backstress keeps evolving with plastic deformation and after the subsequent reverse loading, the backstress term α' has reached a maximum of 0.8 as shown in Figure 5-21(b). Furthermore, the evolution of backstress seems to imitate a banded structure with higher values of α' within the band. This increase in backstress term α' is experimentally justified by the increase in the formation of dislocation cells in the microstructure after the fully reverse loading, as shown in Figure 5-11(a) and (b). The formation of dislocation cells has led to an increase in the volume fraction of cell walls f_w and since, $\alpha' \propto \tau_b \propto f_w$, an increase in the volume fraction of cell walls ultimately leads to an increase in the internal backstresses. After the subsequent fully forward shear loading (Figure 5-21(c)), the average value of α' has increased to approx. 0.65 with a maximum

value of 0.88. Once again this increase in α' after the subsequent forward loading is experimentally supported by the fact that the dislocation cell size has shrunk after the subsequent forward loading (see Figure 5-11), which once again leads to an increase in f_w and therefore the internal backstress τ_b. Thus, this notion of an increase in the value of α' throughout the cyclic shear deformation is consistent with the experimentally observed formation of the underlying dislocation microstructure in TEM images.

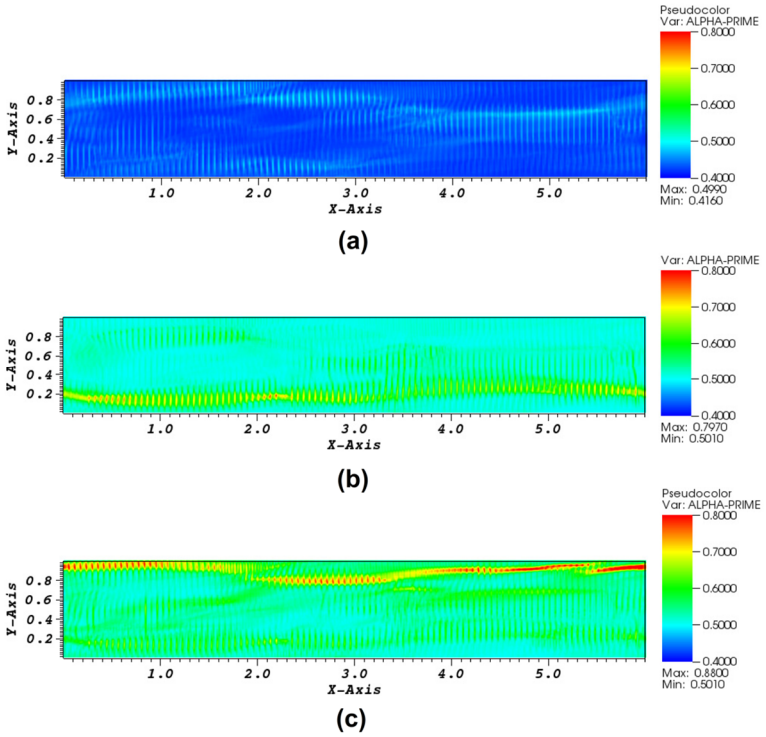

Figure 5-21: The evolution of the backstress term after (a) the initial forward (b) fully reversed and (c) subsequently fully forward shear loadings.

Figure 5-22 (a), (b) and (c) show the predictions of texture evolution during cyclic FRF deformation using the backstress hardening model. The experimental results are reproduced in Figure 5-22 (d), (e) and (f) for an easier visual comparison. It can be observed that the simulated texture evolution results show an excellent qualitative match with the experimental data for each deformation stage. The polycrystal model is able to predict texture rotation due to the simple shear deformation as represented by the experimental data. However, the simulated results show a comparatively higher peak intensity values for fully reversed (Stage 2) and subsequently fully forward (Stage 3) deformations as compared to the experimental peak intensity values for the corresponding deformations.

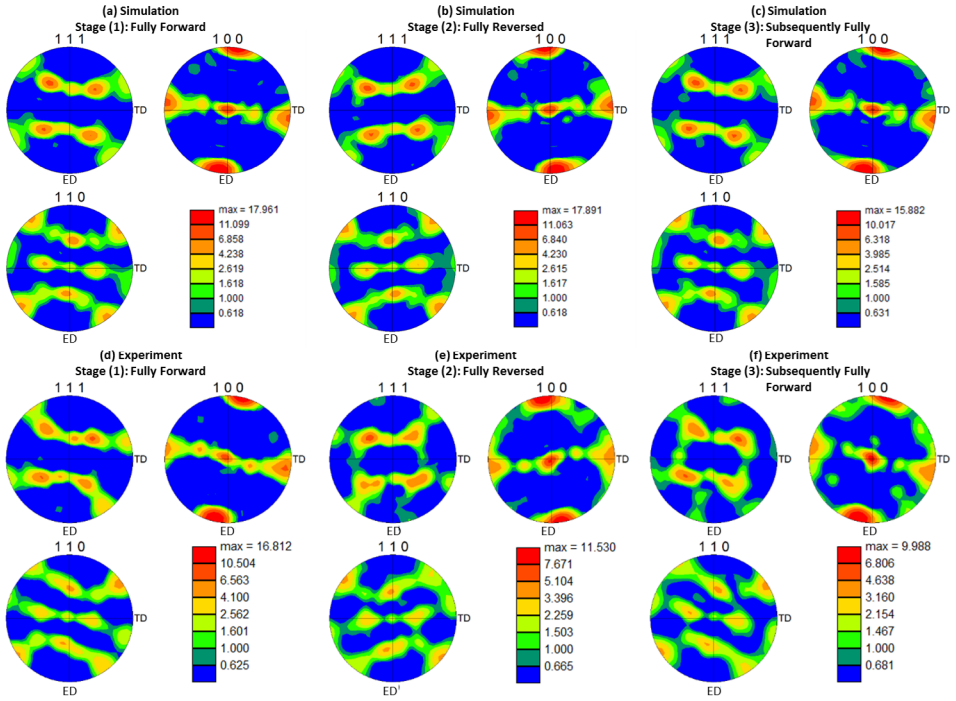

Figure 5-22: Comparison of texture evolution during cyclic FRF loading (a)(b)(c) predicted simulation results and (d)(e)(f) experimental results. Note the experimental results are repeated here for visual comparison.

For a better comparison of the predicted and experimental texture data, Figure 5-23 and Figure 5-24 present the orientation distribution function showing $\varphi_2 = 0^o$ for experimentally measured and the numerically predicted texture using the new backstress hardening model, respectively. For visual comparison, the same texture intensity scale is set for both figures. It is noted that the numerical model is able to predict the overall trends and evolution of the ODF as highlighted in Figure 5-23 and Figure 5-24. For example, it can be observed from Figure 5-23(a) and (b) that the initial forward shear deformation leads to the shifting of the Cube peak along the φ_1 axis signifying rotation of the cube component. A similar behavior is predicted by the numerical model as shown in Figure 5-24(b). Furthermore, the experimental ODF in Figure 5-23(b) shows weakening of the Goss peak at 45º along the ϕ axis after the initial forward shear deformation. Similar trend showing the weakening of the Goss component has been predicted by the numerical model in Figure 5-23(b). The Goss component has been weakened from 13.0 times random in the initial starting ODF (Figure 5-23(a)) to 8.0 times random after the forward shear deformation in Figure 5-23(b). Figure 5-25 shows the ODF for the numerically predicted texture without accounting for the backstress effects. Even though, the numerical texture for the initial forward loading without backstress effects (in Figure 5-25(b)) is reasonably similar to that predicted using the new backstress hardening model (see Figure 5-24(b)), the differences are more pronounced during the subsequent reverse and forward loadings. Contrary to the experimental and numerically predicted texture results with backstress hardening in Figure 5-23(c) and Figure 5-24(c) respectively, the hardening model without backstress is unable to properly predict the strengthening of the near-Goss peak (encircled in red in Figure 5-25(c)) after the fully reversed loading. Furthermore, after

the subsequent forward loading, the numerically predicted texture without backstress shows more pronounced exact-Cube peaks (encircled in red in Figure 5-25(d)) as compared to the experimentally and the numerically predicted texture using the backstress hardening model in Figure 5-23(d) and Figure 5-24(d).

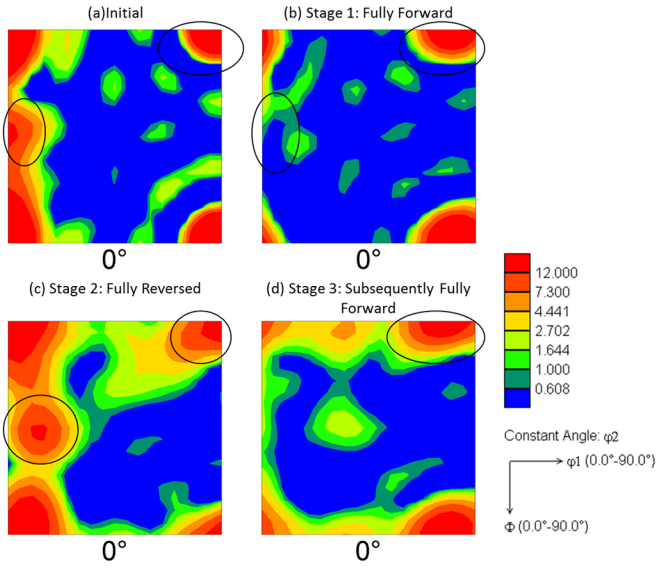

Figure 5-23: Orientation distribution function showing $\varphi_2 = 0^o$ for experimentally measured texture corresponding to (a) initial, (b) fully forward, (c) fully reversed and (d) subsequently fully forward loadings.

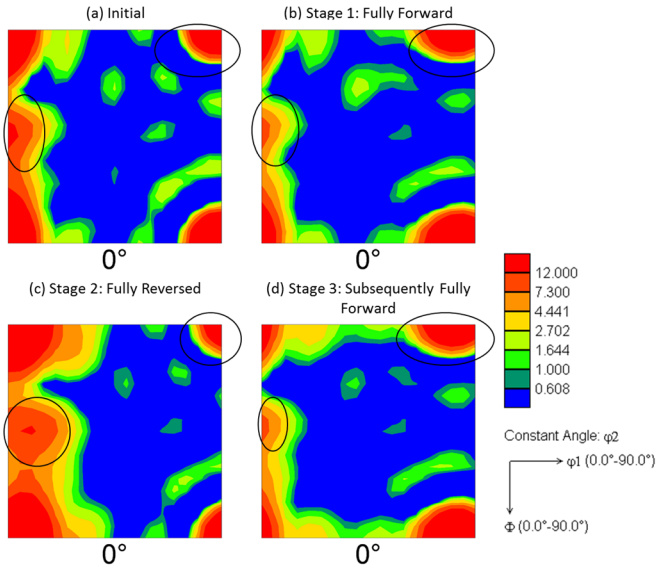

Figure 5-24: Orientation distribution function showing $\varphi_2 = 0^o$ for numerically predicted texture with backstress effects corresponding to (a) initial, (b) fully forward, (c) fully reversed and (d) subsequently fully forward loadings.

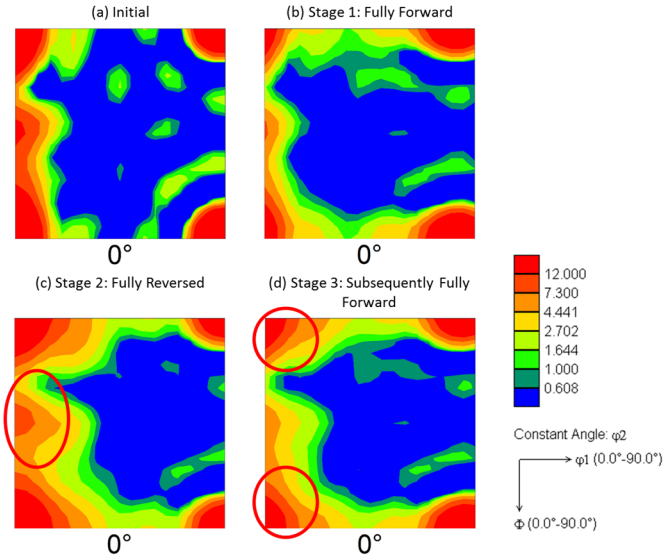

Figure 5-25: Orientation distribution function showing $\varphi_2 = 0^o$ for numerically predicted texture without backstress effects corresponding to (a) initial, (b) fully forward, (c) fully reversed and (d) subsequently fully forward loadings.

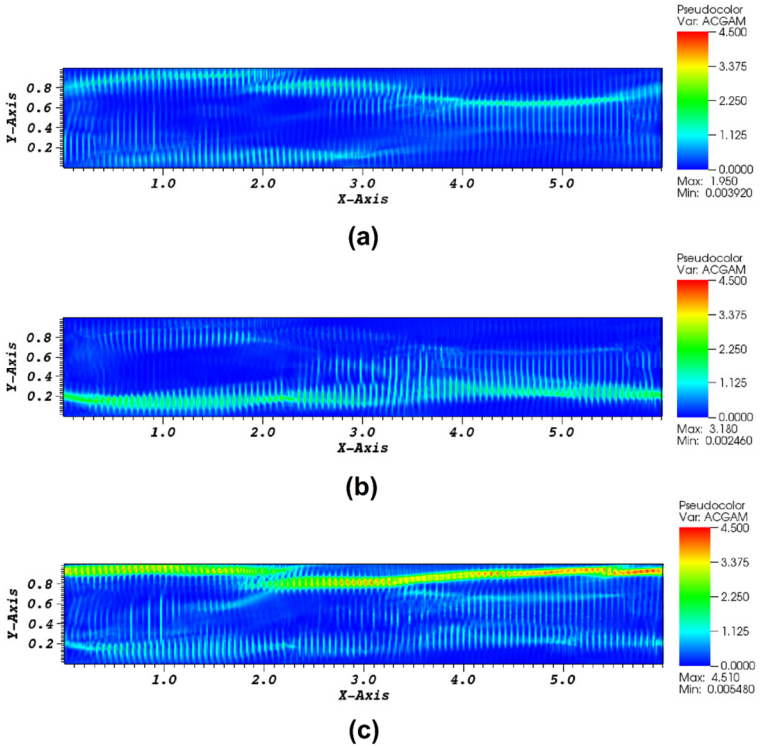

Figure 5-26: Contours of equivalent plastic shear strain computed using the Backstress hardening model for (a) initial forward (b) fully reversed and (c) subsequent forward shear loading.

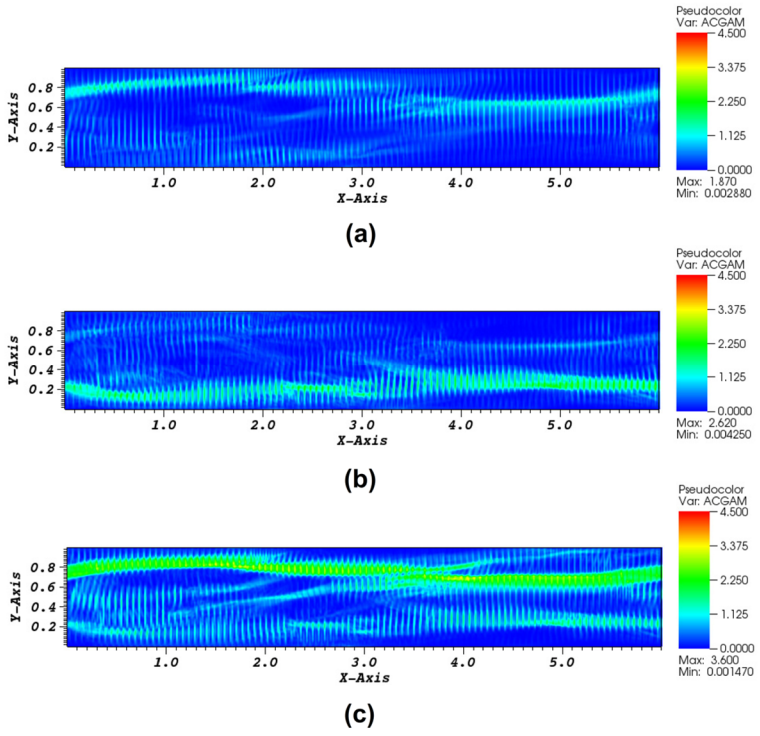

Figure 5-27: Contours of equivalent plastic shear strain without backstress hardening for (a) initial forward (b) fully reversed and (c) subsequent forward shear loading.

Figure 5-26 and Figure 5-27 show the contours of equivalent plastic shear strain computed using the backstress hardening model and without using backstress hardening, respectively. The contours are superimposed on the undeformed mesh and the shear direction (i.e. extrusion direction) is along the x-axis. The equivalent plastic shear strain is calculated using the procedure outlined in Inal et al. [218]. It is observed that the shear strain tends to localize in narrow bands and the localization behavior is rather similar for model with and without backstress effects. However, the shear strains are comparatively higher for model with the backstress hardening effects as shown in Figure 5-26. The differences in the predicted shear strains are more pronounced after the subsequent reverse and forward loadings. This is consistent with the prediction of texture evolution, where the differences in the predicted texture with and without backstress, are more pronounced during subsequent reverse and forward loadings. It is also observed that the shear bands are comparatively narrower when the backstress effects are taken into account.

The proposed backstress hardening model is further validated for its applicability to different strain paths. For this purpose, strain controlled tension-compression-tension (TCT) and compression-tension-compression (CTC) tests were performed in the extrusion direction for AA6063-T6. The cyclic tests were conducted using strain amplitudes of 4%, 6% and 8% for TCT tests, whereas CTC tests were conducted for strain amplitudes of 4% and 6% only. The cyclic test specimen used in the present work has been previously used by Muhammad et al. [176] to characterize the large strain cyclic behavior of magnesium alloys. The test specimen is shown in Figure 5-28. An anti-buckling fixture was also used to prevent buckling of the test specimen during in-plane cyclic compression. The reader is referred to Muhammad et al. [176] for detailed information on the testing procedure. The cyclic tests were conducted using an MTS Landmark 370 Servohydraulic machine with a load cell capacity of 100 KN and an MTS (Model: 632.31F-24) extensometer. The tests were performed at room temperature under strain-controlled condition at a nominal strain rate of 5×10^{-4}/s.

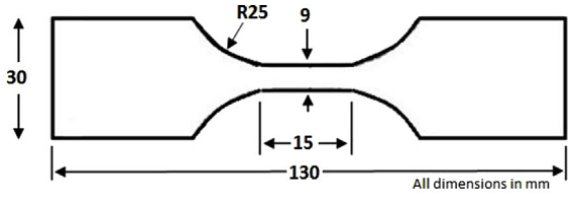

Figure 5-28: The cyclic test specimen for conducting TCT and CTC tests.

The experimental true stress-true strain TCT and CTC curves to several strain levels are shown in Figure 5-29(a) and Figure 5-29(b) respectively. We will refer to the first tensile loading step (in case of TCT) or the first compressive loading step (in case of CTC) as the initial forward loading step. The subsequent second loading steps after unloading will be referred to as 1st reversal and the third loading steps will be referred to as 2nd reversal. It is observed that the material exhibits the classical concave down flow behavior (similar to that observed in Figure 5-7(a)) with decreasing hardening rate throughout the initial forward loading step, which is typical of materials

in which plastic deformation is accommodated by crystallographic slip. Upon unloading the material exhibits an initial linear and a subsequent non-linear portion of unloading behavior. Furthermore, it is observed that the hardening rate during the initial forward loading step is relatively greater than the subsequent hardening rates during the 1st and 2nd reversal. This behavior is consistent with that observed during the cyclic shear deformation (in Figure 5-19) where the hardening rate during initial forward shearing is comparatively higher than that during the subsequent reverse and forward shear deformations. As discussed previously, this behavior is associated with the development of the underlying dislocation substructure. Furthermore, the material also shows a moderate Bauschinger effect during the 1st loading reversal. For completeness, the 0.2% offset yield stresses are reported in Table 5-3.

Table 5-3: 0.2% offset yield stresses for various TCT, CTC and simple shear loadings.

Loading Type	Strain Amplitude	Deformation Stage		
		Initial Forward	1st Reversal	2nd Reversal
TCT	4%	192	152	167
	6%	195	161	181
	8%	197	168	184
CTC	4%	199	170	174
	6%	198	174	180
Simple Shear	-	134	112	144

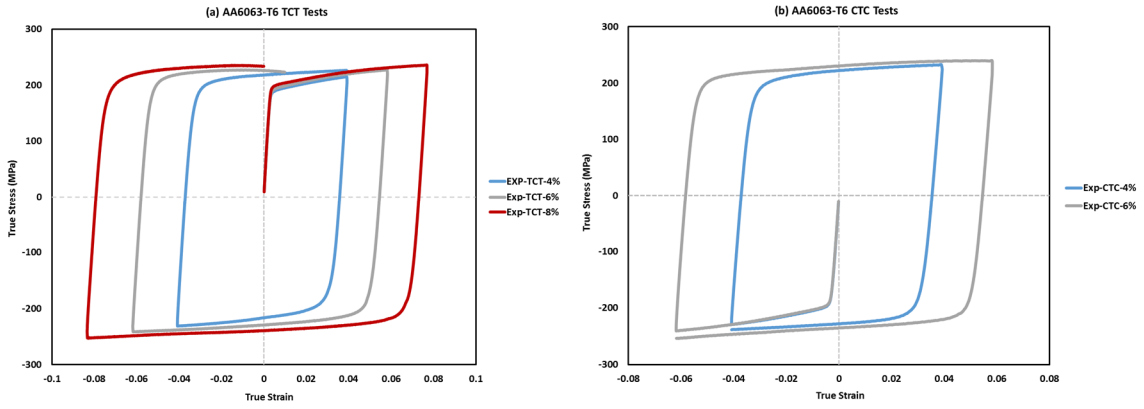

Figure 5-29: (a) TCT and (b) CTC experimental true stress vs. true strain curves for AA6063-T6 with different strain amplitudes for loading along the extrusion direction.

Figure 5-30 shows the comparison between the experimental and the hardening model response to TCT and CTC loading paths for the different strain amplitudes. The TCT and CTC simulations are performed using the same set of parameters (given in Table 5-2), previously determined using the monotonic simple shear data. It is observed that the proposed backstress hardening model successfully reproduced the experimental TCT and CTC cyclic stress-strain curves for AA6063-T6. In particular, the model is able to reproduce the experimentally observed Bauschinger effect. However, there are discrepancies between the simulated and experimental results in vicinity of

stress unloading-reloading regions of the cyclic curves. This discrepancy is associated with the non-linear unloading behavior of the material as observed experimentally in Figure 5-29. The current crystal plasticity formulation does not account for this non-linear unloading behavior.

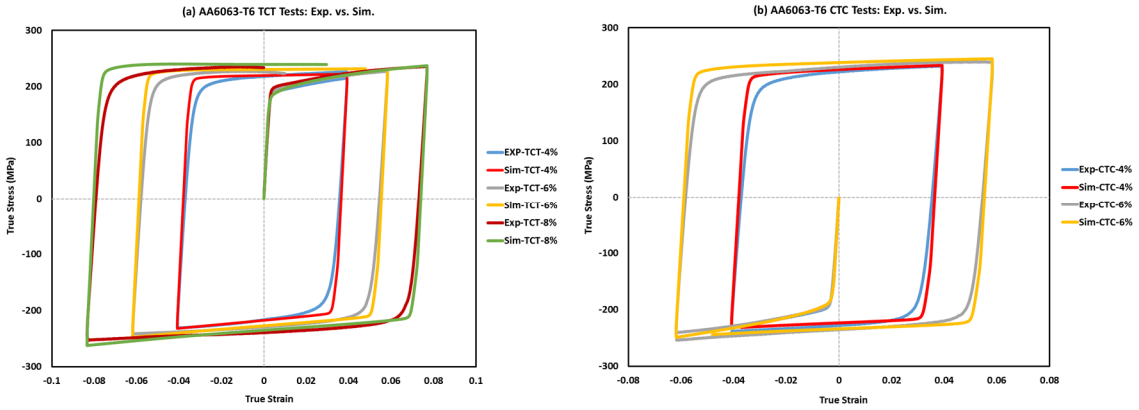

Figure 5-30: Comparison between simulated (a) TCT and (b) CTC flow stress response and experimental data for AA6063-T6.

In the current work, the proposed backstress hardening model has been successfully applied to capture the large strain cyclic simple shear behavior of AA6063-T6. The predicted evolution of backstress is well supported by the TEM observations made on the evolution of dislocation microstructure during different stages of shear deformation. The proposed model is further validated by successfully applying it to complex strain paths such as tension-compression-tension and compression-tension-compression with varying strain amplitudes. The proposed model is able to capture the experimentally observed Bauschinger effect during reverse loading. Furthermore, the texture evolution results predicted using the backstress hardening model show good conformity to the experimental results.

5.5 Chapter Summary and Conclusions

The cyclic simple shear behavior of extruded aluminum alloy AA6063-T6 at room temperature is studied by using a combination of mechanical and microstructural techniques. The techniques include forward-reverse-forward simple shear tests along the extrusion direction, EBSD texture measurements to characterize texture evolution and TEM analysis to analyze the deformation induced dislocation microstructure. A crystal plasticity based backstress hardening model is proposed to account for the intragranular backstresses which arise from the formation of dislocation cell substructure in the microstructure. The proposed model accounts for hardening due to interactions with forest dislocations as well as with dislocation cells. The interaction with dislocation cells is estimated by using backstress effect. The model is numerically implemented within a 2D crystal plasticity finite element framework. The proposed model is calibrated and

cyclic simple shear simulations are performed. The modelling assumptions on the evolution of backstress due to the evolution of the cell structure are qualitatively verified with TEM observations. The predicted flow stresses and texture evolution results are compared against experimental findings. Some important observations and conclusions are summarized as follows.

- The as-received AA6063-T6 extruded material has an average grain size of approximately 63 μm with a through crystallographic texture which is predominantly Cube followed by a comparatively weaker Goss texture.
- The flow behavior of the material is fairly symmetric during cyclic planar simple shear deformation and the hardening rate during the initial forward simple shear deformation is significantly higher than the subsequent reverse and forward deformations. Furthermore, the hardening rate during reverse loading is comparatively similar to that of subsequent forward loading. The occurrence of a moderate Bauschinger effect is also observed during subsequent reverse shear deformation after the initial forward shear deformation.
- EBSD texture measurements show a substantial evolution of texture during all three deformation stages (i.e. initial forward shear, subsequent reverse shear in opposite direction and subsequent forward shear in the initial direction). It is observed that simple shear deformation leads to the rotation of texture components along the normal direction. Furthermore, the Goss component of the texture weakens continuously as the shear deformation proceeds through the three deformation stages. It is concluded that the Goss component of texture is comparatively less stable than the cube component.
- Microstructure analysis using the image quality maps shows the presence of a banded structure indicating localized deformation in slip and shear bands. After the initial forward shear deformation, the microstructure shows presence of short microscopic bands within several grains and a large localized macroscopic band parallel to the loading (i.e. extrusion) direction. As the deformation proceeds further, the presence of multiple macroscopic deformation bands along the length of the shear zone and several smaller intersecting bands making an approximate 90^{o} angle to those large deformation bands have been observed.
- Results from TEM analysis show the presence of dislocation cell substructure within the microstructure. After the initial forward shear deformation, the microstructure shows dislocation tangles with some regions having relatively high dislocation content while others being virtually dislocation free. A tendency towards the formation of this dislocation cell structure is apparent after the initial forward shear deformation. Microstructures after the subsequent reverse and subsequent forward shear deformations show the presence of cell/subgrain structure with majority of dislocations being trapped at the subgrain cell wall boundaries. It is also observed that the subsequent forward shear deformation, after previous reverse shearing, leads to a reduction in the average dislocation cell size.
- The numerically predicted cyclic simple shear flow behavior shows an excellent conformity to the experimental data. More importantly, the new backstress hardening

model is able to reproduce the experimentally observed Bauschinger effect once the loading is reversed.

- The predicted texture evolution results also show an excellent qualitative match with the experimental data for each of the three deformation stages. The polycrystal model is able to predict texture rotations as well as the weakening of Goss component as observed experimentally during the cyclic shear deformation.
- Lastly, the applicability of the proposed numerical model is further validated by performing TCT and CTC simulations for different strain amplitudes. The simulated results show good agreement to the experimental data.

Chapter 6: Development and Application of a Multiscale Modeling Framework to Predict Strain Localization and Surface Roughness

In this chapter, a multi-scale modeling framework is proposed. The multiscale framework along with the new backstress hardening model are applied to predict strain localization and the development of surface roughness that are precursor to failure – fracture. The chapter presents a detailed experimental and numerical study with emphasis on investigating correlations between heterogeneous plastic deformation, strain localization, the accompanying texture evolution and the development of surface topography effects during bending of extruded AA6063.

The chapter presents an accepted manuscript of an article published in International Journal of Plasticity.

International Journal of Plasticity 117 (2019): 93-121. Doi: 10.1016/j.ijplas.2017.09.013

Experimental Analyses and Numerical Modeling of Texture Evolution and the Development of Surface Roughness during Bending of an Extruded Aluminum alloy using a Multiscale Modeling Framework

International Journal of Plasticity 117 (2019): 93-121

Waqas Muhammad[1,2], Usman Ali[1], Abhijit P. Brahme[1], Jidong Kang[2], Raja K. Mishra[3], Kaan Inal[1]

1 Department of Mechanical and Mechatronics Engineering, University of Waterloo, Waterloo, N2L 3G1, Canada

2 CanmetMATERIALS, 183 Longwood Road South, Hamilton, ON L8P 0A5, Canada

3 General Motors Research & Development Center, Warren, MI 48090, USA

Overview

Bending is an important strain path in various metal forming operations as well as vehicle crashworthiness. In the present study, the bending behavior of an extruded aluminum alloy AA6063-T6 is investigated using wrap bending tests. The focus of the work is on understanding the relationship between heterogeneous plastic deformation, strain localization, the accompanying texture evolution and the development of surface topography effects during wrap bending. In these regards, wrap bending experiments are conducted and the bendability of the as-received material is assessed. The development of micro-slip bands, shear localization and the formation of surface undulations through-thickness of the bend are analyzed using conventional metallography and scanning electron microscopy (SEM). The initial microstructure, grain size distribution and texture evolution during bending are analyzed using electron backscatter diffraction (EBSD) measurements. The surface topography of the bent specimen is analyzed using 3D laser scanning profilometry. Next, a 3D multi-scale modeling framework is used to simulate wrap bending using crystal plasticity based finite element methods (CPFEM). The simulated results for strain localization, texture evolution and surface topography development show good agreement to the corresponding experimental findings. The modeling results are further analyzed to understand the relationships between initial microstructure, strain localization and surface topography development. A set of bending simulations is also conducted using 3D synthetic microstructures to further investigate the relationship between through thickness clustering of similarly oriented grains, initial microstructure and the developed surface topography after bending. A possibility to achieve a lower surface roughness by altering the through thickness locations of similarly oriented grain clusters has been demonstrated. Lastly, it has been numerically verified that by eliminating or by reducing the tendency towards clustering of similarly oriented grains within the microstructure, a transition from a ridging to an orange peel type surface topographic behavior can be achieved.

Keywords: wrap bending; surface roughness; crystal plasticity; strain localization; texture; finite elements

6.1 Introduction

Bending is one of the most widely used operations in sheet metal forming and is of special importance to automotive industry. Inner automotive structures may involve bending of thick gauge sheets or extruded tube components, while outer body panels are joined to inner sheets through a two-step bending process, known as hemming. In addition, the bendability of structural components such as the front rails, rockers, pillars, etc. is of special importance for maximum crash energy absorption.

Aluminum alloys, in particular the Al-Mg-Si (AA6xxx) alloys, are increasingly used in automotive structural applications due to their heat-treatable properties leading to higher final strengths compared to conventional aluminum alloys. However, due to the lower ductility, formability and fracture resistance of AA6xxx alloys compared to steels, their bending performance limits their application in automotive [219]. Thus, improvement in bending behavior is one of the main factors to expand the applicability of aluminum alloys to various types of structural members within vehicles [220].

The bending behavior is usually assessed through a wrap bend test or a cantilever bend test [221]. In a wrap bend test, the bendability is assessed by bending the sheet specimen around increasingly severe radii until fracture is observed on the outer bent surface. The bendability of the material is usually defined by the parameter r_{min}/t, where t is the thickness of the material. Several studies have shown that bending of aluminum alloys is limited by surface-induced cracking due to intense strain localization [220–223]. It has been shown that during bending, failure usually occurs with intense strain localization at the outer tensile surface, preceded by the development of surface roughness (i.e. orange peels) and gradually growing surface undulations parallel to the bend axis [219, 223–226]. In other words, the development of surface roughness and undulations on the outer bent surface promotes the onset of strain localization, micro-shear band formation and failure. The importance of surface roughness on the bending behavior of aluminum alloys was first examined by Lloyd using a cantilever bend test [227]. In his study, the author bent several sheet specimens to an initial bend angle, followed by an intermediate polishing step to remove the developed surface topography and bending to a final bend angle. The author concluded that the intermediate polishing step enhanced the bendability of the alloy. Consistent with this observation, several other authors have also attributed damage during bending with the formation of shear bands that initiate at points of local strain concentrations, which generally coincide with locations of high surface roughness [228–231].

Surface roughness during bending can take a variety of forms such as orange-peeling and ridging at different length scales. Orange-peel refers to the general roughening of the bent surface and is characterized by out-of-plane displacements, both negative and positive, which approximately map the grain shape of the material [232, 233]. The so-called ridging or roping phenomenon has a

more directional character and occurs in the form of banded surface undulations [233, 234]. Apart from the adverse effects of surface roughness on bending performance, its presence is also undesirable from visual or aesthetic perspective.

Several studies have been performed to analyze the development of surface roughness. Early studies showed that the amount of surface roughness is proportional to the through-thickness strain and it has a linear dependence on the grain size [233, 235–240]. The explanation of these linear dependencies has been attributed to local incompatibilities in the deformation of adjacent grains. It has been suggested that difference in crystallographic orientations leads to local strain incompatibilities between a grain and its neighbors. Closer to the surface, this incompatibility causes the surface grains to move normal to the surface, developing surface roughness. It has also been suggested that small scale shear band formation near or at the surface can also augment surface roughness by influencing the surface strain distribution and increasing the depth of surface valleys [240]. More recent experimental studies on surface roughness has been focused on understanding the origins of surface roughness and its relationship with the spatial distribution of grain orientations using electron backscatter diffraction (EBSD) methods [232, 241–243]. In particular, Wittridge and Knutsen [244] studied the development of surface roughness during uniaxial tension of AA3002 aluminum alloy with special emphasis on the development of surface ridges and valleys. Based on microtexture analysis, the authors concluded that the observed ridging behavior is attributed to spatial differences in texture at the specimen surface whereby R-component colonies in a cube matrix produce differential straining. This differential straining leads to strain localization through thickness of the specimen, leading to the formation of a ribbed surface profile. Similarly, Baczynski et al. [245] studied the roping behavior of AA6111 automotive alloy sheet during uniaxial tensile deformation. Their study concluded that both ridges and valleys on the upper and lower surfaces are irregularly distributed in the rolling direction and the occurrence of ribbed profiles and corrugations are rare. Furthermore, the authors suggested that the spatial distribution of the Goss component is responsible for the roping behavior in AA6111 automotive sheets. One of the most comprehensive recent studies in the field was published by Raabe et al. [232], where the authors have studied grain-scale micromechanics of polycrystal surfaces during plastic straining. The authors studied the development of surface roughness during tensile and bending deformation of aluminum alloy AA6022 with special focus on understanding the relationship between microstrain heterogeneity and surface roughness in plastically strained polycrystals with respect to the surface and through-thickness microstructure. The authors successfully highlighted a relationship between the heterogeneity of plastic surface microstrains, surface roughness, and microstructure and suggested that the ridging behavior is promoted by the presence of grain clusters consisting of Cube, Goss, rotated Goss and {111}[*uvw*] microtexture components. Apart from the experimental studies, several modeling efforts have been made-to-date to further examine the correlation between strain localization, microtexture and the development of surface roughness during bending.

Finite element modeling has been used extensively to study strain localization in bending. Triantafyllidis et al. [228] studied strain localization and shear band development in pure bending of elastoplastic solids using the J_2 corner theory. Becker [246] studied pure bending of a polycrystalline sheet using a slip-based Taylor-type polycrystal model. By assigning different sets of crystal orientations to each grain, the author analyzed the effects of strain incompatibilities between neighboring grains and its effect on shear band initiation at the free surface and its propagation towards the neutral axis. Lievers et al. [224] analyzed bendability and the development of surface roughness for AA6111 automotive sheets with varying Fe contents using Gurson's model with isotropic and kinematic hardening effects. Using a material model based on non-associative plastic flow, Kuroda and Tvegaard [230] analyzed plane strain bending localizations. Majority of the studies involving localization and surface roughness use conventional phenomenological plasticity based material models. However, in order to study localization and development of surface roughness, a distribution of material anisotropic properties is required to create localized non uniform deformation. For this reason, a crystal plasticity based finite element theory is used in the present work.

Most of the finite element studies on strain localization and development of surface roughness during bending have adopted the 2D plane strain shell element models [219, 228, 230, 247, 248], where bending deformation is studied in the plane normal to the bend axis. It has been shown that the capability of 2D models to represent accurately the state of strain and stress as well as to reveal the presence of surface banding is inadequate [249]. Furthermore, in majority of these studies, the modeling domain consists of a unit cell where pure bending boundary conditions are assigned [219, 228, 247, 250, 251] with the assumption that material in all areas of the bend experiences the same bending deformation. However, actual bending operations are rather complex due to surface contacts between tooling and actual part and the pure bending condition is rarely achieved in practice [248].

The purpose of the current work is twofold. Firstly, a comprehensive experimental study on the bending behavior of extruded AA6063-T6 alloy is presented and secondly, a multi-scale 3D modeling framework is developed to simulate the actual wrap bending process. The experimental work is presented with emphasis on investigating correlations between heterogeneous plastic deformation, strain localization, the accompanying texture evolution and the development of surface topography effects during bending. For this purpose, wrap bending tests are conducted with bend axis perpendicular to the extrusion direction and the bendability of the as-received material is assessed. Optical and scanning electron microscopy has been used to analyze the presence of micro-slip bands, shear localization and the development of surface undulations through-thickness of the bend specimen. Bending deformation leads to significant evolution of the crystallographic texture. Hence, electron backscatter diffraction (EBSD) measurements are performed to characterize the through-thickness evolution of texture after bending. Furthermore, 3D laser scanning profilometry has been used to analyze the development of surface topography after bending. For multi-scale 3D modeling, a component - macro level wrap bending simulation

is performed using conventional phenomenological plasticity within the finite element (FE) framework. Next a region of interest for further analysis is identified and a microstructure based 3D micro-model is developed for that region and the wrap bending simulation is performed using crystal plasticity based finite element methods (CPFEM). The displacement history of the region of interest is taken from the macro-model and is applied as boundary conditions to the micro-model. The CPFEM based 3D bending simulations are performed to further analyze the experimentally observed texture evolution, strain localization and their relationship with surface topography development. Some experimentally measured trends are reproduced for model verification, and a comparison of texture evolution and surface topography development is made with experimentally measured roughening to illustrate the validity of the proposed constitutive framework. Next, a set of bending simulations is performed using synthetic 3D microstructures to further investigate the relationship between through thickness clustering of similarly oriented grains, microstructure and the observed surface topographic behavior.

6.2 Experimental Characterization

6.2.1 Experimental procedures

An age-hardenable aluminum alloy AA6063, in the form of an extrusion, was used in the present study. The chemical composition of the alloy is given in Table 6-1, where magnesium and silicon are the major alloying additions. The extruded alloy was received in a T6 tempered condition and the as-received extrusion profile is shown in Figure 6-1. The extrusion direction is marked in Figure 6-1 as 'ED'. The extrusion profile has a nominal wall thickness of 1.8 mm.

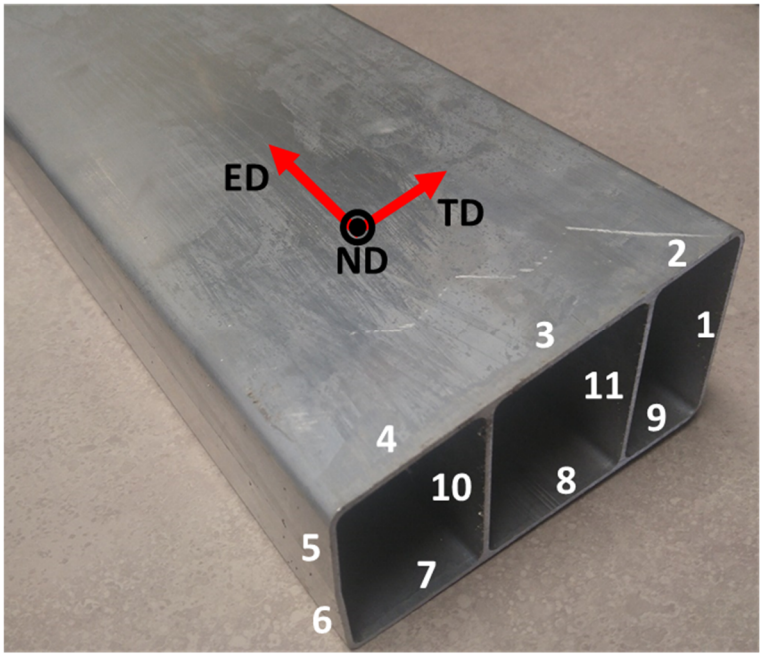

Figure 6-1: The as-received extrusion profile of AA6063-T6 material.

Table 6-1: Chemical composition (max. wt%) of as-received AA6063-T6 extruded material.

Material	Mg	Si	Fe	Mn	Cu	Al
AA6063	0.49	0.4	0.16	0.029	0.01	Bal.

The tensile hardening behavior of the as-received AA6063-T6 material was characterized by conducting quasi-static uniaxial tension tests. For this purpose, standard ASTM-E8M specimens were machined parallel to the extrusion direction (ED) from 11 different locations (see Figure 6-1) across the extrusion. The tensile tests were carried out using an MTS Landmark 370 Servohydraulic machine with a load cell capacity of 100 KN and an MTS (Model: 632.12C-21) extensometer. All tensile testing was conducted at room temperature at a nominal strain rate of 5 x 10^{-4}/s. Each test was conducted at least twice to ensure repeatability. The results of the stress-strain behavior are presented in Section 6.2.2.1.

The bending behavior of the alloy was characterized using the wrap bend test (ASTM-E290). For this purpose, rectangular specimens were cut along the extrusion direction from the as-received material using electrical discharge machining (EDM). The specimen dimensions were 76 mm in length and 30 mm wide. During the wrap bend test, individual specimens were wrapped or bent around mandrels with increasingly severe (i.e. smaller) radii (from r = 0.8 mm down to r = 0.1 mm) until fracture was observed on the outer bent surface. Figure 6-2 shows a schematic of the wrap bend apparatus used in the present study, where r is the radius of mandrel that the specimen is bent around and t is the specimen thickness (i.e. t $\approx$ 1.8 mm which is the extrusion wall thickness). The bend axis was perpendicular to the extrusion direction (i.e. parallel to transverse direction (TD) in Figure 6-2) and the maximum bend angle was fixed to 150°. Before performing the wrap bend tests, the contact surfaces between the specimen and the roller and the specimen and the mandrel were lubricated to minimize any frictional effects. The wrap bend results were further expressed in terms of the bendability parameter (r_{min}/t) where r_{min} is the minimum bend radius of the mandrel to which the specimen can be bent without apparent surface cracking and t is the specimen thickness. A lower r/t value indicates better bendability.

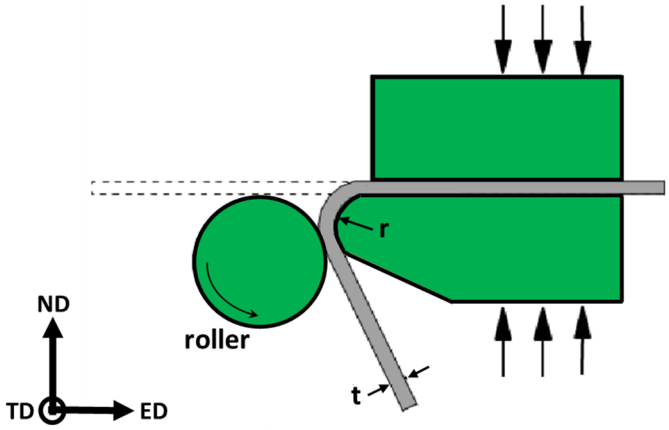

Figure 6-2: Schematic representation of a wrap-bend test.

The outer tensile surfaces of the bent specimens were further examined using a JEOL-7000 field-emission SEM. Next, the bent specimens were sectioned at the mid-plane and mounted using the through-thickness ED-ND plane. The terms 'ED' and 'ND' correspond to the extrusion direction and the through-thickness direction, respectively. The samples were mechanically polished and etched using a hydrofluoric (HF) acid solution for optical microscopy to reveal grain morphology and slip distribution through thickness of the bend. The specimens were analyzed using a Zeiss light microscope equipped with a Nikon digital camera.

Electron backscatter diffraction (EBSD) texture measurements were also performed to characterize the initial texture of the as-received material and texture evolution after wrap-bending deformation. Texture measurements were made on the ED-ND plane (see Figure 5-1) to characterize the through thickness microstructure. All EBSD samples were prepared using standard metallography techniques (such as cold mounting, grinding and fine polishing) followed by a final ion-milling step to achieve the desired surface finish. All texture measurements were performed using a field-emission Nova NanoSEM™ equipped with a TSL EBSD camera. A step size of 0.5 μm was used for all EBSD measurements and the scan data was further analyzed using the TSL OIM™ software. The scan data was cleaned using neighbour CI correlation to remove bad data points within the TSL software.

6.2.2 Experimental results and discussion

6.2.2.1 Initial microstructure and tensile flow behavior

The through thickness microstructure of the as-received AA6063-T6 material is shown in Figure 6-3(a) and the corresponding pole figures are shown in Figure 6-3(b). It can be observed that AA6063-T6 has a recrystallized microstructure with equiaxed grains as shown in Figure 6-3(a). Furthermore, the through thickness grain size and texture of the extruded material are different in the center as compared to in vicinity of the extrusion walls. More specifically, the grains closer to the outer surfaces of the extrusion walls are relatively larger in size as compared to those in the

center of the extrusion and also exhibit a different texture as apparent from the different colors in the IPF map (see Figure 6-3(a)). This inconsistency in grain size and texture may well be related to the differences in strain path and cooling rate experienced by the material closer to the extrusion wall as compared to the center of the extrusion. In addition, the through-thickness texture of AA6063-T6 is predominantly cube texture followed by a comparatively weaker Goss texture as represented by the <111> pole figure in Figure 6-3(b).

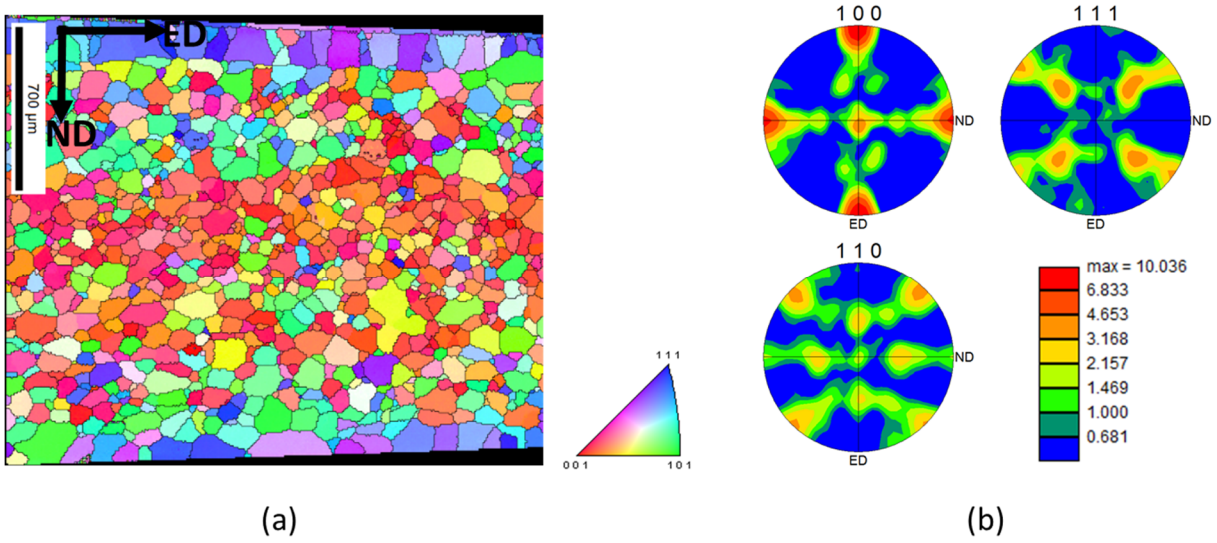

Figure 6-3: Through thickness microstructure of the as-received extruded AA6063-T6 material (a) inverse pole figure map and (b) <100>, <111> and <110> pole figures.

Figure 6-4 compares the texture of the extrusion in vicinity of the extrusion wall (Figure 6-4(a) and (b)) to that at the center of the extrusion (Figure 6-4(c) and (d)). The <111> pole figures clearly show that the texture in vicinity of the wall is indeed very different to that at the center of the extrusion (see Figure 6-4(a) vs. Figure 6-4(c)). It is also observed that the texture closer to the walls is predominantly a {111} texture with majority of the <111> poles aligned parallel to the transverse direction. This is apparent from the inverse pole figure plot in Figure 6-4(b) where the contour plot shows a very high intensity along the <111> direction. On the contrary, the texture at the center of the extrusion is predominantly cube texture as apparent from the <111> pole figure in Figure 6-4(c) and the corresponding inverse pole figure in Figure 6-4(d). Figure 6-5 shows the grain size distribution of the as-received AA6063-T6 material. It is noted that the material shows a wide variance in grain size with grains as small as 15 µm in the center of the extrusion to as large as 200 µm in vicinity of the extrusion walls. However, the average grain size of the material is approximately 75 µm.

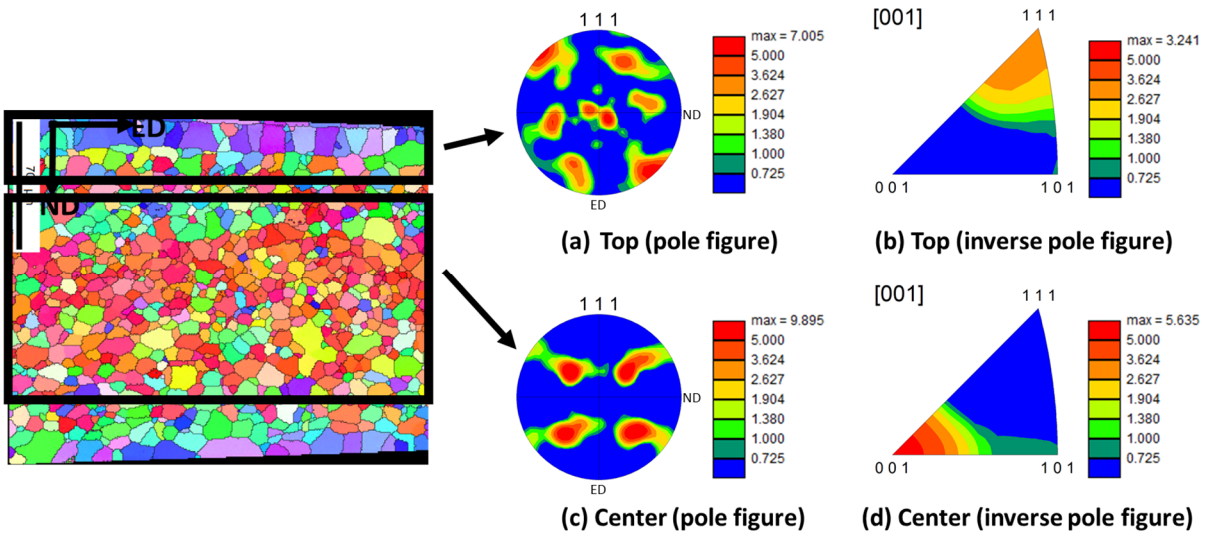

Figure 6-4: Comparison of through thickness microstructure of AA6063-T6 material (a),(b) texture in vicinity of the extrusion walls and (c),(d) texture in the center.

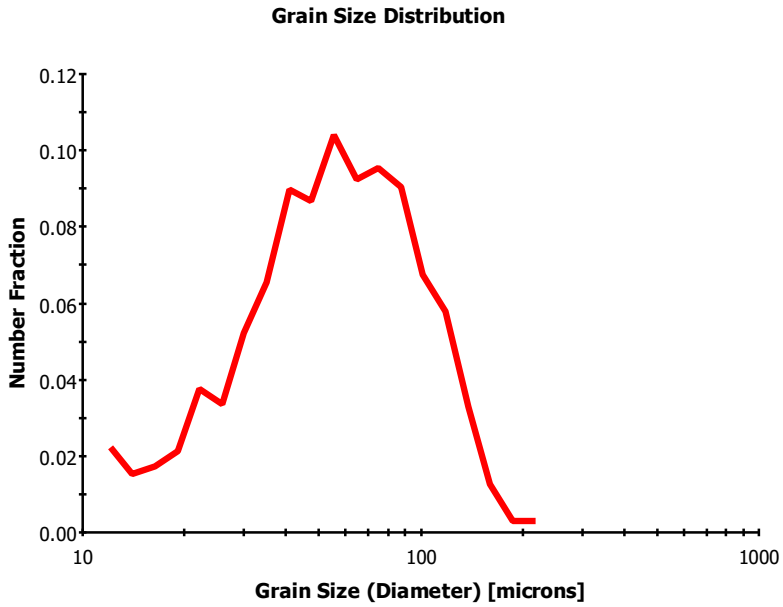

Figure 6-5: Grain size distribution of the as-received extruded AA6063-T6 material.

As mentioned previously, uniaxial tension tests were performed using tensile specimens made from 11 different locations (see Figure 5-1) across the extrusion. The tensile flow behavior is found to be consistent across all 11 locations. Figure 6-6 shows the engineering stress – engineering strain behavior of AA6063-T6 material along the extrusion direction. It can be observed that the as-received material has a yield strength of approximately175 MPa and an ultimate tensile strength of approximately 210 MPa.

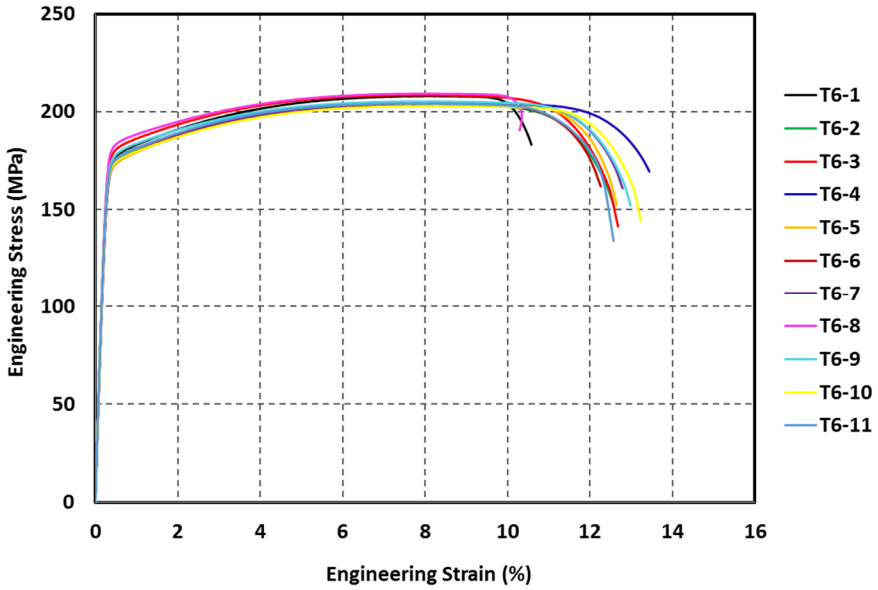

Figure 6-6: Engineering stress vs. engineering strain of as-received AA6063-T6 along the extrusion direction (ED).

6.2.2.2 Bending behavior

6.2.2.2.1 Bendability

As mentioned previously, the bending behavior of AA6063-T6 was characterized using wrap bend tests. Different radii mandrels starting from 0.8 mm down to 0.1 mm (with 0.1 mm being the most severe bend radius) were used to assess the bendability of the material, where bendability is characterized by the geometric parameter r_{min}/t. It is observed that the as-received material showed no apparent signs of cracking or fracture at the outer tensile surface up till a mandrel radius of 0.3 mm. However, cracking at the outer tensile surface was apparent when a mandrel radius of 0.2 mm was used to bend the specimens. Based on the wrap bend results, the minimum bend radius across which the specimen can be bent successfully without visible cracking is r_{min} = 0.3 mm. Since, the thickness of the specimen is 1.8 mm, the geometric bendability parameter $r_{min}/t \approx 0.1667$.

Bendability is one of the important characteristics of precipitation hardening 6xxx aluminum alloys. At the continuum scale, several efforts have been made to relate bendability to other mechanical properties, such as yield strength [252, 253], but the most significant relationship has been proposed by Datsko and Yang [254]. The authors were able to correlate sheet bendability to the reduction in area at fracture in a tensile test and proposed the following empirical relationship:

$$r_{min}/t = (C/RA) - 1 \quad \text{(6-1)}$$

where RA is the percent reduction in area at fracture in a tensile and C is a constant, in the range of 0.5 to 0.7, depending on material's ductility. Reduction in area measurements at tensile fracture were performed using a stereoscopic microscope for the as-received AA6063-T6 alloy and the area reduction was measured to be approx. 54%. Using the experimental values, the constant C (in

Eq. (6-1)) for the present material is calculated to be 0.63, which falls well within the suggested range.

6.2.2.2.2 Microstructure evolution during bending

Figure 6-7(a) shows a through thickness optical micrograph of the specimen bent using a mandrel radius of 0.2 mm. One can clearly see the presence of multiple micro-cracks (encircled in red in Figure 6-7(a)) along the outer tensile surface of the specimen. The specimen in Figure 6-7(a) was further etched to reveal grain boundaries and the corresponding micrograph is shown in Figure 6-7(b). It is observed that during bending deformation, strain tends to localize within certain regions of the bend, which leads to significant changes in grain shape and orientation. Grains closer to the compressive bend region are elongated in the 'ND' direction whereas grains closer to the outer tensile surface are elongated along the 'ED' direction due to large tensile strains (see Figure 6-7(b)). Furthermore, grain rotation and grain deformation has led to the development of surface undulations, which upon continuous deformation led to the formation of grooves at the outer bend surface. These grooves (i.e. valleys) are encircled in red in Figure 6-7(a) and are directly responsible for surface roughness on the specimen surface. Similar observations have been made by many other researchers, where the authors have reported the formation of surface undulations or grooves in vicinity of regions of intense strain localization [219, 221, 231, 252, 253, 255]. It has been further suggested that strain localization can occur at various length scales within the microstructure, which will directly influence the magnitude of surface undulations, depending on the amount of applied deformation and work hardening characteristics of the alloy [219, 223].

It is important to note that cracks appear to initiate form regions of high surface roughness along the outer bend surface. More specifically, Figure 6-7(a) clearly shows that multiple cracks (encircled in red) have initiated from the 'valleys' of the surface, which has been roughened due to intense strain localization. In addition, Figure 6-7(b)) shows that the development of surface undulations (i.e. peaks and valleys) on the outer tensile surface is not a mere surface effect but in fact is linked with strain localization through thickness of the bend. The red arrows in Figure 6-7(b) are pointing towards the regions of high strain localization through thickness of the bend, which have led to the development of surface undulations along the outer tensile region. Strain localization has led to local "necking" within these regions. Strain within these regions tends to localize in coarse slip bands within grains. This development of coarse slip distributions within grains is more obvious in Figure 6-8, which presents a magnified view of the bend region. The red arrows in Figure 6-8 point towards some of the regions which show the presence of coarse slip bands within grains. The magnitude of these coarse slip distributions within grains are very high in vicinity of the compressive and tensile bend regions due to the high local strains. It is also interesting to note that surface roughness (i.e. undulation) regions which show the development of surface 'peaks' are comparatively free of intense strain localization. This can be observed from Figure 6-7(b), where the green arrows are pointing towards 'peak' surface roughness regions and it is apparent that grains within these regions are comparatively less localized. It is believed that

this strain incompatibility between neighboring regions or grains is one of the primary factors which led to the development of surface roughness. Several researchers have suggested that these local strain incompatibilities and the formation of surface roughness are linked with differences in the underlying local crystallographic texture [220, 253, 256, 257].

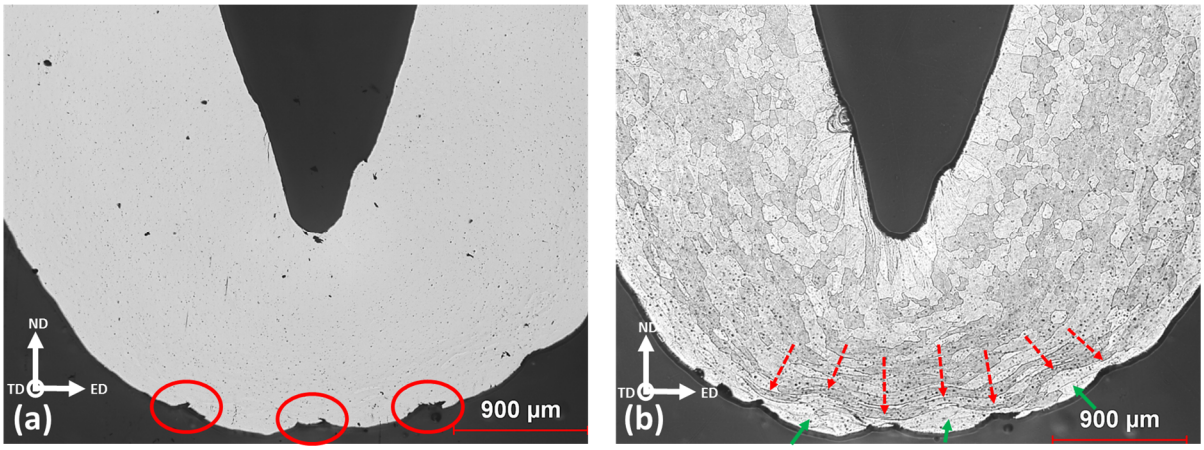

Figure 6-7: Through thickness optical micrograph of AA6063-T6 specimen bent using a mandrel radius of 0.2 mm.

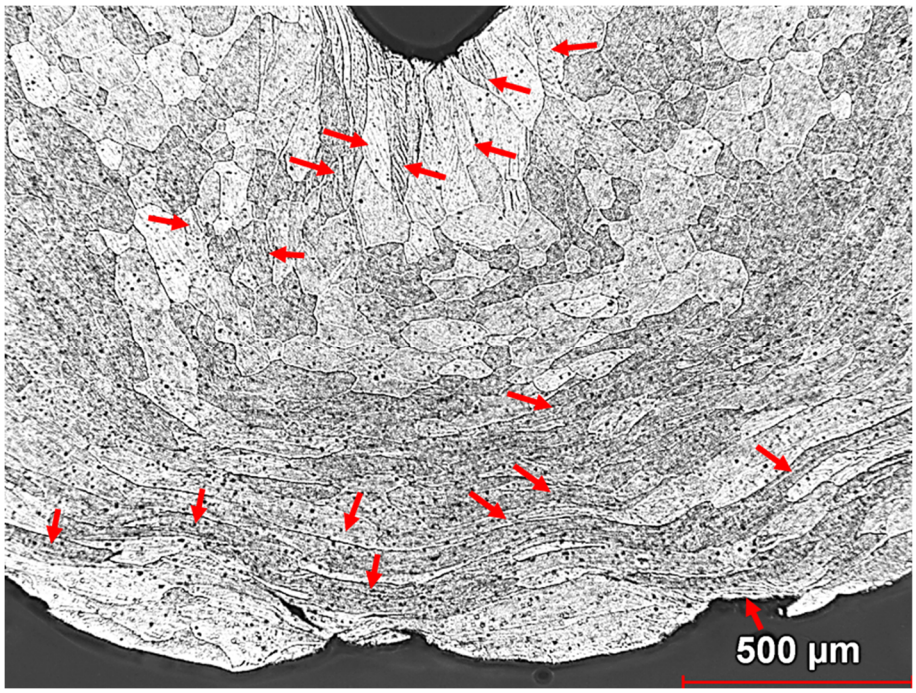

Figure 6-8: Magnified image of through thickness optical micrograph of AA6063-T6 specimen showing the presence of coarse slip distributions within grains.

Figure 6-9 shows the SEM image of the outer (i.e. upper) tensile surface of the wrap bend specimen. It is observed that the polycrystalline structure of the material is apparent on the bend surface and grain boundary relief due to strain accommodation between grains is evident. Strain tends to localise into coarse slip bands within the grains as pointed by green arrows in Figure 6-9(a)

and Figure 6-9(b). The presence of macroscopic surface ridges is also evident. These ridges are approximately parallel to the bend axis and pass through multiple grains, accommodating slip transmission across grain boundaries. Decohesion along grain boundaries, leading to the formation of micro cracks, is also apparent and is pointed by red arrows in Figure 6-9(a). On the other hand, Figure 6-9(b) shows cracks (pointed with green arrows) which are roughly parallel to the bend axis, and a couple of hundred micrometres in length within the middle region of the bend. The cracks, seem to, firstly initiate from the middle region due to a constrained plane strain tension deformation and propagate towards the edges, reaching several hundreds of micrometers in length. Relative sliding of grains with respect to each other results in height changes and the formation of surface undulations. Furthermore, it is observed that this relative sliding has led to some adjacent grains moving perpendicular (i.e. out of) to the surface (see the encircled region in green in Figure 6-9(b). This relative motion between surface grains has led to decohesion along the grain boundary and formation of an intergranular crack.

Figure 6-10 shows a magnified image of the region encircled in red in Figure 6-9(a). The SEM image presents a magnified view of the region in vicinity of a crack. Slip line markings and deformation steps, which are characteristic of inhomogeneous and coarse planar slip within the grains, are visible in vicinity of the micro crack (see regions pointed by green arrows in Figure 6-10). The orientation of the slip traces are different within neighboring grains and may well be related to the difference in local crystallographic texture. It is also interesting to note that the surface of the crack consists of fine micro dimples (regions pointed by red arrows in Figure 6-10), which are formed due to strain localization in the weak grain boundary areas. The presence of these micro dimples is indicative of the fact that heterogeneously nucleated grain boundary particles (see Figure 6-8) have led to the formation, growth and coalescence of micro-voids, assisting the final fracture process. This kind of deformation and fracture behavior has been observed in precipitation hardening aluminum alloys near or close to peak hardening (i.e. T6 temper) condition and is known as grain boundary ductile fracture (GBDF) [44, 126]. Similar fracture behavior has been previously reported by Davidkov et al. [231] during bending of AA6016 aluminum alloy sheets. It is suggested that this kind of fracture behavior is linked with several competing or inter-related mechanisms, (i) the presence of heterogeneously nucleated grain boundary particles, (ii) the formation of precipitation free zones (PFZs) along the grain boundaries and (iii) coarse slip distributions within grians causing stress concentations along the already weakened grain boundaries [126, 231, 258, 259].

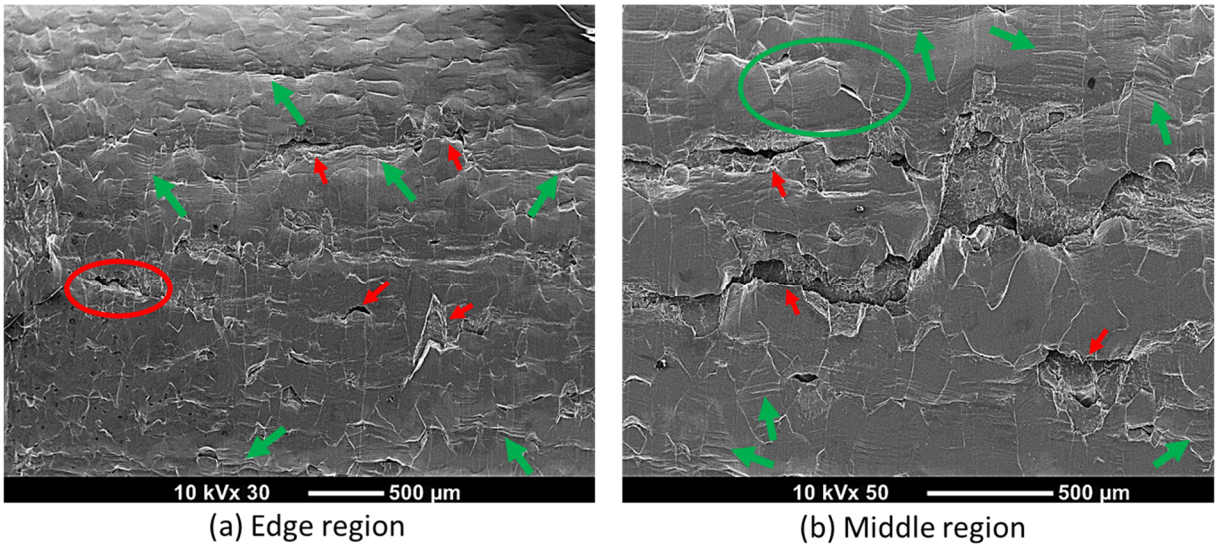

Figure 6-9: SEM micrograph of the outer tensile surface of the wrap bend specimen (a) close to edge of the specimen (b) within the middle region of the bend specimen.

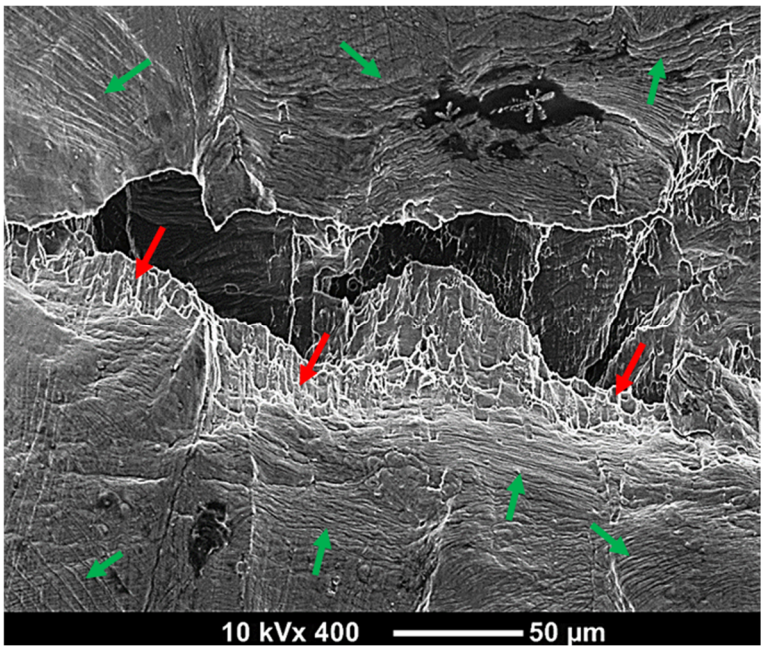

Figure 6-10: SEM micrograph showing the magnified view of the region encircled in red in Figure 6-9(a).

6.2.2.2.3 Texture evolution during bending

Figure 6-11 shows the IPF map of a deformed wrap bend sample using a mandrel radius of 0.2 mm. Due to the extremely large deformations in vicinity of the compressive and outer tensile regions of the bend, the EBSD system was unable to index data in some of those regions. The bad data points (i.e. points with low confidence index) have been removed from the micrograph and from further analysis. It is apparent from Figure 6-11 that crystallographic slip during bending deformation has led to a significant evolution of texture components. For instance, many of the

cube or near cube grains (encircled in black) experienced a significant texture rotation which is apparent from the partial change in the color of these grains from initially red to near orange color. Furthermore, the previously observed coarse slip bands (in Figure 6-8 and Figure 6-9) are also apparent in the IPF map (i.e. see black arrows in Figure 6-11) as banded regions of different colors within the parent grains. It is observed that the specific orientation of these slip bands within grains is linked with the local crystallographic texture of the grain. This is apparent from Figure 6-12, which shows the presence of two different orientations of slip bands within grains. The grains with cube or near cube orientations (pointed with white arrows in Figure 6-12) show slip bands that are oriented approx. 45° to the extrusion direction, whereas, grains with near {111}(*uvw*) orientations (pointed with red arrows in Figure 6-12) show slip bands oriented at approx. 150° to the extrusion direction. Furthermore, the frequency of slip band formation in grains with cube or near cube orientations (see Figure 6-11) is much higher than grains having other orientations. For instance, grains having Goss orientation do not show the presence of these slip bands within grain interiors (see green colored grains in Figure 6-11). In other words, grains with cube or near cube orientations are deforming easily and are able to accommodate comparatively large strains. This behavior is consistent with results reported in the literature, where it has been suggested that the presence of cube recrystallization texture improves formability and a pronounced Goss orientation in the recrystallization texture leads to poor formability [234, 260–263].

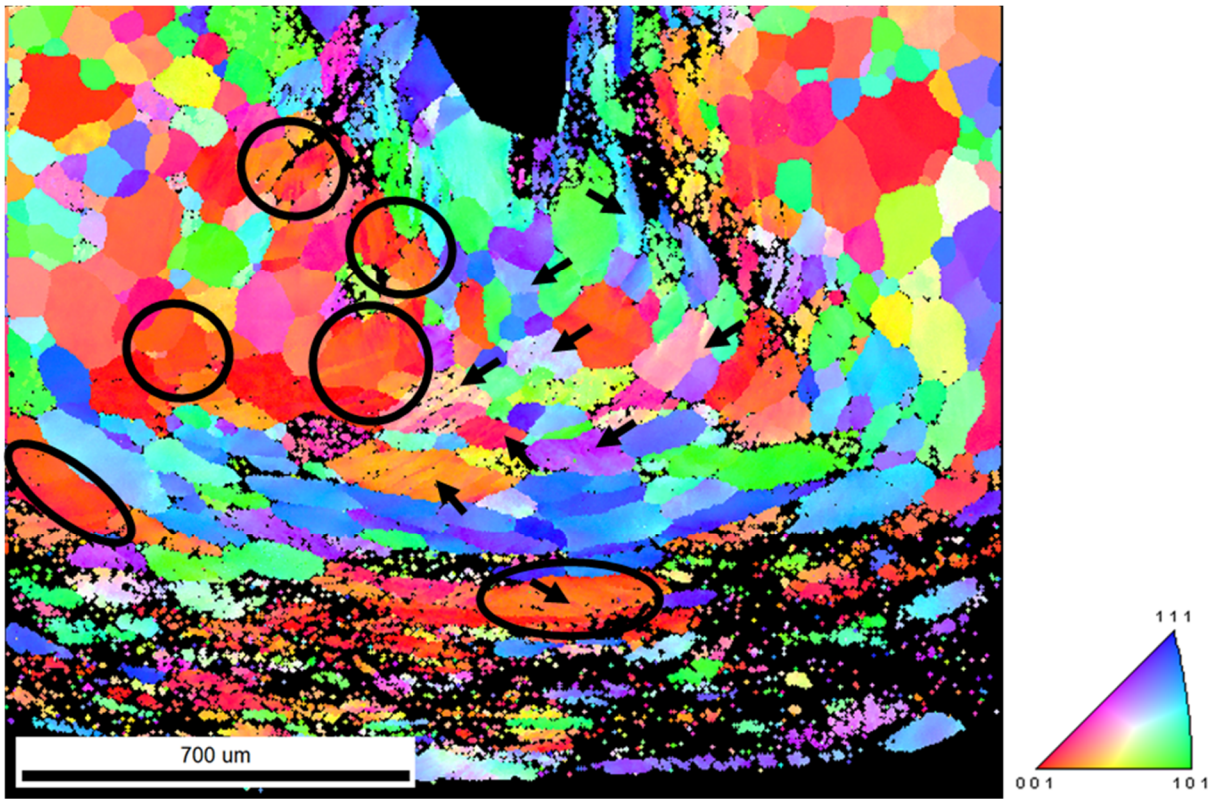

Figure 6-11: Inverse pole figure (IPF) map of through thickness microstructure of the wrap bend sample using a mandrel radius of 0.2 mm.

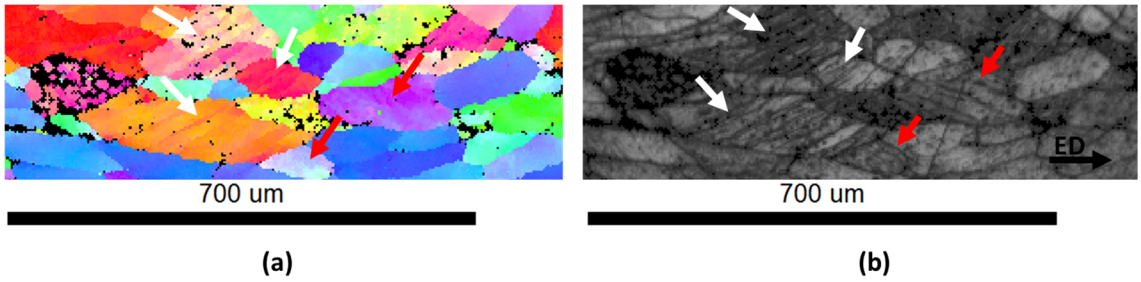

Figure 6-12: Orientation of slip bands within grains after bending (a) Inverse pole figure (IPF) map and (b) corresponding gray scale map showing localization within grains.

Figure 6-13 shows a comparison of grain boundary misorientations between the initial and the final microstructure after bending deformation. It can be observed that bending deformation has led to the formation of several subgrain boundaries within the microstructure. This is apparent from the very high fraction of low angle misorientation boundaries (i.e. boundaries with misorientation angles between 2°-5°) present in the bent specimen. The fraction of these low angle misorientation boundaries has increased from 4.3 % in the as-received microstructure (see Figure 6-13(a)) to 52.6 % in the deformed microstructure (see Figure 6-13(b)). Furthermore, the micro slip bands appearing inside several grains (see red arrows in Figure 6-13(b)) have a misorientation of 5°-10° with the parent grain. It has been shown that within these slip bands, many dislocations form chaotic networks with three dimensional tangling of dislocations [8, 158, 201, 205, 264] . It has been further suggested that these dislocations could move and interact with each other to form a deformation induced cellular dislocation microstructure comprising of cell walls with high dislocation content and cell interiors with a relatively low dislocation content [6, 7, 12, 203, 204, 264]. The presence of such dislocation microstructure may give rise to intragranular backstresses within the material [6–8, 157, 158, 196], which can further affect the deformation and fracture behavior of the material.

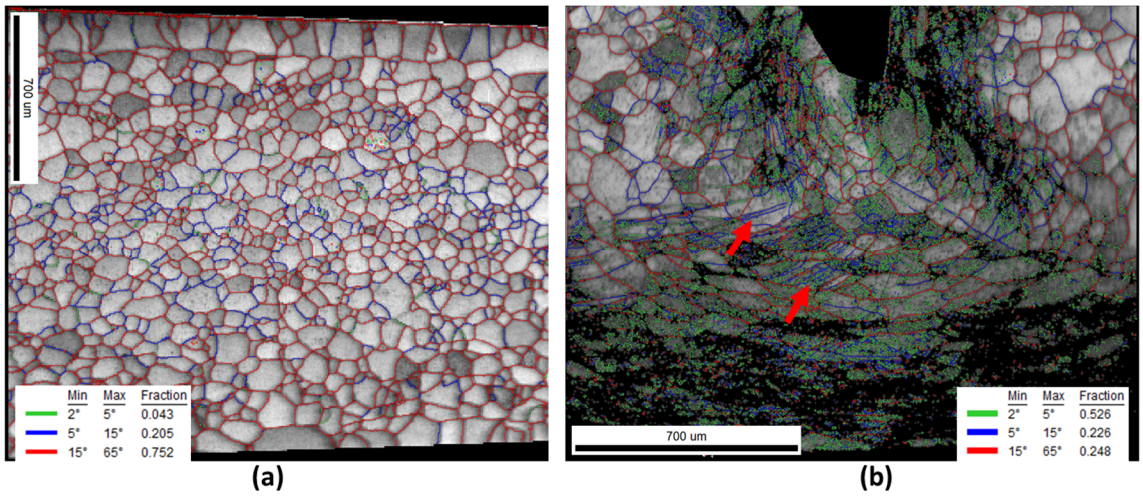

Figure 6-13: Gray scale grain maps showing grain misorientations for (a) as-received AA6063-T6 material and (b) after wrap bending deformation.

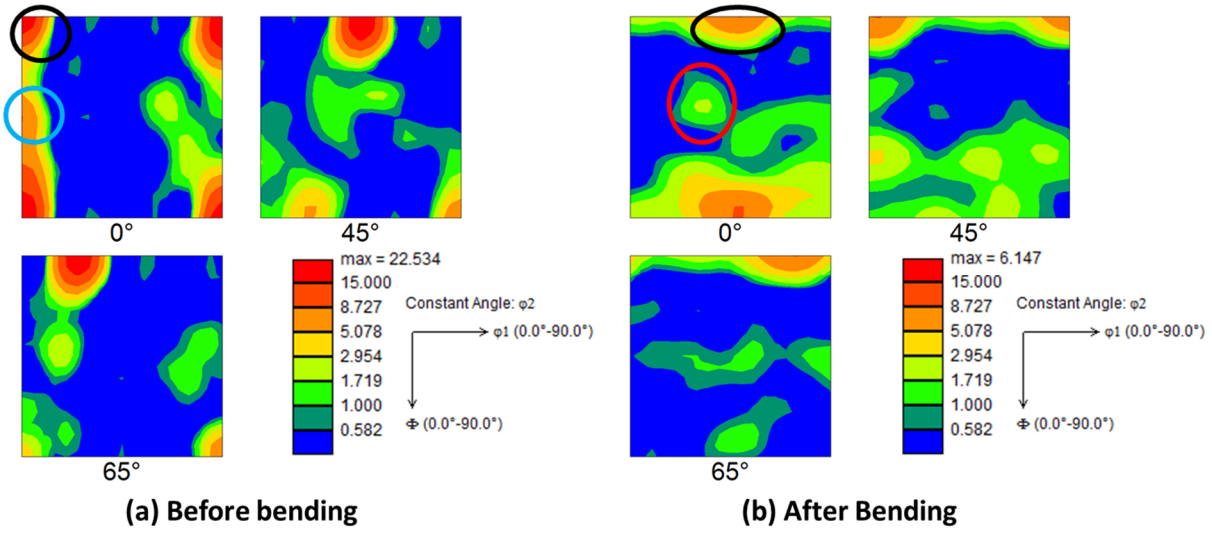

Figure 6-14: Orientation distribution function showing $\varphi_2 = 0°$, $\varphi_2 = 45°$ and $\varphi_2 = 65°$ for experimentally measured texture corresponding to (a) initial as-received material before bending and (b) after wrap bending. Both ODF are plotted using the same reference system.

Figure 6-14 presents the orientation distribution function showing $\varphi_2 = 0°$, $\varphi_2 = 45°$ and $\varphi_2 = 65°$ for the experimentally measured texture corresponding to the as-received material before bending (Figure 6-14(a)) and after bending deformation (Figure 6-14(b)). For visual comparison, the same texture intensity scale is set for both figures. It is noted that bending deformation has led to significant weakening of the overall texture. This is apparent from the maximum texture intensity which has decreased to a value of 6.147 times random after bending from an initial value of 22.534 times random. This weakening of the overall texture after bending is linked with rotation of several texture components. For instance, the bending deformation has led to the shifting or rotation of Cube peaks along the φ_1 axis by approximately 45°. Furthermore, the Goss component peaks (encircled in blue in Figure 6-14(a)) have disappeared after bending. In addition, one can also see the presence of a weak Brass texture (encircled in red in Figure 6-14(a)) after the wrap bending deformation.

Apart from the well-established role of texture in defining the plastic anisotropy and forming behavior of sheet metals [176, 261, 263, 265–269], it is suggested that texture or more precisely, the local distribution of grain orientations has been identified to play a major role in the formation of surface roughness and roping [219, 220, 232–234, 245, 249, 256]. One of the objectives of the present work is to investigate the relationships between heterogeneous plastic deformation, microtexture and the development of surface topography effects during wrap bending of AA6063-T6. In this regards, the crystal plasticity based finite element approach offers the opportunity to analyze these underlying correlations using numerical modeling. In the next section of this manuscript, a multiscale modeling approach (coupling phenomenological plasticity based finite elements with crystal plasticity based finite elements) is proposed to simulate the wrap bending process with emphasis on studying texture evolution, strain localization and the development of surface roughness during bending.

6.3 Multi-scale Modeling

6.3.1 Modeling approach

Several efforts have been made-to-date to study the bending behavior of sheet metals using finite element (FE) modeling. However, most of the bending studies in the literature have adopted a 2D plane strain model [219, 228, 246, 247, 250], where the deformation is analyzed in the plane normal to the bend axis. Furthermore, these approaches make use of pure bending boundary conditions, assuming that the material throughout experiences the same bending deformation. However, in practical bending operations, the pure-bending condition is rarely achieved [248]. Actual bending operations involve contacts between machine tools and material and the deformation is rather inhomogeneous in different sections of the bend [248].

In the present work, a multi-scale modeling approach is used to model the bending behavior of AA6063-T6 during wrap bend test. Firstly, a full - specimen sized, macro level 3D wrap bend simulation is performed using conventional phenomenological plasticity within the finite element (FE) framework. Next, a microstructure based 3D micro-model is developed for the region of interest and the simulation is performed using crystal plasticity based finite element methods (CPFEM). The displacement history of the region of interest is taken from the macro-model and is applied as boundary conditions to the micro-model. All simulations are performed within a commercial finite element package LS-Dyna®. Before discussing the finite element based macro and micro-models, a brief overview of the crystal plasticity framework, employed in the current study, has been provided in the next section.

6.3.2 Constitutive Framework

The polycrystal plasticity framework proposed by Asaro and Needleman [193] has been used in the current work. The details of the framework can be found in Wu et al. [209], Inal et al. [270] and Rossiter et al. [199]. However, for completeness, some of the major ideas are summarized below:

The total deformation of a crystallite is taken to be a function of two different physical mechanisms: crystallographic slip due to dislocation motion on the active slip systems and elastic lattice distortion. The deformation gradient F is written as

$$\mathbf{F} = \mathbf{F}^{*}\mathbf{F}^{\mathbf{p}} \tag{6-2}$$

Where $\mathbf{F}^{*}$denotes elastic stretching and rigid body rotation of the crystal lattice and $\mathbf{F}^{\mathbf{p}}$ represents the deformation solely due to plastic shearing on crystallographic slip systems. The rate sensitive constitutive behavior of each crystal is determined by the following relationship

$$\overset{\nabla}{\boldsymbol{\sigma}} = \boldsymbol{\mathcal{L}}:\boldsymbol{D} - \dot{\sigma}^{0} - \boldsymbol{\sigma}\, tr\boldsymbol{D} \tag{6-3}$$

where $\overset{\nabla}{\boldsymbol{\sigma}}$ represents the Jaumann rate of Cauchy stress, $\boldsymbol{\mathcal{L}}$ is the elastic moduli tensor, $\boldsymbol{D}$ is the strain rate tensor, $\dot{\sigma}^0$ represents a visco-plastic type stress rate which depends on the slip rates of the slip systems. The slip rates are governed by the following power-law relationship

$$\dot{\gamma}_{(\alpha)} = \dot{\gamma}_0 \, sign \, \tau_{(\alpha)} \left| \frac{\tau_{(\alpha)}}{g_{(\alpha)}} \right|^{\frac{1}{m}} \tag{6-4}$$

where $\dot{\gamma}_0$ is a reference shear rate taken to be the same for all the slip systems, $\tau_{(\alpha)}$ is the resolved shear stress on the slip system α, $g_{(\alpha)}$ is the slip system hardening and m is the strain rate sensitivity index. Muhammad et al. [264] recently proposed a slip level crystal plasticity based hardening model to account for the intragranular backstresses which arise from the formation of dislocation cell substructure in the microstructure. The proposed model accounts for hardening due to interactions with forest dislocations as well as with dislocation cells. The proposed slip system hardening relationship $g_{(\alpha)}$ is given below

$$g_{(\alpha)} = \left[(2 + \beta)(\alpha' \mu b)^2 \frac{1}{4b} \gamma \right]^{\frac{1}{(2+\beta)}} C_{(P/A)} \qquad where \tag{6-5}$$

$$\alpha' = \alpha_0 + \frac{3Ct}{b}(1 - \chi_E)\gamma \, , \tag{6-6}$$

$$C_{(P/A)} = C_f \left(\frac{P}{A} \frac{1}{C_1} \right)^{\frac{1}{(2+\beta)}} \tag{6-7}$$

In Eq. (6-5), Eq. (6-6) and Eq. (6-7), μ is the shear modulus and b is the burgers vector. The terms P, A, C_1, C_f, β, α_0, C, and t are microstructure-material dependent parameters and are obtained from stress strain curve and microstructure using the procedures outlined in Muhammad et al. [264]. The significance of these parameters is further discussed in Section 6.3.3.2.

6.3.3 Problem formulation

6.3.3.1 Macro-level model

The macro-scale full 3D model of the wrap bend test is shown in Figure 6-15, where the x-axis is parallel to the extrusion direction (ED), the y-axis is parallel to the through-thickness normal direction (ND) and the z-axis is parallel to the transverse direction (TD). In addition, the bend-axis is parallel to the z-axis. The full scale model consists of AA6063-T6 sheet specimen, the binders to clamp the sheet in position, the mandrel as well as the roller. Consistent with the experimental wrap bend specimen, the finite element sheet specimen has a length, width and thickness of 76 mm x 30 mm x 1.8 mm, respectively. The specimen is meshed using 3D 8-noded brick elements with an element size of 0.2 mm. The mandrel, roller and binders are modeled as rigid bodies and

are meshed using four-node quadrilateral shell elements with Belytschko-Tsay formulation. Consistent with experiments, the radius of the roller and the mandrel are 1 mm and 0.2 mm, respectively. The left edge of the sheet (i.e. x = 0 plane) is kept fixed in the x-direction throughout the simulation. At the beginning of the simulation, the binders are clamped down on to the sheet with a rather nominal load of 1 KN to lock the sheet into position. With both roller and mandrel in contact with the sheet, the bending deformation is applied by rotating the roller around the center of the mandrel. Three surface to surface contacts are defined between the sheet specimen and the three tools (i.e. binders, roller and the mandrel). The coefficients of static and dynamic friction are set to 0.08 for all contacts. This relatively lower frictional coefficient is used in an effort to model the lubrication effects during bending operation. The macro-level wrap bend simulation is performed using an elasto-plastic constitutive model (i.e. MAT_24) included within the commercial FE software LS-Dyna®. Figure 6-16 shows the bent specimen after wrap bend simulation. The displacement histories of the edges (i.e. faces) of the region of interest (see Figure 6-16) are extracted from the macro-model and are applied as boundary conditions to the CPFEM based micro model. The region of interest shown in Figure 6-16 is 1.8 mm x 1.8mm x 1.8 mm in size in the initial un-deformed state.

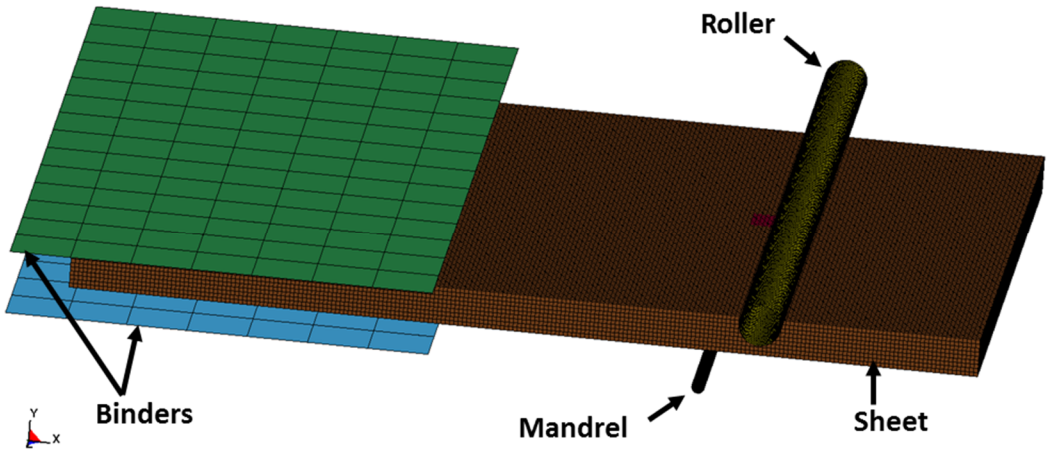

Figure 6-15: Full scale macro-model for finite element simulation of the wrap bend test.

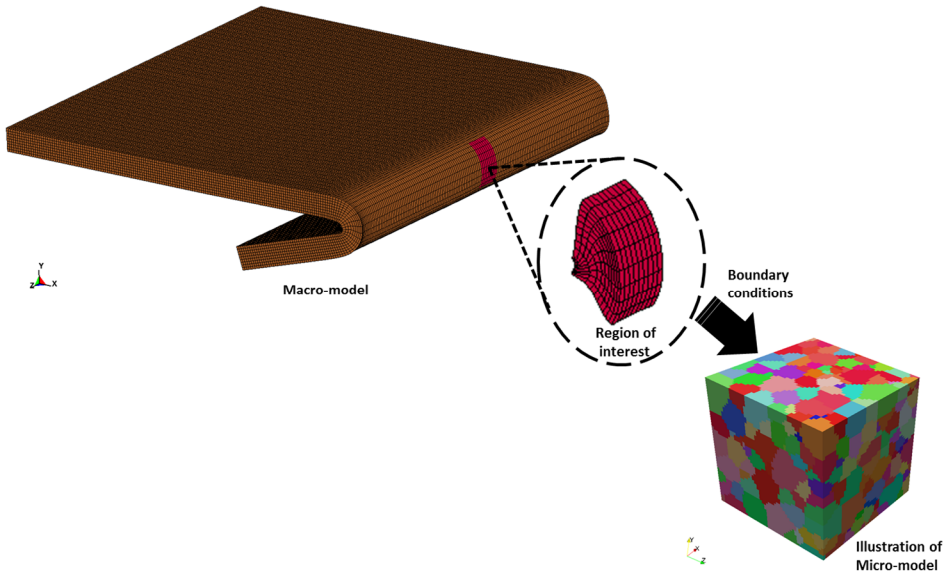

Figure 6-16: Representation of the multi-scale modeling approach employed in the present study.

6.3.3.2 Micro-level model

The micro scale CPFEM model (see Figure 6-17(a)) has the same overall dimensions as that of the highlighted region of interest in Figure 6-16 (i.e. 1800 µm x 1800 µm x 1800 µm). The 3D volume element represents the complete through thickness of the wrap bend specimen. The volume element is meshed using 3D 8-noded brick elements with an element size of 36 µm. A total of 50 x 50 x 50 elements are used to mesh the micro model. Only the x = 0 µm, x = 1800 µm, z = 0 µm, z = 1800 µm and y = 0 µm planes (i.e. faces) are driven by the corresponding displacement histories of the edges determined from the macro model. The y = 1800 µm plane (i.e. face) in Figure 6-17(a) represents the top surface of the wrap bend specimen. It is to be noted that the displacement history from the macro model is not applied to this top surface of the volume element. This enables the development of surface roughness and strain localization arising from the underlying microstructure.

The experimental microstructure in Figure 6-4 has been incorporated into the 3D volume element shown in Figure 6-17(a). For this purpose, a 3D statistically equivalent microstructure (incorporating grain morphology, crystallographic orientation and misorientation distribution) is generated from the experimental EBSD maps using M-builder [55]. The procedure makes use of the experimental EBSD scans (see Figure 6-4) to obtain grain size, grain aspect ratio, orientation distribution, and misorientation distribution data. The 3D volume element is filled with ellipsoids of varying sizes using the experimentally measured grain morphology. A Cellular Automata (CA) procedure is then used to generate a volume filled 3D grain microstructure. The grains are assigned orientations, and the orientation distribution and misorientation distribution are calculated. A simulated annealing approach is then used to adjust the assigned grain orientations until the calculated orientation and misorientation distributions within the generated microstructure match the experimental values obtained through EBSD scans. The details of the method can be found in

Brahme et al. [55] and Brahme et al. [271]. Figure 6-17(b) shows the generated statistically equivalent volume element where the grain colors reflect their true crystallographic orientation. It is noted that the generated microstructure shows excellent conformity to the experimental data as evident by the <111> pole figures presented in Figure 6-18. Furthermore, in line with the experimental observations (made from Figure 6-3 and Figure 6-4), the generated micro-model volume element in Figure 6-17(b) also captures the through thickness gradient in the microstructure. This is apparent in Figure 6-17(b), where the grain size closer to the top and bottom faces (i.e y = 1800 µm and y = 0 µm) is larger than that of gains in the center of the generated microstructure. To the best of author's knowledge, this is the first time that a gradient microstructure, which captures both the experimentally observed morphology and the corresponding texture, has been used in a CPFEM simulation. Details on how the gradient in the generated microstructure was introduced and how the corresponding experimentally observed crystallographic orientations were assigned, are subject of a separate publication (Brahme et al. [271]).

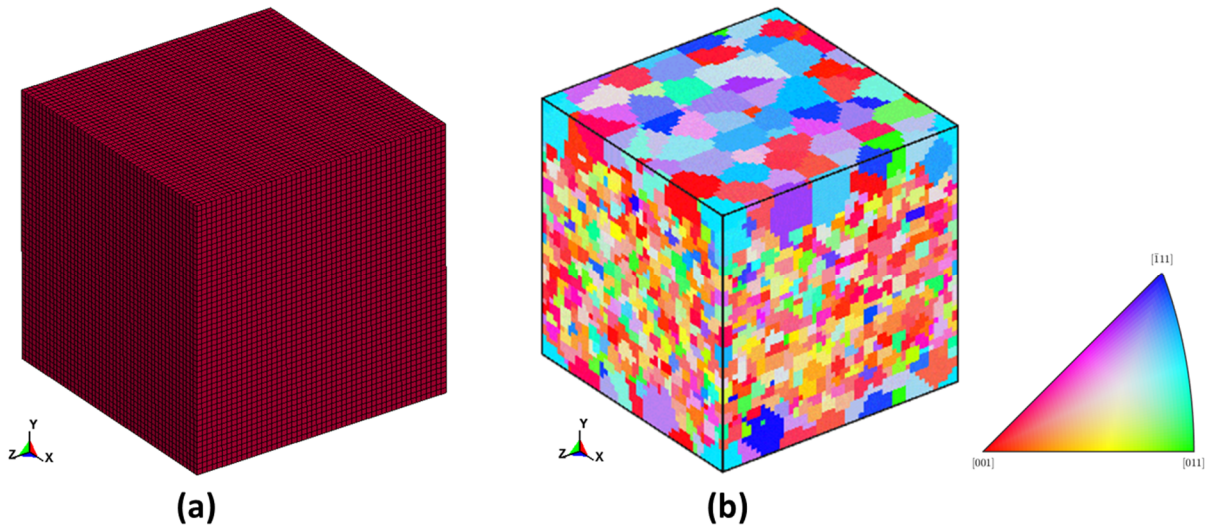

Figure 6-17: Micro scale model (a) meshed volume element and (b) generated representative volume element with microstructural input.

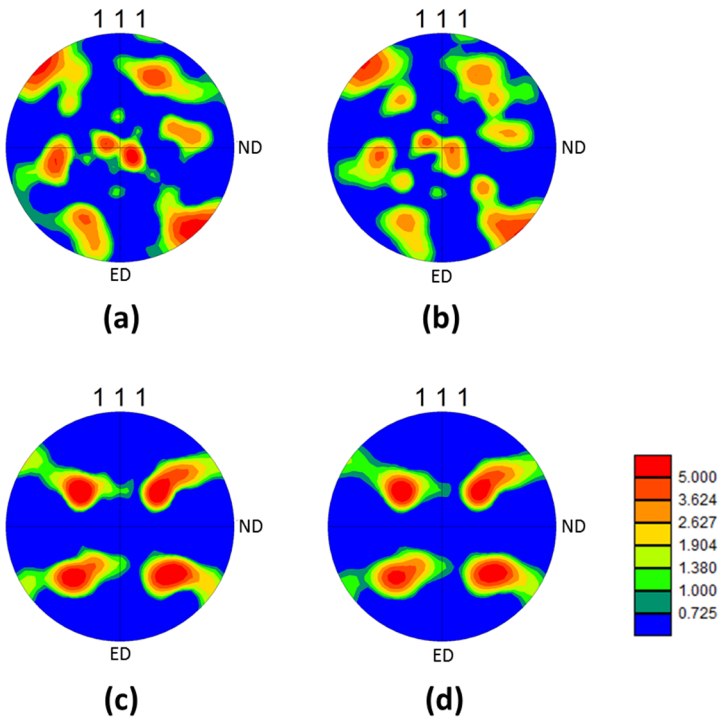

Figure 6-18: Comparison of experimental and generated microstructure. Images (a) and (c) show experimental <111> pole figures corresponding to top and center locations, respectively (see Figure 6-4 for reference). Images (b) and (d) show the corresponding <111> pole figures for the generated statistically equivalent microstructure shown in Figure 6-17(b).

As mentioned previously, the commercial finite element package LS-Dyna® is employed in this study. The rate-dependent crystal plasticity constitutive framework presented in Section 6.3.2 is incorporated as a user defined material subroutine (UMAT) in LS-DYNA/Explicit. The details of the formulation can be found in Rossiter et al. [199]. Before performing the wrap bend simulation using CPFEM, the crystal plasticity hardening model parameters are calibrated using the experimental flow stress data for uniaxial tension, given in Figure 6-6. For this purpose, a uniaxial tension simulation is performed using the representative volume element in LS-Dyna® and the hardening model parameters are tuned to achieve an excellent match to the experimental stress-strain data as shown in Figure 6-19. The calibrated hardening model parameters are given in Table 6-2. A detailed calibration procedure to obtain model parameters from the experimental stress-strain curve is outlined elsewhere [148, 264].

Table 6-2: Material parameters used in simulations.

$\sigma_0\ (MPa)$	P/A	β^{II}	β^{III}	$C_1^{II}(\mu m)$	$C_1^{III}(nm)$	C_f	C	$t\ (nm)$
85.5	0.075	0	0.24	0.162	5.148	2.8	0.15	7.0

In Table 6-2, the superscripts *II* and *III* refer to material parameters corresponding to Stage *II* and Stage *III* hardening respectively. The parameter σ_0 is a yield parameter, the microstructural parameter P/A is related to the creation and dynamic annihilation of dislocations, the terms C_1 and

β relates the mean slip distance to the shear stress τ and the term C_f is a material parameter which assures the continuity of the flow curve during transition from Stage *II* to Stage *III* hardening and the terms C and t are the backstress hardening parameters. The reader is referred to Muhammad et al. [264] for detailed information on the hardening model.

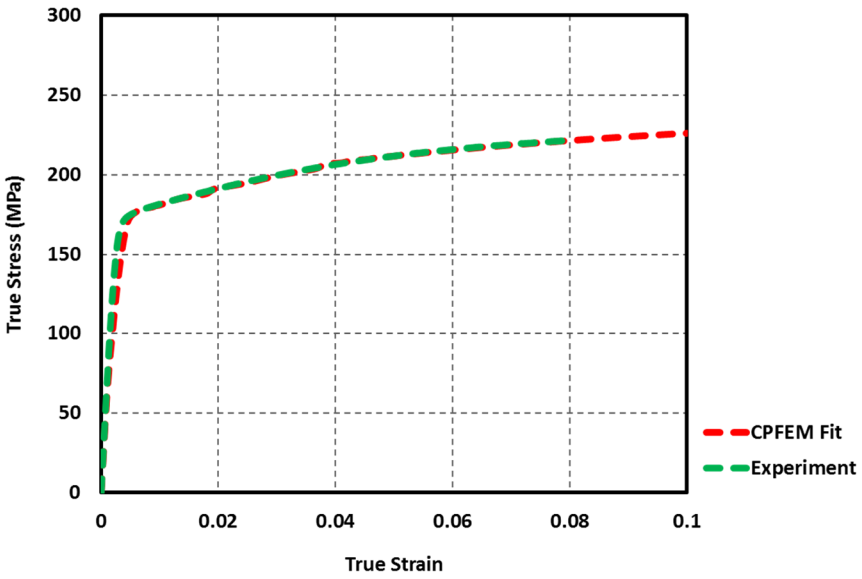

Figure 6-19: CPFEM hardening model calibrated to the experimental uniaxial tension data for AA6063-T6.

6.3.4 Results and discussion

6.3.4.1 Texture evolution during wrap bending deformation

Figure 6-20 presents the orientation distribution function showing $\varphi_2 = 0^o$, $\varphi_2 = 45^o$, $\varphi_2 = 65^o$ for the experimentally measured (Figure 6-20(b)) and the numerically predicted texture (Figure 6-20(c)) after wrap bending deformation. The experimental results are reproduced in Figure 6-20(a) and (b) for an easier visual comparison. It can be observed that the predicted texture evolution after bending shows good conformity to the corresponding experimentally measured texture evolution. It is noted that the numerical model is able to predict the overall trends and evolution of the ODF as shown by the highlighted regions in Figure 6-20(b) and Figure 6-20(c). For example, it can be observed from $\varphi_2 = 0^o$ ODF in Figure 6-20(b) that bending deformation leads to weakening and shifting of the Cube peak along the φ_1 axis signifying rotation of the cube component. A similar behavior is predicted by the numerical model as shown in Figure 6-20(c). It is important to note that a certain degree of orientation change in the texture components is associated with the rigid body rotation during the wrap-bend test. The presence of several other texture peaks in the experimental ODF of $\varphi_2 = 45^o$, $\varphi_2 = 90^o$ are also well captured by the corresponding numerically predicted ODF's. It is noted that a certain degree of orientation change in the texture components is associated with the rigid body rotation during the wrap-bend test. There are some minor discrepancies between the experimental and predicted texture. For instance,

the presence of a rather weak Brass texture component which is encircled in red in Figure 6-20(b) is not well predicted by the corresponding ODF in Figure 6-20(c). However, importantly, the numerical model is able to predict the overall weakening of the texture as observed experimentally. This is apparent from the overall weakening of maximum texture intensity from 22.5 times random before bending to 6.1 times random after bending and the predicted maximum intensity of 6.5 times random after bending (see Figure 6-20). For further comparison of the predicted and experimentally measured texture after wrap bending, Figure 6-21 presents the <111> pole figures showing texture evolution within the compressive and tensile regions of the bend. The experimental <111> pole figures (Figure 6-21(a) and (c)) are plotted by partitioning the full EBSD scan data into corresponding compressive and tensile regions. It is observed that the numerically predicted texture within the compressive and tensile regions of the bend (see Figure 6-21(b) and (d)) show good match to the corresponding experimental data, with majority of the texture poles being well captured. Furthermore, the predicted maximum texture intensities also show a close correspondence to the experimentally measured values.

Figure 6-22(a) presents the inverse pole figure maps showing texture evolution after bending deformation using micro level crystal plasticity model. Only, the top y = 1800 µm and y = 1764 µm planes are shown, where the texture evolution after bending is plotted on the undeformed configuration. The IPF maps clearly show the development of intragranular misorientations, in terms of noticeable color grades inside several grains. It is observed that the grains which initially had cube or near cube orientations show a high degree of internal misorientations after bending. Same could be said for the grains with near {111}[*uvw*] orientations. This behavior is consistent with the experimental findings as shown by the experimental EBSD scan data reproduced in Figure 6-22(b). Several grains that show the above mentioned behavior, are highlighted in Figure 6-22. Based on the presented texture analysis, it can be concluded that the constitutive framework in conjunction with the multi-scale modeling approach used herein, are able to successfully capture the experimentally observed texture evolution during wrap bending.

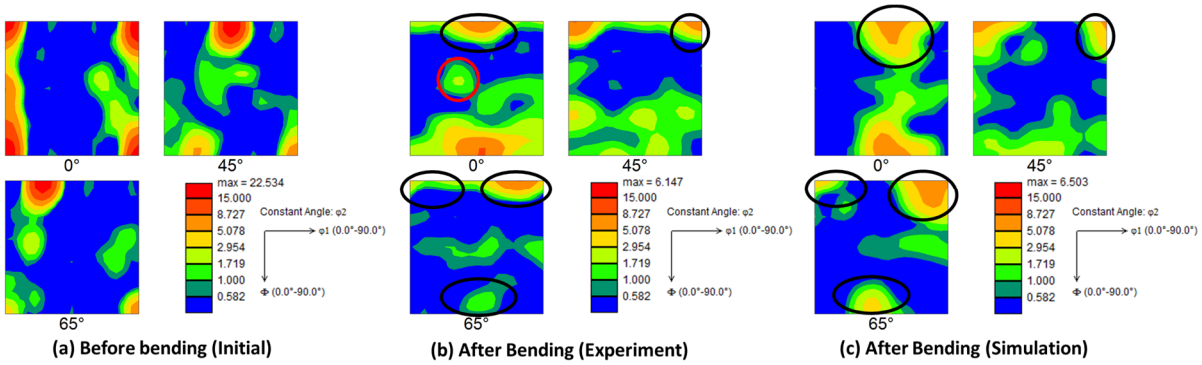

Figure 6-20: Comparison of experimental and predicted texture evolution after wrap bending deformation. Figures present orientation distribution function showing φ2 = 0°, φ2 = 45° and φ2 = 65° for texture corresponding to (a) initial as-received material before bending, (b) experimentally measured texture after wrap bending and (c) predicted texture from wrap bend simulation.

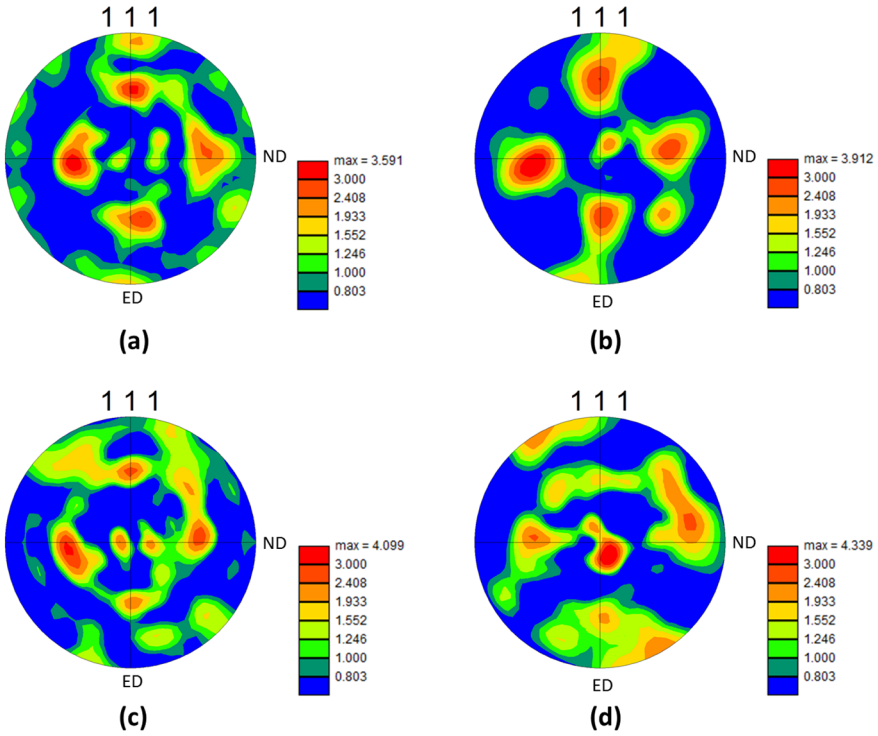

Figure 6-21: Comparison of texture evolution during bending deformation. (a) experimental and (b) predicted <111> pole figures showing texture after bending for a region which experiences compression during bending deformation. (c) experimental and (d) predicted <111> pole figures showing texture after bending for region which experiences tensile deformation during bending.

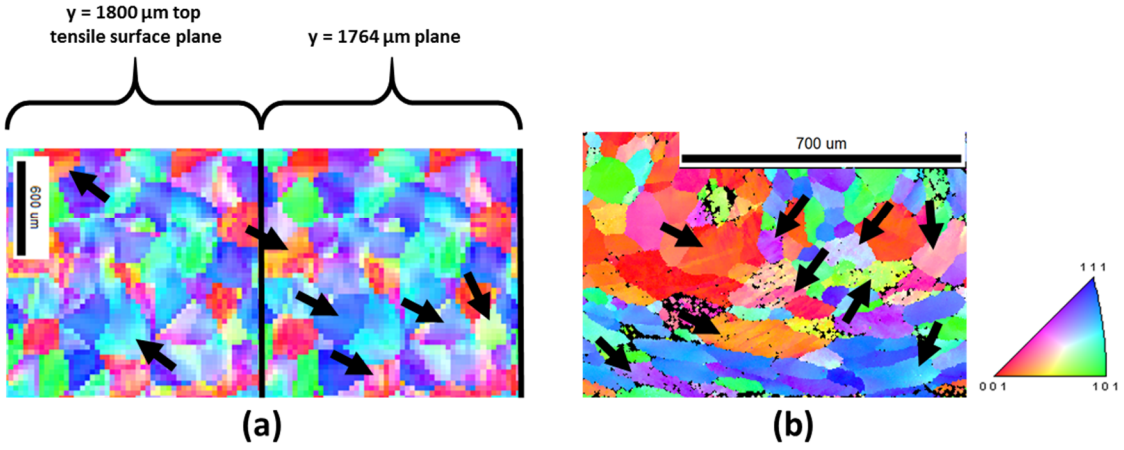

Figure 6-22: (a) Inverse pole figure map showing texture evolution after bending deformation using micro crystal plasticity model. Y = 1800 µm plane corresponds to the top tensile surface. (b) Experimental EBSD scan showing a small cropped region of the tensile portion, reproduced from the IPF map in Figure 6-11.

As the numerical texture evolution results show good conformity to the experimental data, one can analyze these results to further investigate the general trends in texture evolution associated with the wrap bending deformation. Figure 6-23 shows the inverse pole figure of the initial orientation (encircled) of selected grains before bending and the predicted trajectories of the mean orientations of these grains during wrap bending simulation. Grains with different initial orientations are selected in an effort to sample majority of the experimentally observed orientations. The orientation of each selected grain is calculated at the initial, an intermediate and the final bend angle and a dotted line-arc is drawn to demonstrate the trajectory of the grain orientation evolution. It is observed that grains with initial orientations close to the <001> corner in Figure 6-23, rotate towards the <001>-<111> line. A similar behavior is observed for grains having their starting orientations along the mid-section of <001>-<101> line. It is also noted that grains are going through different amount of rotations depending on their initial orientation and experienced strain path. Furthermore, grains that are staring along the mid-section of <101>-<111> line, move towards the <111> corner. It is well established that <001> and <111> are the two stable texture orientations in FCC materials deformed under tension [272, 273]. However, it is rather difficult to determine stable texture orientations after wrap bending deformation based on the results shown in Figure 6-23.

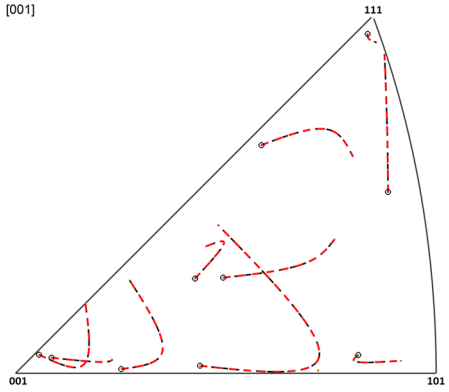

Figure 6-23: Inverse pole figure of the initial orientation of selected grains before bending (encircled) and the predicted trajectories of the mean orientations of these grains during wrap bending simulation.

6.3.4.2 Strain localization and development of surface undulations

It has been suggested that failure in bending usually initiates from local regions of intense strain localization along the outer tensile surface, where these regions of high strain concentration are typically associated with surface grooves or valleys [219–221]. This behavior is further analyzed in Figure 6-24 which shows the distribution of accumulated shear strain after wrap bending simulation. The bend-axis is parallel to the global z-direction. As expected, the strain values are comparatively higher along the outer tensile and inner compressive regions of the bend (see Figure 6-24(a)). One can also see the presence of local regions of high strains along the upper tensile surface of the bend in Figure 6-24(a). The top tensile surface of the bend reveals regions of banded microstrains which are approximately aligned parallel to the bend-axis. Figure 6-24(b), (c) and (d) show slices of the through-thickness strain evolution along three different planes (i.e. (b) z = 450

µm plane, (c) z = 900 µm plane and (d) z = 1350 µm plane). The through thickness strain distribution images show regions of high strain localization which are pointed at by black arrows. Upon careful observations of these regions in Figure 6-24(b), (c) and (d), it is noted that these regions also show the development of surface valleys (i.e. grooves) within the profile. Furthermore, regions that demonstrate the development of surface peaks (pointed by red arrows) are comparatively less localized. This is consistent with the experimental findings shown in Figure 6-7(b). Furthermore, it is apparent from Figure 6-24(d) that there are several through thickness layers right underneath the top tensile surface (pointed by magenta color arrows) which show intense strain localization. A similar behavior is observed experimentally (see Figure 6-7(b) and Figure 6-8), where strain localization within these layers of grains have led to heterogeneous plastic deformation and development of surface undulations along the outer tensile region. It can be concluded that the development of surface roughness and undulations is a cumulative effect of through thickness strain incompatibilities, as the underlying grains (below the surface) have a significant effect on the formation of surface undulations [249].

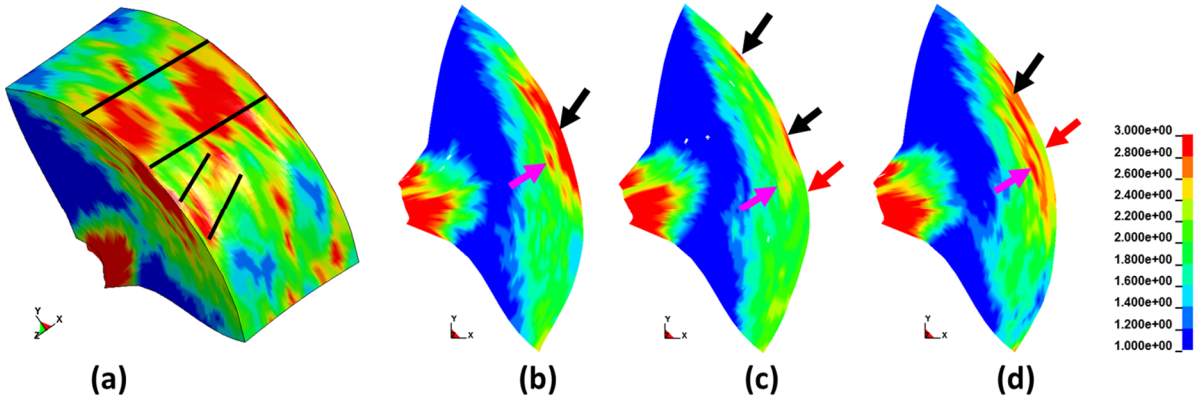

Figure 6-24: Contours of accumulated shear strain after wrap bending shown on (a) the 3D micro model, (b) z = 450 µm plane, (c) z = 900 µm plane and (d) z = 1350 µm plane.

6.3.4.3 Surface roughness and ridging

The development of surface roughness during bending is assessed using surface roughness parameter S_a. The parameter S_a represents the arithmetical mean height and describes the mean absolute deviation from the mean normal displacement [232],

$$S_a = \frac{1}{NM} \sum_{1}^{N} \sum_{1}^{M} |\Delta S| \qquad \textbf{(6-8)}$$

where N and M are the number of nodal points at the top surface, in the two in-plane axis directions (i.e. x-axis and z-axis), respectively, and $|\Delta S|$ are the absolute values of the residual displacements

perpendicular to the plane. The term ΔS represents the topographic profile of the surface. Figure 6-25 shows the evolution of surface topography at different bend angles θ during the wrap bending simulation. The scale on all figures is set fixed for comparison purposes. At the bend angle of 25° in Figure 6-25(a), it is observed that the surface roughness reveal the presence of an equiaxed pattern characteristic of orange peel. The maximum peak to valley distance is approximately 16 μm. After the bend angle of 50°, one can see the presence of a more elongated surface pattern and after 75° bend angle, the surface appearance seems to be dominated by ridging rather than orange peel. The maximum hill/peak to valley height difference is approximately 80 μm. A similar behavior of surface topography development during bending has been previously reported by Raabe et al. [232], where the authors have experimentally observed a gradual transition from an orange peel type surface pattern at low bending strains to a ridging pattern at larger bending strains. After this point, a further increase in bending angle θ leads to the further deepening and widening of the hills and valleys. This is apparent from Figure 6-25, where an increase in bend angle from 100° to 150° has led to a significant deepening of the valleys. The presence of these valleys has been observed experimentally (see Figure 6-7(b)), where strain localization has led to the development of surface grooves apparent in the through thickness optical micrograph.

Figure 6-26 shows the experimentally measured surface topography on the outer bend surface of a wrap bend specimen at bend angle of 150°. The surface topography measurements were made using Keyence® VK-X 200 series 3D laser scanning microscope. The surface topography image shows the presence of a ridging pattern on the outer tensile surface. Multiple peak/hills and valleys are apparent as they appear in an alternating pattern. A similar ridging behavior has been predicted by the numerical model at a bend angle of 150° (see Figure 6-25(f)). However, a more quantitative comparison between the numerically predicted and the experimentally measured surface topography has been made and the results are presented in Table 6-3. At the bend angle of 150°, it is noted that the experimentally measured surface roughness parameter S_a is approximately 42 μm and that predicted by the simulation is approximately 47 μm, a percentage error of approximately 10.8 %. The percentage error is even lower (approx. 4.8 %) between the experimental and predicted maximum hill to valley distance (S_z). In general, the numerically predicted results using the micro-level CPFEM model show good agreement with the experimentally measured surface topography data.

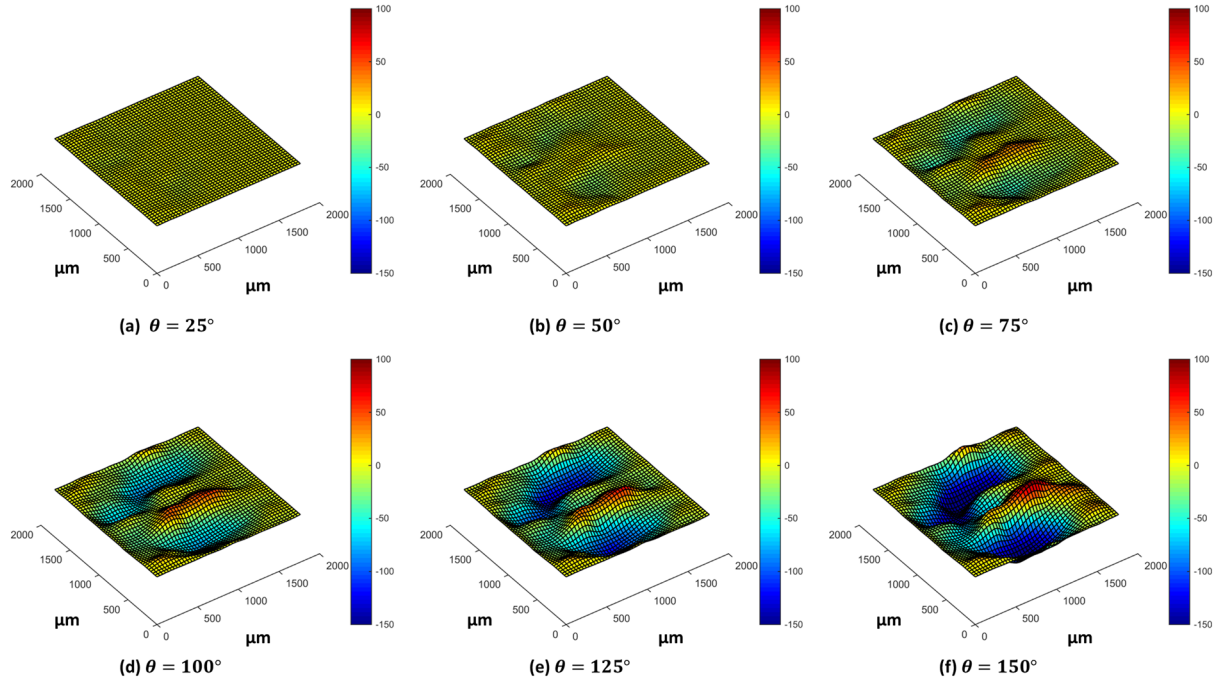

Figure 6-25: The development of surface topography (in µm) at different bend angles θ, during wrap bending simulation using the micro-level CPFEM approach.

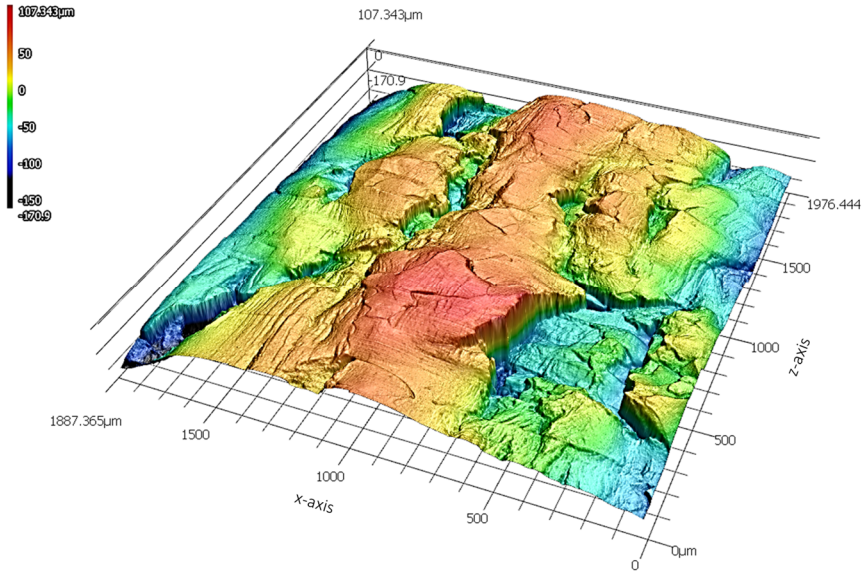

Figure 6-26: Experimentally measured surface topography (in µm) of wrap bend specimen at bend angle θ = *150°*.

Table 6-3: Experimental and numerically predicted surface roughness values.

Roughness Parameters (μm)	Experiment	Simulation	% Error
Arithmetical Mean Height (S_a)	41.91	46.98	10.8
Maximum peak height (S_p)	106.73	112.94	5.5
Maximum valley depth (S_v)	171.52	179.48	4.4
Maximum Height (S_z)	278.24	292.42	4.8

6.3.4.4 Ridging behavior and microtexture

The CPFEM based modeling approach provides a way of analyzing the interdependence of microtexture and the observed roughness - ridging behavior. In this section, the numerical results are further analyzed to shed some light on this interdependence and the causes of the observed ridging behavior. Figure 6-27 presents inverse pole figures showing the initial microtexture corresponding to regions that developed hills and valleys at the top surface after bending. The inverse pole figures are plotted using initial elemental texture data from the top surface layers corresponding to both hills and valleys. It is noted that the regions that developed surface peaks or hills had an initially predominant {111}[*uvw*] texture before bending, whereas the regions corresponding to surface valleys had an initial dominant Cube or near-Cube texture. In other words, grains with predominant {111}[*uvw*] texture experience a positive out-of-plane displacement leading to the formation of peaks or hills at the surface, whereas grains with Cube or near Cube texture experience displacement in the opposite direction (i.e. a negative out-of-plane displacement) forming surface valleys during wrap bending deformation. It is further noted that the average effective strain within valleys is approximately 15% higher than that of hills. This behavior is in line with the texture results as Cube orientations are generally regarded as softer orientations and tend to accommodate more deformation. This behavior is also consistent with experimental through thickness optical metallography results in Figure 6-8, where it is observed that the surface valleys show a comparatively higher level of local strain concentrations.

It has been suggested that the ridging phenomenon is promoted by the collective co-deformation of similarly oriented crystals assembled in bands or grain clusters [232, 240]. Furthermore, the topographic ridging behavior of the surface is directly affected by the through thickness distribution or spacing of these crystallographically similar clustered regions or grains. This through thickness clustering of similar grains is apparent from the starting 3D microstructure in Figure 6-17(b) and the experimental EBSD scan in Figure 6-4, where one can see the presence of {111}[*uvw*] oriented grain clusters (i.e. near blue color grains), Cube oriented grain clusters and some Goss oriented grain clusters. In addition, the experimental EBSD data after bending in Figure 6-11 and Figure 6-12, shows local strain concentrations in the form of shear banding within several Cube and {111}[*uvw*] oriented grains. Furthermore, the observed localization is comparatively negligible within Goss or near Goss oriented grains. This displacement mismatch between neighbouring grains leads to stress concentrations, out-of-plane displacements and strain

localization across grain boundary interfaces, as observed experimentally in Figure 6-9. Such localization phenomena has been regarded as starting points for ridging [232, 240].

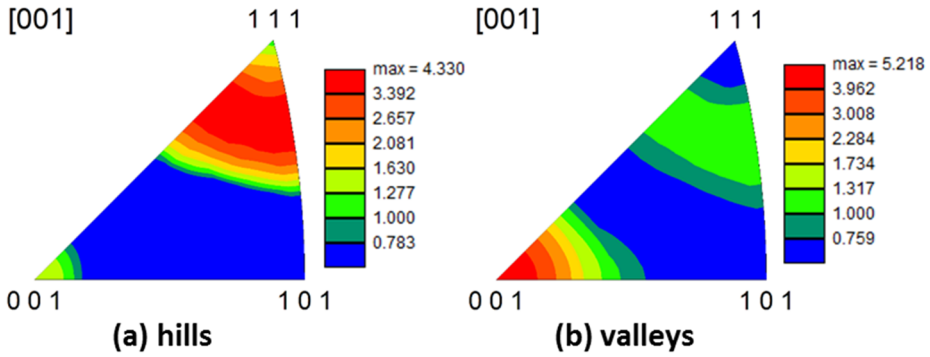

Figure 6-27: Inverse pole figure showing the initial microtexture of regions that developed (a) peak - hills and (b) valleys during wrap bending simulation.

It is well know that the orange peel phenomenon is characterized by out-of-plane displacement fields (both negative and positive) that approximately map the grain shape of the material. The grains at the surface usually undergo individual out-of-plane displacements leading to a rather equiaxed surface topology. On the other hand, the so-called ridging or roping phenomenon is associated with the collective deformation of similalry oriented grain clusters typically leading to the formation of a banded surface topology. In the next section of the manuscript, the current knowledge basis is further explored by perfroming a set of wrap bending simulaitons using different rearrangements (i.e. clustering) of the through thickness microstrucutre within the 3D volume element. The CPFEM based modeling approach offers a chance to change the through thickness distribution of grain clusters to study the effect of texture distribution and grain morphology on the development of surface topography during bending.

6.3.5 A systematic study on the development of surface roughness

6.3.5.1 Synthetic microstructure

The analysis presented above suggests that the banded surface topology is due to the collective deformation of similarly oriented clusters. This idea is explored by changing the through thickness distribution of texture and grain morphology, the two independent factors, and used to generate different 3D synthetic microstructures. Figure 6-28 shows the synthetic microstructures created for studying the effects of texture clustering and microstructure morphology on the development of surface roughness. The coloring of each grain represents its orientation in the IPF space. These microstructures are created to study the effect of different texture clustering (i.e. ‘Top-all’, and ‘Center-all’), locations of the clusters (i.e. ‘Top-center switched’) and grain morphology (i.e. ‘Equiaxed’) on the development of surface topography. Figure 6-28(a) shows the original statistically equivalent microstructure previously presented in Figure 6-17(b), reproduced here for completeness. The microstructures in Figure 6-28(b), (c) and (d) have the exact same grain morphology as that of the original microstructure shown in Figure 6-28(a). The ‘Top-all’

microstructure in Figure 6-28(b) is created using the texture of the top layers as shown in Figure 6-4(a). This microstructure has a dominant {111}[*uvw*] oriented texture as shown by its near blue color. The 'Center-all' microstructure is created using only the texture in the center of the extrusion (see Figure 6-4 (c)) and has a dominant Cube (i.e. near red color) and a comparatively weaker Goss (i.e. green color) texture. As the name suggests, the 'Top-center switched' microstructure is created by switching the texture of the top and center as shown in in Figure 6-28(d). Finally, the 'Equiaxed' microstructure in Figure 6-28(e) is a statistically equivalent microstructure, which is only representative of the experimentally measured texture and misorientation distribution. However, it is not representative of the experimentally observed clustering of grains or the bimodal distribution of grain size. It is obvious from Figure 6-28(e) that the 'Equiaxed' microstructure does not have the predominant {111}[*uvw*] oriented texture close to the top and bottom surfaces and it also does not show the clustering of Cube component in the center. However, it does correlate well with the overall experimentally measured texture as shown by the <111> pole figures in Figure 6-29. The Top-all, Center-all and Top-center switched synthetic microstructures are generated to study the effects of through-thickness texture clustering on the observed surface ridging behavior during wrap bending. The behavior of the 'Equiaxed' microstructure during wrap bending is being studied to understand whether the absence of texture clustering would promote a more orange peel type surface roughness behavior. Since the overall texture of the original microstructure and the Equiaxed microstructure is similar and is equivalent to the experimentally measured texture, any difference in the predicted surface roughness values would also shed some light on the importance of incorporating the experimentally observed grain morphology and texture distribution into CPFEM 3D volume elements.

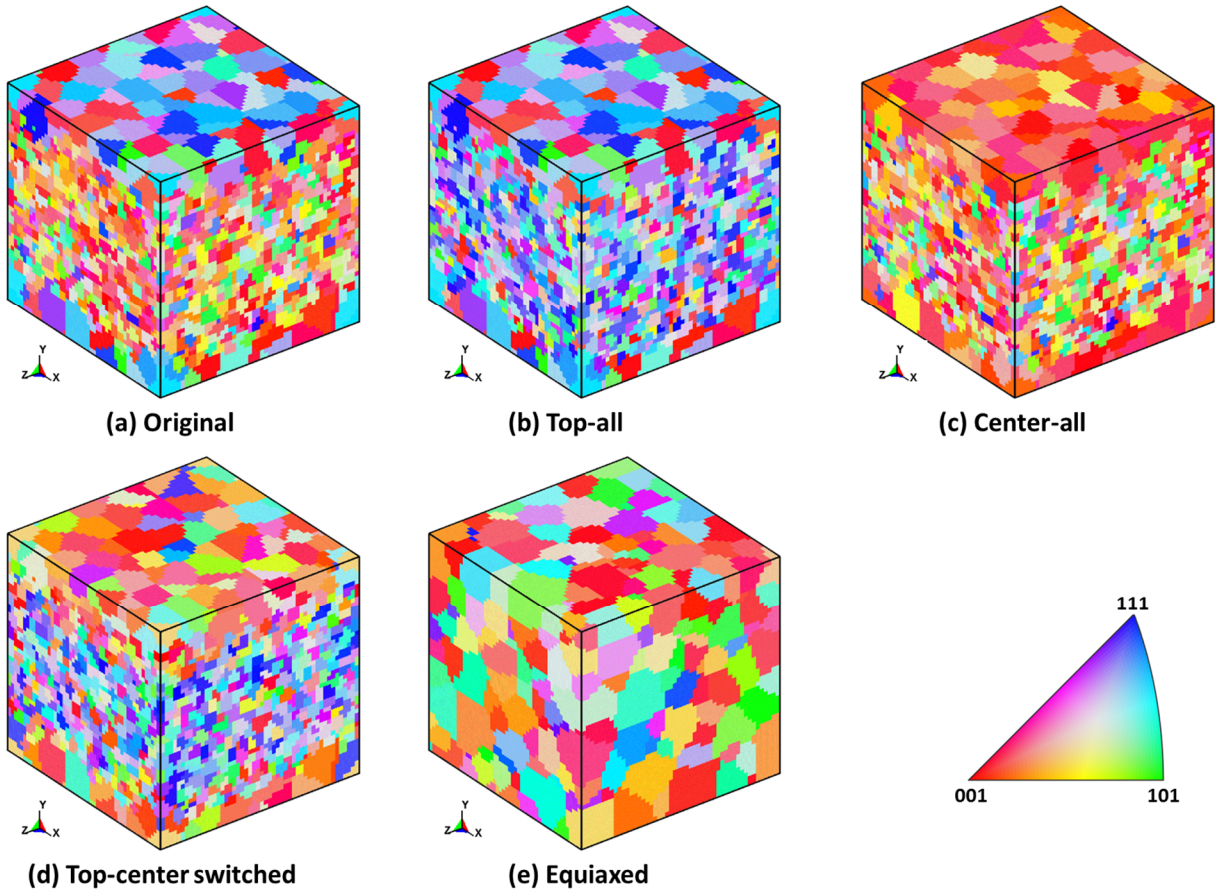

Figure 6-28: Synthetic 3D microstructures used for systematic surface roughness study.

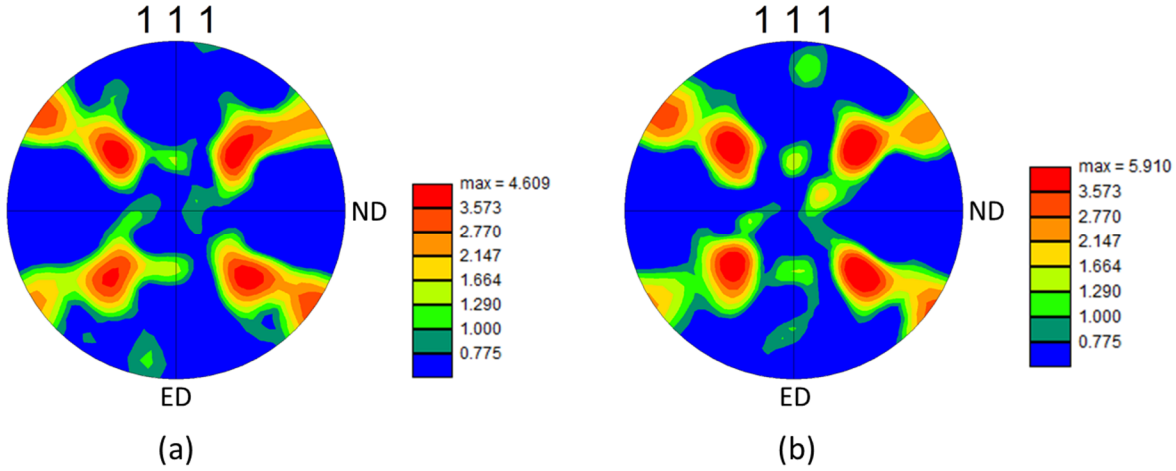

Figure 6-29: Comparison of (a) experimentally measured <111> pole figure and (b) generated <111> pole figure for equiaxed microstructure shown in Figure 6-28(e).

6.3.5.2 Analysis & Discussions

Figure 6-30 compares the numerically predicted surface topographies at bend angle $\theta = 150°$ after wrap bending simulations using the different synthetic microstructures. The surface topography result for the original microstructure has been reproduced in Figure 6-30(a) for visual comparison. It is apparent from the predicted surface topographies that the through thickness clustering or layering of the similarly oriented grains and their location within the microstructure have a significant impact on the overall surface roughness behavior during wrap bending. It is further noted that the Top-all and Top-center switched microstructures also show a surface ridging behavior, similar to that observed previously for the original microstructure (see Figure 6-30(a) vs. Figure 6-30(b) and (d)). However, the relative height intensities of hills and valleys and their corresponding locations are different for all these microstructures. All these microstructures (Original, Top-all, Center-all, Top-center switched) have the exact same grain morphology, with the only difference being the through-thickness location of the assigned cluster of texture orientations. Hence, it is apparent that the overall ridging behavior observed for these microstructures is due to through-thickness texture clustering of similar orientations, whereas the difference in the relative height intensities of hills and valleys and their corresponding locations on the surface, is linked to the exact through-thickness locations of those similarly oriented texture clusters.

Figure 6-30(b) shows the surface topography for Top-all microstructure at 150° bend angle. The presence of surface ridging is apparent from the surface. The microstructure shows comparatively higher surface peaks and relatively less deep surface valleys as compared to the original microstructure. It has been previously observed in Section 6.3.4.4 that the surface peaks are associated with {111}[*uvw*] oriented texture component, which favors a positive out-of-plane displacement during wrap bending. It is interesting to note that the Top-all microstructure has a dominant {111}[*uvw*] oriented texture throughout its entire thickness (i.e. apparent from its near blue color in Figure 6-28(b)) and as a result a relatively high volume of surface peaks are apparent in the surface topography after wrap bending (Figure 6-30(b)). On the contrary, the Center-all microstructure in Figure 6-28(c) has a dominant Cube – near Cube texture and it has been previously observed in Section 6.3.4.4, using the original microstructure, that the surface valleys are associated with Cube texture component, which favors a negative out-of-plane displacement during wrap bending. Consistent with the previous observations, the Center-all microstructure with its dominant Cube texture, shows rather deep surface valleys and very few peaks (Figure 6-30(c)). As mentioned previously, the top-center switched microstructure (Figure 6-28(d)) has been generated by switching the position of texture components. The original top {111}[*uvw*] dominant texture has been assigned to grains within the center region and the middle dominant Cube texture has been assigned to the near surface grains. It is noted that the height intensities of the hills and valleys are comparatively less pronounced for the switched microstructure. Lastly, the 'Equiaxed' microstructure presents a rather different surface roughness behavior when compared to all other microstructures. The surface topography of the Equiaxed microstructure shows the presence of

equiaxed regions of surface peaks and valleys, which are more indicative of an orange peel type of roughness behavior. This behavior will be later discussed in more details.

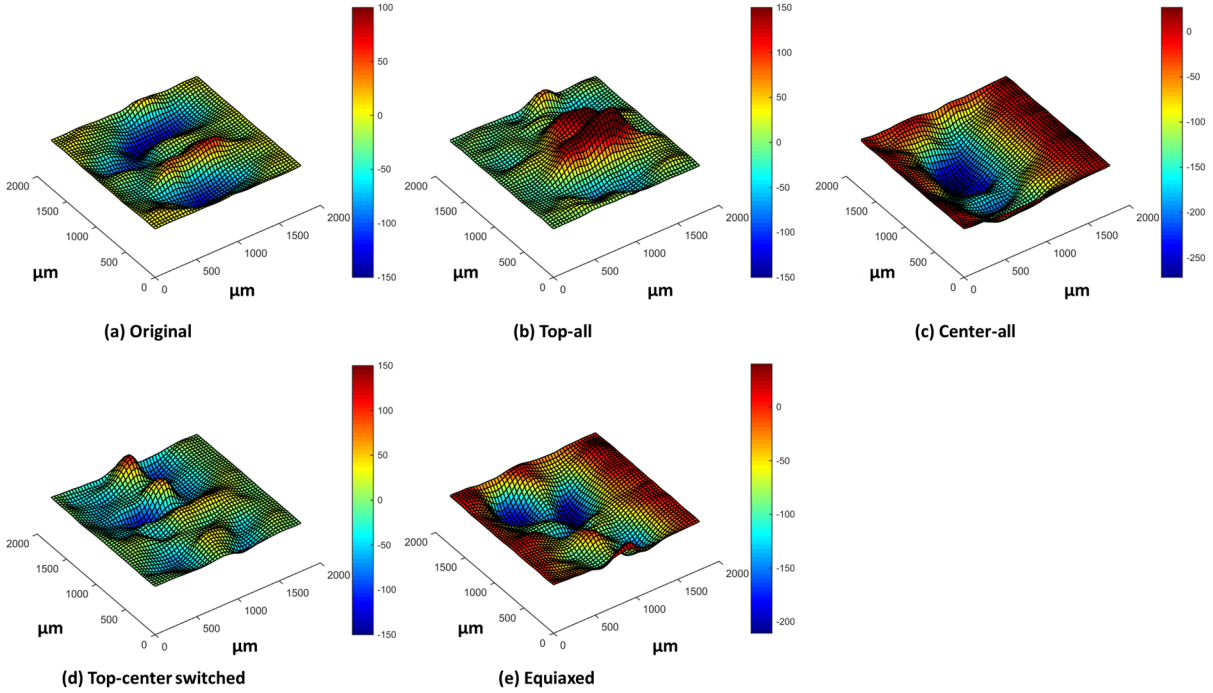

Figure 6-30: Comparison of numerically predicted surface topographies (in µm) at bend angle θ = 150° for the different synthetic microstructures.

It has been previously shown in Figure 6-27 that for the Original microstructure, the regions that developed surface peaks or hills had an initially predominant {111}[*uvw*] texture before bending, whereas the surface regions that developed valleys had an initial dominant Cube or near-Cube texture. This observation is further investigated in Figure 6-31, which shows the inverse pole figures of the initial microtexture corresponding to regions that developed into hills and valleys at the top tensile surface after bending, for all synthetic microstructures. The same plotting procedure was followed as that of Figure 6-27 and the inverse pole figures corresponding to the Original microstructure are reproduced in Figure 6-31 for completeness. It is noted that for all the studied microstructures, the regions corresponding to surface valleys show a predominant Cube or near-Cube texture. This is to say that grains with Cube or near-Cube initial orientations that are in vicinity of the top tensile surface, experience a negative out-of-plane displacement during the wrap bending deformation leading to the formation of surface valleys. It is also observed that grains with a near {111}[*uvw*] oriented texture experience a positive out of plane displacement leading to the formation of peaks or hills at the surface. In general this behavior is consistent across all the studied microstructures with the exception of 'Top-all' microstructure (Figure 6-31). This

exception is rather misleading as the 'Top-all' microstructure does not have a significant number of grains with {111}[*uvw*] orientations and its texture is dominantly Cube. However, since this particular microstructure does not have a significant number of {111}[*uvw*] oriented grains, its surface topography after wrap bending does not show the formation of surface peaks and the topography is dominated by rather deep surface valleys. Thus, a clear correlation has been found between the initial orientations of grain clusters and the developed surface topography during wrap bending.

Figure 6-32 shows the development of surface roughness for all studied microstructures expressed in terms of the surface parameter S_a (Figure 6-32(a)) and S_z (Figure 6-32(b)) as a function of the bending angle. All microstructures show a rather linear dependence between the roughness parameter S_a and the bending angle below 75°. This behavior is also true for the roughness parameter S_z and the bending angle. After bending angle of 75°, all microstructures show an increase in the slope of the S_a and S_z curves. Previously, for low bending angles, Raabe et al., [232] also observed a similar linear dependence between the roughness parameter S_a and the bending angle. The authors suggested that the change in the slope of the S_a curve does not provide reliable insight into the basic microstructural mechanism behind roughening. However, in the present work, it is observed that below 75° bend angle, the surface roughness show a gradual development towards surface ridging behavior. At the bend angle of 75°, the majority of topographical features (i.e. ridges and valleys) are already present (see Figure 6-25). However, an increase in bend angle from 75° leads to the further deepening and widening of the surface hills and valleys. This observation is also supported by the increase in the slope of the S_z parameter after 75° bend angle (see Figure 6-32(b)), highlighting the fact that the maximum peak to valley distance has started to increase more rapidly. A similar behavior was experimentally observed by Lloyd et al. [221] during cantilever bend test of AA 6111 automotive sheet material. The authors observed that the surface roughness parameter S_z showed an initial linear increase up to a bend angle of approximately 50° and thereafter the S_z parameter increased more rapidly until fracture. The authors also reported an increase in the severity of topographical features such as surface ridges and valleys with an increase in the bend angle.

It is observed that the Center-all microstructure shows a comparatively much higher surface roughness with a S_a value of approx. 80 µm at a bend angle of 150° (see Figure 6-32(a)). The microstructure for Center-all has a predominant cube texture followed by a relatively weaker Goss texture. It is observed that the Cube oriented grains clusters experience the highest degree of surface roughness during wrap bending. In comparison, the Top-all microstructure which has a predominant {111}[*uvw*] texture develops a much lower surface roughness, with a S_a value of approx. 39 µm. It is noted that the Original microstructure which has both Cube and {111}[*uvw*] texture components develops a higher surface roughness (i.e. S_a value of approx. 47 µm) in comparison to Top-all microstructure. It is suggested that the presence of the clustering of Cube oriented grains in the microstructure has led to this rather nominal increase in the roughness value.

It is rather interesting to note that the Top-center switched microstructure has produced the lowest surface roughness. This microstructure has Cube or near-Cube grains clustering in vicinity of the top (i.e. tensile) and bottom (i.e. compressive) surfaces and the near {111}[*uvw*] oriented grains are in the middle of the microstructure. Based on the previous observations, it is suggested that since Cube oriented grain clusters experience a negative out-of-plane displacement during the wrap bending deformation and the {111}[*uvw*] oriented grain clusters experience a positive out of plane displacement during wrap bending, the two displacement vectors would oppose each other. This means that the cube oriented clusters are not as free to have a negative out-of-plane displacement since we have a relatively harder {111}[*uvw*] oriented clusters in the middle and the cube clusters would have to flow around the harder {111}[*uvw*] oriented clusters, thereby nullifying some of the inherent effects (such as through thickness displacements) that lead to the development of surface roughness. Furthermore, the maximum peak to valley height surface roughness parameter S_z for this microstructure is also the lowest amongst all the studied microstructures (see Figure 6-32(b)), which further suggests that the out-of-plane displacements (positive or negative) at the top tensile surface are the lowest. Consequently, the developed surface roughness (i.e. $S_a \approx 25$ µm) is comparatively much lower. This further highlights the fact that proper tailoring of through thickness microstructure through processing can significantly minimize the development of surface roughness.

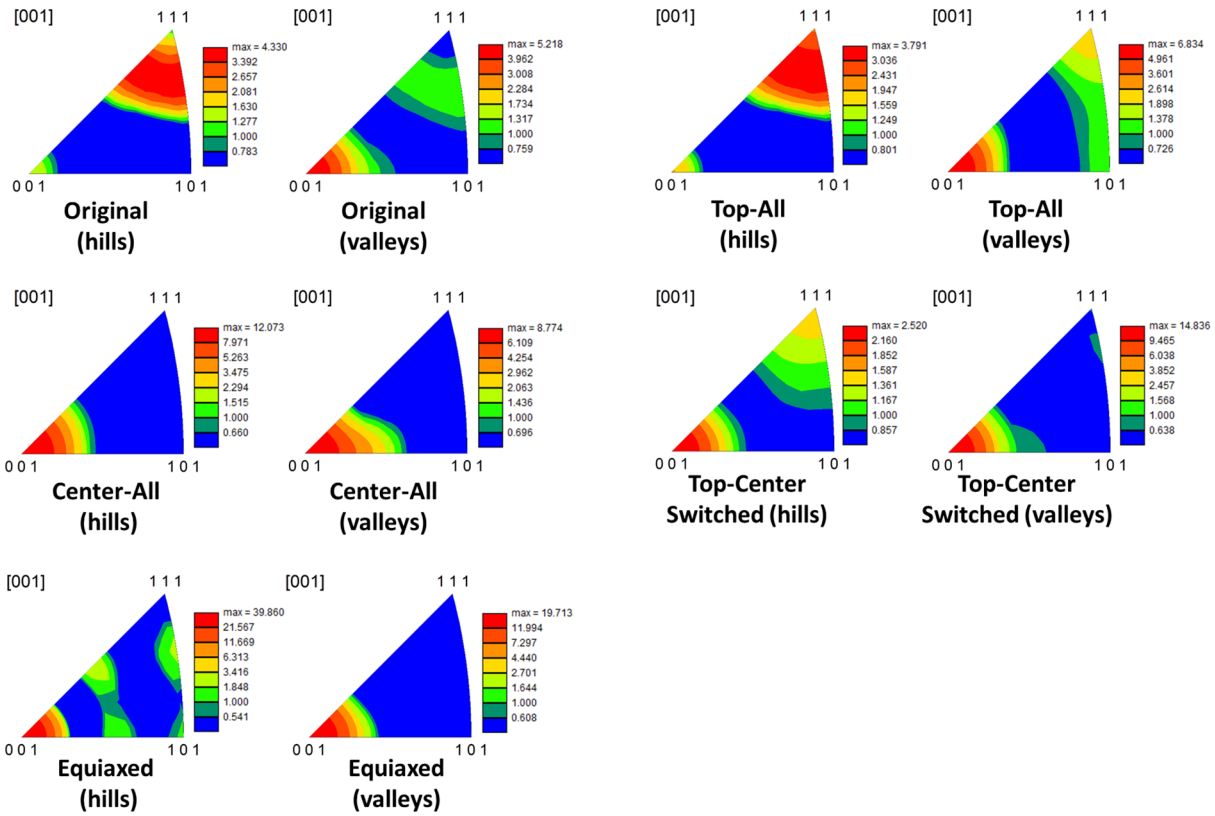

Figure 6-31: Inverse pole figure showing the initial microtexture of regions that developed peak - hills and valleys during wrap bending simulation for the different microstructures.

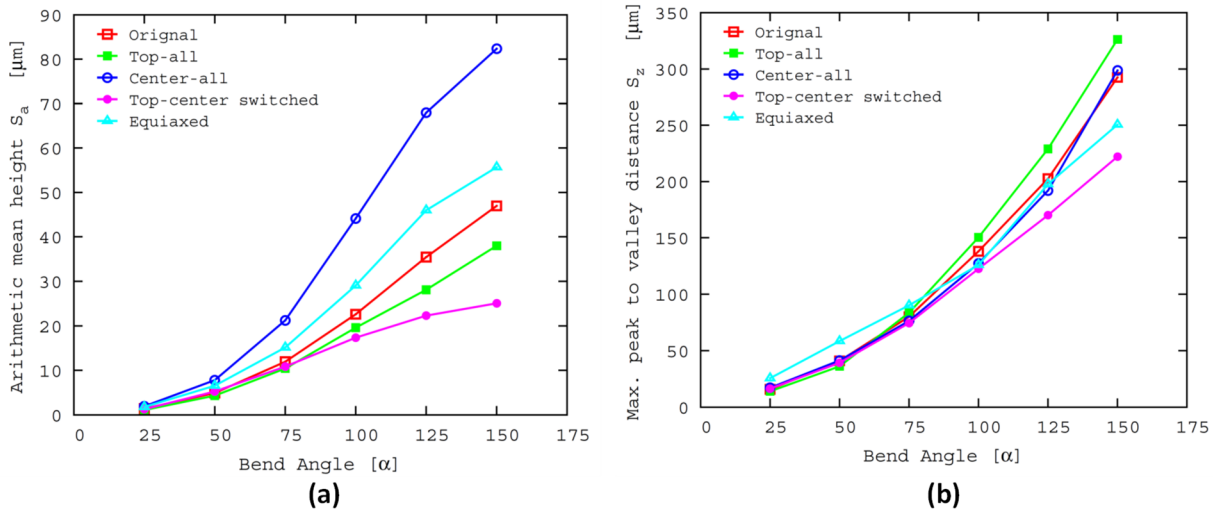

Figure 6-32: The evolution of surface roughness parameters (a) arithmetic mean height and (b) maximum peak to valley distance as a function of wrap bend angle for the different microstructures.

As mentioned previously, the surface ridging phenomenon is associated with the collective deformation of similalry oriented grain clusters typically leading to the formation of a banded surface topology. It has already been shown that indeed the through-thickness clustering of similar grains, their through-thickness location and spacing, are important factors that define the ridged surface topography. On the other hand, the orange peel phenomenon is usually associated with the out-of-plane displacements (positive or negative) of individual surface grains, leading to the formation of surface topography that rougly maps the grain shape of the material. In this regards, the development of surface topography for the Equiaxed microstructure (which has negligible clustering of similarly oriented grains) is further investigated.

Figure 6-33 shows the evolution of surface topography at different bend angles θ during the wrap bending simulation for the Equiaxed microstructure. The scale on all figures is set fixed for comparison purposes. At the bend angle of 25° in Figure 6-33(a), one can see the presence of grain scale equiaxed features which become more pronounced after bend angle of 50°. At this bend angle, the maximum peak to valley distance (S_z) is approximately 58 µm which further increases to approximately 90 µm at the bend angle of 75°. After this point, a further increase in bending angle θ leads to the rapid increase in the intensification of the surface peaks and valleys.

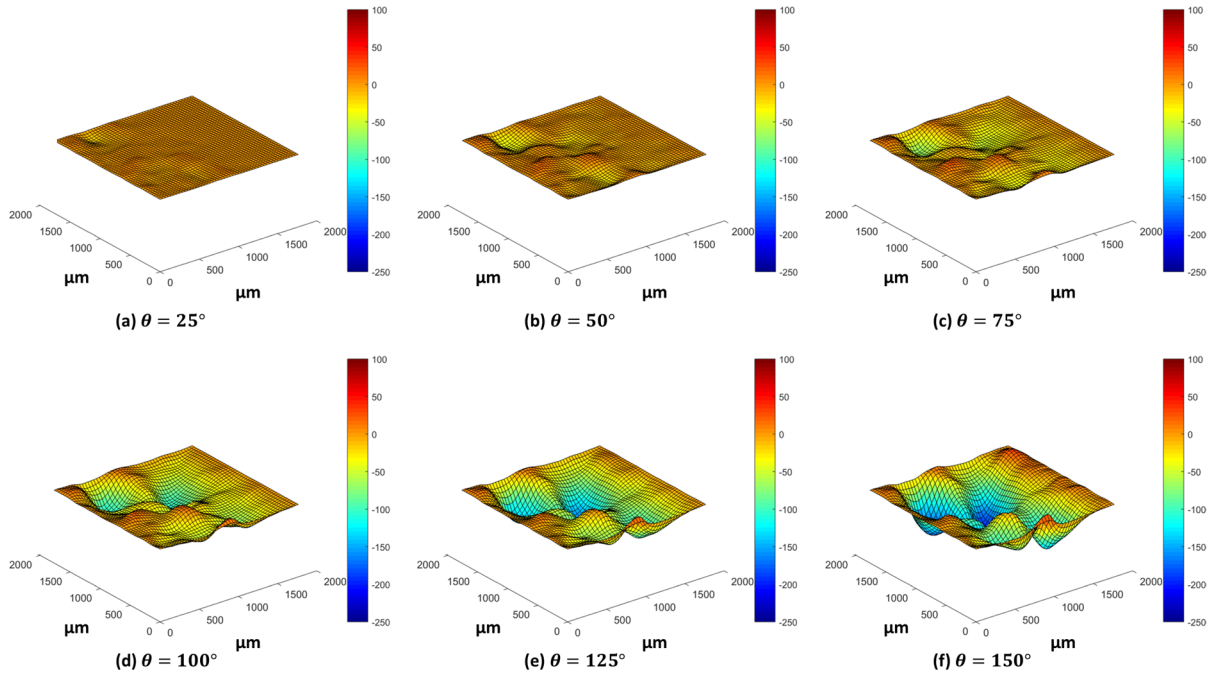

Figure 6-33: The development of surface topography (in µm) at different bend angles θ, during wrap bending simulation for the 'Equiaxed' microstructure.

It is important to note that even though the generated 'Equiaxed' microstructure is representative of the overall experimentally observed texture, the developed surface roughness (S_a) for this microstructure at 150° bend angle, is slightly higher than the Original microstructure (see Figure 6-32(a)). On the other hand, the maximum peak to valley distance (S_z) is somewhat lower which might be related to the fact that the Equiaxed microstructure shows an orange peel type surface roughness behavior whereas the Original microstructure shows a dominant surface ridging behavior. Purely from a visual quality standpoint, the surface ridging behavior might be more unpleasant/apparent to eyes and therefore undesirable. Furthermore, from a fracture standpoint, the interest might be to avoid surface topographical features that may lead to fracture initiation, and this is likely to occur in regions of stress concentration and therefore the surface roughness parameter (S_z) might be more significant. Thus, once again the surface ridging behavior which is usually associated with higher S_z values is undesirable.

Lastly, as the Equiaxed microstructure is a statistically equivalent 3D microstructure, representative of the overall experimentally measured texture, it is worth analyzing the through thickness microstructure evolution and the general texture rotation trends for this microstructure during wrap bending. Figure 6-34 shows the inverse pole figure maps of through-thickness slices along the global y direction, presenting texture evolution during wrap bending at different bend angles for the Equiaxed microstructure. The y = 0 µm slice corresponds to the bottom surface of the 3D volume element which undergoes compression and the y = 1800 µm slice corresponds to

the top tensile surface. The texture evolution is plotted on the undeformed grain morphology. It is noted that the Equiaxed microstructure also shows the development of intragranular misorientations within the near {111}[*uvw*] orientated grains (i.e. grains with near blue color) and near Cube oriented grains ((i.e. grains with near red color). These intragranular misorientations are apparent in the IPF maps in terms of noticeable color grades inside these grains. In addition, grains with initial Goss orientation do not show a significant development of those internal misorientations. The observed texture evolution behavior is consistent with the previously discussed experimental findings. Figure 6-34(d) shows a schematic presenting the observed texture rotation path during wrap bending of the Equiaxed microstructure. The schematic has been drawn based on visual observations of the regions encircled in black starting from the initial (Figure 6-34(a)) to the final bend angle (Figure 6-34(c)). It is observed that grains that have their initial orientations within region 1 (Figure 6-34(d)) of the IPF space experience a rotation towards the top <001>-<111> line. However the exact amount of texture rotation is dependent on the amount of deformation experienced by the grain. Grains with initial orientations within region 2 (Figure 6-34(d)) of the IPF space, experience a rather limited rotation. Lastly, grains with their initial orientations within region 3 of the IPF space experience a rotation towards the top <111> corner. It is noted that the overall texture evolution behavior for the 'Equiaxed' microstructure is consistent with the previously determined behavior for the Original microstructure presented in Figure 6-23. This further suggests that texture evolution during wrap bending is rather independent of the overall grain morphology and is more closely linked with the applied strain path.

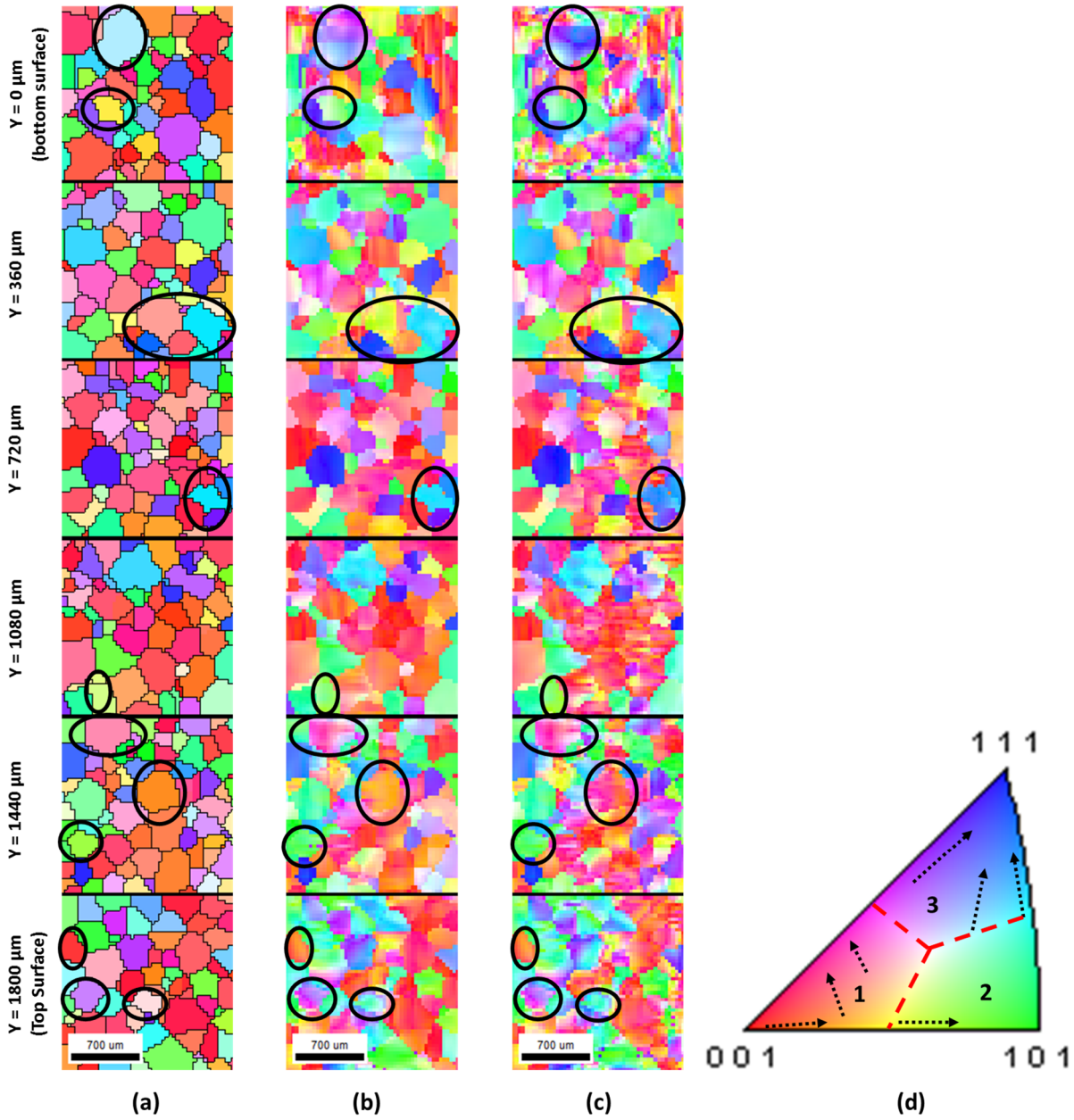

Figure 6-34: The inverse pole figure maps of through-thickness slices showing texture evolution during wrap bending at (a) initial 0°, (b) 85° and (c) 150° bend angles for the Equiaxed microstructure. Image (d) shows a schematic of the observed texture rotation path.

6.4 Chapter Summary and Conclusions

In the present work, a combined experimental and numerical study has been performed to characterize the bending behavior of precipitation hardening AA6063 aluminum alloy. A special emphasis is placed on examining the relationship between initial microstructure (i.e. texture, grain morphology), texture evolution, strain localization and the development of surface topography during wrap bending. A mix of mechanical and microstructural analysis techniques are used to examine the bending behavior of the alloy. The techniques include wrap bend tests with bend axis perpendicular to the extrusion direction, EBSD texture measurements to characterize the initial through-thickness microstructure and its evolution during bending, optical and scanning electron microscopy to study shear localization and damage development and 3D laser profilometry to analyze surface topography development after bending. Furthermore, a multiscale modeling approach has been proposed and applied to simulate wrap bending deformation using 3D crystal plasticity based finite element modeling. The numerically predicted results for texture evolution, strain localization and surface topography are compared against experimentally measured results. An additional systematic CPFEM based study is performed to analyze the role of microstructure in the development of different surface topographic behaviors such as ridging and the orange peel phenomenon. Some of the important observations and conclusions are summarized as follows.

- The as-received AA6063-T6 material has an average grain size of approximately 75 μm. However there is a significant through-thickness gradient in grain size distribution with grains that are as small as 15 μm in the center of the extrusion to as large as 200 μm in vicinity of the extrusion walls. The as-received material also shows a significant gradient in through-thickness texture distribution. The grains closer to the extrusion walls - surfaces have a dominant $\{111\}[uvw]$ orientated texture and those close to the center have a predominant Cube texture followed by a weaker Goss texture. This through-thickness gradient in grain size and texture is attributed to the differences in strain path and cooling rates experienced by the material closer to the extrusion wall as compared to the center of the extrusion.
- The bendability of the material is characterized using the geometric parameter r_{min}/t and is measured to be approximately 0.1667. The reduction in area at tensile fracture is measured to be approx. 54%. It is observed that bendability results for the extruded material are consistent with the empirical relationship proposed by Datsko and Yang [254], which relates sheet bendability to the reduction in area at fracture in a tensile test.
- The through-thickness optical metallography results after bending show shear localization close to the inner compressive and outer tensile regions of the bend. The localization has led to significant changes in grain shape and orientation. It is concluded that the development of surface undulations (i.e. peaks and valleys) on the outer tensile surface is not a mere surface effect but in fact is linked with strain localization through thickness of the bend. Furthermore, it is observed that microscopic cracks initiate form regions of high

surface roughness along the outer bend surface and those regions generally correspond to the surface valleys.

- The SEM images of the outer tensile surface show signs of grain boundary relief and other regions with intense strain localization. Within these regions, strain tends to localise into coarse slip bands and the presence of several macroscopic surface ridges is also evident. Furthermore, the relative out-of-plane movement of several grains has led to height changes and the formation of surface undulations.
- It has been shown that crystallographic slip during bending deformation has led to significant evolution of the overall texture with many texture components (i.e. in particular Cube component) showing a high degree of texture rotation. EBSD texture maps show the presence of coarse slip bands within several grains. The presence of these coarse slip bands is highest within Cube oriented grains, followed by grains with near {111}[*uvw*] orientations. It is further noted that grains having Goss orientation do not show the presence of these slip bands within grain interiors. This mismatch of strain accommodation amongst neighboring grains or cluster of grains, directly influences the surface topography during wrap bending.
- The proposed multiscale modeling approach to wrap bending in conjunction with the backstress crystal plasticity hardening model are able to successfully predict the experimentally observed texture evolution, slip band formation within grains and through thickness strain localization. Results from wrap bending simulation show regions of high strain localization through-thickness of the bend. It is observed that regions corresponding to surface valleys show high localized strains as compared to regions that correspond to surface peaks. Consistent with experimental findings, several regions of high strain localization are also present underneath the top tensile surface.
- The numerically predicted surface topography after wrap bending show good agreement to the experimentally measured surface profile using 3D laser profilometry. Consistent with experimental results, the numerically predicted surface topography shows the presence of a ridging pattern, with multiple hills and valleys appearing in an alternating pattern.
- The observed ridging phenomenon is promoted by the collective co-deformation of similarly oriented crystals assembled in layers or grain clusters. It is observed that grains with predominant {111}[*uvw*] texture experience an out of plane displacement leading to the formation of peaks or hills at the surface, whereas grains with Cube or near Cube texture experience a negative out-of-plane displacement forming surface valleys during wrap bending deformation.
- Through a systematic numerical wrap bending study, it has been shown that all microstructures with through-thickness clustering of similarly oriented grains produce a ridged surface topography. It is concluded that the differences in the severity of hills and valleys and their location on the outer bend surface are linked to the exact through-thickness locations of those similarly oriented grain clusters.

- It has been shown that it is possible to achieve a significantly lower surface roughness by altering the through thickness locations of the kinematically different grain clusters (i.e. cube grain clusters vs. {111}[*uvw*] grain clusters) in a way that minimizes the out-of-plane (positive or negative) displacements, as in the case of Top-center switched microstructure.
- Lastly, it has been numerically shown that by eliminating or by reducing the tendency towards clustering of similarly oriented grains within the microstructure, a transition from a ridging to an orange peel type surface topographic behavior can be achieved.

Chapter 7: Development and Validation of Failure Criterion for Precipitation Hardened Aluminum Alloys

In this chapter, a new constitutive model is proposed to predict failure in precipitation hardened aluminum alloys. The failure criterion is based on the existing nano-void theory of ductile failure that is extended to precipitation hardened aluminum alloys by incorporating the effects of dynamic microstructure evolution due to the formation of deformation and precipitation induced cellular dislocation substructure. The proposed failure model is employed to predict failure strains for extruded and rolled AA6xxx alloys subjected to different loading conditions.

The chapter presents a manuscript of an article submitted to the journal of Metallurgical and Materials Transactions A.

Metallurgical and Materials Transactions A (2019): Submitted

A Criterion for Ductile Failure in Age-Hardenable Aluminum Alloys

Metallurgical and Materials Transactions A (2019): Submitted

Waqas Muhammad[1], Abhijit P. Brahme[1], Rama K. Sabat[1], Raja K. Mishra[2], Kaan Inal[1]

[1] Department of Mechanical and Mechatronics Engineering, University of Waterloo, Waterloo, N2L 3G1, Canada

[2] General Motors Research & Development Center, Warren, MI 48090, USA

Overview

In this study, a new constitutive model is proposed to predict failure in age-hardenable aluminum alloys. In this regard, the existing nano-void theory of ductile failure is extended to precipitation hardened aluminum alloys by incorporating the effects of dynamic microstructure evolution due to the formation of deformation and precipitation induced cellular dislocation substructure. As per the nano-void theory, nano-voids form at pre-existing nano-particles and grow by accumulation of point defects that are generated dynamically during deformation, ultimately leading to ductile failure by void coalescence. The newly proposed constitutive model accounts for the effects of precipitation induced dislocation substructure on point defect generation by incorporating a new evolution law for the effective obstacle strength associated with substructure evolution. The model is calibrated and successfully validated against experimental data by predicting failure strains for tensile loading along different in-plane directions for three different AA6xxx series age-hardened aluminum alloys with very different starting microstructures and processing history. The error between predicted failure strains and corresponding experimental values is less than 7%. In addition, the versatility of the proposed constitutive model is demonstrated by coupling the failure criterion with stress-strain data generated through crystal plasticity simulations, to predict failure strain for arbitrary loading – stress triaxiality conditions. Such failure strain versus stress-triaxiality data is invaluable as it is routinely used as an input for modeling fracture within finite element (FE) based simulations. Furthermore, the approach developed herein, is suitable for use with computer aided engineering (CAE) tools to overcome current limitations in failure prediction for aluminum components.

Keywords: Aluminum alloys; Ductile failure; Age-hardening; Point defects; Dislocation substructure

7.1 Introduction

Age-hardenable, Al-Mg-Si (AA6xxx) aluminum alloys are widely in automotive applications due to their ability to achieve higher final strengths after the automotive paint-bake cycle [231, 274]. Apart from their heat treatable properties, these alloys also possess excellent rollability, extrudability, weldability, high thermal conductivity and good corrosion and dent resistance, etc [275, 276]. Hence, they are widely used in outer body panels, where high strength, dynamic dent

resistance and high surface quality are needed, and bumper and crush rails, where good strength and shock absorption are required. During the design phase of such automotive components, CAE based numerical tools are extensively used for crashworthiness and structural optimization. However, due to the complexity involving additional hardening mechanisms associated with precipitation strengthening, the numerical models for hardening and fracture prediction are rather not well developed for these alloys. Consequently, majority of vehicle components are over-designed because the existing material models are unable to predict failure – fracture accurately, thereby requiring large safety margins to be incorporated in the final design. In this regard, the availability of accurate failure models continues to remain a major challenge, for optimizing the impact performance and formability of designed parts.

Failure of AA6xxx aluminum alloys is still not well understood due to their intricate microstructures. Many metallurgical and processing aspects in their rather complex combinations can have a significant influence on it. One of the observed failure modes in AA6xxx aluminum alloys is the intergranular or grain boundary ductile fracture (GBDF) [126]. In this failure mode, microcracks tend to initiate and propagate predominately along the existing grain boundaries within the material and the occurrence of such failure is typically associated with an improperly conducted heat treatment that leads to heterogenous nucleation of second phase particles along grain boundaries [126]. Several potential causes of intergranular failure have been reported such as the formation, growth and coalescence of micro-voids along heterogeneously nucleated grain boundary particles, strain localization in precipitation free zones (PFZs) along such grain boundaries, promotion of coarse slip distribution within grains, and grain coarsening [44, 126, 253, 259, 277]. It is shown that the tendency to premature intergranular failure can be reduced significantly by promoting multi-slip and grain refinement through alloying additions [44, 278], thereby reverting to the commonly observed ductile failure mode in aluminum alloys, which is governed by necking and ductile rupture.

Ductile failure in aluminum alloys has been studied extensively over the past few decades [72, 86, 90, 279, 280]. Currently, two major theories are generally accepted to explain fracture in aluminum alloys: one based on damage accumulation and the other based on point defect generation, nano-void formation and growth. The damage accumulation theory is based on the nucleation, growth and coalescence of micro-voids [58–61, 281]. According to this theory, the presence of initial inclusions and second phase particles in the ductile matrix, offers sites where damage can nucleate in the form of micro-voids. These voids nucleate heterogeneously at such pre-existing sites either by particle cracking or de-cohesion of particle-matrix interface [68, 70, 71, 84, 99]. These micro-voids and any pre-existing cracks grow around by means of continued plastic deformation and induced stress triaxiality [82–85]. At a certain stage of plastic deformation, the plastic strain tends to concentrate along a sheet of voids, promoting local necking instabilities, which further triggers the process of void coalescence leading to the formation of macroscopic cracks and an eventual failure through ductile rupture [70, 87, 97–101, 282–286]. The nano-void formation theory is based on the notion that nano-voids form at grown-in nano-particles and grow with continued

deformation, ultimately leading to coalescence of nano-voids and failure [287, 288]. The theory suggests that finely dispersed particles are present in the starting material which act as nuclei for nano-void formation. These voids grow by the accumulation of point defects generated dynamically due to dragging of dislocation jogs during deformation [217, 289]. Nano-void coalescence and failure by micro-plastic activity occurs when the ratio of the growing void diameter to inter-void spacing reaches a critical value.

As per the nano-void theory of failure, the nano-void nuclei grow by accumulation of point defects that are generated dynamically with deformation within the mean volume element associated with each nucleus. As such, it is vital to devise a reliable approach that can predict this dynamic generation and accumulation of point defects. Primary methods to calculate point defect generation during deformation rely on dislocation theory and atomistic modeling and are extremely complicated as accurate simulation of the types of jog formation due to dislocation-dislocation interaction [290–295] and dragging of stair-rod dislocation [296, 297] is extremely challenging. Recently, studies have shown that for aluminum alloys the nominal yield stress is correlated linearly with the fracture strain, which implies that ductile fracture must be linked in some way to the starting microstructure of the material [298–301]. In keeping with this notion, Saimoto and co-workers [217, 289] employed a microstructure-based constitutive relation [147] that uses Taylor slip analysis, to predict failure strain of several solid solution strengthened aluminum alloys with reasonable accuracy. The authors proposed a homogenized approach to calculate the volume fraction of point defect generation and accumulation during deformation from the experimental stress-strain data, applicable to single phase materials. However, the proposed approach treats forest dislocations as the main obstacles beyond yielding and does not account for dislocation-precipitate interactions which play a crucial role during plastic deformation of age-hardenable aluminum alloys. Many studies have shown that the age-hardenable aluminum alloys tend to form deformation and precipitation induced cellular dislocation microstructure that evolves with plastic deformation [6–8, 10, 12, 150, 201, 264] and effectively alters the mean slip distance, obstacle strength and adds extra complication in prediction of jog formation and point defect generation. Hence, applications of these failure models to age-hardenable aluminum alloys require the effects of deformation induced dislocation substructure to be accounted for within the formulation.

The purpose of the present work is twofold. Firstly, a new constitutive approach to predict failure strain in precipitation hardened aluminum alloys is proposed. For this purpose, the nano-void failure theory is extended to precipitation hardened aluminum alloys by incorporating the effects of dynamic microstructure evolution due to the formation of deformation and precipitation induced cellular dislocation substructure. The proposed failure criterion is applied to predict failure strains of a series of precipitation hardened aluminum alloys under uniaxial tensile loading and the results are validated against experimental data. Secondly, the versatility of the proposed model is shown by generating failure strain data for a series of AA6xxx aluminum alloys under different stress triaxiality conditions using stress-strain data from crystal plasticity simulations. Such failure strain

versus stress-triaxiality data is very valuable as it is typically used as an input for modeling fracture within finite element based phenomenological plasticity simulations.

7.2 Constitutive Model Development

In his pioneering work on the mechanism of plastic deformation in crystals, Taylor [302] attributed the incremental strain during plastic deformation to the areal increase of slip patches due to movement of dislocation arrays and their increase in the total dislocation density. In keeping with this notion, more recently Saimoto and Van Houtte [147] proposed a constitutive relationship between the flow stress and strain by equating the energy required to create the new dislocation line lengths necessary for producing the imposed slip patches to the energy of the retained dislocation density derived from the flow stress, while accounting for the possibility of dynamic annihilation during deformation. The amount of new dislocations generated $\Delta\rho^{create}$ are calculated using the following relationship

$$\Delta\rho^{create} = \frac{P\Delta\gamma}{\lambda b} \tag{7-1}$$

where λ is the mean slip distance, b is the burgers vector P is a variable factor related to the perimeter of newly created slip patches and γ is the shear strain. The amount of retained dislocation density can be assessed from the flow stress as follows [303]

$$\tau_f = \alpha\mu b\rho^{\frac{1}{2}} \tag{7-2}$$

where α is a parameter related to the strength of obstacles and μ is the shear modulus. Using the relationships in Eq. (7-1), Eq. (7-2) and considering the possibility of dynamic annihilation by introducing an annihilation factor A, the constitutive relationship between shear stress and shear strain as proposed by Saimoto and Van Houtte [147] is given by

$$\tau = \left[\left(\frac{P}{4A}\right)(2+\beta)(\alpha\mu b)^2\frac{1}{C_1 b}\right]^{\frac{1}{(2+\beta)}}\gamma^{\frac{1}{(2+\beta)}} \tag{7-3}$$

In Eq. (7-3), $\tau = (\sigma - \sigma_0)/M$, with σ being the measured stress, M being the Taylor factor and σ_0 being the back extrapolated stress obtained from stress strain curve using the procedure outlined in Saimoto and Van Houtte [147] and Brahme et al. [148]. The parameters C_1 and β are microstructure dependent parameters and are related to the mean slip distance and flow stress as $\lambda = C_1\tau^{\beta}$ [147]. The parameter P/A is related to the creation and annihilation of new dislocation line lengths and is defined as $P/A = 2\varphi/\alpha^2$; where $1/\varphi = (1/2\alpha)(\mu/\theta)$ with θ being the work hardening rate. The parameter φ is determined from the experimental $\sigma - \varepsilon$ curve as outlined by Saimoto and Van Houtte [147].

It has been validated that a quantitative measure of the volume fraction of point defects generated during deformation can be computed from the experimental shear stress τ – shear strain γ data [217]. The point defect generation is evaluated in a homogenized manner based on the number count of interactions between mobile and forest dislocations and by further assessing the percentage of such intersections that have the capability of dragging jog and producing vacancies. It is assumed that those intersections that can drag jogs produce λ/b vacancies. If the fraction X of intersections produce vacancies per N_0, the number of atoms per m^3, then the volume fraction of deformation induced point defects C_V for an arbitrary shear strain interval between γ_1 to γ_2 can be assessed as follows [217]

$$C_V = \frac{X}{N_0 b^3}\left(\frac{P}{4A}\right)(2 + \beta)\frac{\gamma^2}{2}\Big|_{\gamma_2}^{\gamma_1} \tag{7-4}$$

The C_V relationship in Eq. (7-4) implies that the volume fraction of point defect generation can be effectively determined by microstructural parameters P/A and β, both of which can be measured from experimental stress-strain data. The value of N_0 for polycrystalline aluminum is 6.026×10^{28} m^{-3}. The parameter X is dependent on the selection of slip systems within each crystallite and is therefore a function of crystallographic texture. However, due to the large number of grains involved and considering many possible types of crystal orientations and jog formation, a statistical mean value is invoked, where $X = 0.5$ for polycrystalline materials. The readers are referred to Saimoto et al. [217] for further details.

The nano-void nucleation and growth theory postulates that pre-existing particles (solute particles, GP zones etc.) or clusters of point defects that affect yielding also act as sites for nano-void nucleation. The growth of these nano-voids is controlled by the point defects diffusing to these nuclei as they get generated during plastic deformation. Typically, Eq. (7-3) replicates experimental stress-strain data using at least two calibrated curves. The intersection of the two calibrated curves is characterized by the parameters designated as τ_3 and γ_3, whereas the intersection itself signifies a pseudo-transition from Stage II to Stage III hardening. The parameter β_1 from the first calibration using Eq. (7-3) corresponds to pinning effects that result in the yield phenomenon and the parameter β_2 from the second calibrated curve corresponds to obstacles that oppose dislocation motion at strains beyond macro-yield, such as lattice friction, solute clusters, particles and grain size effects. It is postulated that nano-voids form at pre-existing nano-particles with spacing l_p during initial axial straining to γ_3, which represents the shear strain at the intersection of the two calibrated curves. The initial inter-void spacing at γ_3, designated as l_v^{nano}, is computed as follows [289]

$$l_v^{nano} = l_p \exp(-\gamma_3/rM) \tag{7-5}$$

where $l_p = \alpha\mu b/\tau_p$ and the parameter r depends on the principal strains, being two for ideal tensile and one for plane strain and balanced biaxial cases. After straining to γ_3, the point defect production increases and the inter-void spacing l_v evolves as follows

$$l_v = l_v^{nano} \exp(-(\gamma - \gamma_3)/rM) \quad \textbf{(7-6)}$$

The growing nano-void diameter d_v is linked with volume fraction of point defects generation and is measured using the following relationship [289]

$$d_v = l_p \{(6/\pi) C_V\}^{1/2} \quad \textbf{(7-7)}$$

As per the nano-void failure criterion proposed by Saimoto and co-workers [217, 289], only the interaction of mobile and forest dislocations are taken into account for calculating point defect generation C_V and nano-void growth. As such, the obstacle strength parameter α is taken to be a constant 0.4 for forest dislocations as obstacles [289]. However, research has shown that strain hardening in precipitation hardened aluminum alloys is accompanied by the formation of deformation - precipitation induced dislocation substructure due to blockage of dislocations passage [164, 196, 264, 304–306]. The dislocation substructure manifests itself in the form of dislocation cells or nets that are characterized by three-dimensional tangles of dislocations that serve as "cell walls – hard phase" and less dense internal regions (cell interiors - soft phase) [6–9, 12, 201]. A schematic of a precipitation induced dislocation substructure is shown in Figure 7-1(a), where the cell walls are formed by regions of high dislocation content and the cell interiors are relatively dislocation free. Such cell structure induces internal or pinning stresses due to blockage of mobile dislocations, thereby altering the perceived obstacle strength α. It has been shown that the magnitude of the induced internal stresses does not remain constant and depends on the size and volume fraction of dislocation cell walls, which evolve with deformation [6, 7, 307]. Furthermore, the obstacle strength parameter α evolves with deformation [264] as the moving dislocations encounter obstacles of varying strength due to the evolving dislocation substructure. Since point defect generation C_V and the accompanying nano-void growth are dependent on the nature of dislocation interactions (i.e. parameter α), it is therefore important to incorporate the effects of this precipitation induced dislocation substructure into the existing nano-void ductile failure theory, for failure strain predictions of age-hardenable aluminum alloys, as discussed next.

Using a homogenized approach, dislocation cells can be modeled as spheres having a cell radius R and cell wall thickness t, as shown schematically in Figure 7-1(b). Based on the assumption that dislocation cells are spherical (i.e. equiaxed) in nature and using Eshelby's analysis of spherical inclusion [163], Muhammad et al. [264] proposed a constitutive formulation to calculate the induced internal stresses τ_i due to dislocation substructure formation given by

$$\tau_i = 3Ct\mu(1 - \chi_E)\gamma\rho^{\frac{1}{2}} \quad \textbf{(7-8)}$$

where C is a material parameter and χ_E is Eshelby's factor for spherical inclusion given by

$$\chi_E = \left(\frac{2}{15}\right)\left(\frac{4-5v}{1-v}\right) \tag{7-9}$$

In Eq. (7-9), v is the Poisson's ratio of the material. Furthermore, in materials which exhibit dislocation cell formation, the total flow stress can be expressed as follows

$$\tau = \tau_f + \tau_i \tag{7-10}$$

and by substituting Eq. (7-2) and Eq. (7-8) in Eq. (7-10), one can rewrite the total flow stress as

$$\tau = \alpha_{eff}\mu b\rho^{\frac{1}{2}} \tag{7-11}$$

where the effective obstacle strength α_{eff} is given by

$$\alpha_{eff} = \alpha + \frac{3Ct}{b}(1-\chi_E)\gamma \tag{7-12}$$

In Eq. (7-12), the first term α is a constant related to the obstacle strength of a forest dislocation and the second term can be viewed as the obstacle strength of a dislocation cell that evolves with shear strain. Lastly, the constitutive relationship in Eq. (7-3) is updated to incorporate the effects of precipitation induced dislocation substructure formation by replacing the term α in Eq. (7-3) with α_{eff} as follows

$$\tau = \left[\left(\frac{P}{4A}\right)(2+\beta)(\alpha_{eff}\mu b)^2\frac{1}{C_1 b}\right]^{\frac{1}{(2+\beta)}}\gamma^{\frac{1}{(2+\beta)}} \tag{7-13}$$

The calibration procedure to obtain the material parameters from measured stress-strain data, is described in details elsewhere [147, 148, 289]. Ductile failure through nano-void coalescence occurs when the ratio between inter-void spacing l_v and void diameter d_v reaches a critical value. Given that the experimental fracture strain γ_f is known, the critical l_v/d_v ratio to trigger void coalescence and ductile failure can be calculated using Eq. (7-6) and Eq. (7-7) for a given straining condition. The measured ratio is than treated as a material constant to predict failure under arbitrary loading conditions using respective stress-strain data.

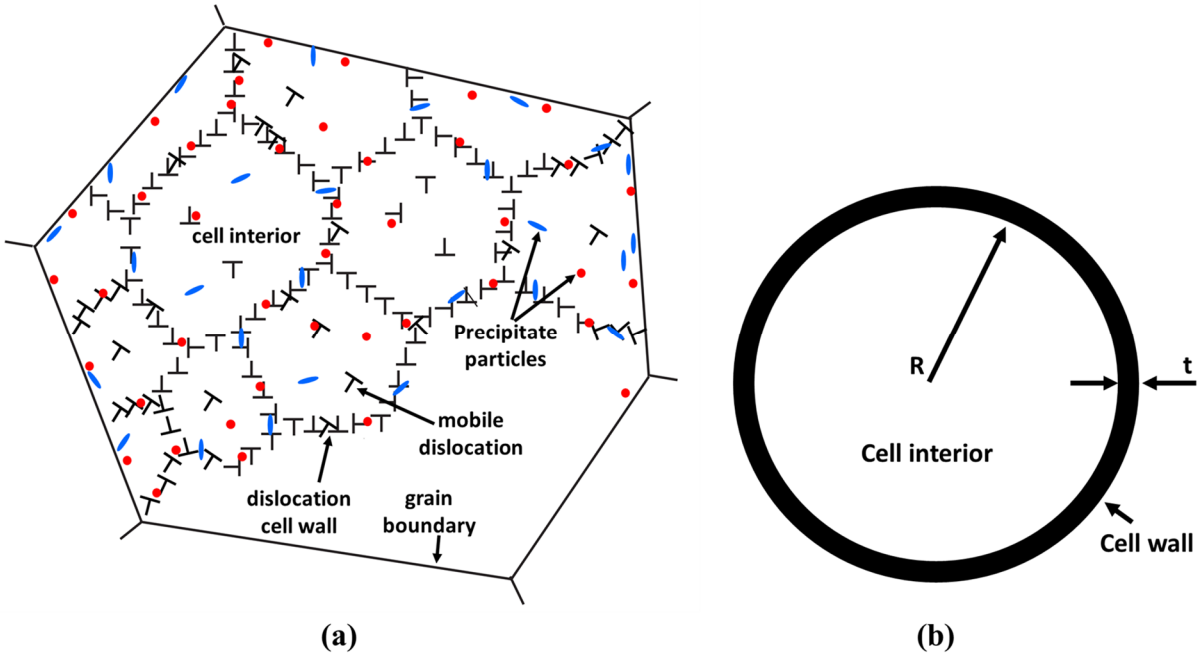

Figure 7-1: Microstructural schematic of an age-hardenable aluminum alloy showing the formation of dislocation substructure and (b) schematic of a single dislocation cell where R represents the radius and t is the cell wall thickness.

7.3 Experimental Procedures

Commercial grade AA6061 rolled sheet, extruded AA6063 and extruded AA6082 profiles are chosen for the calibration and validation of the proposed model. The chemical compositions of the alloys are listed in Table 7-1. All alloys were received in a T6 temper condition and the nominal thicknesses of rolled sheet and extruded profiles are approx. 2 mm.

Table 7-1: Chemical composition (max. wt%) of as-received AA6XXX materials.

Material	Mg	Si	Fe	Mn	Cu	Ti	Cr	Zn	Al
6061	1.01	0.59	0.45	0.02	0.28	0.04	-	-	Bal.
6063	0.49	0.4	0.16	0.029	0.01	0.01	-	-	Bal.
6082	0.78	1.2	0.3	0.5	0.08	-	0.14	0.05	Bal.

Electron backscatter diffraction (EBSD) texture measurements were performed to characterize the microstructure of each as-received material. The EBSD measurements were performed on the RD-TD plane for AA6061 sheet material and ED-ND plane, with ND being the through thickness direction, for AA6063 and AA6082 extruded materials. The specimens were cold-mounted, grinded and polished using standard metallography techniques followed by a final ion-milling step to achieve the desired surface finish. All texture measurements were made using a field-emission Nova NanoSEM™ equipped with a TSL EBSD camera. A step size of 0.5 µm was used for texture measurements and the data was further analyzed using the TSL OIM™ software. The data is cleaned using a single iteration of neighbour CI correlation to remove bad data points.

Tensile tests were carried out along RD (or ED), 45° and 90° (i.e. TD) loading directions using standard ASTM-E8M specimens. The tests were performed at room temperature using an MTS Landmark 370 Servo-hydraulic tensile machine with a load cell capacity of 100 KN and a constant cross-head speed of 1.0 mm/min. Each test was repeated at least three times to ensure repeatability and accuracy of experimental data. A commercially available digital image correlation (DIC) system "ARAMIS®" was used to capture surface strain evolution within the specimen gage section. Prior to testing, a random black-white speckle pattern was spray painted on the specimen surface and the DIC measurements were made from a set of snapshots collected automatically at a preset frame rate of 1 fps during the straining process. The recorded data was later analyzed to extract axial tensile strains and local failure strain values of each sample.

7.4 Results and Discussion

Figure 7-2(a-c) shows the inverse pole figure (IPF) maps for the as-received microstructure of AA6061, AA6082 and AA6063, respectively and the corresponding textures are shown as <111> pole figures in Figure 7-2(d-f) , respectively. It is apparent at first glance that the microstructures for the three AA6xxx age-hardenable aluminum alloys are quite different. The microstructure for AA6016 sheet material exhibits a rather equiaxed and uniform grain size distribution whereas both extruded materials (i.e. AA6082 and AA6063) show a variance in the through thickness texture and grain size distribution as apparent from the difference in grain size and texture in the center as compared to in vicinity of the extrusion walls (see Figure 7-2(b-c)). This is rather expected as the material closer to the extrusion wall experiences a somewhat different deformation history and cooling rate as compared to the center of the extrusion. Furthermore, it is apparent that AA6082 has a dominant fibrous microstructure whereas AA6063 exhibits a recrystalized microstructure with near-equiaxed grains. The texture for the three as-received materials are also very different as exhibited by the <111> pole figures. The AA6061 sheet material shows a predominant Cube texture followed by S component texture, the AA6063 extruded material shows the presence of Goss component in addition to the Cube component and the AA6082 extruded material shows a dominant {001} <110> texture. Based on the uniform grain size, grain morphology and uniformity in texture between the sheet surface and sheet center, the rolled microstructure is considered homogeneous. The extruded materials, in contrast, exhibit a heterogeneous microstructure characterized by difference in grain size distribution, grain morphology and through thickness texture gradient.

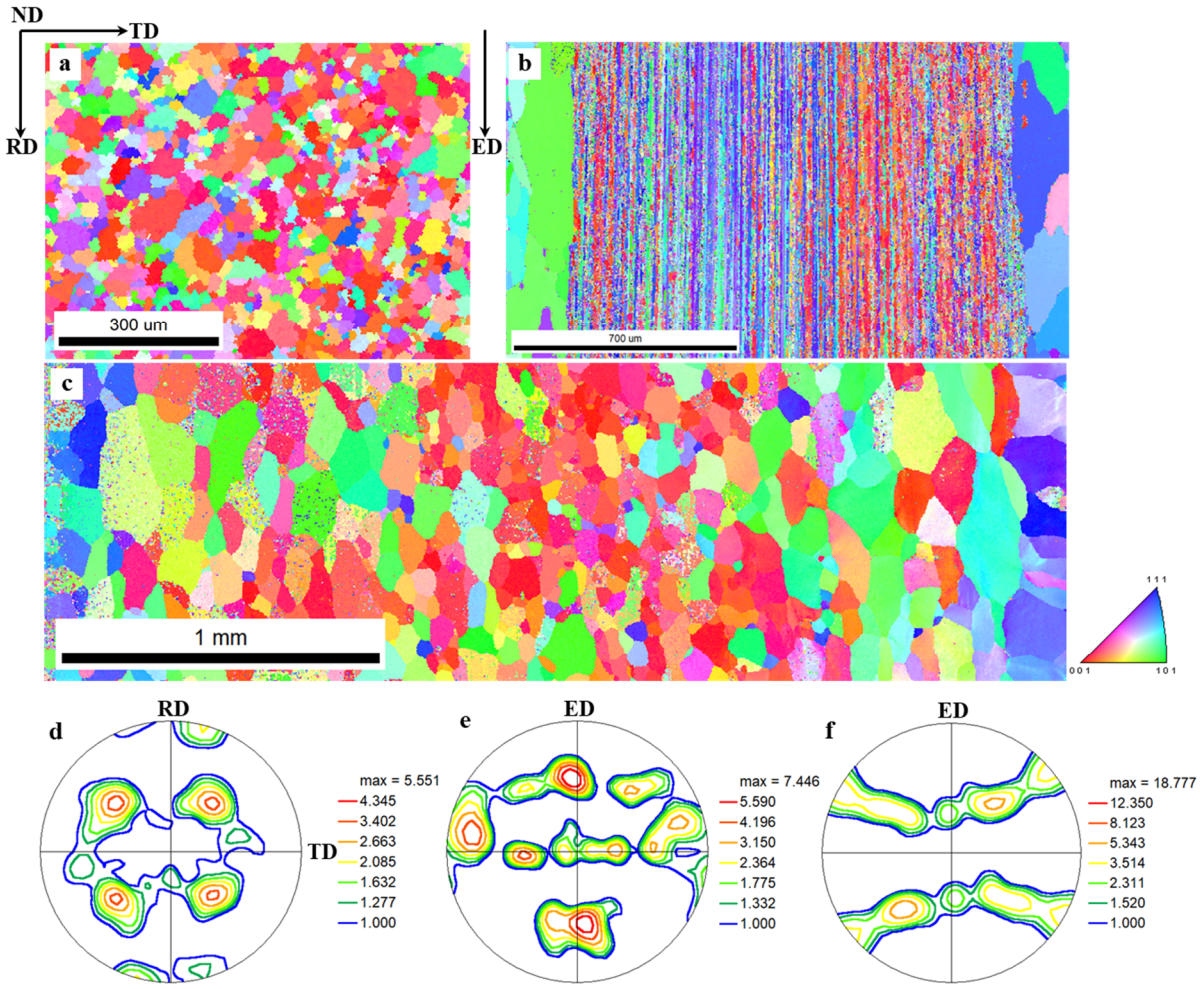

Figure 7-2: IPF maps and the corresponding <111> pole figures for as-received microstructure of (a)(d) AA6061, (b)(e) AA6082 and (c)(f) AA6063 aluminum alloys.

Figure 7-3(a-c) shows the uniaxial tensile flow curves along the different in-plane loading directions for AA6061, AA6082 and AA6063, respectively. As expected, the yield stress and the ultimate tensile strength are highest for AA6082 due to the comparatively higher weight percentage of alloying additions and finer grain size, followed by AA6061 and AA6063 materials. It is also interesting to note that the in-plane anisotropy (in terms of yield stress, work hardening behavior and macroscopic failure along different loading directions) is highest for AA6082, followed by AA6063 and AA6061. This behavior is consistent with the as-received microstructure of these materials, where the extruded AA6082 material shows the highest heterogeneity in terms of grain size, grain morphology and texture. This highest heterogeneity within the starting microstructure (see Figure 7-2(b)) manifests as comparatively higher planar anisotropy during tensile loading (see Figure 7-3(b)). Furthermore, the starting microstructure for AA6061 is relatively homogeneous (see Figure 7-2(a)) and as such, its tensile loading response along the different in-plane directions is equally consistent (see Figure 7-3(b)). The experimental tensile hardening curves for the three materials are simulated using the two-curve calibration approach

(as outlined elsewhere [147, 148, 264, 289]) using different β_1 and β_2 values. The calibrated curves for the three materials along the reference directions (i.e. RD for rolled sheet and ED for extrusions) are shown in Figure 7-3(d-f). The corresponding constitutive parameters obtained from the calibration procedure are listed in Table 7-2. Using these calibrated parameters and Eq. (7-4), Eq. (7-6) and Eq. (7-7), the evolution of C_V, l_V and d_V is calculated with strain. The evolution of void diameter d_V and inter-void spacing l_V till failure along the reference directions (RD for rolled sheet and ED for extrusions) is shown in Figure 7-4. It is to be noted that after γ_3, the intersection point of two-curve calibration, the nano-void density remains constant, but its size grows as more point defects are generated by subsequent straining. As observed from Figure 7-4, the inter-void length l_V decreases with strain and the nano-void diameter d_V, grows linearly with shear strain until the coalescence of these voids by plastic deformation occurs when l_V/d_V ratio attains a critical value. The critical ratio as shown in Figure 7-4, is determined for the three materials using the experimentally measured local value of failure strains from DIC data of tensile tests along the reference loading direction. Assuming the determined l_V/d_V ratio for the reference direction to be a material constant, the failure strain values along other in-plane test directions are subsequently predicted using Eq. (7-6) and Eq. (7-7) and are listed in Table 7-2. It is noted that the proposed nano-void failure criterion successfully predicts the experimentally measured failure strains for the three alloys along different in-plane loading directions with less than ± 7% error.

The evolution of the volume fraction of point defects along different loading directions for the three materials is calculated using Eq. (7-4) and is plotted in Figure 7-5. For rolled AA6061 in Figure 7-5(a), it can be observed that the production rate of the volume fraction of point defects is highest for tensile loading along TD and lowest for loading along the 45˚ direction. As failure through nano-void coalescence is dependent on the rate at which such point defects are being generated, the corresponding predicted failure strain is higher in 45˚ direction as compared to TD direction, which conforms well with the experimentally measured strains shown in Table 7-2. Given that the AA6061 sheet material has a relatively homogeneous microstructure, with similar values of obstacle strength along different in-plane loading directions, the observed and predicted failure strain values along different loading directions are also quite similar (see Table 7-2). Similarly for the extruded AA6082 alloy, the volume fraction of point defects is minimum along 45˚ direction and maximum along extrusion direction (ED), which correlates well with the experimentally measured failure strain that is higher in 45˚ direction as compared to ED. Similar consistent behavior is observed for the extruded AA6063 material, where the higher rate of point defects generation along ED leads to an early failure (i.e. lower local failure strain) as the critical nano-void coalescence condition is satisfied much earlier during the straining process.

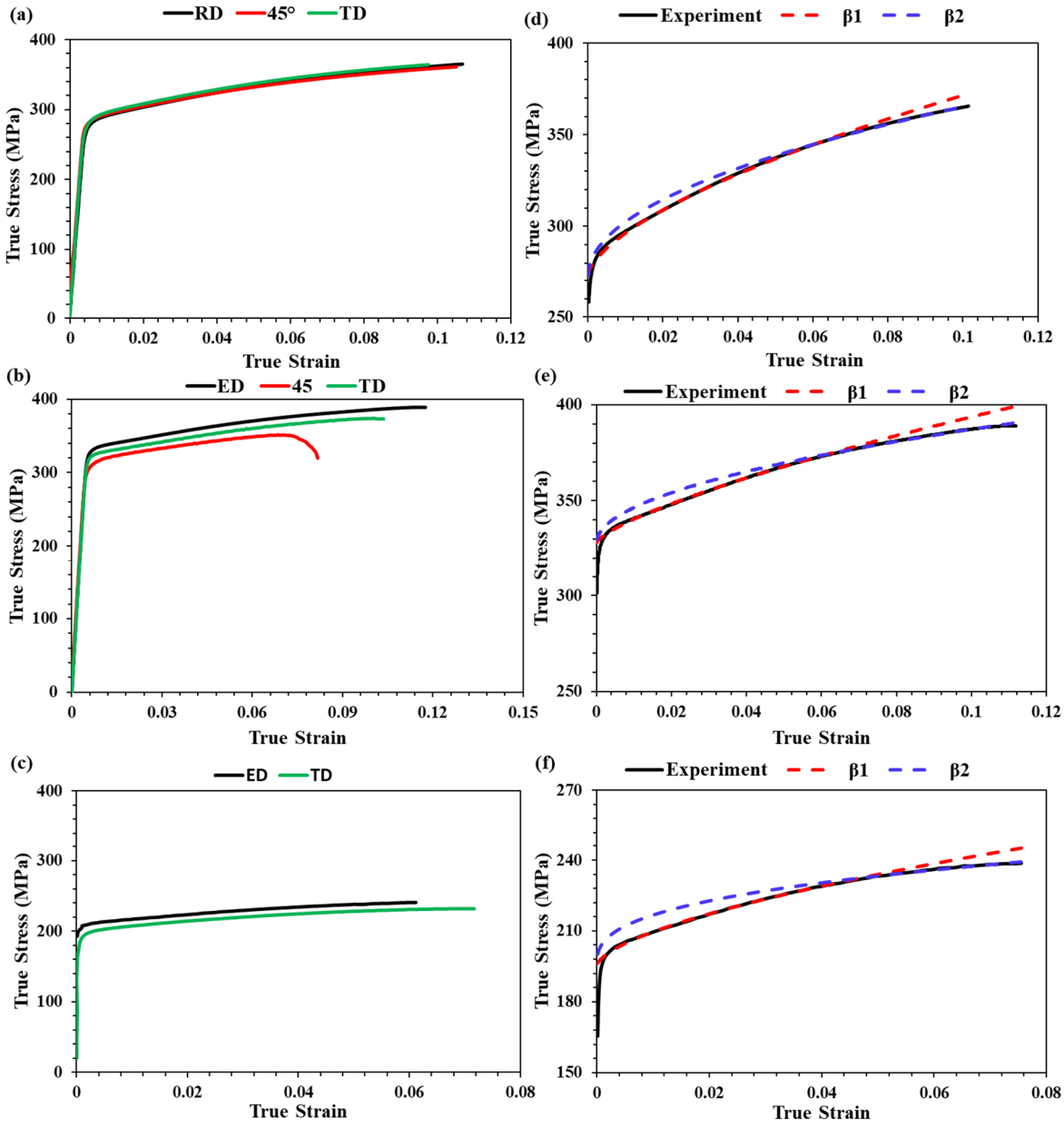

Figure 7-3: True stress – true strain curves of (a) AA6061 sheet, (b) AA6082 extrusion and (c) AA6063 extrusion; Simulated curves of (d) RD tensile data for AA6061 sheet, (e) ED tensile data for AA6082 extrusion and (f) ED tensile data for AA6063 extrusion.

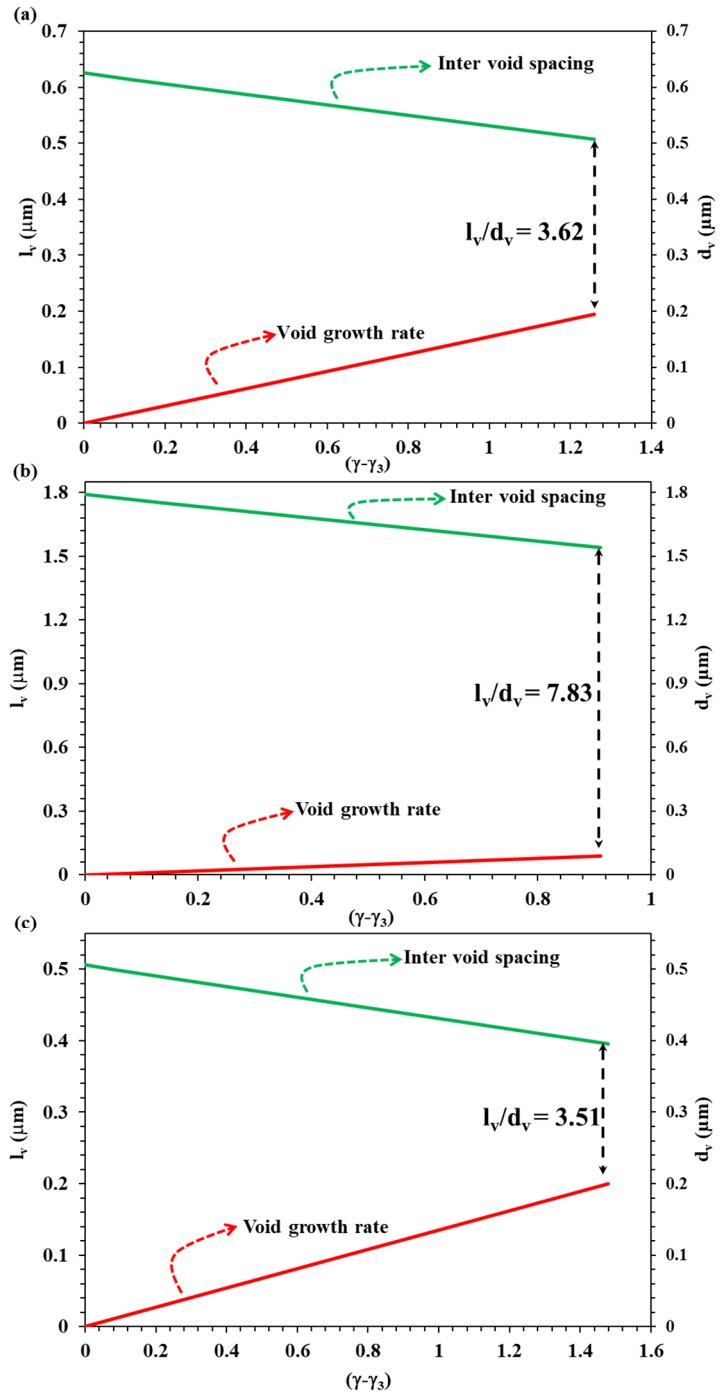

Figure 7-4: Inter void spacing (l_v) / void growth rate (d_v) (secondary axis) evolution versus shear strain for (a) AA6061 sheet along RD, (b) AA6082 extrusion along ED and (c) AA6063 extrusion along ED.

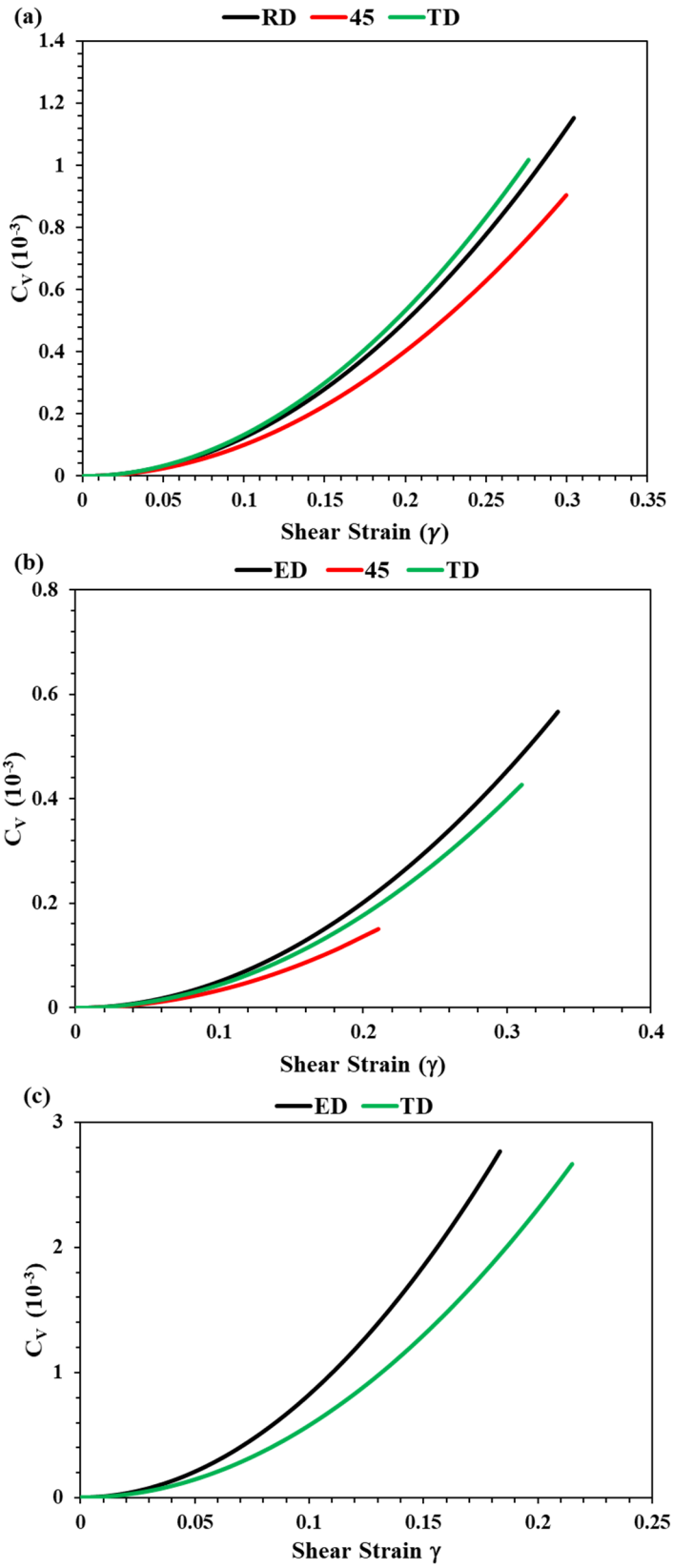

Figure 7-5: Evolution of volume fraction of point defects with strain in (a) AA6061 rolled, (b) AA6082 extruded and (c) AA6063 extruded materials.

Table 7-2: Calibrated microstructural parameters and experimental and predicted failure strains

Sample Name	α	β_1	P/A	β_2	τ_3 (MPa)	γ_3	l_v/d_v	ε_f(Simu) /ε_f(Exp.)	Error (%)
6061_RD	0.430	-0.409	0.146	0.012	114.97	0.181	**3.62**	0.48/0.48	-
6061_45	0.446	-0.232	0.125	-0.095	115.12	0.195	**3.62**	0.52/0.5	4.0
6061_TD	0.435	-0.386	0.158	-0.007	115.41	0.170	**3.62**	0.46/0.44	4.5
6082_ED	0.484	-0.416	0.060	-0.028	125.36	0.199	**7.83**	0.37/0.37	-
6082_45	0.472	-0.026	0.030	0.692	110.31	0.069	**7.83**	0.42/0.45	6.6
6082_TD	0.491	-0.40	0.042	0.513	121.81	0.193	**7.83**	0.38/0.4	5.0
6063_ED	0.496	-0.171	0.080	0.826	77.50	0.141	**3.51**	0.54/0.54	-
6063_TD	0.487	0.402	0.060	1.397	75.96	0.145	**3.51**	0.58/0.60	3.3

The evolution of volume fraction of point defects for AA6082 material is replotted in Figure 7-6 for the case of evolving microstructure (Solid lines) and non-evolving microstructure (dotted lines). The obstacle strength (α) has significant influence on the volume fraction of point defect generation. Figure 7-6 shows that for constant α values (value listed in Table 2 corresponding to shear strain value τ_3), the order of the three curves from high to low rate of point defect generation is 45˚, followed by TD and ED directions while the very order for calibration with variable α is ED, followed by TD and 45˚ directions. For constant α, deformation along 45˚ test direction for AA6082 corresponds to lowest predicted failure strain (see table within Figure 7-6) which is contrary to the experimentally measured failure strain that is highest along the 45˚ test direction. Thus, the importance of treating α as an evolving microstructural parameter in calculating failure strain of age-hardenable aluminum alloys can't be over emphasized.

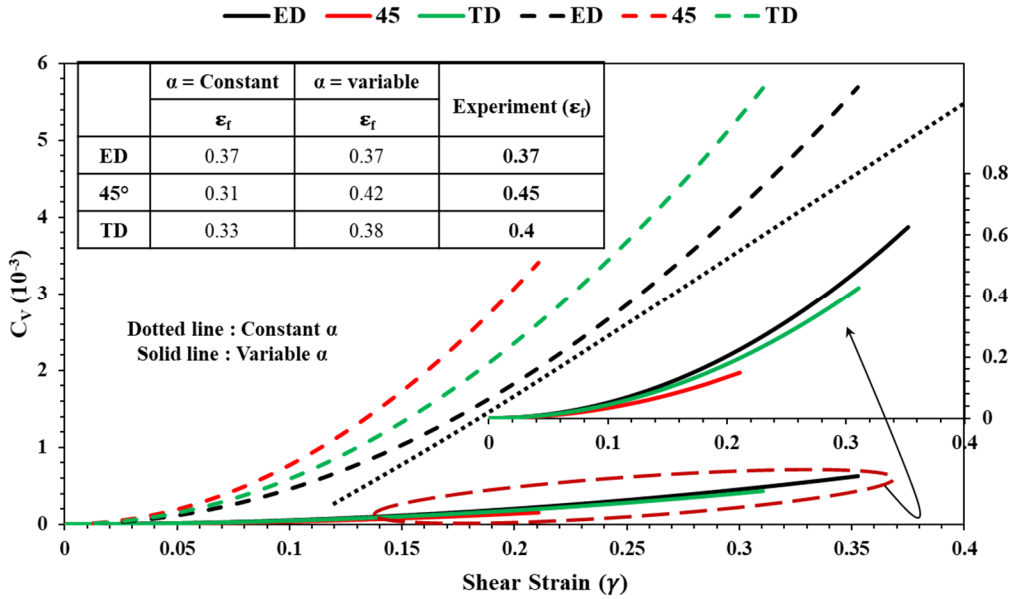

Figure 7-6: Effect of obstacle strength (α) on the evolution of volume fraction of point defects in extruded AA6082. The insert table lists the values of failure strain predicted along different directions of AA6082 for constant α and variable α (at τ_3 and γ_3).

The power and versatility of the proposed constitutive model lies in its ability to predict failure strains for arbitrary loading paths (i.e. stress triaxiality conditions) using stress-strain curves generated using crystal plasticity formulations. As such, the crystal plasticity-based approach is used to predict stress-strain behavior for the three studied materials, subjected to different stress triaxiality conditions. The proposed nano-void failure model is than applied to the predicted stress-strain curves and the failure strain for each alloy along different strain paths (i.e. stress triaxialities) is calculated using the experimentally calibrated l_v/d_v ratio. Figure 7-7 shows a plot of the calculated failure strain values for different triaxiality conditions for the three studied alloys along the reference direction (RD for rolled sheet and ED for extrusions). The predicted ε_f vs. η plots show a very consistent behavior to what is typically observed for age-hardenable aluminum alloys, with high failure strains in-vicinity of the shear regime, followed by an almost linear decrease in failure strain with increasing triaxiality, and subsequent low failure strains within the plane strain and biaxial loading regimes.

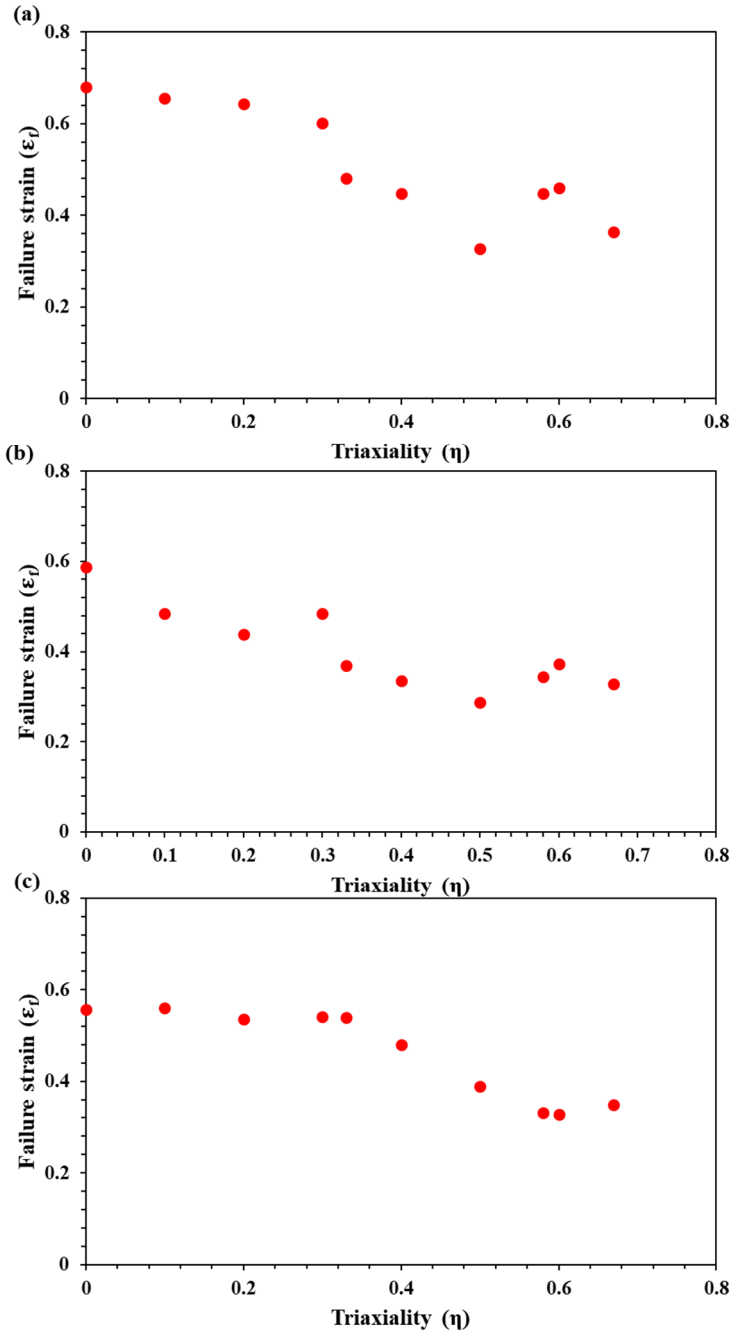

Figure 7-7: Failure strain predicted for different triaxiality conditions along RD of (a) AA6061 sheet material, ED of (b) AA6082 and (c) AA6063 extruded materials.

7.5 Chapter Summary and Conclusions

In the current study, a new constitutive approach to predict failure in age-hardenable aluminum alloys is proposed. As such, the existing nano-void theory of ductile failure is extended to precipitation hardened aluminum alloys by incorporating the effects of dynamic microstructure

evolution due to the formation of deformation and precipitation induced cellular dislocation substructure. As per the nano-void theory, nano-voids form at grown-in nano-particles and grow by accumulation of point defects that are generated dynamically during deformation. Ductile failure through nano-void coalescence occurs when the ratio between inter-void spacing and void diameter reaches an experimentally determined critical value. The newly proposed constitutive model accounts for the effects of precipitation induced dislocation substructure on point defect generation by incorporating a new evolution law for the effective obstacle strength related to substructure evolution. The proposed model is calibrated and successfully validated against experimental data by predicting failure strains for tensile loading along different in-plane directions for three different AA6xxx series age-hardened aluminum alloys with very different starting microstructures and compositions. It is further shown that the failure strain values predicted without considering the effects of precipitation induced microstructural evolution, are lower than the experimentally measured values, thereby emphasizing the importance of treating the perceived obstacle strength as an evolving microstructural parameter for predicting failure in age-hardenable aluminum alloys. Lastly, the versatility of the proposed constitutive model is demonstrated by coupling the failure criterion with stress-strain data generated through crystal plasticity simulations, to predict failure strain for arbitrary loading – stress triaxiality conditions. Such failure strain versus stress-triaxiality data is valued as it is typically used as an input for modeling fracture within finite element based computer simulations. For the first time, an approach to computationally determine the formability and failure of AA6XXX aluminum alloys subjected to complex strain paths as encountered in component forming or vehicle crash conditions, has been developed.

Chapter 8: Relationship between Microstructure, Plastic Deformation and Fracture behavior of Precipitation Hardened Aluminum Alloys

In this chapter, a comprehensive experimental study is presented to analyze the plastic deformation and fracture behavior of age-hardenable aluminum alloy AA6016 during bending. The study also presents an investigation into bendability enhancement of AA6016 by cladding using thermomechanical roll-bonding. The focus of the experimental study is to characterize the bendability and to investigate correlations between microstructure, the nature of plastic deformation, slip distribution, texture evolution, strain localization, surface topography development, macro-crack initiation and propagation during wrap bending.

The chapter presents an accepted manuscript of an article published in Materials Science & Engineering A journal.

Materials Science & Engineering A 753 (2019): 179-191. Doi: https://doi.org/10.1016/j.msea.2019.03.053

Bendability Enhancement of an Age-Hardenable Aluminum alloy: Part I – Relationship between Microstructure, Plastic Deformation and Fracture

Materials Science & Engineering A 753 (2019): 179-191

Waqas Muhammad[1,2], Jidong Kang[2], Abhijit P. Brahme[1], Usman Ali[1], Jürgen Hirsch[3], Henk-Jan Brinkman[4], Olaf Engler[3], Raja K. Mishra[5], Kaan Inal[1]

[1] Department of Mechanical and Mechatronics Engineering, University of Waterloo, Waterloo, N2L 3G1, Canada

[2] CanmetMATERIALS, 183 Longwood Road South, Hamilton, ON L8P 0A5, Canada

[3] Hydro Aluminium Rolled Products GmbH, Research and Development Bonn, D-53014 Bonn, Germany

[4] Hydro Aluminium Rolled Products GmbH, Product Area Automotive, D-41515 Grevenbroich, Germany

[5] General Motors Research & Development Center, Warren, MI 48090, USA

Overview

In this study, the bendability of two 1 mm thick sheets of monolithic AA6016 and composite AA6016X alloys is investigated using a series of wrap-bend tests, with emphasis on understanding the relationship between microstructure, the nature of plastic deformation and fracture behavior. The composite AA6016X alloy consists of a central core of AA6016 sandwiched between 100 μm thick clad layers of AA8xxx series aluminum alloy, processed using thermomechanical roll-bonding. It is shown that the bendability of monolithic AA6016 alloy is limited due to the formation of severe surface undulations and surface cracking, which is associated with the heterogenous nature of slip that concentrates into 5° - 15° misoriented coarse slip bands of very high dislocation content in the order of $10^{14}/m^2$, and intense shear bands originating from surface low cusps in the form of mutually orthogonal transgranular bands. The micro-cracks initiate at the surface and propagate along these intensely sheared regions, primarily consisting of grains with near S texture component. Grain boundary decohesion occurs along boundaries that are highly misoriented with misorientations ranging from 40˚ up to as high as 60˚, further assisting crack propagation. The composite AA6016X alloy exhibits unlimited bendability with no signs of fracture even after a maximum bend angle of 180°. The extremely high bending strains in AA6016X are accommodated in a homogeneous manner through a grain subdivision process within the AA8xxx clad layers, promoting the formation of deformation induced high angle boundaries. This homogeneous accommodation of strain within the clad layers reduces surface roughness and further enhances the bendability of the alloy.

Keywords: Clad aluminum alloy; Bending test; roll bonding; Plastic deformation; Deformation inhomogeneities; Fracture mechanisms

8.1 Introduction

Bending is the most commonly observed strain path in sheet metal forming operations. Hence, bendability of sheet materials is an important forming property and is of special importance to automotive industry. Inner automotive structures may involve bending of thick gauge sheets, while outer and inner body panels are joined together through a two-step, 180°, bending process, known as hemming. Age-hardenable aluminum alloys, in particular, the Al-Mg-Si (AA6xxx) alloys, are widely used for automotive body panels due to their heat-treatable properties, providing higher final strengths during the automotive paint-bake cycle [231, 253, 255, 257]. However, due to the lower ductility and fracture resistance of these alloys compared to steels, bendability and hemmability of these alloys is comparatively inferior [221, 223–225, 253, 263, 308]. Thus, improvement in bendability of AA6xxx alloys is of special importance to expand their applicability to various body and structural components within vehicles.

The bend performance of sheet materials is usually assessed, by bending the sheet across increasingly severe radii until fracture is apparent on the outer bent surface, using a wrap bend test [221, 254]. Several studies have been performed to relate the bend performance of precipitation hardened aluminum alloys to microstructural changes occurring during bending [219, 252, 309–311]. It is suggested that bendability in these alloys is limited by surface induced cracking due to intense strain localization, preceded by the development of surface roughness and progressively increasing surface undulations [220–222, 224, 231–233, 240, 312]. In other words, the development of surface roughness during bending is a key component that controls the overall bending performance. Several studies have focused on understanding the origins of surface roughness and ridging behavior and related it to the arrangement of the underlying crystallographic texture which can lead to individual or collective out-of-plane surface displacements resulting in orange peeling or banded surface topology [232, 236, 243, 250, 313–315].

Bendability of age-hardenable aluminum alloys is still not well understood because of their complex microstructure and many metallurgical and processing aspects in their rather intricate combinations can have a considerable influence on it. One of the most commonly observed fracture modes in AA6xxx aluminum alloys is the intergranular or grain boundary ductile fracture (GBDF), which is typically associated with an improperly conducted heat treatment that leads to heterogenous nucleation of second phase particles along grain boundaries [44, 126, 277, 316]. Several possible causes of intergranular failure have been reported including the formation, growth and coalescence of micro-voids along heterogeneously nucleated grain boundary particles, strain localization in precipitation free zones (PFZs) along such grain boundaries, promotion of coarse slip within grains, and grain size coarsening [44, 126]. Furthermore, it has been shown that intergranular fracture promotes premature failure, severely impacting bendability of these alloys [126, 231, 253].

As bendability of aluminum alloys is limited by surface induced cracking, the addition of a ductile clad layer at the surface has the potential of improving bendability of age-hardenable aluminum

alloys. Recently, few studies have employed a newly developed fusion technology to produce clad material by direct chill (DC) casting [317–319]. Jin et al. [318] studied the bendability of AA2124 sheets, cladded with lower strength and higher ductility AA1200, produced via direct chill casting fusion technology. It is reported that the more ductile clad layer, which has a comparatively higher fracture strain, delays the onset of surface cracking during bending, thereby achieving higher bend angles prior to failure. The authors suggested that the clad alloy releases strain by necking when a crack is initiated, usually near the clad-core interface, and further assists in blunting the crack tip, thus preventing the crack from quickly propagating to the outer bent surface. Lloyd et al. [317] studied the tensile and bending response of AA6111 sheets cladded with up to100μm layers of AA3003 using direct chill casting and the authors reported a significant improvement in bendability. The authors observed that crack initiates from within the lower bendability AA6111 core and eventually propagates through the more ductile cladding, leading to final failure. Jin and Lloyd [319] further studied the aforementioned cladded alloy, processed to different final gauges and artificially aged to different strengths. The authors reported improvement in bendability before and after peak aging, even when the thickness of cladding is less than the mean grain size of the material.

Clad aluminum sheets are also produced commercially by the roll bonding process, where the typical application is brazing sheet for use in automobile heat exchangers. Roll bonding is a well-developed process, but its application is limited due to fewer possible combinations of aluminum alloys that can be roll bonded effectively. Aluminum alloys with high Mg content such as the AA5xxx alloys are not easily bondable due to their high vulnerability to oxidation during the roll bonding process, which is typically conducted at elevated temperatures [317]. Furthermore, little to no information is found in literature on the bendability and deformation behavior of AA6xxx series cladded aluminum sheets processed using thermomechanical roll bonding. The AA6xxx series alloys due to their precipitation hardening properties can provide the required strength, whereas the soft clad layer can provide the necessary ductility. It is therefore of significant interest to study the bending behavior of such an alloy, with direct application for automotive body panels and structural components.

In the present work, a comprehensive experimental study is conducted to analyze the bendability and fracture behavior of an age-hardenable aluminum alloy AA6016. Two different sheet alloys are used: (i) monolithic AA6016 alloy, and (ii) composite AA6016X alloy with a core of AA6016 cladded with much softer AA8xxx series aluminum alloy using roll bonding. The focus of the experimental study is to characterize the bendability and to investigate correlations between microstructure, the nature of plastic deformation, slip distribution, texture evolution, strain localization, surface topography development, macro-crack initiation and propagation during wrap bending. A further emphasis is placed on understanding the mechanisms responsible for enhancing the bendability of AA6016 through cladding using thermomechanical roll bonding.

8.2 Experimental Procedure

8.2.1 Materials and thermomechanical processing

The alloys used in the present study are 1 mm thick sheets of commercially produced AA6016, which is a heat treatable aluminum alloy used in automotive skins, and 1 mm thick sheets of AA6016X composite alloy, with a core alloy of AA6016 sandwiched between clad layers of AA8xxx series aluminum alloy, viz. alloy AA8079. The approximate thickness of each clad layer is 100 microns, which is 10 pct. of the total package thickness. The monolithic AA6016 and composite AA6016X alloys were both produced on industrial scale. At the beginning, rolling slabs of alloy AA6016 were DC-cast as large ingots with dimensions up to 600 mm thick, 2 m wide and 4 - 9 mm in length. In preparation for subsequent hot rolling, the cast ingot surfaces were scalped to remove surface blemishes and were preheated to a temperature between 500 °C and 570 °C, in a homogenization cycle which may last up to 24 h. The homogenized ingots were then transferred to the hot rolling line. During hot rolling, the composite AA6016X alloy was produced by cladding the AA6016 core alloy with a layer of a non-age hardenable low strength AA8079 alloy using thermo-mechanical roll-bonding. The two hot bands with a thickness of around 6 mm were coiled and allowed to cool before they were further cold rolled to their final gauge of approx. 1.0 mm. Both alloys were inter-annealed in order to improve surface quality by reducing the susceptibility to roping. Subsequently, the cold rolled 1 mm thick monolithic AA6016 and composite AA6016X sheets were solution heat treated by passing through a continuous annealing line with temperatures of around 550 °C where recrystallization occurs. The sheets were then quenched to keep the alloying elements in solid solution. Finally, the sheets were leveled and pre-aged for stabilization and improved age hardening response, before being delivered in T4 temper. Note that the final in-service T6 strength is achieved after the forming operations by artificial age hardening, which is typically achieved during the automotive paint bake cycles.

8.2.2 Mechanical behavior characterization

The tensile hardening behavior of the monolithic AA6016 and the composite AA6061X alloys was characterized by conducting quasi-static uniaxial tension tests. Standard ASTM-E8M tensile specimens were machined along the rolling direction (RD) and the testing was conducted at room temperature using a nominal strain rate of 5×10^{-4}/s. Each tensile test was performed at least three times to ensure repeatability. The bendability and fracture behaviors of both alloys were investigated using the wrap bend tests (ASTM-E290). A schematic of the wrap bend test is shown in Figure 8-1, where r is the radius of mandrel that the specimen is bent around, and t is the sheet thickness (i.e. 1.0 mm in the present study). The rectangular, 76 mm in length and 30 mm wide, wrap-bend specimens were cut along the RD from the as-received sheet materials using electrical discharge machining (EDM). During the wrap bend test, individual sheet specimens were bent around mandrels with increasingly severe (i.e. smaller) radii (from r = 0.8 mm down to r = 0.1 mm) until cracking was observable on the outer bent surface. Specimens were also bent using a 0.1mm radius mandrel to several different final bent angles to analyze the fracture behavior. The

bend axis was perpendicular to RD (i.e. parallel to transverse direction (TD) in Figure 8-1) and before performing the tests, the contact surfaces between the specimen, roller and mandrel were lubricated to minimize any frictional effects.

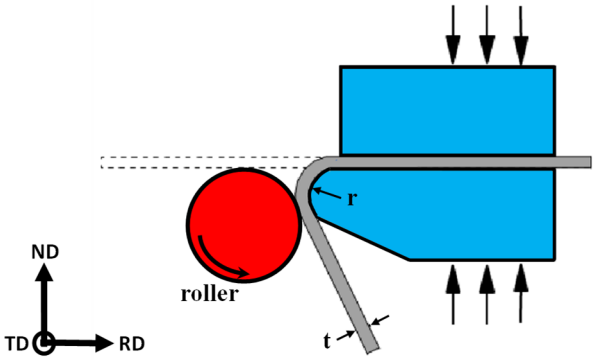

Figure 8-1: Schematic representation of a wrap-bend test.

8.2.3 Microstructure characterization

The microstructure of the as-received material and bent specimens was analyzed using a series of characterization techniques. The methods include electron backscatter diffraction (EBSD) measurements to characterize the initial through-thickness microstructure and its evolution during bending, optical and scanning electron microscopy (SEM) to study shear localization and damage development and 3D laser profilometry to analyze surface topography development during bending. The optical microscopy samples were prepared using standard metallography techniques and were etched using a hydrofluoric (HF) acid solution to reveal grain morphology and slip distribution through thickness of the bend. The samples were analyzed using a Zeiss light microscope equipped with a Nikon digital camera. After conventional polishing, the EBSD samples were further processed by a final ion-milling step to achieve the desired surface finish. All SEM imaging and EBSD measurements were performed using a field-emission Nova NanoSEM™ equipped with an EDAX® EBSD camera. A step size of 0.75 µm was used for EBSD measurements and the scan data was further analyzed using the TSL OIM™ software. The scan data was cleaned using single iteration of neighbour CI correlation to remove bad data points. The surface profile - roughness measurements were made using Keyence® VK-X 200 series 3D laser scanning microscope.

8.3 Results

8.3.1 Initial microstructure and tensile behavior

The microstructures of the monolithic AA6016 and the composite AA6016X materials are shown in Figure 8-2. The through-thickness EBSD texture measurements are shown along the two orthogonal RD-ND and TD-ND planes, with ND being the through-thickness direction. The presence of an approximate 100 µm clad layer is apparent on either side of the AA6016X rolled

sheet, as shown in Figure 8-2(g-h). It is observed that both alloys have nearly equiaxed grains, indicative of the occurrence of recrystallization during the continuous annealing step of thermomechanical processing. Figure 8-3(a) shows the grain boundary character distribution computed from the EBSD data. The results show slightly higher number fraction of low angle grain boundaries (<15˚) as compared to the high angle grain boundaries (>15˚). It is also observed that both the monolithic AA6016 and composite AA6016X alloys show nearly identical grain boundary character distribution. Furthermore, both alloys also show nearly identical Gaussian distribution of grain size, as shown in Figure 8-3(b). The average grain size of AA6016 and AA6016X is approx. 45.5 μm and 46.5 μm, respectively. However, the grain size closer to the edges (i.e. sheet surfaces) is smaller than that in the center (see Figure 8-2) and this difference is more apparent for the AA6016X alloy and will be discussed later. Figure 8-3(c) shows the area fraction of typical FCC texture components for both alloys. The texture of both alloys is very comparable and is dominated by the Cube orientation, accompanied by some scattering or rotations about Cube (i.e. rotated cube) followed by the rolling texture S component. Other texture components such as Copper, Brass and Goss are also present in comparatively lower fractions.

The microstructure of the composite AA6016X material is further analyzed by partitioning and separating the central core and outer clad layer regions. The grain size distribution comparison between the core and clad material is shown in Figure 8-3(d). It is apparent that grains within the clad layers are much smaller in size with an approximate average grain size of 30 μm whereas the average grain size within the core is 56 μm. This difference in grain size between the core and outer clad regions may well be associated with grain breakage within the soft AA8079 clad alloy due to the applied loading conditions during rolling of the sheet. Lastly, no significant difference in crystallographic texture components has been observed between the core and clad regions, as shown in Figure 8-3(e). Both regions show a dominant cube texture followed by S and rotated Cube texture components.

The tensile stress-strain response of AA6016 and AA6016X alloys is shown in Figure 8-3(f). The composite AA6016X alloy has a comparatively lower yield, UTS and somewhat greater tensile elongation, which reflects the presence of the 10-vol pct. AA8079 clad layer on each side of the central AA6016 core alloy. The 0.2% yield stress and UTS of AA6016 are 143 MPa and 266 MPa, respectively and that of AA6016X are 93 MPa and 189 MPa, respectively.

8.3.2 Bendability

Bendability of sheet metals is typically quantified by a normalized geometric parameter r_{min}/t, where r_{min} is the minimum radius of the mandrel that the specimen can be bent around without cracking, and t is the specimen thickness. A lower r_{min}/t value indicates better bendability. In the present study, different radii mandrels starting from 0.8 mm down to 0.1mm were used to assess the bendability of both alloys. The monolithic AA6016 alloy showed no apparent signs of cracking at the outer tensile surface up till a mandrel radius of 0.2 mm. However, cracking was apparent when a mandrel radius of 0.1 mm was used. As the thickness of the sheet specimen is 1.0 mm, the

geometric bendability parameter for AA6016 is $r_{min}/t \approx 0.2$. On the contrary, the cladded AA6016X alloy did not show any sings of cracking or fracture at the outer tensile surface, even using the most severe bend radius of 0.1 mm. Based on the current observations, AA6016X has unlimited bendability or in other words $r_{min}/t \approx 0$.

8.3.3 Bending and fracture behaviors

The bending and fracture behaviors of both alloys are further investigated by bending the sheet specimens to different bend angles using the smallest bend radius of 0.1 mm. Figure 8-4 shows the through thickness optical micrographs of AA6016 specimens bent to final bend angles of 120˚, 135˚ and 150˚, respectively. The distribution of second phase particles is apparent from the unetched micrographs, whereas the grain morphology and crack path are visible in the etched micrographs shown in Figure 8-4. At 120˚ bend angle, one can clearly see the presence of few micro-cracks originating from the outer tensile surface along with a central macro crack which has already propagated few hundred microns through thickness of the specimen (see Figure 8-4 (a-b)). Several macroscopic surface grooves (i.e. valleys) are also present along the outer tensile surface and are encircled in red in Figure 8-4. It is important to note that cracks appear to initiate from within those local grooves or valleys along the outer tensile region. Similar fracture behavior is observed for the specimen bent to a final bend angle of 135˚, as shown in Figure 8-4 (c-d). In this case, the crack has nearly propagated through half the thickness of the specimen and appears to stop near the central region in vicinity of the neutral axis of the bend. At an even larger bend angle of 150˚ (see Figure 8-4 (e-h)), the macro crack has almost propagated through the entire thickness of the sheet specimen. In some areas the crack path appears to follow a zig-zag pattern having sharp edges typical of intergranular fracture, whereas in others, a more planar – flat propagation path indicates transgranular fracture. Decohesion along several grain boundaries is also observed, especially along regions ahead of the crack tip as pointed by red arrows in Figure 8-4 (b-c). Based on the results shown in Figure 8-4, it is apparent that the crack path is different in each specimen and is governed by the local microstructure (i.e. crystallographic texture, particles distribution and grain boundary precipitation free zones) and the local stress field. However, the fracture mode is similar in all cases and is predominantly transgranular in nature with some areas exhibiting intergranular fracture.

Figure 8-5 shows the SEM image of the outer (convex) tensile surface of the 120˚ bend specimen. Macro cracks which are almost parallel to the bend axis and several hundred micrometers in length are apparent within the central region of the outer bend surface (see blue arrows in Figure 8-5(a)). These cracks seem to firstly initiate from the central region of the bend due to the constrained plane strain tension deformation and propagate towards the edges of the sheet. Furthermore, the polycrystalline structure of the material is apparent on the outer bend surface and relative sliding of grains with respect to each other results in height changes and grain boundary relief due to strain accommodation between grains. This relative sliding amongst grains has caused several surface grains to move outwards (i.e. out-of-plane) normal to the bend surface and has led to grain boundary decohesion (see encircled regions in Figure 8-5(b)) promoting intergranular failure. It is

further observed that during bending of AA6016 alloy, strain tends to localize within a set of parallel coarse slip bands within grains as pointed by green arrows in Figure 8-5(b). The orientation of the slip traces is different within neighboring grains and is influenced by the local crystallographic texture. In addition, several macroscopic surface ridges are also evident on the outer tensile region as pointed by yellow arrows in Figure 8-5(a-b). These ridges are a couple of hundred micrometers in length and are approximately parallel to the bend axis, accommodating slip transmission across multiple grains. Figure 8-5(c) shows the magnified view of the crack surface region encircled in Figure 8-5(a). It is noted that the surface of the crack consists of very fine dimples (as pointed by the red arrow) which are formed due to strain localization in vicinity of the grain boundaries. The shape of the dimples has also been somewhat smeared in direction of the principal strain axis due to the local tensile deformation. The heterogeneously nucleated grain boundary particles typically lead to the nucleation, growth and coalescence of these micro-voids, thereby assisting the fracture process.

Figure 8-6 shows the through thickness optical micrographs of the composite AA6016X sheet specimens bent to final bend angles of 150˚ and 180˚. It is observed that AA6016X alloy does not show any signs of failure even at the maximum possible bend angle of 180˚, confirming the previously reported results (in section 8.3.2) of unlimited bendability exhibited by the composite AA6016X alloy. The presence of clad layers, along the inner compressive and outer tensile regions, is not apparent from micrographs in Figure 8-6(a) and (b). In fact, the only indication of the interface is the microstructural change from the somewhat high density of fine constituent particles in the AA8079 clad alloy to the coarse microstructure in the AA6016 core alloy (see Figure 8-6(b)). However, the presence of clad layer is apparent after the specimen has been etched to reveal the grain morphology, as shown in Figure 8-6(c). It is observed that grains closer to the compressive bend region are elongated in the 'ND' direction causing thickening of the clad layer, whereas grains closer to the outer tensile surface are elongated along RD due to extremely large tensile strains, leading to significant thinning of the outer clad layer. After 180˚ bend angle, the clad layer on the compressive side has almost doubled from its initial thickness of approx. 100 μm, whereas the layer thickness along the outer tensile surface is approximately half (i.e. ≈ 0.55 μm in Figure 8-6(f)). Unlike the monolithic AA6016 alloy in Figure 8-4, the cladded AA6016X alloy shows lesser tendency towards the formation of surface undulations and grooves along the outer tensile surface even after 180˚ bend angle (see Figure 8-6(e)). This behavior is further evident from SEM micrographs of the outer tensile surface of the 180˚ bend specimen, shown in Figure 8-7. Apart from some regions showing signs of grain boundary relief (see red arrows Figure 8-7(a)) and some slip traces ((see green arrows Figure 8-7(b)), the SEM micrographs for the cladded AA6016X alloy are rather featureless when compared to the results for AA6016 alloy in Figure 8-5. In addition, no signs of cracking or failure are noticeable.

8.3.4 Surface topography after bending

Figure 8-8 shows the 3D laser scanning profilometry measurements of surface topography along the outer tensile surface of AA6016 and AA6016X after a bend angle of 135˚ and 150˚,

respectively. The presence of severe topographic features is evident for AA6016 after bending to 135˚ (see Figure 8-8(a)). The through thickness cross-sectional view of the very specimen is previously shown in Figure 8-4(c). In Figure 8-8(a), one can clearly see the presence of a through thickness macro crack across the entire width of the bent specimen and several macroscopic surface ridges that are aligned approximately parallel to the bend axis. It is noted that these surface ridges are linked with the formation of surface undulations and grooves when observed from the through thickness cross-section. On the contrary, the cladded AA6016X alloy show a comparatively smoother surface profile with very fine topographic features and signs of surface relief due to strain accommodation between grains (Figure 8-8(b)). The surface roughness results are further quantified using typical roughness parameters S_a, which represents the difference in height of each point compared to the arithmetical mean of the surface and S_q, which represents the standard deviation of surface heights within the definition area and the results are reported in Table 8-1. As expected, both surface roughness parameters increase with subsequent bending deformation and it is interesting to note that after the bend angle of 150˚, both S_a and S_q values are approx. 45 pct. higher for AA6016 as compared to AA6016X. Furthermore, even after the maximum possible bend angle of 180˚, the S_a value for AA6016X is approx. 7 pct. lower than the corresponding value for AA6016 at a significantly lower bend angle of 120˚. Thus, consistent with the bending and fracture results, the surface topographic behavior of both alloys is significantly different.

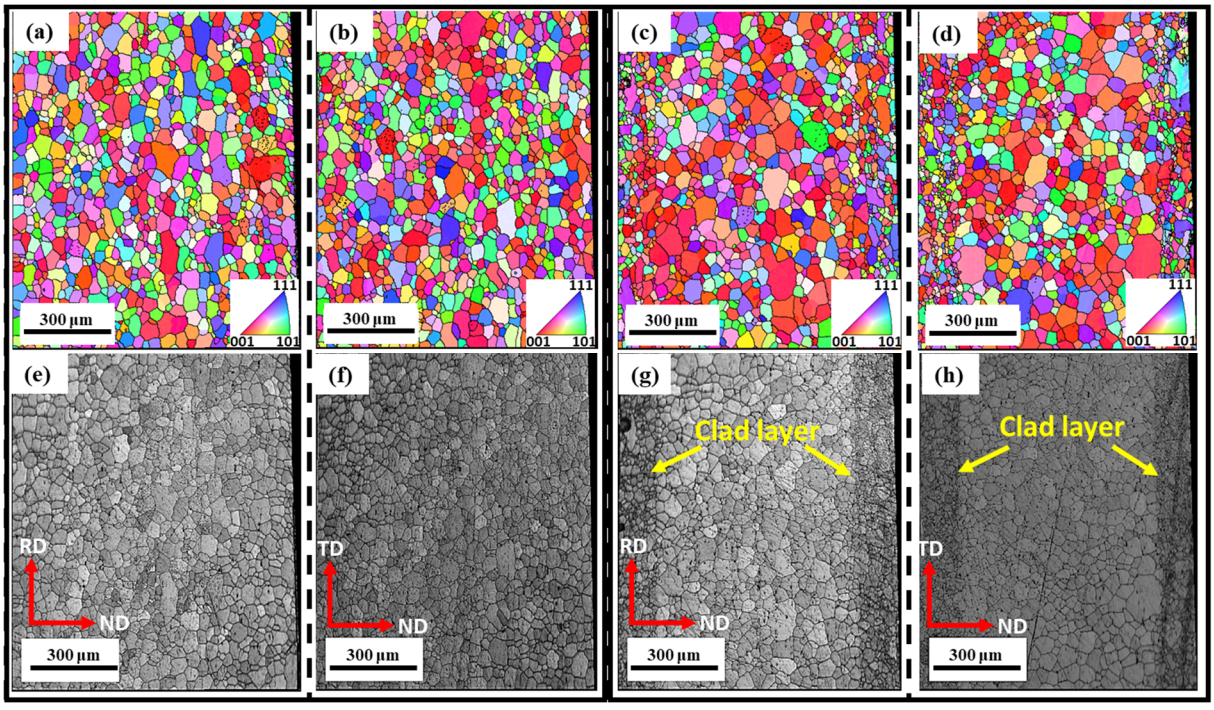

Figure 8-2: IPF and gray scale grain maps showing the through thickness microstructure for as-received monolithic AA6016 alloy along (a),(e) RD-ND plane (b),(f) TD-ND plane and for the composite AA6016X alloy along (c),(g) RD-ND plane (d),(h) TD-ND plane.

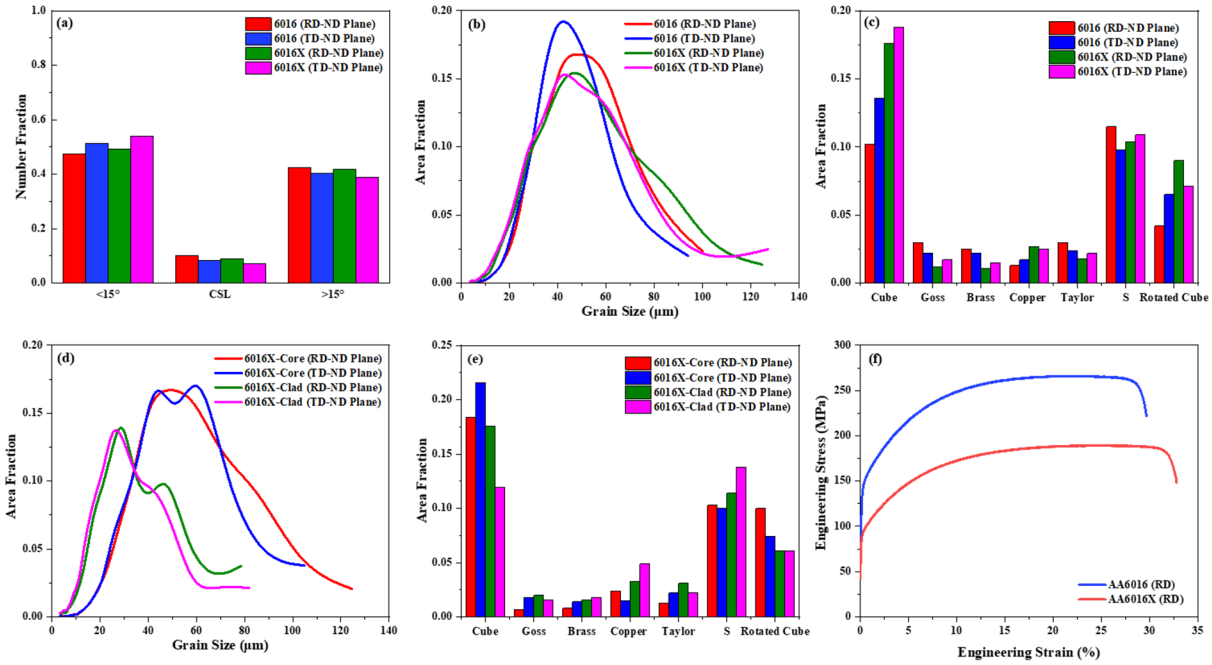

Figure 8-3: (a) Grain boundary character distribution, (b) grain size distribution, (c) area fraction of FCC texture components for AA6016 and AA6016X alloys. (d) Comparison of grain size distribution and (e) texture components for the centre core and clad layers of AA6016X alloy. (f) stress-strain behavior of AA6016 and AA6016X alloys.

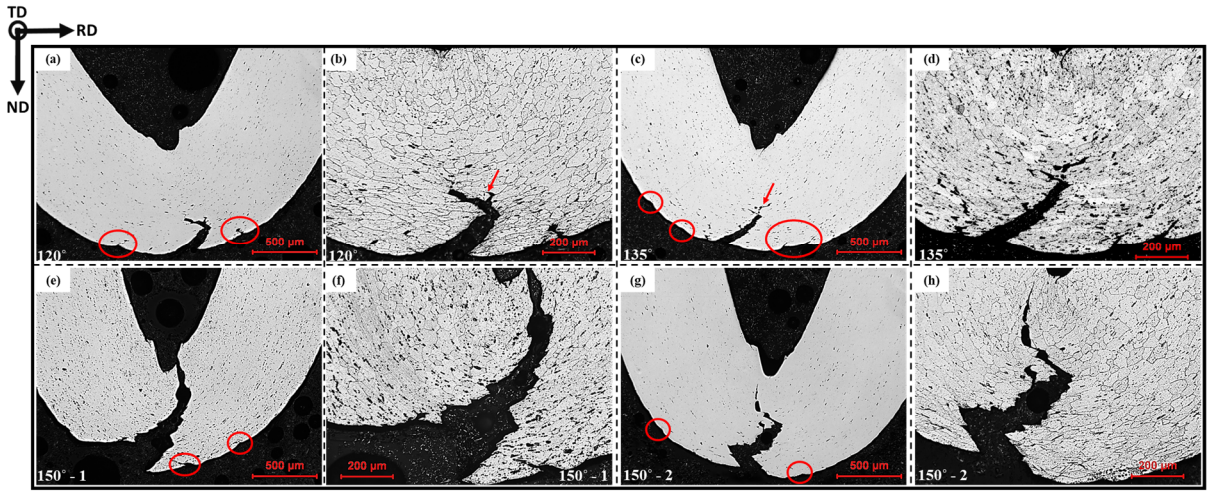

Figure 8-4: Through thickness optical micrographs of AA6016 sheet specimens bent to different final bend angles of (a)(b) 120˚, (c)(d) 135˚, (e)(f) 150˚ specimen -1 and (g)(h) 150˚ specimen - 2. An unetched and etched micrograph of each specimen is shown.

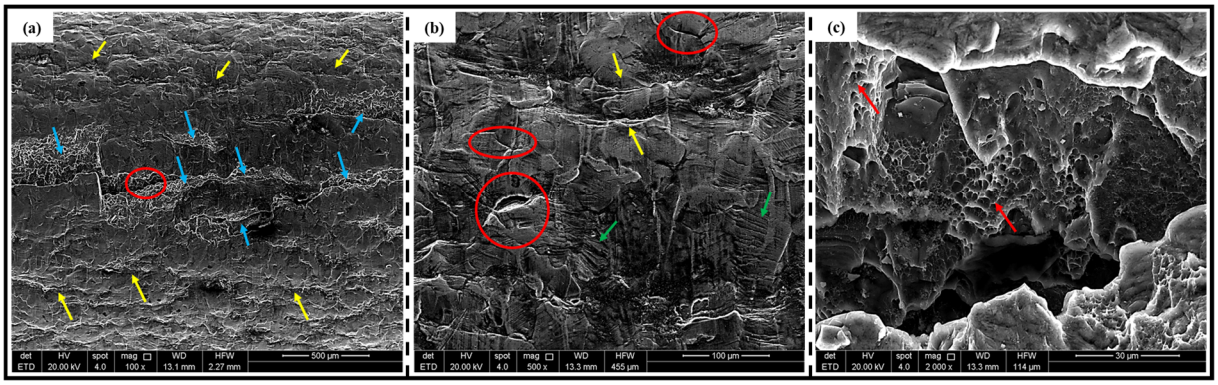

Figure 8-5: SEM micrographs of the outer tensile surface of AA6016 specimen bent to 120˚ (a) middle region of the bent specimen, (b) region closer to the edge, (c) magnified view of region encircled in red in micrograph (a).

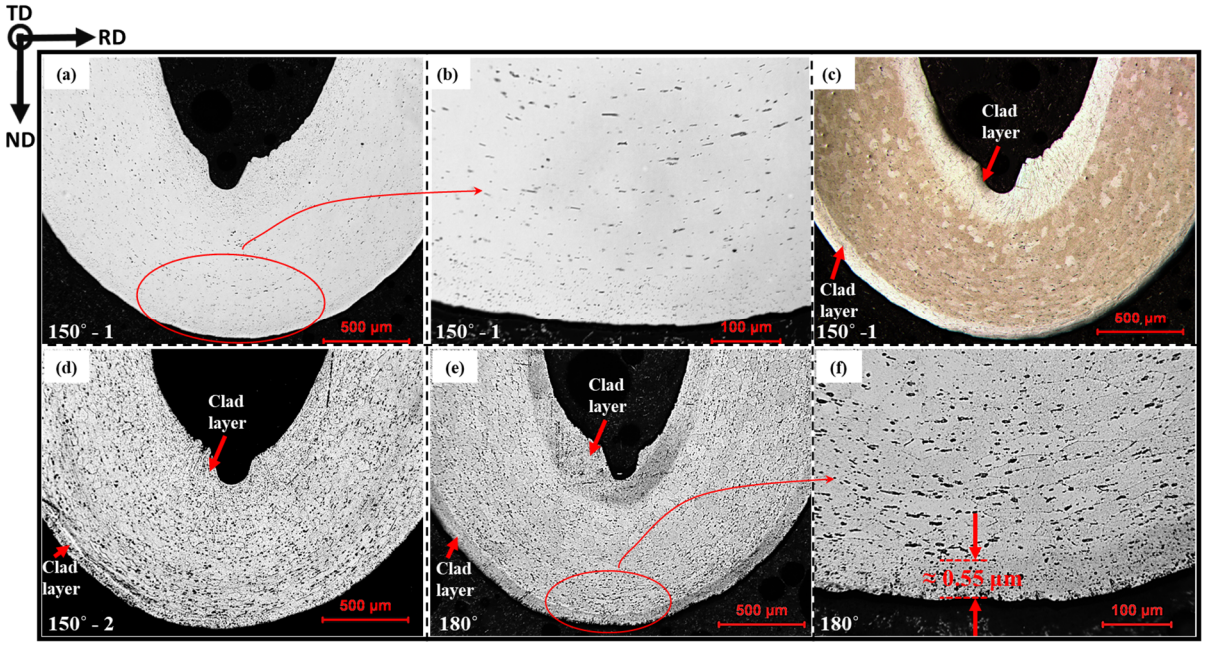

Figure 8-6: Through thickness optical micrographs of AA6016X sheet specimens bent to different final bend angles of (a)(b)(c) 150˚ specimen – 1, (d) 150˚ specimen - 2 and (e)(f) 180˚.

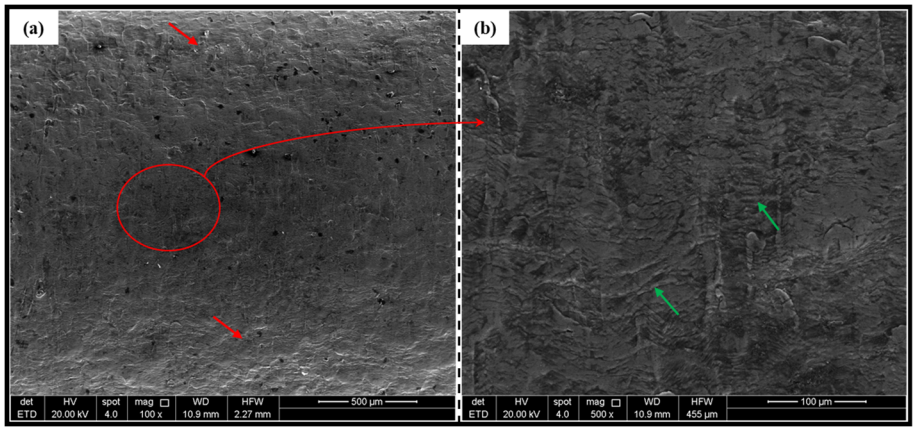

Figure 8-7: SEM micrographs of the outer tensile surface of AA6016X specimen bent to 180° (a) middle region of the bent specimen, (b) magnified view of region encircled in red in micrograph (a).

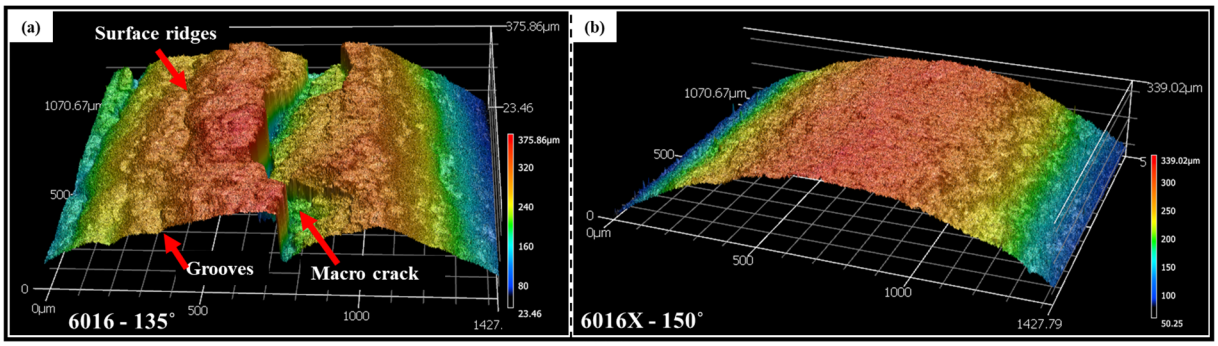

Figure 8-8: Surface topography development for (a) AA6016 at 135° bend angle and (b) AA6016X at 150° bend angle.

Table 8-1: Surface roughness measurements for AA6016 and AA6016X at different bend angles

Alloy	Bend Angle (°)	S_a (µm)	S_q (µm)
6016	120	3.73	4.82
6016	135	4.99	6.38
6016	150	5.79	7.41
6016X	150	2.95	3.92
6016X	180	3.48	4.71

8.4 Discussion

Based on the microstructure characterization results in Figure 8-3, both AA6016 and AA6016X alloys have a similar grain size distribution and starting texture. The alloys have a typical recrystallization texture, exhibited by most rolled aluminum alloys, which is characterized by the cube orientation with strong scattering about the RD towards the Goss orientation, together with intensities of the rolling texture S orientation, also referred to as R component in literature [234, 320–322]. Also, as expected, the cladded alloy AA6016X has a comparatively lower yield and UTS, together with somewhat greater elongation to failure, as shown in Figure 8-3(f). It is

interesting to note that the comparative difference between the yield and UTS values of AA6016 (i.e. 123 MPa) is much higher than that of AA6016X, which is 96 MPa. This behavior is reflective of the much higher hardening rate exhibited by the monolithic AA6016 alloy in comparison to AA6016X, and this higher hardening rate is also visually apparent from the initial slopes of the stress strain curves in Figure 8-3(f). These results show that the work hardening rate decreases with the introduction of the clad layer and further indicates that a significant proportion of the strain is being accommodated by the softer, lower work hardening rate AA8079 alloy.

8.4.1 Fracture of AA6016 alloy during bending

Aluminum alloys, more precisely the AA6xxx series age hardenable alloys, can fail by a variety of mechanisms depending on the alloy microstructure, strength and ductility. Bendability and fracture of these alloys is still not well understood, but recent publications have shown that their bendability is limited by surface cracking which is usually preceded by particle cracking, voiding and the development of surface undulations along the outer bend surface [44, 126, 219, 220, 313, 323, 324]. Based on the results presented in the previous section, it is suggested that fracture of the monolithic AA6016 alloy during bending is an outcome of several competing micro-mechanisms, which are discussed next.

8.4.1.1 Coarse slip distribution

Figure 8-9 provides a comprehensive view of several competing damage mechanisms involved in the fracture process of AA6016 alloy. The EBSD microstructure measurements are performed on the same bent specimens shown in Figure 8-4. It is apparent from the IPF maps (in Figure 8-9(a-b)) that crystallographic slip has led to a significant evolution of texture during bending and several coarse slip bands are also apparent as banded regions of different colors within the parent grains. The longitudinal growth of these bands is limited by the high angle grain boundaries and their specific orientation within grains is linked with the local crystallographic texture of the parent grain as shown in Figure 8-9(c). The lateral growth of these bands is inhibited by the formation of subgrain boundaries within the microstructure. These boundaries form a misorientation of 5˚ - 15˚ with respect to the parent grain as shown in Figure 8-10(a). It is observed that deformation tends to localize within these bands, promoting dislocation pileup against subgrain boundaries, as apparent from the geometrically necessary dislocation (GND) density map in Figure 8-10(b). The dislocation content within these bands is an order of magnitude higher than adjacent regions and it is suggested that with persistent deformation, these dislocations could move and interact with each other to form a deformation induced cellular dislocation microstructure comprising of cell walls with high dislocation content and cell interiors with a relatively low dislocation content, thereby giving rise to intragranular backstresses within the material which can further assist the fracture process [6, 7, 12, 264]. Several of these bands are impinging on the grain boundaries which can give rise to local stresses at the grain boundaries (due to dislocation pile-ups at the end of slip lines at the grain boundaries as shown in Figure 8-10(b)) causing grain boundary decohesion, as shown within the encircled region in Figure 8-9(c), and ultimately promoting intergranular failure.

8.4.1.2 Shear banding, development of surface undulations and crack initiation

Figure 8-9(d) shows the gray scale grain map after 150˚ bend angle. One can see a clear tendency towards gathering of multiple slip bands into transgranular mutually orthogonal shear bands, which are several hundred micrometers in length (see red arrows in Figure 8-9(d)). Several sets of such shear bands are emanating from the outer tensile edge and are propagating inwards through multiple grains. Similar shear banding behavior has been observed for the 120˚ bent specimen, where one can see multiple micro-cracks initiating and propagating along such shear bands. Furthermore, an area of intense shear banding is present in front of each crack tip as indicated by regions within the green arrows in Figure 8-9(c). This banded area tends to develop ahead of the crack tip due to the high local stresses and is characterized by very high dislocation content in the order of $10^{14}/m^2$ (see Figure 8-10(b)), which further accommodates crack propagation. The formation of such shear bands across multiple grains leads to planar crack propagation, thereby promoting transgranular fracture behavior.

Upon careful observation of the through thickness micrographs in Figure 8-4 and Figure 8-9, it is noted that these shear bands tend to initiate and propagate from local valleys along the outer tensile surface. Hence, the development of surface undulations - grooves during bending (see Figure 8-4) plays a significant role in controlling the bendability of the present alloy. This apparent grooving behavior in the through thickness micrographs is in fact the surface ridging behavior which is spread along the entire width of the bent specimen as shown in Figure 8-8 and is also linked with through thickness shear bands or sheared planes spreading across the entire width of the specimen. These intensely sheared planes make way for cracks that initiate along the outer tensile surface, to propagate both inwards and along the width of the specimen. Raabe et al. [232] in their work on rolled AA6022 and more recently Muhammad et al. [313] in their work on the development of surface roughness in an extruded AA6063 alloy, have shown that this apparent ridging phenomenon is promoted by the collective co-deformation of a large set of similarly oriented crystals assembled in layers or grain clusters, leading to a banded surface morphology and can be influenced by altering the through-thickness texture of the material. The formation of such surface undulations can also cause some of the adjacent surface grains to move perpendicular (i.e. out-of-plane) to the bend surface causing an intergranular crack to nucleate, as shown by encircled regions in Figure 8-5(b).

8.4.1.3 Influence of local texture on crack propagation

The EBSD data for 120˚, 135˚ and 150˚ bend specimens is partitioned to separate microstructural regions away and along crack path and the resulting texture data is plotted as <111> pole figures in Figure 8-11. The EBSD data has been rotated in an average manner to exclude the effects of rigid body rotations inherent to the bending process. It can be observed that the texture away from crack regions shows the presence of a dominant cube – near cube component, whereas the texture along the crack path indicates the presence of S component. This behavior is more apparent from the orientation distribution function (ODF) plots of constant φ_2 angle for the 150˚ bend specimen in Figure 8-12, plotted using orthotropic sample symmetry. The $\varphi_2 = 90°$ section in Figure

8-12(a) shows the presence of Cube (encircled in red) texture components within microstructure away from the crack regions. On the contrary, the $\varphi_2 = 65°$ section in Figure 8-12(b) clearly indicates the presence of near S component texture along the crack path. The results demonstrate that the Cube texture component show high resistance to shear banding and crack propagation and is therefore a high bendability component, whereas the S texture component is prone to shear banding and failure during bending.

8.4.1.4 Influence of local misorientations on decohesion along grain boundaries

In the previous sections, it has been shown that the development of surface undulations during bending and coarse slip distribution within neighboring grains can lead to decohesion along grain boundaries. The EBSD data is further analyzed to characterize grain boundary misorientations along such regions. Figure 8-13 (a),(b) show the IPF and optical micrographs of the analyzed grain boundary decohesion regions encircled in red along with the profile vectors corresponding to the 'point to origin' misorientation plot in Figure 8-13(c). The 'point to origin' misorientation plot clearly indicates that all the boundaries where decohesion has occurred, are highly misoriented with a minimum misorientation of greater than 40˚, whereas in some regions the misorientation along such boundaries is as high as 60˚. Such high misorientations are a direct consequence of coarse slip distributions and dislocation pileup along such boundaries as indicated by the high GND content in Figure 8-10(b). These high local misorientations have a direct effect on reducing the local cohesive strength of the grain boundaries, thereby assisting intergranular crack nucleation.

8.4.1.5 The overall sequence of microstructural events to fracture

The fracture sequence starts with signs of grain boundary relief and surface roughness due to strain accommodation between grains as well as formation of fine slip lines within grains (see Figure 8-5). As the deformation proceeds further, the surface roughness continues to increase, and strain tends to localize into intense slip bands within the grains, with occasional voids formation within the microstructure due to grain boundary decohesion, typically associated with the high local stresses caused by slip bands impingement at boundaries and presence of second phase particles. Further deformation leads to the development of surface undulations – grooving behavior along the outer tensile surface which further manifests itself as surface ridging. Multiple mutually orthogonal transgranular shear bands originate from surface low cusp points due to surface roughening and propagate inwards through multiple grains. This intense shear banding gives rise to a subsurface sheared zone which in many cases spans across the entire width of the specimen. Eventually, this intense shearing promotes the formation of surface cracks which propagate inwards in a transgranular manner through the sheared regions. In areas with high volume fraction of grain boundary particles, high grain boundary misorientations or intense slip band impingements along boundaries, intergranular crack propagation is favored due to the reduction in local cohesive strength of such boundaries. The crack continues to propagate in this mix intergranular - transgranular manner towards the neutral axis of the bend, until complete failure.

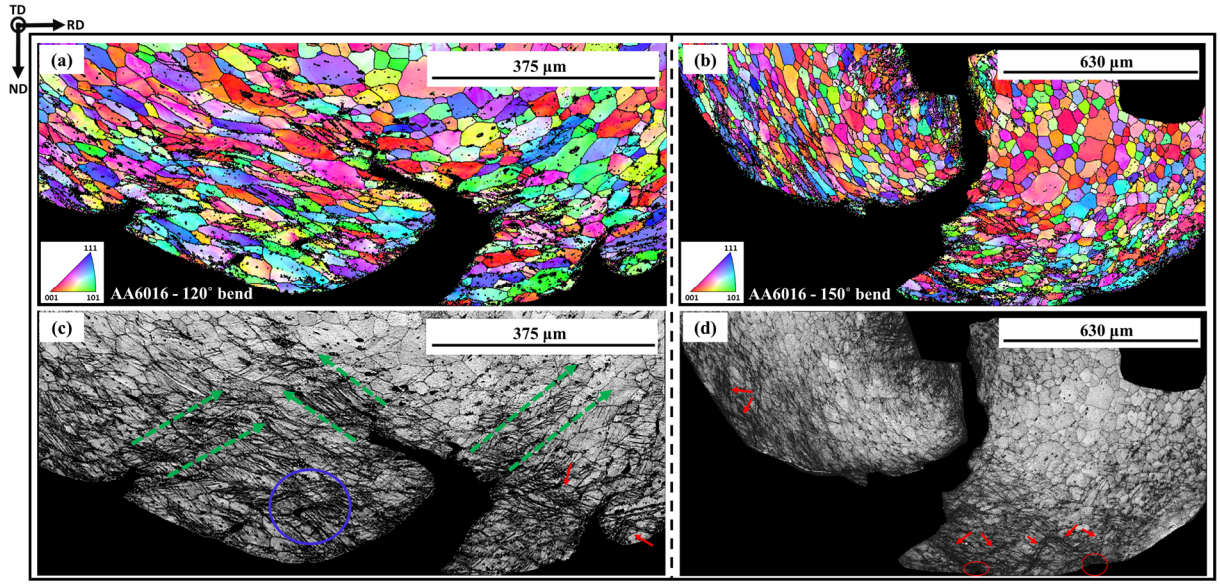

Figure 8-9: AA6016 EBSD measurements showing (a)(b) IPF maps and (c)(d) gray scale grain maps for specimens bent to 120˚ and 150˚ bend angles, respectively.

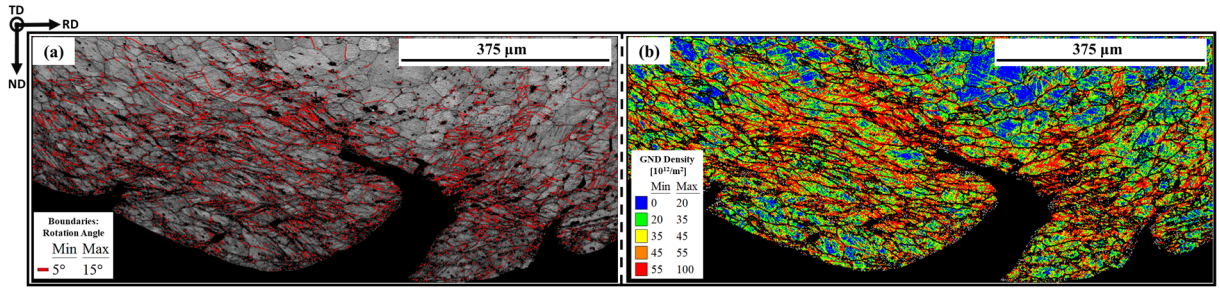

Figure 8-10: (a) Gray scale grain map showing misorientations across coarse slip bands and (b) GND density map for AA6016 specimen bent to 120˚.

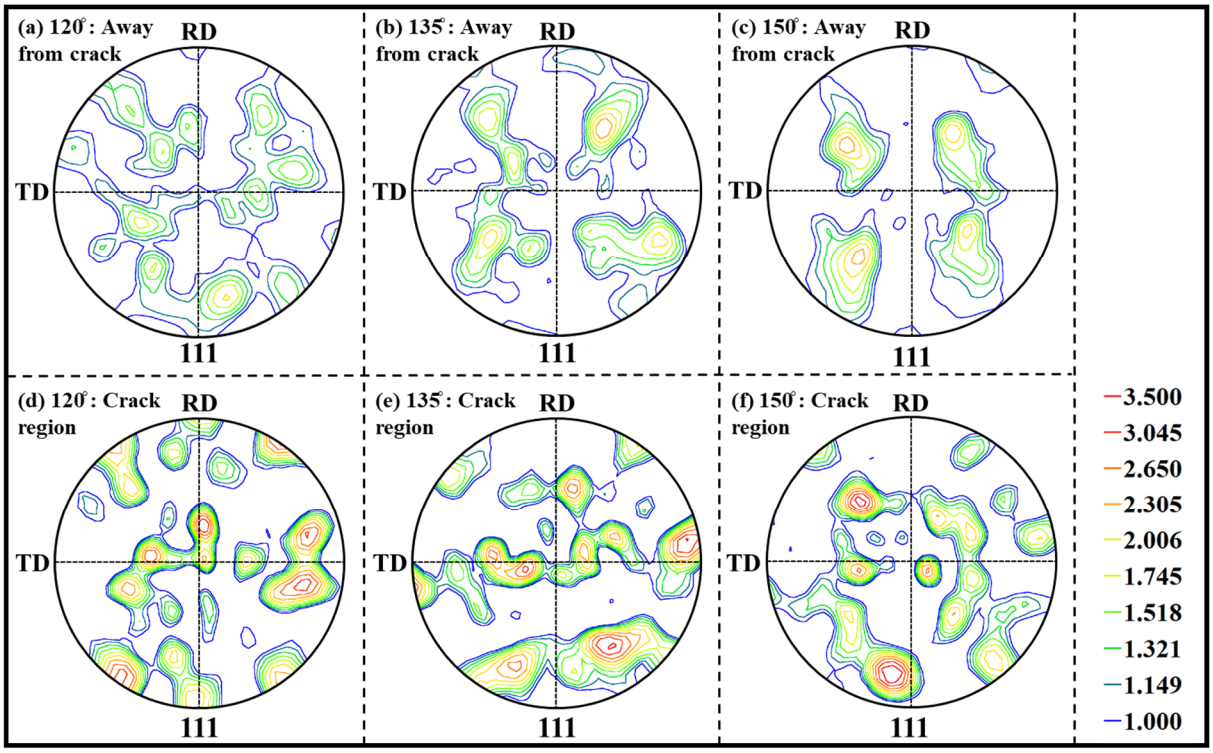

Figure 8-11: <111> pole figures after bending for (a) 120° (b) 135° and (c) 150° bend specimens for microstructure away from crack regions and (d) 120° (e) 135° and (f) 150° bend specimens for microstructure along crack region.

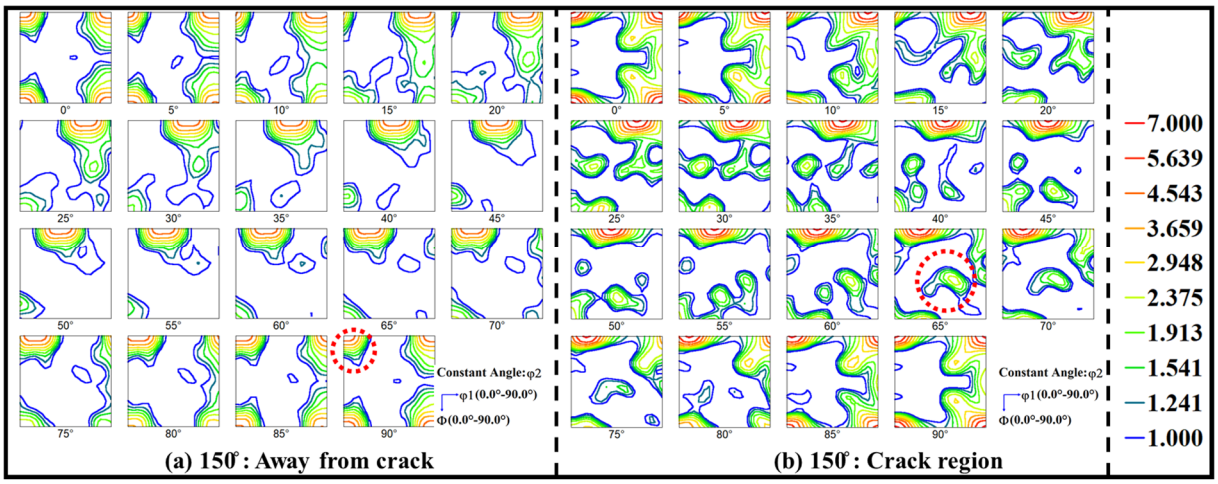

Figure 8-12: Orientation distribution function showing texture after bending for 150° bend specimen for microstructure (a) away from crack regions and (b) along crack region.

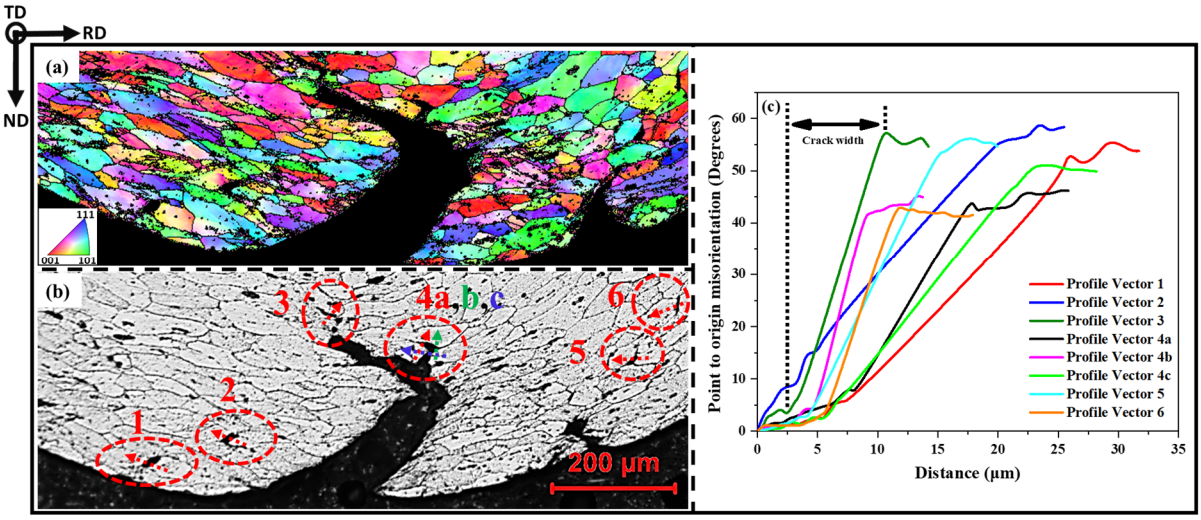

Figure 8-13: (a) IPF map, (b) optical micrograph of 120˚ bend specimen showing grain boundary decohesion regions encircled in red and (c) point to origin misorientation measured along profile vectors marked in micrograph (b).

8.4.2 Bending behavior of composite AA6016X alloy

As discussed in the previous section, bendability of monolithic AA6016 alloy is controlled by surface cracking, thereby the addition of a ductile clad layer at the surface has the potential of improving bendability. The introduction of ductile phase to improve bendability of rolled aluminum alloys has been studied by Lloyd and co-workers [222, 317, 325], where the authors have shown improved bendability behavior of AA6111 fusion cladded with AA3003 and AA2124 sheet fusion cladded with AA1200. A common learning from these studies is the ability of the ductile clad layer to blunt the propagating crack initiated in the core, causing a delay in failure of outer surface layers, thereby improving bendability. The author have shown that the outer cladded surface experiences significant surface roughening and due to strain compatibility, the clad layer experiences significant strain after the onset of subsurface voiding and crack formation [222]. Contrary to these results, the presented AA6016X alloy does not exhibit any subsurface cracking within the core even at the maximum bend angle of 180˚. The 180˚ bent specimens were also scanned using 3D X-ray Nano-CT scanner and the results showed no apparent subsurface cracking within the core alloy. Hence, the specimens were further analyzed to investigate the mechanisms responsible for this near unlimited bendability of the cladded AA6016X.

8.4.2.1 Bending deformation and microstructure development

The bending behavior of the cladded AA6016X alloy is significantly different as compared to the monolithic AA6016 alloy. The through thickness optical micrographs (in Figure 8-6) do not exhibit the grooving behavior along the outer tensile surface and the grains within the clad layer are severely deformed and elongated along the inner compression and outer tensile regions. Significant thinning of the clad layer with minor signs of surface rumpling are apparent along the outer tensile surface after 180˚ bend (see Figure 8-6(d)). Apart from minor surface relief, the SEM

and surface topography micrographs (in Figure 8-7 and Figure 8-8, respectively) do not show the presence of any significant microstructural features typically associated with heterogenous deformation and fracture. It is noted that although the initial microstructures (i.e. texture and grain size distribution) of both alloys are very comparable, yet there lies a significant difference in surface topography development and the overall deformation behavior of both alloys. Hence, it is suggested that this difference is associated with the way in which the ductile clad layer tends to accommodate the imposed plastic deformation, as discussed next.

8.4.2.2 Strain accommodation, grain subdivision and deformation induced boundaries

Figure 8-14(a) shows the IPF map of the cladded specimen bent to 150˚. The EBSD measurements were performed on the same specimen shown in Figure 8-6(c). It is apparent that grains within the clad layers along the inner compressive and outer tensile regions of the bend are significantly deformed. Furthermore, majority of the imposed bending deformation has been accommodated by the soft clad layers as apparent from the localized banded regions of high KAM values in Figure 8-14(b). Upon careful observation of the IPF map in Figure 8-14(a), it is noted that the intense deformation within clad layers has led to significant amount of local rotations within grains, promoting grain breakage. This grain breakage behavior is more prominent after bend angle of 180˚ as shown by the IPF map in Figure 8-14(c). Due to the extreme level of deformation after bending to 180˚ and associated difficulties of acquiring EBSD data at low SEM magnifications, the selected IPF regions, along the inner compressive and outer tensile regions in Figure 8-14(c), are rescanned at a much higher SEM resolution using a much finer step size of 200 nm. The corresponding IPF maps are shown in Figure 8-14(d)-(e). It is observed that the microstructure within the cladded regions consists of newly formed deformation induced boundaries along with the original grain boundaries. Figure 8-15 shows the grain boundary character distribution results for the monolithic and cladded alloys and it is observed that the monolithic AA6016 alloy shows a typical behavior of increasing number fraction of low angle (i.e. <15˚) boundaries with increasing bend angle and a corresponding decrease in the number fraction of high angle (i.e. >15˚) grain boundaries. Although to a much lesser extent, the cladded AA6016X alloy also shows a decrease in the number fraction of high angle grain boundaries after 150˚ bend angle. Contrary to previous observations, a sharp increase in the number fraction of high angle grain boundaries is observed after 180˚ deformation. Furthermore, the number of deformation-induced high angle boundaries is rather significant, and their formation is linked with the grain subdivision process which results in the formation of different texture components within original grains, as shown in Figure 8-14(d)-(e). The formation of such deformation induced high angle boundaries by cold working of 99.8% pure polycrystalline aluminum has been reported by Hughes and Hansen [203]. The authors, through their comprehensive experimental investigation, have linked the formation of such boundaries to two major mechanisms, viz. (i) the evolution of the underlying dislocation microstructure, which starts as a typical cell block structure consisting of dense dislocation walls, which eventually reorients itself into a lamellar structure at large strains, with dislocation boundaries having large misorientations; and (ii) the evolution of preferred texture during deformation which leads to the rotation of a subdivided grain to a different preferred end

crystallographic orientation [203]. The authors further reported that the creation of such high angle boundaries based on texture mechanisms will occur only after some finite level of deformation when the preferred end texture is well developed [203]. For the present AA6016X alloy, the sharp increase in the number fraction of high angle grain boundaries as the bend angle increases from 150˚ to 180˚, suggests that the evolved texture is near to the end orientation (characteristic for the observed strain path) after bending to 150˚ and subsequent deformation to 180˚ has assisted in the creation of high angle grain boundaries.

Strain accommodation during bending of AA6016X by grain subdivision process within the clad layers is contrary to what has been observed for the monolithic AA6016 alloy, where majority of deformation is accommodated heterogeneously by the formation of coarse slip bands and intense shear banding. It is suggested that the comparatively homogeneous accommodation of strain through the grain subdivision process within the clad layers of AA6016X, is responsible for the low surface roughness and absence of microstructural features such as coarse slip bands, surface undulations and ridging. The cladding layer also prevents or delays strain localization within the core by accommodating a major portion of the imposed bending deformation. Furthermore, the formation of high angle grain boundaries due to deformation induced grain subdivision leads to a reduction in grain size within the clad layers, which further improves the bendability of the cladded material as finer grain size is typically associated with better fracture resistance. Lastly, the results presented demonstrate that the bendability of the age-hardenable aluminum alloy AA6016 can be improved drastically by the presence of a ductile AA8079 clad layer.

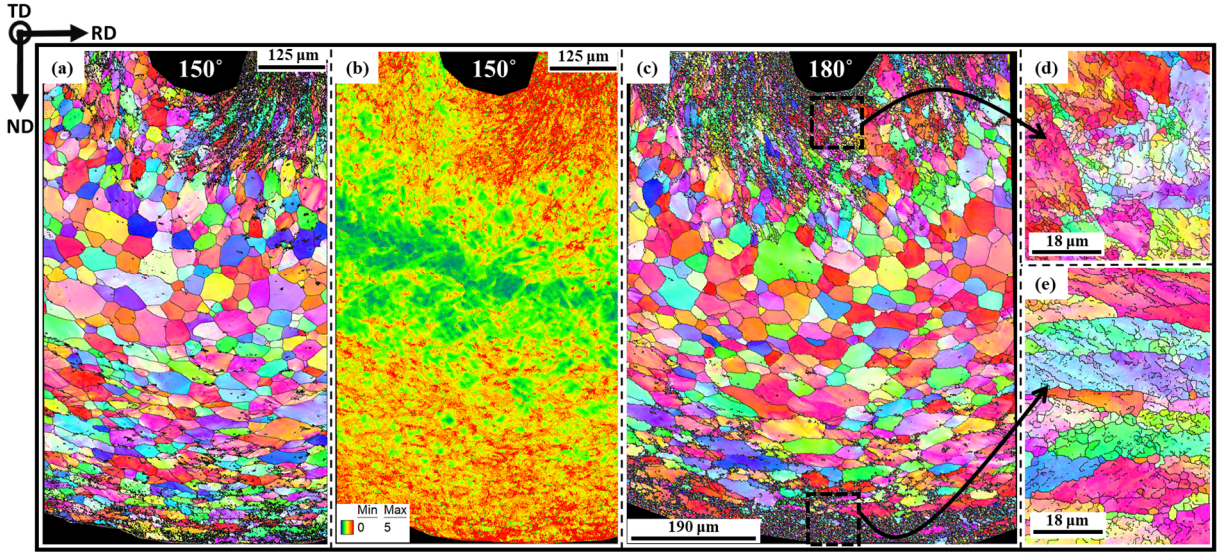

Figure 8-14: AA6016X EBSD measurements showing (a) IPF and (b) KAM map of specimen bent to 150˚ bend angle and (c)(d)(e) IPF maps of specimen bent to 180˚ bend angle.

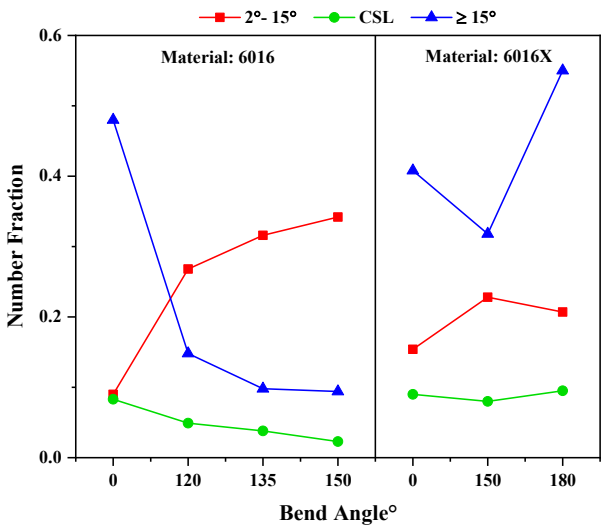

Figure 8-15: Grain boundary character distribution for monolithic 6016 and cladded 6016X alloys after deformation to different final bend angles.

8.5 Chapter Summary and Conclusions

In the present work, a thorough experimental study has been performed to characterize the plastic deformation and fracture behavior of 1 mm thick sheets of age hardenable aluminum alloys AA6016 and AA6016X subjected to bending deformation. AA6016X is a composite alloy, consisting of AA6016 core which is cladded with 100 µm thick layers of non-age hardenable AA8xxx series aluminum alloy (AA8079) on each side using thermomechanical roll bonding. A mix of mechanical and microstructural analysis techniques, including tensile tests, wrap bend tests, EBSD texture measurements, optical and scanning electron microscopy and 3D laser profilometry, are used to examine the bendability and fracture behavior of both alloys. A special emphasis is placed on examining the relationship between microstructure, the nature of plastic deformation, surface topography development, shear banding, grain boundary decohesion, macro-crack initiation and propagation during wrap bending. Some of the important observations and conclusions are summarized as follows.

- Both AA6016 and AA6016X alloys have a typical recrystallization texture, which is characterized by the Cube orientation, accompanied by some scattering or rotations about Cube, followed by the S or R texture component. Other FCC texture components such as Copper, Brass and Goss are present in comparatively much lower fractions. Both alloys also have a comparable grain size distribution with an average grain size of approx. 45 µm. The composite AA6016X alloy has a comparatively lower yield, UTS and slightly greater tensile elongation to failure.
- The bendability of both alloys is quantified using the geometric parameter r_{min}/t, and is measured to be $r_{min}/t \approx 0.2$ for AA6016 and $r_{min}/t \approx 0$ for AA6016X which indicates unlimited bendability of the latter.

- The bendability of monolithic AA6016 alloy is limited by the formation of severe surface undulations and surface cracking, which is associated with the heterogenous nature of slip concentrating into coarse slip bands (comprising of regions with very high dislocation content in the order of $10^{14}/m^2$, which are misoriented by 5˚ - 15˚ degrees with respect to the parent grain) and intense shear banding originating from surface low cusps in the form of mutually orthogonal transgranular bands. These bands propagate inwards through multiple grains and lead to the formation of subsurface sheared zones spanning across the width of the bent specimens.
- It is concluded that the fracture behavior of AA6016 is dominantly transgranular in nature with micro-cracks originating from low cusp regions along the outer tensile surface and propagating along the intensely sheared planes within shear bands. It is further concluded that grains with S texture component are prone to shear banding and failure during bending and the contrary is true for Cube oriented grains.
- It is further shown that regions where grain boundary decohesion occurs are highly misoriented with misorientations ranging from 40˚ up to as high as 60˚. It is therefore concluded that intergranular micro-void nucleation and crack propagation is favored in areas with high grain boundary misorientations and intense slip band impingements along boundaries, perhaps due to the reduction in local cohesive strength of such boundaries.
- The cladded AA6016X alloy shows no signs of fracture even after a maximum bend angle of 180˚. Apart form minor surface relief, the cladded alloy does not show the presence of any significant microstructural features (such as coarse slip distributions, shear banding and surface ridging behavior), typically associated with heterogenous deformation.
- It is concluded that the significant bending strains in AA6016X are accommodated homogeneously through a grain subdivision process within the clad layers, which leads to the formation of deformation induced high angle boundaries and different texture components within original grains. It is this homogeneous accommodation of strain within the clad layers, which is responsible for the low surface roughness and extremely high bendability of the alloy.
- In conclusion, it is shown that the bendability of an AA6xxx series precipitation hardened aluminum alloy can be improved drastically by cladding it with a non-age hardenable AA8xxx series aluminum alloy through a properly conducted thermomechanical roll bonding process.

Chapter 9: Multiscale Modeling of Strain localization, Shear Banding and Fracture

In this chapter, a detailed crystal plasticity finite element based numerical study, which couples the multiscale modeling framework and the developed hardening and fracture models, is conducted to study the sequence of microstructural events leading to final fracture of AA6016 during bending. A special emphasis is put on investigating the correlations between local crystallographic texture, shear band development, micro-crack initiation and propagation during wrap bending of monolithic AA6016 and cladded AA606X aluminum alloys.

The chapter presents an accepted manuscript of an article published in Materials Science & Engineering A journal.

Materials Science & Engineering A 754 (2019): 161-177. Doi: https://doi.org/10.1016/j.msea.2019.03.050

Bendability Enhancement of an Age-Hardenable Aluminum alloy: Part II – Multiscale Numerical Modeling of Shear Banding and Fracture

Materials Science & Engineering A 754 (2019): 161-177

Waqas Muhammad[1,3], Abhijit P. Brahme[1], Usman Ali[1], Jürgen Hirsch[2], Olaf Engler[2], Holger Aretz[2], Jidong Kang[3], Raja K. Mishra[4], Kaan Inal[1]

[1] Department of Mechanical and Mechatronics Engineering, University of Waterloo, Waterloo, N2L 3G1, Canada

[2] Hydro Aluminium Rolled Products GmbH, Research and Development Bonn, D-53014 Bonn, Germany

[3] CanmetMATERIALS, 183 Longwood Road South, Hamilton, ON L8P 0A5, Canada

[4] General Motors Research & Development Center, Warren, MI 48090, USA

Overview

In this study, the sequence of microstructural events leading to failure and the relationship between crystallographic texture, shear band development, micro-crack initiation and propagation during wrap-bending of monolithic AA6016 and composite AA6016X sheet alloys are studied using crystal plasticity based finite element methods (CPFEM). The numerically predicted results for texture evolution, shear bands development and fracture behavior after wrap bending show good agreement to the corresponding experimental observations. It is shown that failure during bending of AA6016 is controlled by the development of intense shear bands that emanate from surface low cusps along the outer tensile edge and provide a minimum energy path for micro-cracks to propagate, promoting a predominant transgranular failure. Upon intersection with another shear band, the advancing crack tip alternate from a less critical localization condition to a more critical one, as it requires lesser energy for the creation of new fracture surfaces while sustaining the imposed plastic deformation. Grains with Cube or near Cube texture are rather resistant to shear banding and crack propagation whereas the contrary is true for grains with near S and near Goss orientations. It is also shown that the ductile clad layers within the composite AA6016X alloy act as an efficient barrier against the development and propagation of shear bands within the less ductile inner core, thereby significantly enhancing the bendability of the alloy. Through a systematic study, it is further shown that the bendability of AA6016 alloy can be improved significantly through proper engineering of the through thickness microstructure.

Keywords: Clad aluminum alloy; Bending test; Crystal Plasticity; Shear banding; Fracture; Crack propagation

9.1 Introduction

Age-hardenable aluminum alloys are increasingly used in automotive applications due to their combination of low density and higher final strength achieved after the automotive paint-bake cycle [42, 206, 326–331]. However, their widespread use in outer body panels and structural

components is still limited due to their lower ductility and bendability as compared to steels. Automotive sheets and profiles are usually formed into final components such as body panels or bumper beams using several cold deformation processes. One such process, hemming around the periphery is the primary practice employed by automobile manufacturers to join the inner and outer body panels [257, 332]. Furthermore, bending of structural components such as the front rails, rockers, pillars, etc. is of special importance for optimal crash energy absorption [313, 333]. Hence, improvements in bendability of age-hardenable aluminum alloys is of primary interest to further promote their across-the-board applicability within vehicles.

Bendability of age-hardenable aluminum alloys, in particular the Al-Mg-Si (AA6xxx) alloys, is an area of active research and studies have shown that bendability of these alloys is limited by the formation of severe topographical features and the accompanying cracking along the outer tensile surface [219–221, 252, 255, 274, 334]. Several studies have related failure in these alloys with intense strain localization which is followed by the development of gradually growing surface undulations and ridging behavior across the outer bent surface [223, 225–227, 232, 251, 335]. It is shown that micro-cracks typically initiate along areas of local strain concentrations along the outer tensile edge, which generally coincide with locations of high surface roughness [313]. Several authors have also associated damage with the development of macroscopic shear bands during bending [228, 230, 247, 323, 336]. Apart from the above-mentioned studies, which primarily focus on understanding the development of damage mechanisms during bending, few researchers have also studied the potential of improving the bendability of age-hardenable aluminum alloys by cladding using a low strength and high ductility aluminum alloy. Jin et al. [325] investigated the bending behavior of AA2124 sheets cladded with AA1200, and the authors reported significant improvement in bendability of the developed composite alloy. Lloyd et al. [317] and Jin and Lloyd [319] studied the bendability of AA6111 sheets cladded with thin layers of AA3003, produced using direct chill casting. The authors have shown that the ductile clad layer delays the onset of micro-cracking along the outer tensile surface, thereby improving bendability.

Computational techniques such as finite element (FE) modeling have been employed by many researchers to study the strain localization phenomenon in bending. Triantafyllidis et al. [228] studied the development of shear bands during pure bending of a plate with an initial periodic imperfection using the J2 corner theory. The authors reported that the initial imperfection leads to the development of surface undulations on both the compressive and tensile sides of the plate, promoting strain localization and shear banding. Becker [246] studied shear localization during pure bending of a polycrystalline sheet using a Taylor-type polycrystal model. Dao and Li [219] studied strain localization during pure bending using a crystal-plasticity-based computational micromechanics model. The authors suggested that constituent particles near the outer tensile surface can significantly influence strain localization and surface roughening behavior. The authors further reported that crystallographic textures with high volume fractions of rolling texture components exhibit inferior surface roughening behavior as compared to random texture. Lievers et al. [335] analyzed bendability of AA6111 automotive sheets with varying Fe contents using

Gurson–Tvergaard–Needleman (GTN) model with isotropic and kinematic hardening effects. Kuroda and Tvergaard [230] studied shear band development by simulating pure bending using a plasticity model combined with a non-associative flow rule. In another study [336], the very authors studied the effects of individual FCC texture components on shear band formation by performing plane strain pure bending simulations and reported that Cube texture is very advantageous for preventing shear band development. More recently, Muhammad et al. [313] studied strain localization and development of surface roughness during bending of extruded AA6063 using crystal plasticity based finite element methods (CPFEM).

Majority of the computational studies on strain localization and shear band development during bending utilize conventional phenomenological plasticity based constitutive models. However, the experimentally observed strain localization and shear banding behavior are microstructural driven phenomena. Hence, information of local microstructure such as grain morphology and crystallographic texture are important factors for consideration. For this reason, a crystal plasticity based finite element theory is used in the present work. Furthermore, in majority of bending studies to date, the modeling domain consists of a unit cell with pure bending boundary conditions [219, 228, 230, 246, 247, 249, 251, 336]. Pure bending assumes that the material in all areas of the bend experiences the same bending deformation. This is contrary to actual bending operations which are rather complex, and the pure bending condition is rarely achieved in practice due to surface contacts between tooling and the sheet part being bent [248, 313]. Lastly, studies on micro-cracks and failure during bending are even scarcer and are primarily focused on understanding the effects of particle distribution on failure using phenomenological plasticity [222, 248].

In a companion paper, hereafter referred to as Part I [337], a comprehensive experimental investigation is conducted to study the fracture behavior of an age-hardenable aluminum alloy AA6016 during wrap-bending and it is shown that its bendability can be improved significantly by cladding it with a lower strength and higher ductility aluminum alloy AA8079. Correlations between microstructure, texture evolution, surface topography development, shear banding, micro-crack initiation and propagation during wrap bending are established. However, the sequence of such damage events leading to final failure and their relationship with the local crystallographic texture are not well understood, as their evolutions during bending deformation are difficult to be monitored experimentally. Using a multiscale computational approach, the goal of this paper is to provide complementary information to support the interpretation of our experimental observations, given in Part I, and to study the sequence of damage events promoting failure and further explain the relationship between crystallographic texture, shear band development, micro-crack initiation and propagation during bending. The manuscript also presents CPFEM based systematic studies aimed at exploring bendability enhancement of AA6016 rolled sheets through texture engineering and to further understand the role of cladding in improving bendability.

9.2 Experimental characterization and simulation methodology

9.2.1 Experimental procedures

1 mm thick sheets of commercially produced heat treatable AA6016 and AA6016X aluminum alloys were used in the current study. AA6016X is a composite alloy consisting of AA6016 core sandwiched between clad layers of AA8079. Each clad layer is approx. 100 microns thick. Quasi-static, room temperature, uniaxial tensile tests were performed to characterize the hardening behavior of the monolithic AA6016 and the composite AA6016X alloys along the rolling direction (RD) using standard ASTM-E8M specimens. Wrap bending tests (ASTM-E290) were also performed to characterize the bending and fracture behavior of both alloys. Figure 9-1(a) shows the schematic of the wrap bend test, where r is the radius of mandrel that the specimen is bent across, t is the sheet thickness and the bend axis is perpendicular to RD. Apart from wrap-bend tests which are rather qualitative in nature, a series of V-bend tests (VDA 238-100), with bend axis perpendicular to RD, were also performed to obtain the load-displacement response and failure strains along the outer tensile surface, using digital image correlation (DIC) strain measurements. The experimental setup for V-bend tests and DIC data analysis has been discussed in details by Cheong et al. [338]. For the purpose of present study, results from V-bend tests were only used to obtain the approximate local failure strains at fracture initiation, to be used in CPFEM modeling.

Apart from mechanical testing, the bent specimens were also sectioned at the mid-plane and mounted using the through-thickness RD-ND plane, with 'ND' being the through-thickness direction. The specimens were prepared for optical microscopy to reveal grain morphology, slip distribution, crack initiation and propagation through thickness of the bend. Electron backscatter diffraction (EBSD) texture measurements were also performed to characterize the initial microstructure of the as-received material and its evolution after wrap-bending deformation. EBSD measurements were made on the RD-ND plane. Further details on the experimental procedure are provided in Part I.

9.2.2 Microstructure and mechanical properties

The through thickness microstructure of AA6016 and AA6016X alloys are shown in Figure 9-2(a-d) as inverse pole figure (IPF) maps and gray scale grain maps. Both alloys have an equiaxed grain morphology and the existence of an approximate 100 microns clad layer of AA8079 is apparent on both sides of the AA6016X rolled sheet, as shown in Figure 9-2(d). The <111> pole figures in Figure 9-2(e-f) indicate that the texture of both alloys is predominantly Cube texture followed by a comparatively weaker S texture. These observations are further supported by typical FCC texture components analysis (in Figure 9-2(g)), where a comparatively higher area fractions of Cube, rotated Cube and S components are noted for both alloys. The tensile true-stress vs. true-strain curves of both alloys are shown in Figure 9-2(h). As expected, the composite AA6016X alloy has lower yield and ultimate tensile strength as compared to AA6016, due to the presence of much softer clad layers of AA8079.

Figure 9-3(a) shows the V-bend test output in terms of bending load versus bend angle for both AA6016 and AA6016X alloys. Each test was conducted at least four times to ensure repeatability and accuracy of the experimental data. It is apparent that for a given bend angle, the bending loads are significantly higher for the monolithic AA6016 alloy as compared to the composite AA6016X alloy. For AA6016, the load versus bend angle results show an initial elastic region, followed by a second region which shows an almost linear increase in load with increasing bend angle until a maximum bending load is achieved. Thereafter, there is a rapid decrease in load, which is usually associated with crack initiation and failure [221]. Based on this load drop, it is estimated that crack initiation for AA6016 started around an approximate bend angle of 105°. On the contrary, AA6016X shows a comparatively gradual increase in load with increasing bend angle and more importantly, the bending load kept increasing up till the maximum bend angle achievable (i.e. ~ 150°) during V-bend test. These observations are consistent with the wrap bending results reported in Part I, where it has been shown that AA6016X can be wrap-bend to 180° without failure. Figure 9-3(b) shows the 3D DIC contour map of effective strain distribution along the outer tensile surface of the bend at the initiation of failure (i.e. load drop) for specimen 'AA6016 - 1'. As expected, the bending strains are maximum across the apex of the bend and upon quantitative analysis of DIC data (as outlined in [338]) across all four specimens of AA6016, the effective strain at fracture initiation is approximated to be 0.51.

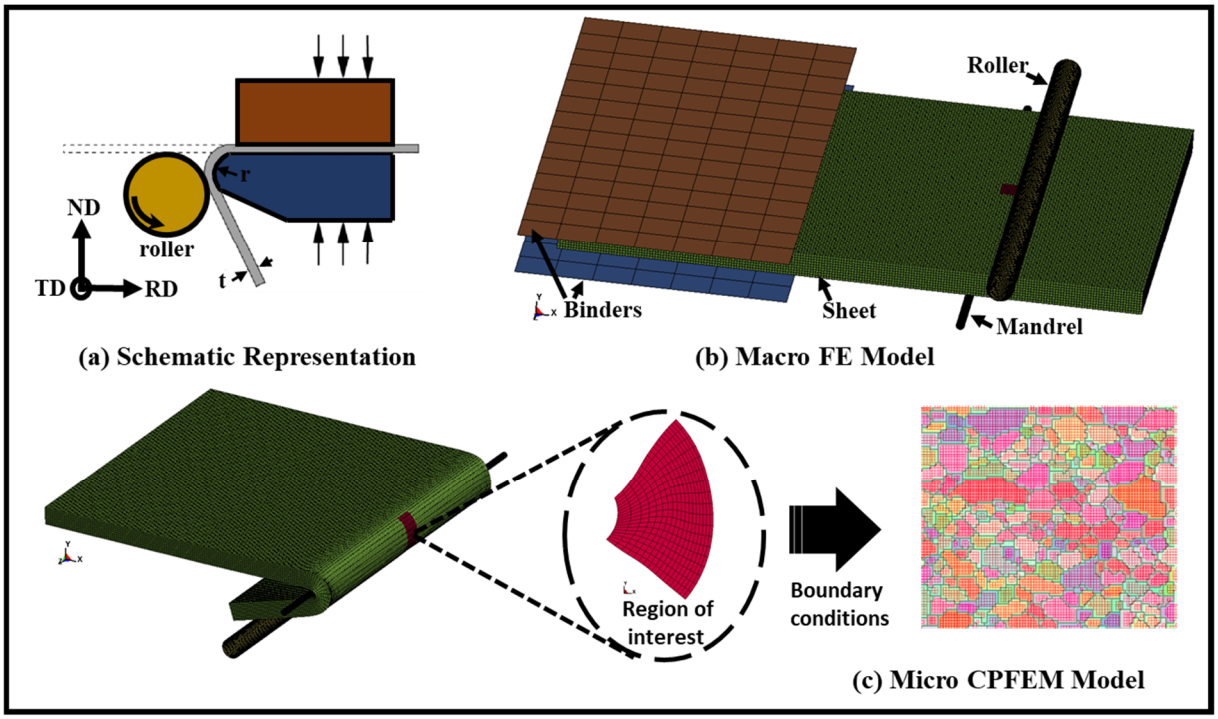

Figure 9-1: (a) Schematic representation of the wrap bend test and (b), (c) multiscale FE modeling approach

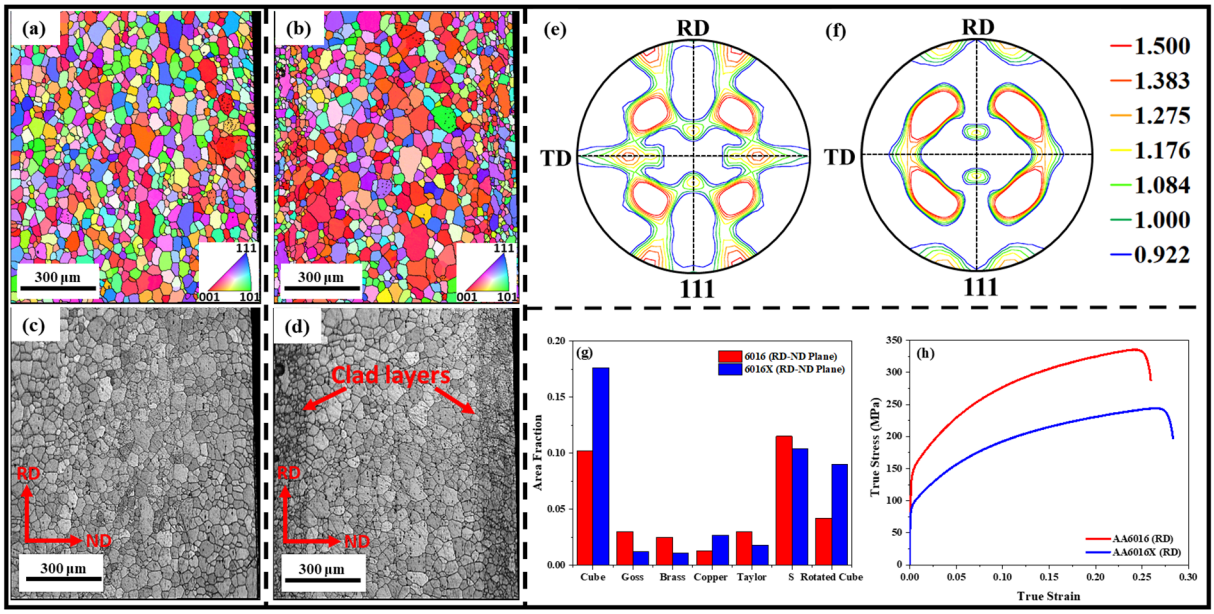

Figure 9-2: (a), (b) IPF maps, (c), (d) gray scale grain maps and (e), (f) <111> pole figures showing the microstructure for as-received monolithic AA6016 and composite AA6016X alloys, respectively. (g) area fraction of typical FCC texture components and (h) true stress - true strain behavior of AA6016 and AA6016X alloys.

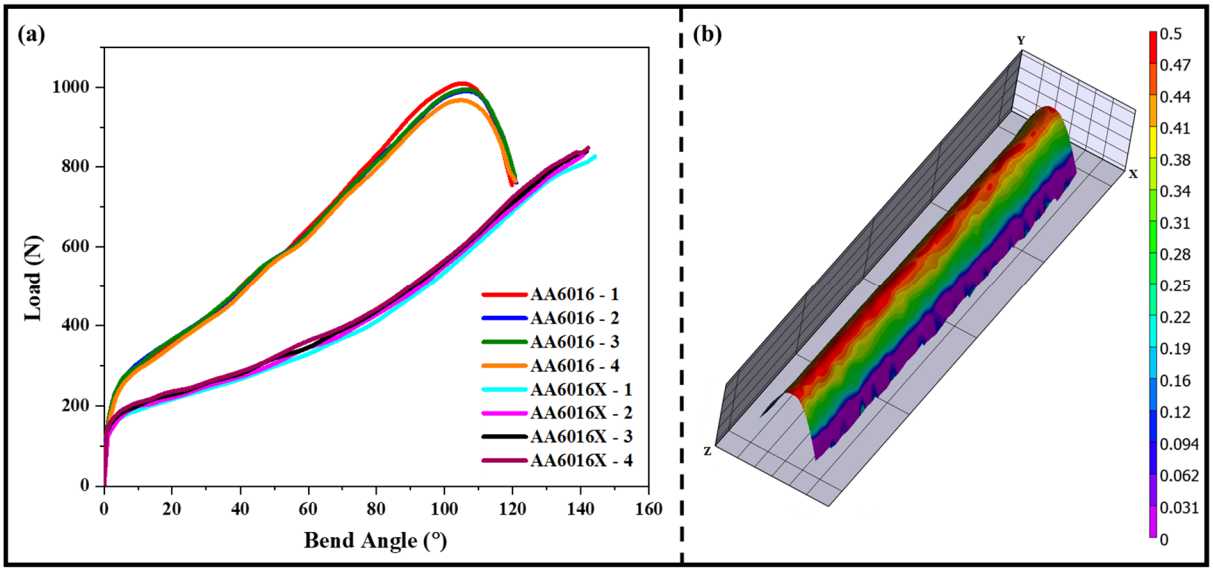

Figure 9-3: (a) Load vs. bend angle during V-bend test of AA6016 and AA6016X alloys and (b) 3D DIC contour map of effective strain at failure for AA6016.

9.2.3 Modeling approach

The general framework of modeling the wrap-bending process is similar to the multiscale approach proposed by Muhammad et al. [313] and is shown schematically in Figure 9-1(b-c). In this

approach, a full scale – specimen sized, macro level wrap bending simulation (see Figure 9-1(b)) is performed using conventional phenomenological plasticity and the displacement history of the region of interest is extracted and applied to a CPFEM based micro-model Figure 9-1(c), which accounts for the microstructure and slip system level micromechanics. All simulations are performed using a commercially available finite element package LS-Dyna® and a rate-dependent crystal plasticity constitutive framework is incorporated as a user defined material subroutine (UMAT) in LS-DYNA/Explicit. The details of the constitutive formulation are outlined elsewhere [196, 199, 209, 210]. However, for completeness, a very brief description of the model is given next.

9.2.3.1 Constitutive framework

Based on the polycrystal plasticity framework proposed by Asaro and Needleman [193], the total deformation of a crystallite is a consequence of crystallographic slip due to dislocation motion on the active slip systems and elastic lattice distortion. Accordingly, the deformation gradient **F** is divided into an elastic and a plastic part as follows

$$\mathbf{F} = \mathbf{F}^{*}\mathbf{F}^{\mathbf{p}} \tag{9-1}$$

Where $\mathbf{F}^{*}$represents elastic distortion and rigid body rotation of the crystal lattice and $\mathbf{F}^{\mathbf{p}}$ represents plastic deformation on crystallographic slip systems. The rate sensitive constitutive behavior of the crystallite is governed by the following relationship

$$\overset{\nabla}{\boldsymbol{\sigma}} = \boldsymbol{E}:\boldsymbol{D} - \dot{\boldsymbol{\sigma}}^{\mathbf{0}} - \boldsymbol{\sigma}\, tr\boldsymbol{D} \tag{9-2}$$

where $\overset{\nabla}{\boldsymbol{\sigma}}$ denotes the Jaumann rate of Cauchy stress, $\boldsymbol{E}$ is the elastic moduli tensor, $\boldsymbol{D}$ is the strain rate tensor, and $\dot{\boldsymbol{\sigma}}^{\mathbf{0}}$ is a visco-plastic type stress rate that depends on the slip rates of the slip systems. The slip rate $\dot{\gamma}_{(\alpha)}$ for the α_{th} slip system is calculated as follows

$$\dot{\gamma}_{(\alpha)} = \dot{\gamma}_0\, sign\, \tau_{(\alpha)} \left|\frac{\tau_{(\alpha)}}{g_{(\alpha)}}\right|^{\frac{1}{m}} \tag{9-3}$$

where $\dot{\gamma}_0$ is a reference shear rate, $\tau_{(\alpha)}$ is the resolved shear stress on slip system α, m is the strain rate sensitivity index and $g_{(\alpha)}$ represents slip system hardening. The slip level hardening model proposed by Muhammad et al. [264] is employed in the present work. Apart from conventional dislocation interactions, the model accounts for the intragranular backstresses that arise from the formation of deformation induced dislocation cellular substructure. The slip system hardening relationship $g_{(\alpha)}$ is given by

$$g_{(\alpha)} = \left[(2+\beta)(\alpha'\mu b)^2 \frac{1}{4b}\gamma\right]^{\frac{1}{(2+\beta)}} C_{(P/A)} \qquad where \tag{9-4}$$

$$\alpha' = \alpha_0 + \frac{3Ct}{b}(1 - \chi_E)\gamma \,, \tag{9-5}$$

$$C_{(P/A)} = C_f \left(\frac{P}{A}\frac{1}{C_1}\right)^{\frac{1}{(2+\beta)}} \tag{9-6}$$

In Eq. (9-4), Eq. (9-5) and Eq. (9-6), the term b is the Burgers vector, μ is the shear modulus, m is the strain rate sensitivity index and χ_E is the Eshelby's inclusion factor. The terms P, A, C_1, C_f, β, α_0, C, and t are material dependent parameters and are obtained from stress strain curve and microstructure as outlined in Muhammad et al. [264].

9.2.3.2 Problem formulation

The component level macro FE model of the wrap bend test is shown in Figure 9-1(a) and consists of a sheet specimen, the binders to clamp and hold down the sheet in position, the mandrel and the roller. Consistent with the experimental specimen's dimensions, the FE sheet specimen has a length, width and thickness of 76 mm x 30 mm x 1mm, respectively and is meshed using 8-noded brick elements with an element size of 0.1 mm. The radius of the roller and the mandrel are 1 mm and 0.1 mm, respectively. The binders, roller and mandrel are modeled as rigid bodies and are meshed using quadrilateral shell elements with Belytschko-Tsay formulation. In the macro FE model, the global x-axis is parallel to RD, the y-axis is parallel to the through thickness direction ND and the z-axis is parallel to the transverse direction (TD). The left edge of the sheet (i.e. x = 0 plane) is kept fixed in the x-direction and while the binders are clamped on to the sheet, the wrap-bending deformation is applied by rotating the roller around the center of the mandrel. Surface to surface contacts are defined between the sheet and the tooling and the coefficient of static and dynamic friction are set to 0.08 between all contacts. The simulations are performed using a phenomenological elasto-plastic constitutive model (i.e. MAT_24), which is included within LS-Dyna. The experimental flow curves are used as an input to the constitutive model for simulating wrap bending of both alloys.

During bending, micro-cracks usually initiate from the central region along the width of the specimen as this region experiences plane-strain tension. These cracks originate along the outer tensile surface and propagate inward through thickness of the sheet, as observed experimentally in Part I. Since the focus of the present CPFEM study is to investigate the initiation and through-thickness propagation of such micro-cracks during wrap bending, the region of interest is chosen as a central through-thickness sliced region encircled in Figure 9-1. At the end of the component level macro simulation, the displacement histories of the edges corresponding to the region of interest are extracted and are applied as boundary conditions to the micro CPFEM model. The region of interest encircled in Figure 9-1 is 1.0 mm x 1.0 mm in size in its initial un-deformed state.

The through thickness microstructure along with the corresponding meshes for the micro CPFEM models of AA6016 and AA6016X are shown in Figure 9-4. The micro-scale CPFEM models have

the same overall dimensions as that of the encircled region of interest in Figure 9-1 and the experimentally observed through-thickness grain morphologies and texture are exactly implemented into CPFEM analyses by incorporating EBSD maps in numerical simulations. Each point in the EBSD map is represented by an element in the FE mesh with an element size of 6 μm. The grain boundary zones (i.e. points on either side of a grain boundary) are meshed as separate regions to help in crack propagation analysis. However, these zones are given the same material properties as their parent grains. Consistent with the full-scale FE model, the global x-axis of the micro CPFEM model is aligned with RD, the y-axis is aligned with the through thickness ND direction and the bend-axis is parallel to the z-axis. In Figure 9-4(b-d), the y = 0 plane represents the compression side whereas y = 1 mm plane represents the outer tensile edge of the bend. Only the y = 0, x = 0, and x = 1.0 mm planes (i.e. edges) are driven by the corresponding displacement histories of the edges from the macro model. It is to be noted that the displacement history from the full-scale model is not applied to y = 1.0 mm plane (i.e. outer tensile edge) as it represents the top free surface. This further enables the development of surface undulations and the experimentally observed through-thickness grooving behavior along the outer tensile edge. The conventional element deletion approach in conjunction with effective plastic strain-based failure criterion is used to model the fracture process. The region across the outer tensile edge is of primary interest as it is the preferential site for crack initiation and propagation. Typically, failure is not observed along the inner compressive regions and therefore, the CPFEM based fracture is not considered within the compressive region.

Before performing the micro CPFEM based wrap-bending simulations, the crystal plasticity hardening model parameters are calibrated using an inverse CPFEM approach. For this purpose, 3D statistically equivalent microstructures (incorporating grain morphology, crystallographic orientation and misorientation distribution) are generated from the experimental EBSD data of AA6016 and AA6016X. The microstructures are generated using 'M-builder' and details of the procedure can be found in Brahme et al. [55]. The generated 3D microstructures for AA6016 and AA6016X are shown in Figure 9-5(a) and Figure 9-5(b) and the corresponding <111> pole figures are shown in Figure 9-5(c) and Figure 9-5(d), respectively. It is noted that the generated microstructures show excellent conformity to the experimental data as evident by the <111> pole figures comparison in Figure 9-5(c) and Figure 9-5(d) with corresponding experimental pole figures in Figure 9-2(e) and Figure 9-2(f). The 3D microstructures are 1.0 mm x 1.0 mm x 1.0 mm in size and are meshed using 8-noded brick elements with an element size of 20 microns. The x-axis is aligned with RD, y-axis is aligned with ND and z-axis is aligned with TD. The 3D microstructure for the composite AA6016X alloy consists of a central AA6016 core and outer clad layers of AA8079, with different material properties. Firstly, a uniaxial tension simulation along RD is performed using the AA6016 microstructure (see Figure 9-5(a)) and the hardening model parameters are tuned to achieve an excellent match to the experimental stress-strain data for the monolithic AA6016 alloy. Once the hardening parameters for AA6016 are obtained, those parameters are also used as hardening parameters for the central core region (in Figure 9-5(b)) of AA6016X. While keeping those parameters constant, uniaxial tension simulation is performed

using the composite AA6016X microstructure (see Figure 9-5(b)) and the hardening parameters for the softer AA8079 clad layers are tuned to calibrate the simulated stress-strain response to the experimental stress-strain data of composite AA6016X alloy. The calibrated model parameters are given in Table 9-1.

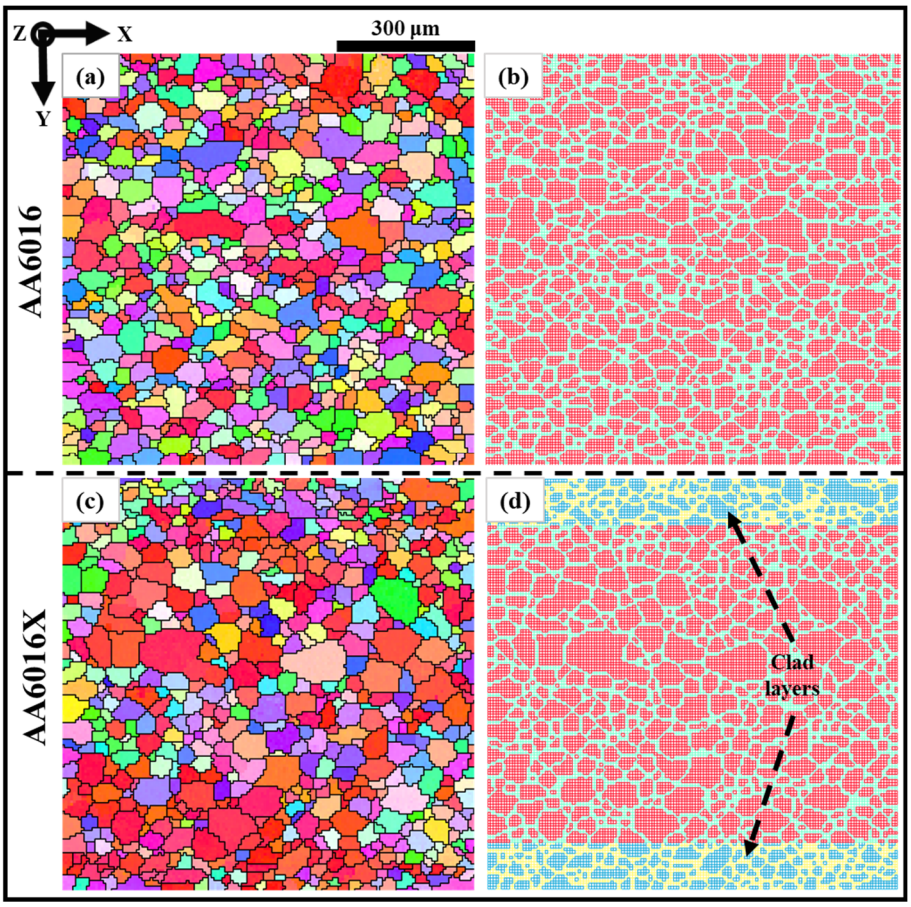

Figure 9-4: (a), (c) the through thickness microstructure and (b), (d) the corresponding meshes of micro CPFEM model of AA6016 and AA6016X, respectively.

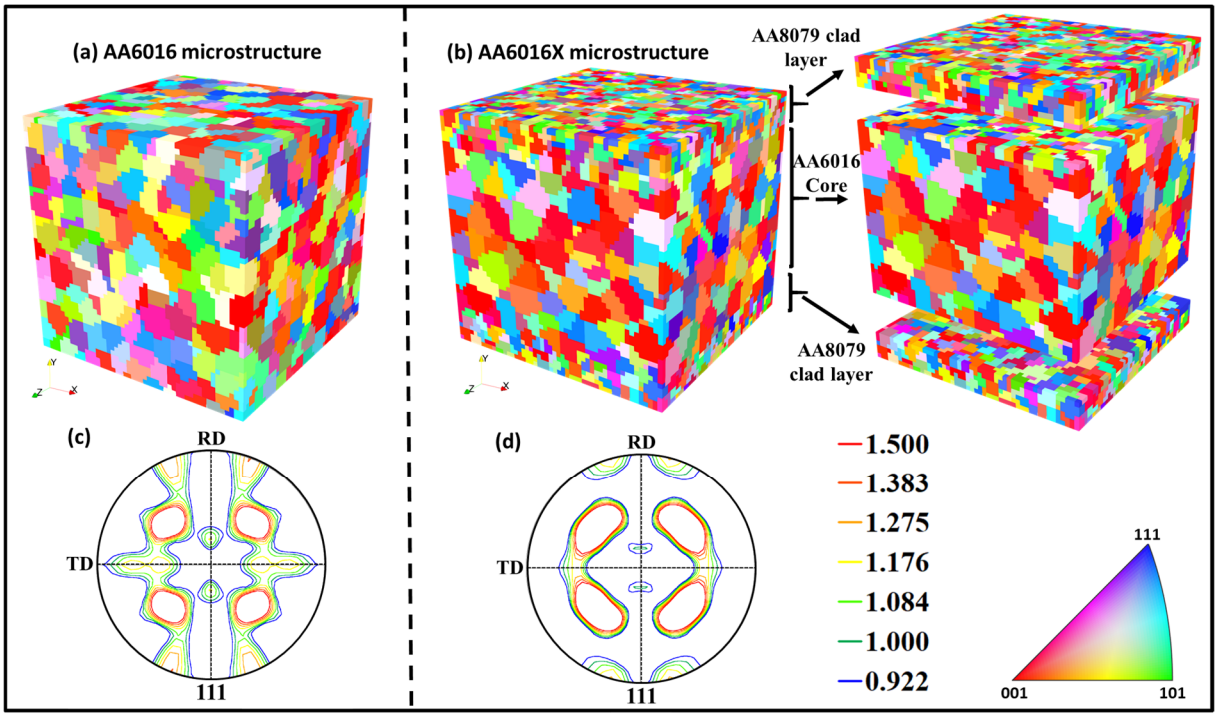

Figure 9-5: (a), (b) the generated 3D microstructures and (c), (d) the corresponding <111> pole figures for AA6016 and AA6016X, respectively

Table 9-1: Model parameters used in simulations

Alloy	$\sigma_0\ (MPa)$	P/A	β^{II}	β^{III}	$C_1^{II}(\mu m)$	$C_1^{III}(nm)$	C_f	C	$t\ (nm)$
AA6016	74.5	0.076	0.33	0.71	0.661	1.961	2.4	0.22	7.0
AA8079	14.1	0.039	0.28	1.41	0.154	0.851	1.2	0.22	7.0

9.3 Results

Figure 9-6 shows the comparison of the calibrated stress-strain response of AA6016 and AA6016X with respective experimental data. The results show an excellent match to the experimental flow stresses. It is further noted that once the CPFEM model is properly calibrated for the experimentally observed AA6016 and AA6016X flow behaviors, the model successfully predicts the experimental flow behavior of the softer AA8079 clad layers, as shown in Figure 9-6. Figure 9-7 shows the deformed meshes and equivalent stress distribution for AA6016 and AA6016X after 15 pct. uniaxial tensile strain along RD (i.e. x-axis). One can observe the presence of several microstructurally driven stress hot spots for AA6016 in Figure 9-7(a). Furthermore, the equivalent stress distribution within the composite AA6016X alloy (see Figure 9-7(b)) shows that the local stresses within the outer clad layers are approx. 2 to 3 times lower than the stresses experienced by the central core.

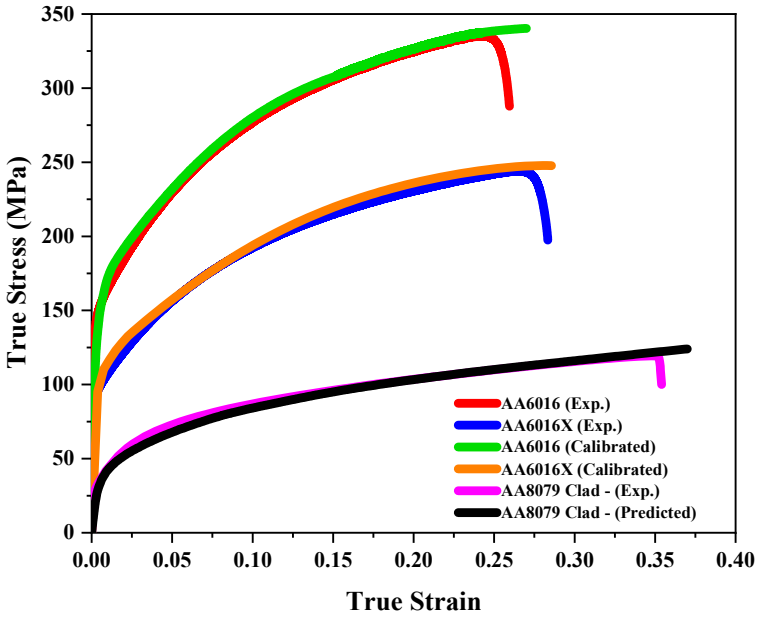

Figure 9-6: Calibrated and predicted uniaxial stress-strain behavior using CPFEM hardening model and corresponding experimental data.

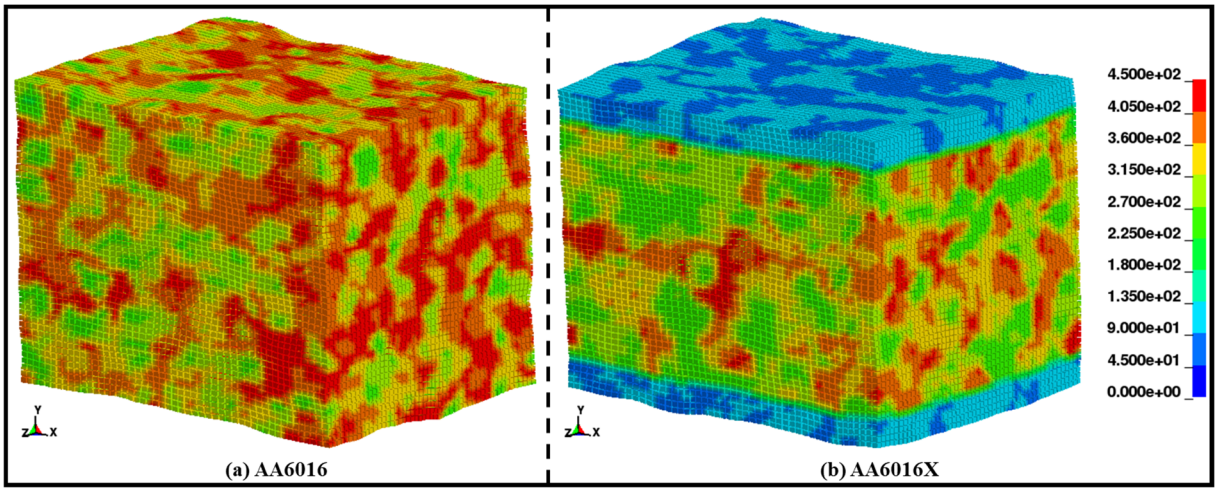

Figure 9-7: Deformed meshes showing contour of equivalent stress distribution for (a) AA6016 and (b) AA6016X after 15 pct. uniaxial tension along RD (i.e. x-axis).

9.3.1 Simulated bending behavior

Figure 9-8(a) shows the contour plot of effective strain for AA6016 after a bend angle of 150°. It is observed that multiple micro-cracks have originated from the outer tensile surface and have propagated several micrometers inward through thickness of the bend. Furthermore, the deformation is quite inhomogeneous near the outer tensile surface, where the strain tends to localize within multiple shear bands. In addition, it is observed that the bending deformation has led to surface rumpling and formation of several microscopic grooves along the outer tensile

surface (see Figure 9-8(a)). The contour map also shows a gradient in strain distribution starting from the outer tensile surface where the strain is maximum, passing through the neutral axis where the strain reduces to near zero, and towards the inner compressive region where the strain is equally high. This deformation behavior is unique to bending where a strain gradient is present across the sheet thickness. It is noted that the simulated bending behavior of AA6016 (in Figure 9-8(a)) is very similar to what has been observed experimentally as shown by the through thickness optical micrograph in Figure 9-8(b). The experimental optical micrograph also shows the presence of few micro-cracks originating from the outer tensile surface along with a central macro crack and the presence of several microscopic surface grooves along the outer tensile surface (see Figure 9-8(b)).

Figure 9-8(c) shows the contour plot of effective strain for the composite AA6016X alloy after a bend angle of 150°. It is to be noted that fracture within the clad layers is not modeled as the composite alloy shows unlimited bendability and does not show any signs of failure even at the maximum bend angle of 180°, as shown experimentally in Part I. However, fracture within the AA6016 core of the composite alloy is modeled as the experimental failure strains are known. It is apparent from the strain contour map in Figure 9-8(c) that the composite alloy is successfully bent to 150° without any failure within the central core. Furthermore, consistent with the experimental optical metallography result in Figure 9-8(d), the simulated response (in Figure 9-8(c)) shows considerable thinning and thickening of clad layers along the outer tensile and inner compressive regions of the bend, respectively. Moreover, the experimentally observed behavior of grain elongation within those regions is also well captured. It is also noted that strain tends to localize within certain regions of clad layer along the outer tensile surface (see the region encircled in red in Figure 9-8(c)), thereby promoting considerable thinning – necking within those regions. Furthermore, while comparing the simulated response of AA6016 (in Figure 9-8(a)) and AA6016X (in Figure 9-8(c)), it is observed that AA6016 alloy shows a much greater propensity towards shear banding through thickness of the bend. It appears as if the softer AA8079 clad layer in AA6016X inhibits the tendency towards strain localization and shear banding within the central core region. This behavior will be discussed in further details in section 9.4.4 of this manuscript.

9.3.2 Texture evolution during wrap-bending

Figure 9-9 shows the orientation distribution function (ODF) sections $\varphi_2 = 0°$, $\varphi_2 = 45°$, and $\varphi_2 = 65°$ for the initial (Figure 9-9(a)), the experimentally measured (Figure 9-9(b)) and the numerically predicted texture (Figure 9-9(c)) after wrap bending deformation for AA6016. For visual comparison, the same texture intensity scale is used in all figures. The initial texture shows the presence of several FCC texture components which are encircled in Figure 9-9(a). Furthermore, the experimental ODF after bending shows a significant weakening of the overall texture as apparent from the maximum texture intensity which has decreased from an initial value of 8.11 times random (see Figure 9-9(a)) to a value of 4.89 times random after bending (see Figure 9-9(b)). This weakening of the texture is associated with rotation of texture components during bending deformation. For example, the Cube texture peaks have shifted by approximately 45° along the φ_1 axis after deformation. Moreover, the Brass, Copper, Goss and S component peaks have almost

disappeared after bending. The numerically predicted texture evolution after bending in Figure 9-9(c) shows good conformity to the experimentally measured texture evolution. The overall trends and the rotation of texture peaks have been captured with reasonable accuracy, as highlighted by the encircled peaks in Figure 9-9(b) and Figure 9-9(c). There are some discrepancies between the experimental and predicted texture but importantly, the numerical model successfully predicts the overall weakening of the texture as observed experimentally. It is important to note that a good portion of the observed texture evolution during bending is associated with the rigid body rotation about TD during the wrap-bend test. Experimentally, it is not possible to quantify that rigid body rotation effect with reasonable accuracy as different regions within the bend experience varying degrees of rigid body rotation. However, numerically it is possible to exactly quantify that rigid body rotation as the initial and final positioning of each FE element is known and the local rigid body rotations can be calculated. Hence, the texture is replotted by excluding the effect of those local rigid body rotations and the results are shown in Figure 9-9(d). Unlike the simulated results in Figure 9-9(c) where the Cube texture peak have shifted by approximately 45° along the φ_1 axis partly due to rigid body rotation during wrap-bending, the new results in Figure 9-9(d) show widening - rotation of the original cube peaks along the φ_1 axis promoting the formation of a rotated Cube fiber along that axis. Furthermore, it is noticed that once the rigid body rotation is removed, the other common FCC texture components such as Brass, Copper and S components are also identifiable (see Figure 9-9(d). However, the peak intensities of these components are comparatively much lower than their corresponding starting intensities in the initial microstructure.

9.3.3 Strain localization and intragranular misorientations

Figure 9-10(a) and Figure 9-10(b) show the comparison of simulated and the experimentally observed shear localization behavior for AA6016. Figure 9-8(a) is reproduced here as Figure 9-10(a) for ease of comparison. The simulated result in Figure 9-10(a) shows that strain tends to localize in intense shear bands which originate from surface low cusps along the outer tensile surface. Furthermore, several set of mutually orthogonal shear bands are also apparent within the microstructure (see blue colored arrow in Figure 9-10(a)). It is noticed that the simulated behavior shows an excellent agreement to the observed experimental behavior in Figure 9-10(b), which also shows a clear tendency towards gathering of multiple slip bands into transgranular mutually orthogonal shear bands, which are emanating from the outer tensile edge and are propagating inwards through multiple grains (see blue arrows in Figure 9-10(b)). Furthermore, both the simulated and experimental results show an area of intense shear banding ahead of multiple crack tips as pointed by black and red colored arrows in Figure 9-10 (a) and Figure 9-10 (b), respectively. The formation of these shear bands and their effect on micro-crack initiation and propagation will be discussed in further details in section 9.3.4 and section 9.4.1, respectively.

Figure 9-10(c) presents IPF map of the numerically predicted texture evolution after bending for AA6016. The IPF map clearly show the development of intragranular misorientations within several grains along the inner compressive and outer tensile regions. These intragranular

misorientations are manifested as noticeable color differences inside grains. Grains with initial Cube or near Cube orientations show a high degree of internal misorientations after bending, which is apparent from the partial change in the color of these grains from initially red to near orange color. Similar behavior is observed for grains with near {111}[uvw] initial orientations. These results are consistent with the experimental findings as shown by the experimental IPF of AA6016 bent specimen in Figure 9-10(d). Few grains showing such behavior are encircled in Figure 9-10(c) and Figure 9-10(d).

Based on the results presented herein, it can be concluded that the CPFEM based constitutive framework in conjunction with the multi-scale modeling approach are able to successfully predict the experimentally observed bending behavior. Hence, one can analyze the simulated bending results in further details to investigate the relationship between local crystallographic texture, the development of surface undulations, shear banding, micro-crack initiation and propagation.

9.3.4 Shear banding and surface undulations as a precursor to micro-crack initiation and propagation

Figure 9-11 shows effective strain contours presenting the evolution of surface undulations, shear bands development, micro-cracks initiation and propagation at different time intervals during wrap bending simulation of AA6016. Starting with an initial deformation free state at time t = 0 ms in Figure 9-11(a), strain has already started to localize within multiple regions along the outer tensile edge (as pointed by arrows in Figure 9-11(b)) after t = 398 ms. However, at this stage, the surface rumpling behavior along the outer tensile edge is not apparent. As the deformation proceeds further (in Figure 9-11(c)), strain has started to localize into mutually orthogonal localization bands that originated from the outer tensile surface. One can also see, the development of surface waviness – rumpling along the outer tensile edge. This waviness results from the formation of surface low cusps (i.e. valleys) along regions of higher strain localization, as shown by the encircled areas in Figure 9-11(c). Furthermore, the deformation is already highly non-uniform although the intense macroscopic shear bands are not yet fully developed. With further straining, strain localizes into intense shear bands which are propagating through multiple grains and a micro-crack has initiated along one of the surface grains due to intense shear banding within a surface low cusp region (see the region pointed at in Figure 9-11(d)). As the deformation continues, the micro-crack propagates further through the intensely sheared region (see Figure 9-11(e)) and shear bands have started to develop within adjacent regions along the outer tensile edge (see black colored arrows in Figure 9-11(e)). It is also noted that while the micro-crack is propagating through the pre-existing shear band, another mutually orthogonal banded region has started to develop ahead of the crack tip as shown by the white colored arrow in Figure 9-11(e). As soon as the crack-tip approaches that orthogonal shear banded region, the crack changes its direction and starts propagating along this new localized region, as shown in Figure 9-11(f) and Figure 9-11(g). A similar behavior is observed once again, as the advancing crack tip approaches another banded region which is oriented at approx. 45° with respect to the advancing crack (see the region within the white colored arrows in Figure 9-11(g)). Upon intersection with this shear band, the advancing crack changes its

direction once again and starts propagating along this new banded region, as shown in Figure 9-11(h) and Figure 9-11(i). It is observed that a second micro-crack initiates from another surface low cusp and starts propagating inwards through-thickness of the bend along an intensely sheared region as shown by the encircled region in Figure 9-11(h). Decohesion along several grain boundaries ahead of the crack tip, is also observed within those intensely sheared regions, as shown by the magnified images in Figure 9-11(h) and Figure 9-11(i). These are highly misoriented regions with local misorientations of greater than 45° across the boundaries. Similar decohesion along grain boundaries has been observed experimentally as shown by the encircled regions in Figure 9-10(b). As deformation continues, the micro-cracks keep advancing through the intensely sheared regions, towards the neutral axis of the bend, as shown in Figure 9-11(j).

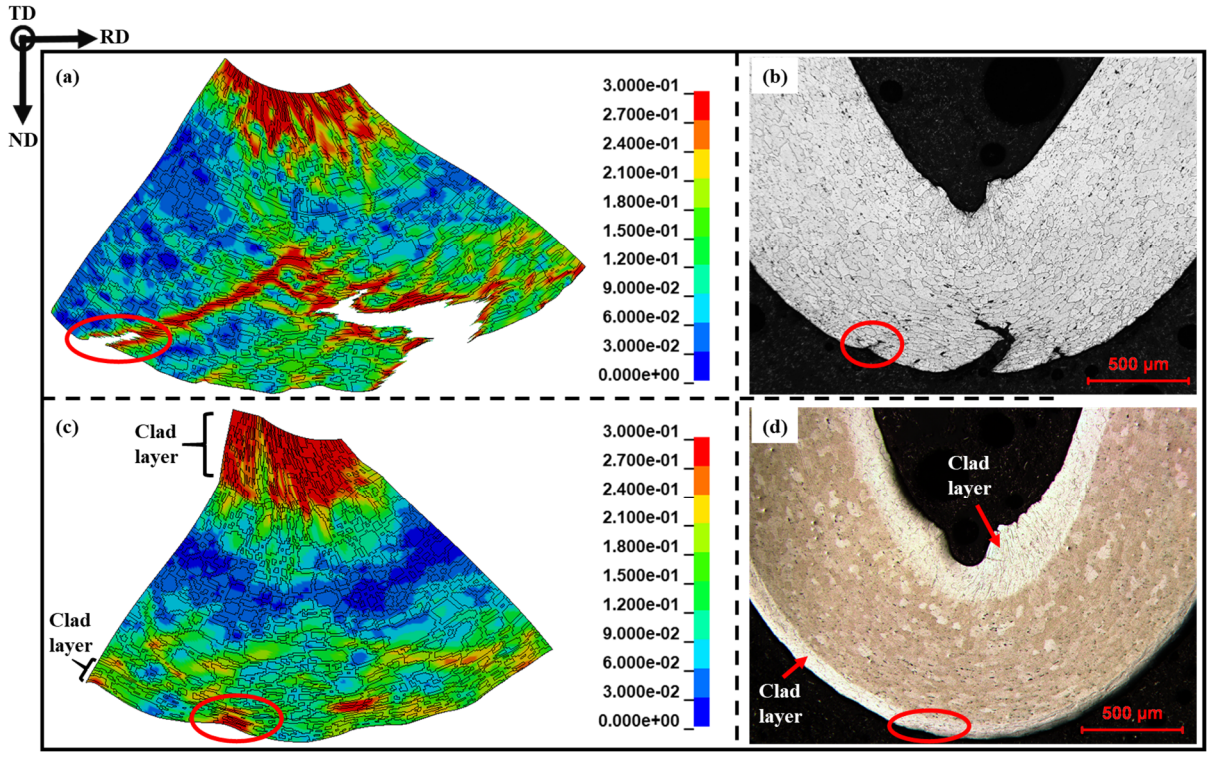

Figure 9-8: (a), (c) Deformed CPFEM meshes showing contours of effective strain and (b), (d) experimental optical microscopy images after wrap bending of AA6016 and AA6016X, respectively.

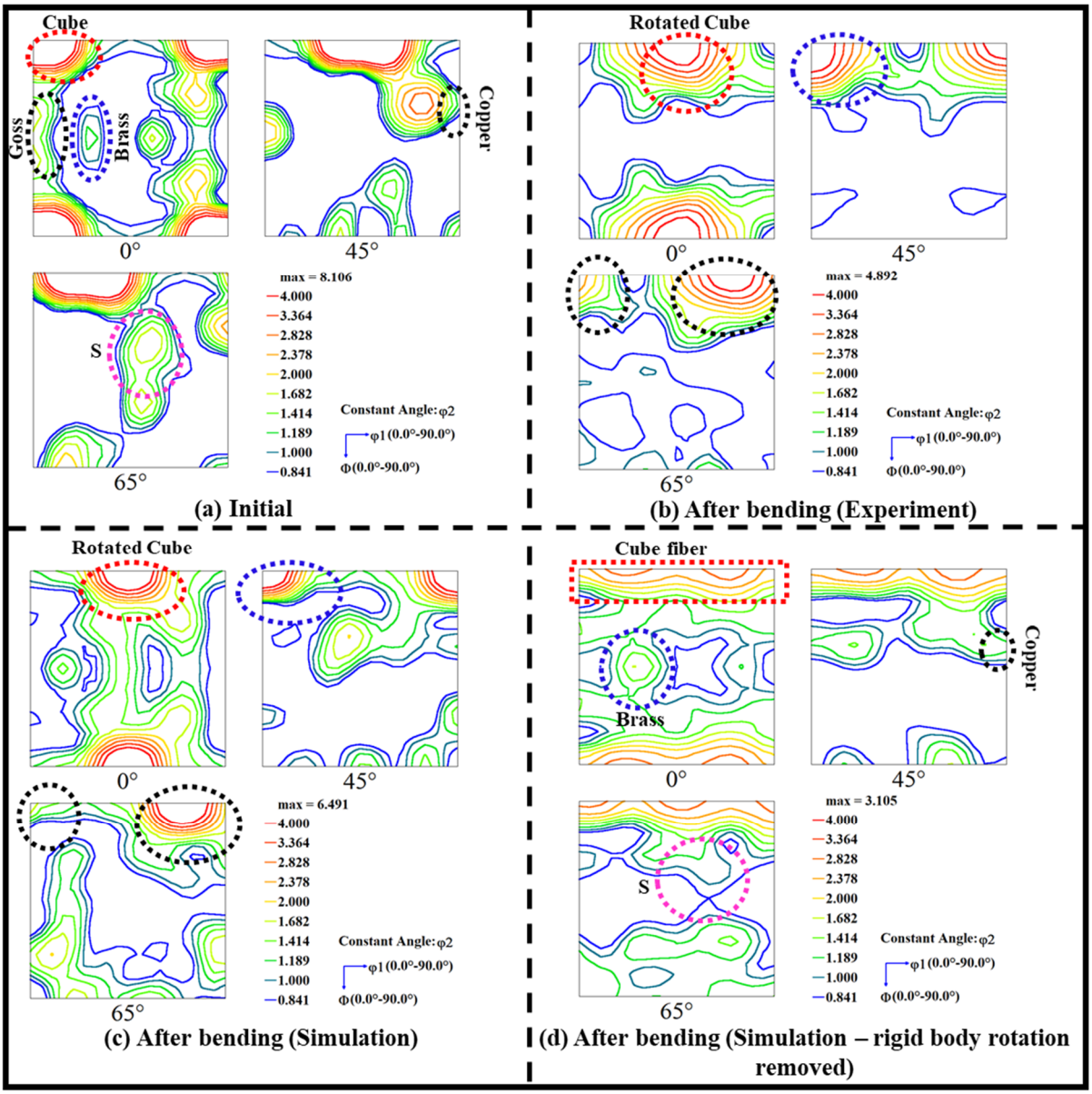

Figure 9-9: Comparison of experimental and predicted texture evolution after wrap bending deformation of AA6016. Figures present ODF sections of $\varphi_2 = 0°$, $\varphi_2 = 45°$, and $\varphi_2 = 65°$ for (a) initial texture before bending, (b) experimental texture after wrap bending, (c) predicted texture after wrap bending simulation and (d) predicted texture after removing the inherent rigid body rotation.

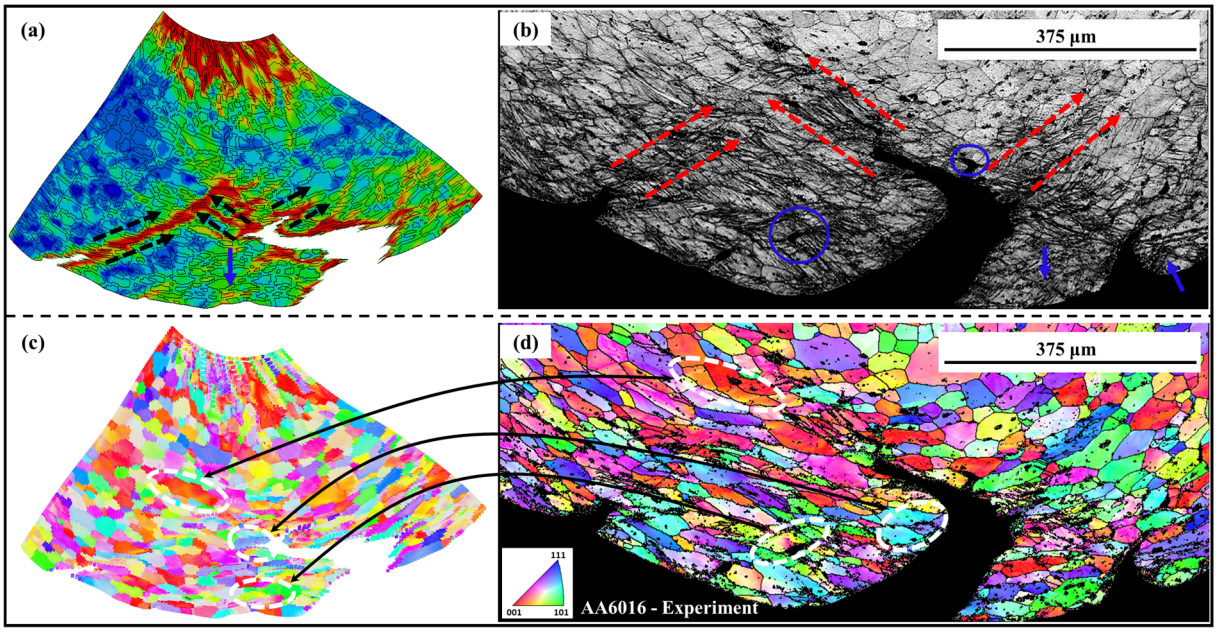

Figure 9-10: Deformed CPFEM meshes showing (a) contour of effective strain distribution and (b) IPF map of texture evolution after bending of AA6016. (c) experimental EBSD gray scale grain map and (d) IPF map after wrap bending of AA6016.

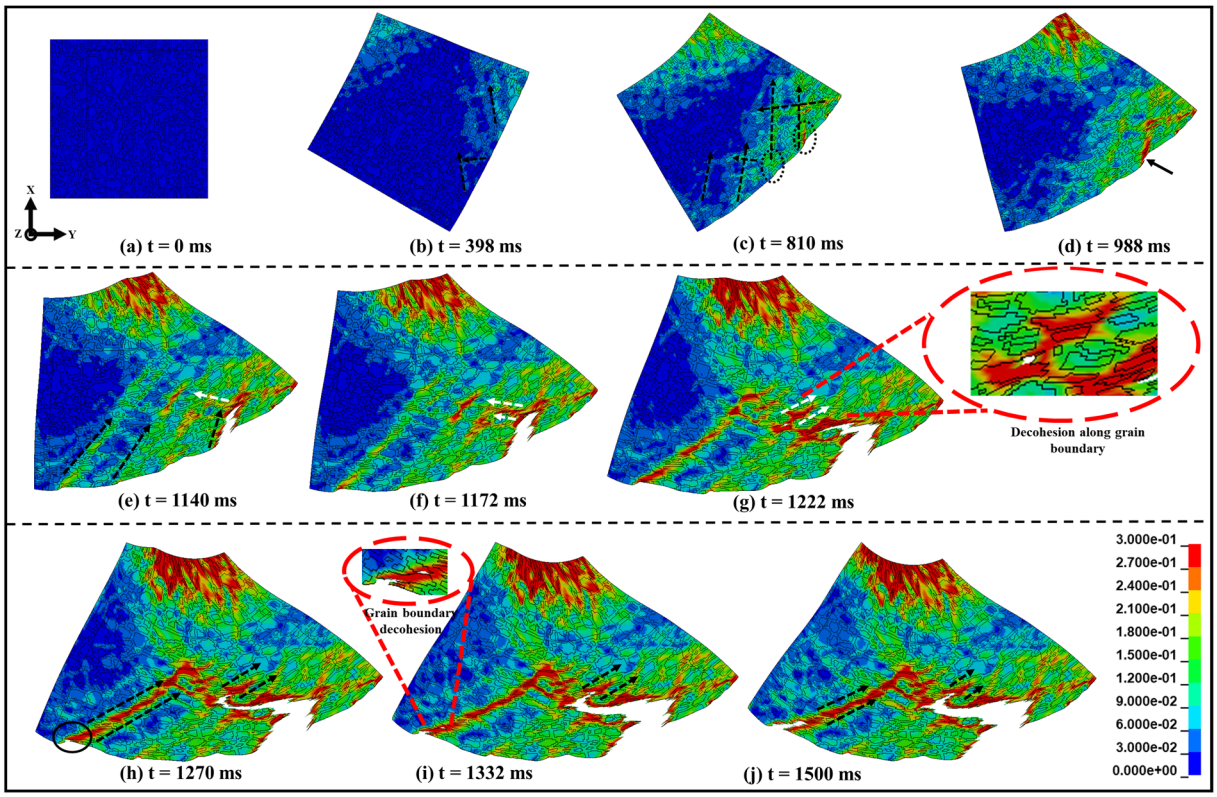

Figure 9-11: Effective strain contours showing evolution of surface undulations, shear bands development, micro-cracks initiation and propagation at different time intervals during CPFEM wrap bending simulation of AA6016.

9.4 Discussion

Bending of precipitation hardened aluminum alloys is still not well understood, but several authors [219, 221, 252, 324, 339] have shown that during bending the outer tensile surface develops severe topographical features, where strain localizes into intense bands. However, there are conflicting views reported on the sequence of such events prior to final fracture. Some authors assume surface undulations to be the cause of strain localization [228], while others considered the development of surface undulations a consequence of strain localization [215, 219, 230, 336, 340]. Furthermore, the development of shear bands, micro-cracks initiation and propagation during bending and their relationship with the local crystallographic texture are not well understood, as their evolutions are difficult to be monitored experimentally. The CPFEM based approach presented herein, provides a perfect tool to further explore the development of these damage events leading to final failure, as discussed next.

9.4.1 The influence of shear banding on crack initiation and propagation

The shear banding behavior observed during wrap-bending of AA6016 alloy is characteristic of heterogeneous deformation and is associated with the development of surface rumpling and grooves along the outer tensile edge of the bent specimen. It is noted that through-thickness strain localization within certain regions of the bend, starts early during bending deformation (see Figure 9-11(b)) and acts as a precursor to the formation of surface undulations. Upon persistent plastic deformation, strain starts to localize into orthogonal shear bands emanating from the tensile free surface, thereby promoting the formation of surface low cusps and grooving along the outer tensile edge, as shown in Figure 9-11(c). The grooving behavior, in turn, further promotes strain localization within its vicinity, leading to the formation of well-developed intense shear bands through-thickness of the bend. Strain levels within these shear bands are several folds higher than the adjacent outside regions. This apparent grooving and intense shear banding behavior are in fact related to intensely sheared planes through thickness of the bend. These crystallographic sheared planes provide a minimum energy path for micro-cracks (that initiate along the outer tensile surface) to propagate through such regions, thereby promoting a predominant transgranular failure. Furthermore, the results presented in Figure 9-11 demonstrate that the crack path is strongly linked with the inherent shear banding behavior. The micro-crack tends to alternate from one shear band to another under the influence of applied loading. In other words, upon intersection with a shear band, the advancing crack tip alternate from a less critical localization condition to a more critical one, as it requires lesser energy for the creation of new fracture surfaces while still sustaining plastic deformation. The fracture process is further assisted by decohesion along some of the highly misoriented grain boundaries (see Figure 9-11(g,i)), promoting intergranular fracture in some areas.

9.4.2 The influence of crystallographic texture on shear banding and crack propagation

The influence of local texture on the formation of shear bands and crack propagation in AA6016 is further analyzed by plotting the numerically predicted texture after bending on an initial

undeformed mesh, as shown in Figure 9-12(b). The micro-crack initiation and propagation are also plotted on the undeformed mesh in Figure 9-12(b) and the corresponding kernel average misorientation (KAM) plot after bending is shown in Figure 9-12(c). For comparison, the IPF map of the initial microstructure is also shown in Figure 9-12(a). It is apparent that the fracture behavior is dominantly transgranular as both micro-cracks are passing through several grains (see Figure 9-12(b)). However, there are some regions within the microstructure where the crack propagates along grain boundaries. One such region is encircled in Figure 9-12(b), where the crack is propagating along the boundary with near rotated Cube orientation grain on one side and near Goss orientation grain on the other side and the misorientation along the boundary is approx. 46°. These results are consistent with the experimental observations presented in Part I, where decohesion along grain boundaries is observed across several grains with misorientations greater than 40°.

It is apparent that crack propagation follows region of high KAM values (see Figure 9-12(c)) and these region of high KAM values also correspond to regions of high strain localization and intense shear banding. Three such regions of intense shear banding are shown by blue arrows and marked as '1', '3' and '4' in Figure 9-12(c) and another localization-free region is marked as '2'. The corresponding regions are marked on the IPF map in Figure 9-12(b). It is observed that the localization free region (i.e. region '2') has several grains with Cube or near Cube orientations, whereas the other three regions have several grains with near Goss, near {111}[uvw] and other orientations in between. Nevertheless, in order to properly analyze the influence of local microstructure on crack initiation and propagation, the microstructure in Figure 9-12(b) is partitioned to separate microstructural regions that are along the crack path from all other areas that are away from the crack path and the resulting texture data is shown as ODF in Figure 9-13. It is observed that areas away from micro-cracks have a dominant cube – rotated cube microstructure as shown by $\varphi_2 = 0°$ section in Figure 9-13(a). For regions away from crack path, the presence of comparatively weaker Brass and Copper texture components is also apparent from $\varphi_2 = 0°$ and $\varphi_2 = 45°$ sections, respectively. On the contrary, the areas along the crack path (in Figure 9-13(b)) show presence of near rotated Goss and rotated S texture components (as encircled) in $\varphi_2 = 0°$ and $\varphi_2 = 65°$ ODF sections, respectively.

Based on these observations it can be concluded that grains with Cube or near Cube texture can deform rather easily during wrap-bending and are less susceptible to shear banding and crack propagation. On the other hand, grains having near S or near Goss orientations show a much greater propensity towards formation of shear bands and are more prone to crack initiation and propagation during bending. In the next section of the manuscript, the current knowledge basis is further explored by performing a set of CPFEM based wrap bending simulations using different distributions of the through thickness microstructure, with emphasis on understanding relationship between local texture, shear banding and the overall bendability.

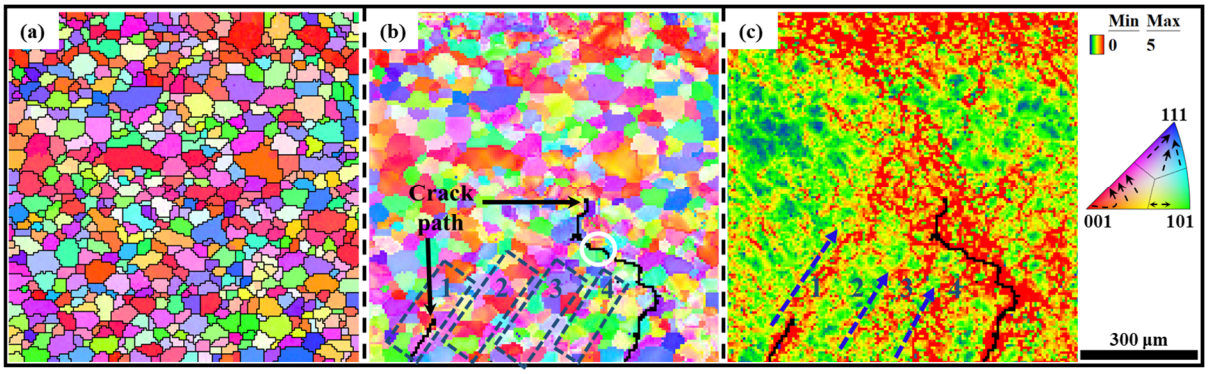

Figure 9-12: IPF maps of AA6016 showing (a) initial texture before bending and (b) deformed texture after bending along with the crack paths plotted on the undeformed initial configuration. (c) Kernel average misorientation (KAM) distribution plot after bending simulation.

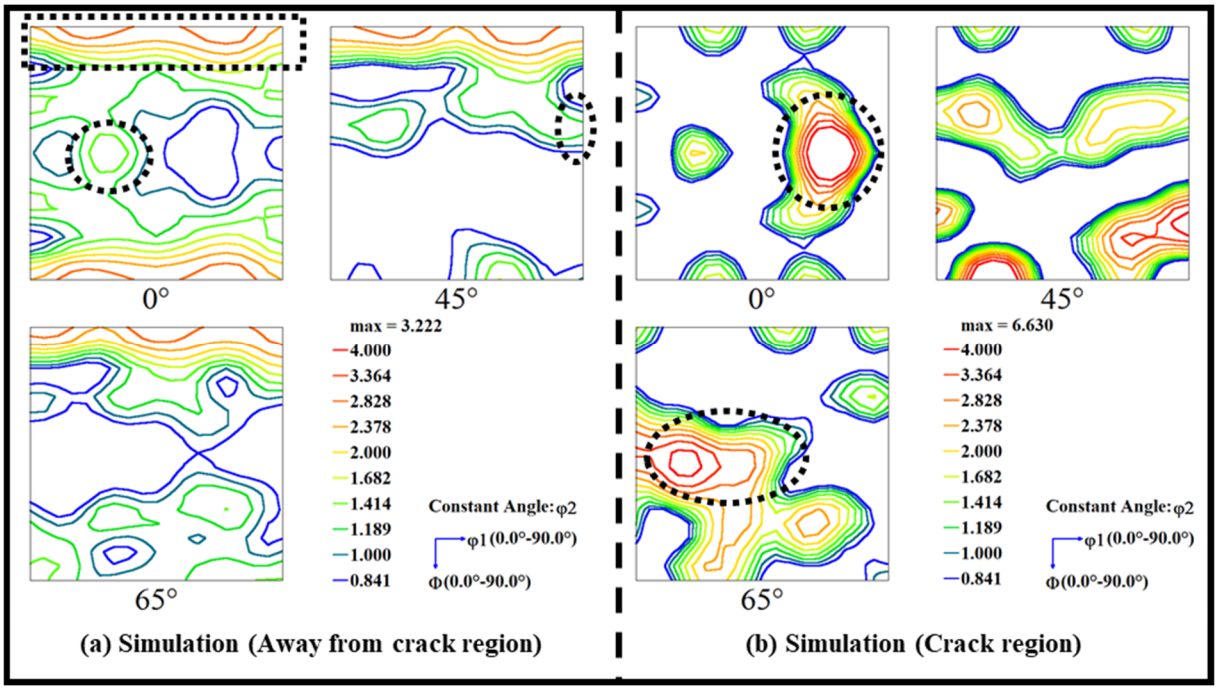

Figure 9-13: Comparison of simulated texture after wrap bending of AA6016 for (a) regions away from micro-cracks and (b) regions along the micro-cracks.

9.4.3 A systematic study on the relationship between microstructure and bendability

In this section, the influence of crystallographic texture on bendability is investigated by conducting CPFEM based wrap bending simulations using synthetic microstructures. Staring with the original AA6016 microstructure, five synthetic microstructures are generated by artificially assigning volume fraction of one FCC texture component to 25 % within each of the five microstructures. For each generated microstructure, the experimentally observed volume fractions for all remaining texture components and the experimentally observed grain morphologies are still maintained. The experimental grain morphologies are maintained in all generated microstructures

so that one can single out the effect of crystallographic texture on bendability. Furthermore, only the volume fraction of one texture component per microstructure is increased to study its effects on bendability of the generated polycrystalline microstructure. Moreover, by maintaining the experimental volume fractions of all other texture components, the generated synthetic microstructures are rather close to typically observed FCC rolling microstructures. The five texture components under investigation are Brass, Copper, Goss, S and rotated Goss and the generated microstructures are named 'B', 'C', 'G', 'S' and 'RG', respectively. Apart from these five microstructures, two more microstructures (i.e. G&C and RG&C) are generated. The 'G&C' microstructure consists of 50 % Goss and 50 % Cube grains by volume fraction whereas the 'RG&C' microstructure consists of 50 % rotated Goss and 50 % Cube grains by volume fraction. The IPF maps of the generated synthetic microstructures and their corresponding <111> pole figures are shown in Figure 9-14 and Figure 9-15, respectively. Apart from the rolling texture of AA6016, the presence of a relatively higher volume fraction of a single FCC texture component is apparent within the <111> pole figures of each of the first five generated microstructures (see Figure 9-15(b-f)). The CPFEM based wrap-bending simulations are performed using the same boundary conditions as for AA6016.

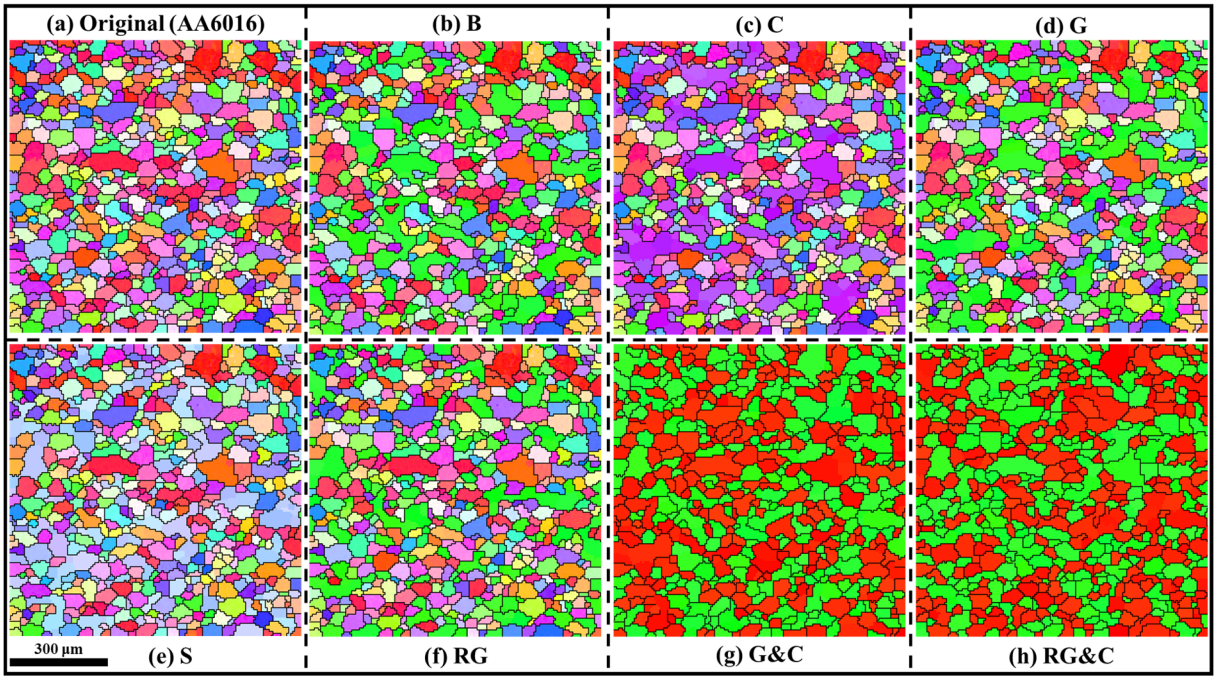

Figure 9-14: IPF maps of (a) the experimental AA6016 and (b-h) the generated synthetic microstructures for wrap bending simulations.

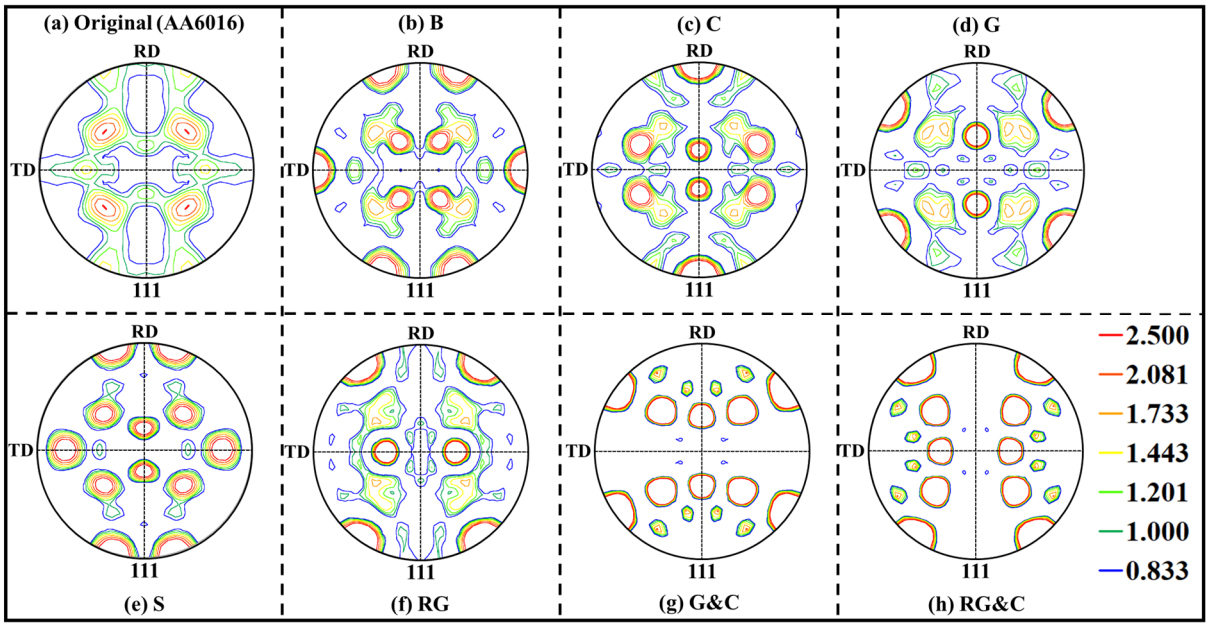

Figure 9-15: <111> pole figures of (a) the experimental AA6016 and (b-h) the generated synthetic microstructures for wrap bending simulations.

Figure 9-16 shows bend angle to failure during wrap-bending for the different studied microstructures. Failure here is defined as the initiation of a micro-crack along the outer tensile edge during CPFEM based wrap-bending simulations. It is observed that microstructure 'C', having excess Copper texture component, shows the highest bendability amongst all microstructures with a bend angle to failure of approx. 128°. This is closely followed by microstructure 'B' and microstructure 'G&C' with bend angles to failure of approx. 122° and 119°, respectively. The original AA6016 microstructure with predominant Cube, rotated Cube and S texture (see Figure 9-2(g)) has a bend angle to failure of approx. 100°. The worst bendability is demonstrated by the 'S' microstructure with a bend angle to failure of approx. 85°. Furthermore, the microstructures with excess Goss (i.e. microstructure 'G') and rotated Goss (i.e. microstructure 'RG') texture components show inferior bendability in comparison to microstructures with excess Copper and Brass texture components. These results demonstrate that polycrystalline microstructures with excess S or Goss – rotated Goss texture components exhibit inferior bendability, with S being by far the worst texture component for bendability.

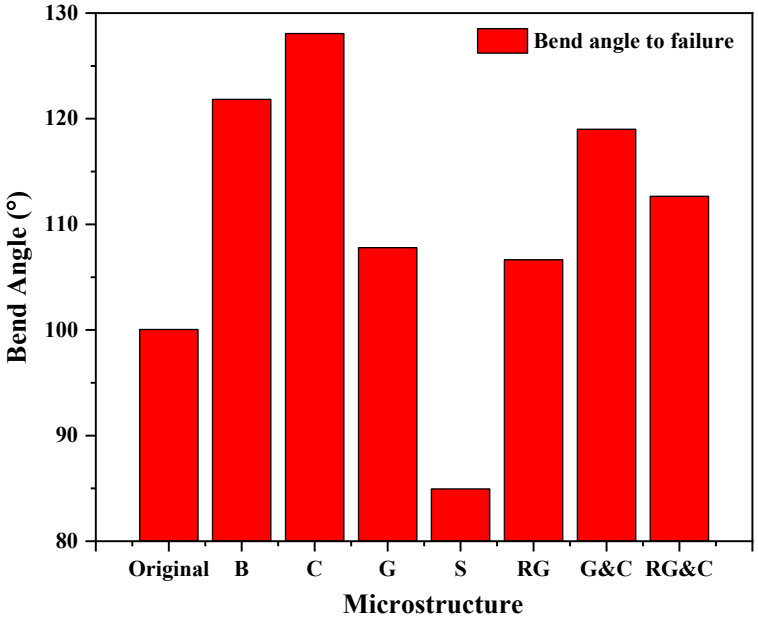

Figure 9-16: Comparison of bend angle to failure for the different microstructures after wrap bending

Figure 9-17 shows the contour plots of effective strain along with the corresponding IPF maps of the synthetic microstructures after wrap-bending to 150°. The results of the original AA6016 microstructure are repeated in Figure 9-17(a) for ease of comparison. It is apparent that the 'Original', 'G', 'S' and 'RG' microstructures show presence of larger micro-cracks as compared to 'B' and 'C' microstructures. At first glance, it is noticed that the strain contours of all microstructures show similar features of non-homogeneous slip distribution with several areas of intense strain localization and shear banding within the microstructure. However, upon careful observation, it is noted that the two microstructures with highest bendability (namely 'B' and 'C') show a significantly lower tendency towards formation of macroscopic surface undulations and grooves (which serve as a precursor to crack initiation) along the outer tensile edge as compared to other microstructures. It is also observed that the shear bands (that emanate from the outer tensile edge) within these two microstructures are not well developed and their through-thickness propagation has been inhibited prematurely. This is obvious from the strain contour maps in Figure 9-17(b) and Figure 9-17(c) where several set of localization bands that initiated at the surface (see the red encircled regions in Figure 9-17(b) and Figure 9-17(c)) are unable to propagate further due to the presence of Brass and Copper oriented grains in their vicinity. Furthermore, some of the micro-cracks that initiated along the outer tensile edge are also unable to propagate further for the same reason. Some of these areas of high Brass and Copper oriented grains are encircled in black in Figure 9-17(b) and Figure 9-17(c), respectively. Microstructures 'G', 'S' and 'RG' (in Figure 9-17(d), Figure 9-17(e) and Figure 9-17(f)) show comparable strain localization and shear banding features. However, it is observed that the 'RG' microstructure has the largest micro-crack amongst all microstructures. The strain contour maps of 'G&C' and the 'RG&C' microstructures (see

Figure 9-17(g) and Figure 9-17(h)) exhibit extremely non-uniform deformation, which has led to the formation of deep valleys along the outer tensile region. This is consistent with the results reported by Muhammad et al. [313] where the authors have shown that grain clusters with Cube or near-Cube initial orientations, that are in vicinity of the outer tensile surface, promote the formation of these surface valleys during wrap-bending. It is also observed that Cube texture significantly enhances the resistance to shear banding by accommodating deformation rather easily whereas the Goss oriented grains show a much higher propensity towards shear banding. This is apparent from Figure 9-17(g) (see encircled regions), where multiple shear bands are predominantly propagating through Goss oriented grains. It is very interesting to note that even though the 'G&C' and the 'RG&C' microstructures show higher bendability as compared to the 'Original', 'G', 'S' and 'RG' microstructures (see Figure 9-16), their surface roughness characteristics are far worst due to the higher strain incompatibility between the Cube and Goss oriented grains. The higher bendability of these microstructures is associated with the presence of large number of Cube oriented grains that can accommodate deformation by experiencing high degree of crystallographic rotations as shown by the encircled region in Figure 9-17(h).

Figure 9-18 shows IPF maps of texture after bending along with crack paths for the different synthetic microstructures. The results are plotted on the initial undeformed mesh. The results show that the fracture behavior across all generated microstructures is mainly transgranular, as micro-cracks propagate through majority of the grains. However, amongst all microstructures, it is noted that microstructure 'G' and 'RG' show a comparatively greater tendency towards intergranular crack propagation. Although, the 'RG' microstructure has better bendability when compared to the 'Original' and 'S' microstructures, it has the largest crack length amongst all microstructures. The intergranular crack propagation along several boundaries in the 'RG' microstructure might have influenced this behavior. It is also observed that microstructures 'B', 'C' and 'G' show several areas where decohesion has occurred along high misorientation grain boundaries (see encircled regions in Figure 9-18(b-d)). Furthermore, the 'G&C' microstructure (in Figure 9-18(g)) clearly shows that the micro-crack initiates at a highly misoriented grain boundary between Cube and Goss grain and propagates solely through the grains with Goss texture, which are also areas of intense shear banding as shown by the strain contour maps in Figure 9-17(g).

Based on the results of this systematic study it can be concluded that the bendability of polycrystalline sheet materials can be improved significantly through proper engineering of the through thickness microstructure. Copper and Brass texture components show excellent resistance to the development of severe surface undulations, shear banding and crack propagation and are therefore excellent candidates for enhancing bendability of rolled sheet materials. Goss and rotated Goss components can develop intense shear bands and show little resistance to crack propagation. Furthermore, the presence of these components within the microstructure can also promote intergranular crack propagation. S texture component is prone to shear banding and offers little to no resistance to crack propagation and therefore, exhibits poor bending characteristics. The results further show that Cube texture enhances resistance to shear banding and is characterized as high

bendability component. However, excess volume fraction or through thickness clustering of cube grains within the microstructure can severely worsen the surface roughness characteristics due to induced strain incompatibilities and hence the final surface appearance of the bent sheet.

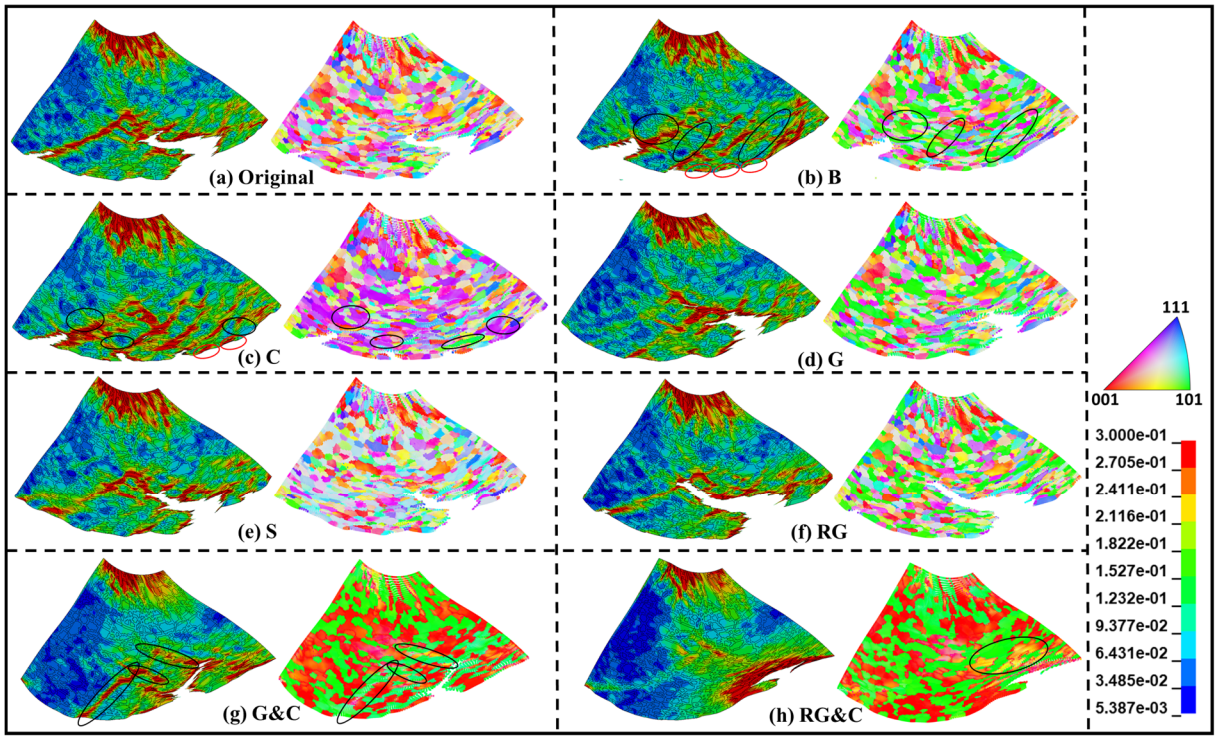

Figure 9-17: Deformed CPFEM meshes showing (a) contour of effective strain distribution and (b) IPF map of texture evolution after wrap bending for the studied microstructures.

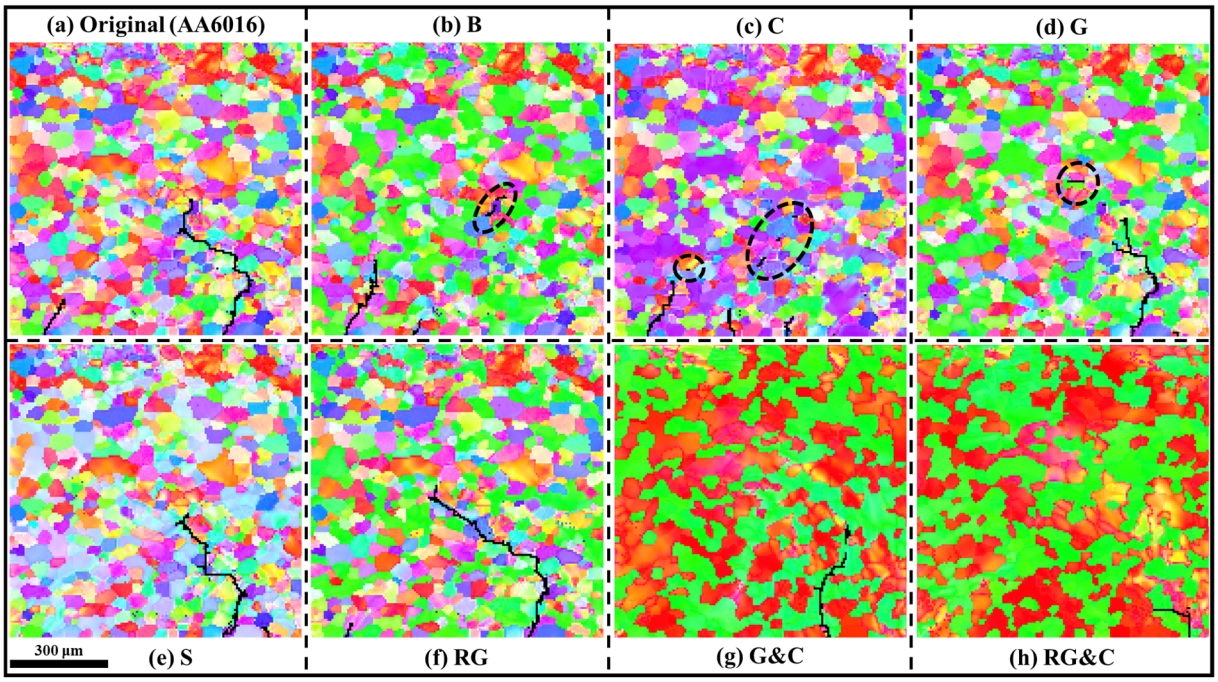

Figure 9-18: IPF maps showing texture evolution after bending along with the crack paths plotted on the undeformed initial configuration for the studied microstructures.

9.4.4 Bendability enhancement through cladding

In the previous section, it is shown that the bendability of a sheet alloy can be improved significantly by tailoring its through thickness microstructure. Texture engineering has its limits and may not be adequate for applications with extremely high bendability requirements, such as the hemming process. The results presented in Part I and within section 9.3.1 of this manuscript, demonstrate that the introduction of thin clad layers of a low strength and high ductility alloy (i.e. AA8079), along the outer rolled surfaces of a relatively higher strength and lower ductility sheet alloy (i.e. AA6016), can significantly enhance bending characteristics of the resulting composite alloy (i.e. AA6016X). Consistent with the experimental results, it is numerically shown that the composite AA6016X alloy can be wrap bent to 150° without any signs of failure along the outer tensile edge (see Figure 9-8(c-d)). It is further observed that the AA8079 clad layer experiences significant thinning in some areas along the outer tensile edge (see Figure 9-8(c)), while acting as an efficient barrier against the development of shear bands within the AA6016 core. In this section, the tendency of the cladding layer, to resist the development of shear bands within the central core, is further analyzed by performing few CPFEM based wrap-bending simulations of the composite AA6016X alloy with reduced cladding layer thicknesses of approx. 75 microns, 60 microns and 50 microns.

Figure 9-19 shows the contour plots of effective strain for the composite AA6016X alloy after wrap-bending to 150° using different initial clad layer thicknesses. The strain contour plot of the actual microstructure, with 100 microns thick cladded layers, are reproduced (in Figure 9-19(a)) for ease of comparison. Although failure is not observed, it is noted that the cladding layer has

started to lose its effectiveness when its thickness is reduced from 100 microns to 75 microns. This is apparent from Figure 9-19(b) where one can see an increasing tendency towards strain localization in mutually orthogonal bands within the core. Majority of such bands are emanating from locations of local thinning within the clad layer and the surface rumpling behavior has further intensified. Such local thinning and surface rumpling behavior is previously reported by Lloyd et al. [317] in their experimental study of AA3003/AA6111 clad system. As the clad layer thickness is reduced to 60 microns, a micro-crack initiates within the less ductile core in vicinity of the clad–core transition region, as the bending strains are reasonably high in that area (see magnified image in Figure 9-19(c). It is further observed that the ductile cladding layer is effective in blunting the crack nucleated in the core and restricting its propagation to the outer tensile surface. As the initial clad layer thickness is further reduced to 50 microns, the micro-crack propagates inward along a highly sheared region within the core, whereas strain localizes within the cladding layer in vicinity of the micro-crack, promoting significant thinning – necking of the ductile clad layer.

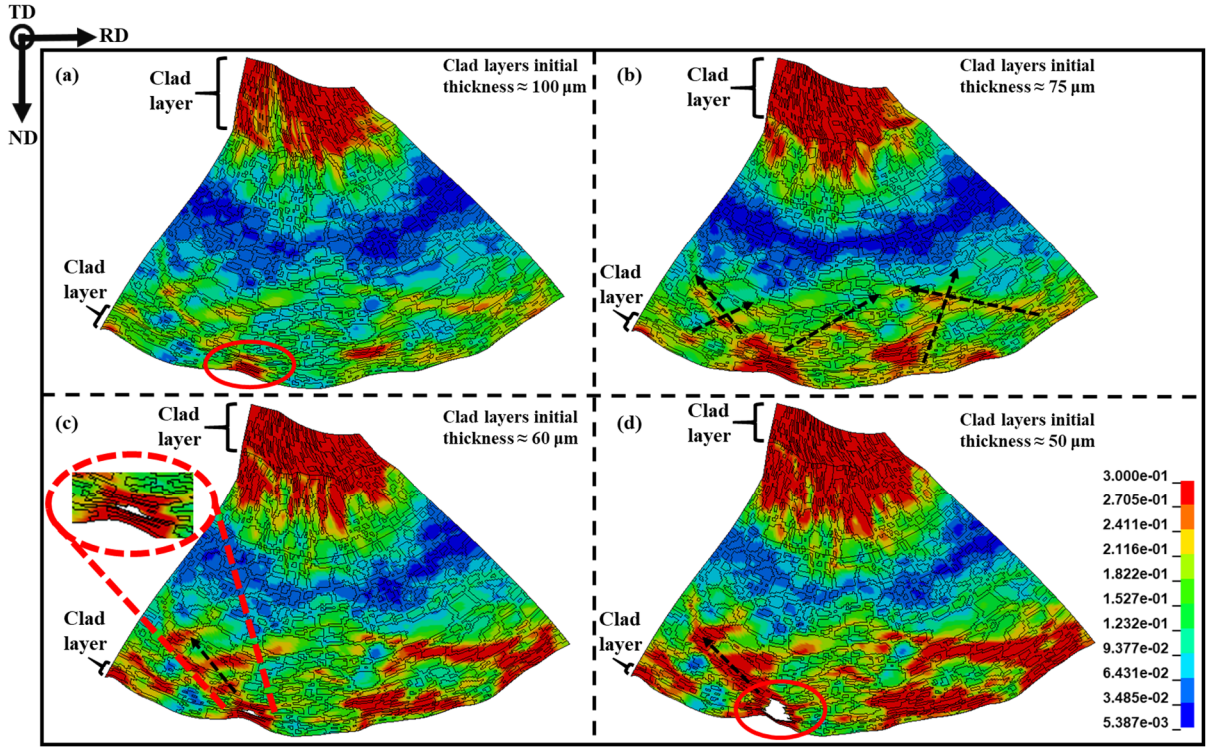

Figure 9-19: Deformed CPFEM meshes of composite AA6016X alloy showing contour of effective strain distribution after wrap bending using different initial clad layer thicknesses.

The results show that the initial thickness of AA8079 clad layers can significantly influence the bendability of the composite alloy. As the cladding thickness is decreased, the effective radius for the core increases, thereby exposing the comparatively lower ductility core to increasingly higher stresses and strains, promoting shear banding and failure within the AA6016 core. Furthermore, the thinner the cladding layer, the easier it will be for the crack that initiated within the core to propagate through the surface cladding layer. Eventually, at a sufficiently lower cladding

thickness, the bending behavior of the alloy will be controlled by failure within the cladding itself, nulling the usefulness of the cladding layer. Based on the results presented herein, it is concluded that a minimum cladding layer thickness of approx. 75 microns is required for successful wrap-bending of a 1 mm thick sheet of composite AA6016X across a 0.1 mm bend radius. Furthermore, the CPFEM based approach, presented above, can be used as a guiding tool for designing cladded aluminum alloy sheets of enhanced bendability with minimal cladding material.

9.5 Chapter Summary and Conclusions

In this work, a comprehensive CPFEM based numerical study is conducted to analyze the bending and fracture behavior of 1 mm thick sheets of AA6016 and AA6016X. AA6016X is a composite alloy, consisting of AA6016 core sandwiched between 100 μm thick clad layers of AA8079 using thermomechanical roll bonding. A multi-scale modeling approach is employed to simulate the wrap bending behavior of both alloys and the accompanying microstructural evolution, shear band development, micro-crack initiation and propagation are analyzed. A special emphasis is put on understanding the sequence of microstructural damage events and their role in promoting the eventual failure during bending. Furthermore, the relationship between local crystallographic texture, shear banding and failure (i.e. crack initiation and propagation) during bending, is examined in detail. Some of the important observations and conclusions are as follows.

- The proposed multi-scale modeling approach to wrap-bending is successfully applied to predict the experimentally observed bending and fracture behavior of AA6016 and AA6016X alloys. Numerically predicted results of texture evolution, the development of surface undulations across the outer tensile edge and the through thickness shear banding behavior after bending, show excellent conformity to the experimental data.

- Consistent with experimental observations, the simulated results show that micro-cracks initiate from the low cusp regions along the outer tensile edge and propagate inwards, predominantly in a transgranular manner along the intensely sheared planes within shear bands. Decohesion along grain boundaries (within some areas of high local misorientations) ahead of the advancing crack tip, also seems to assist crack propagation. It is concluded that grains with Cube or near Cube texture are less susceptible to shear banding and crack propagation whereas grains having near S or near Goss orientations show a much greater propensity towards formation of shear bands and failure during bending of AA6016.

- It is shown that the through-thickness strain localization in vicinity of the outer tensile region of the bend acts as a precursor to the formation of surface undulations. Upon subsequent bending, strain starts to localize into orthogonal shear bands emanating from those newly developed surface low cusp regions, further facilitating the formation of microscopic grooves along the outer tensile edge. In turn, the grooving behavior further promotes shear localization across multiple grains, leading to the formation of well-developed mutually orthogonal transgranular shear bands through-thickness of the bend.

- It is concluded that failure during bending of AA6016 is controlled by the development of these intense sheared planes that provide a minimum energy path for micro-cracks to propagate through such regions, thereby promoting a predominant transgranular failure. It is shown that the propagating micro-crack tends to alternate from one shear band to another under the influence of applied loading. It is concluded that the advancing crack tip alternate from a less critical localization condition to a more critical one, as it requires lesser energy for the creation of new fracture surfaces while still sustaining the imposed plastic deformation.

- Through a systematic study on the relationship between microstructure and bendability, it is shown that bendability of polycrystalline sheet materials can be improved significantly by altering the through thickness microstructure. It is shown that one can achieve significantly higher bend angles prior to failure by introducing relatively higher volume fractions of Copper or Brass texture components within the rolling microstructure of AA6016.

- It is concluded that Copper and Brass texture components show good resistance to the development of severe surface undulations, through-thickness shear banding and crack propagation and are therefore excellent candidates for enhancing bendability of rolled sheet materials. Goss and rotated Goss components can develop intense shear bands and it is shown that higher volume fraction of these components within the microstructure can also promote intergranular crack propagation. The S texture component is susceptible to shear band development and offers little to no resistance to crack propagation and thus exhibits by far the worst bending characteristics. It is to be noted that these conclusions regarding bendability of different texture components are valid for the bending direction being analyzed and may vary for other bending directions.

- It is further concluded that the Cube texture component enhances resistance to shear banding by accommodating plastic deformation rather easily and is therefore characterized as high bendability component. However, excess volume fraction or through thickness clustering of Cube oriented grains within the microstructure can induce local strain incompatibilities during bending, which can severely degrade the surface roughness characteristics and final appearance of the bent sheet.

- It is numerically shown that the initial thickness of the AA8079 clad layers can significantly influence the bendability of the composite AA6016X alloy. It is concluded that the ductile clad layer provides an efficient barrier against development of shear bands within the less ductile inner core by accommodating a substantial portion of the imposed bending strains along the outer tensile edge through significant thinning and even local necking within certain regions. It is further shown that once a micro-crack initiates within the central core, the ductile clad layer can blunt its propagation towards the surface.

- Lastly, the developed CPFEM based approach presented herein, can be employed as a guiding tool for developing aluminum alloy sheets with enhanced bendability.

Chapter 10: Development of Planar Deformation Bands and Coincidence Site Lattice Boundaries in a Precipitation Hardened Aluminum alloy

In this chapter, some novel experimental findings related to the occurrence of deformation banding and the formation of coincidence site lattice (CSL) boundaries in an AA6xxx series precipitation hardened aluminum alloy during simple shear deformation are reported. It is well-known that CSL boundaries have special characteristics (i.e. boundary mobility and energy). Depending on the degree of coincidence (i.e. Σ value), such boundaries can show resistance to crack propagation. The results presented in this chapter form basis for the future work on improving the hardening model and fracture criterion.

The chapter presents an accepted manuscript of an article published in Scripta Materialia journal.

Scripta Materialia 162 (2019): 300-305. Doi: 10.1016/j.scriptamat.2018.11.032

Deformation Banding in a Precipitation Hardened Aluminum alloy during Simple Shear Deformation

Scripta Materialia 162 (2019): 300-305

Waqas Muhammad[1,2], Rama K. Sabat[1], Abhijit P. Brahme[1], Jidong Kang[2], Raja K. Mishra[3], Babak Shalchi-Amirkhiz[2], Jürgen Hirsch[4], Kaan Inal[1]

1 Department of Mechanical and Mechatronics Engineering, University of Waterloo, Waterloo, N2L 3G1, Canada

2 CanmetMATERIALS, 183 Longwood Road South, Hamilton, ON L8P 0A5, Canada

3 General Motors Research & Development Center, Warren, MI 48090, USA

4 Hydro Aluminium Rolled Products GmbH, Research and Development, D-53117, Germany

Overview

Simple shear deformation of a precipitation hardened aluminum alloy showed the formation of planar deformation bands on a set of parallel {111} planes. Band formation is more profuse in the near {101}[*uvw*] and {111}[*uvw*] oriented grains and their lateral growth is limited by the formation of special coincident site lattice boundaries. Irrespective of the parent grain orientation, these deformation bands are misoriented by approx. 40˚ with respect to the parent grain. The extended dislocations could not cross-slip, promoting planar slip and the formation of planar deformation bands upon persistent plastic deformation.

Keywords: Simple shear; Mechanical properties; Electron backscatter diffraction (EBSD); Coincidence lattice; Aluminum alloys

10.1 Introduction

Planar slip and wavy-distributed glide are the most common slip modes observed during plastic deformation of metals and alloys. Planar slip, characteristic of inhomogeneous plastic deformation, is concentrated on few slip systems and is usually observed in alloys with low stacking-fault energy (SFE) [341–347]. With persistent plastic deformation, these alloys tend to develop coarse deformation bands accompanied by extensive strain localization within the bands [348]. Planar slip within these bands continues until an obstacle such as a high-angle grain boundary impedes further dislocation motion, thereby activating adjacent slip systems to accommodate the applied stress and further deformation [349, 350]. Wavy glide, on the other hand, is considered homogenous deformation which operates on many slip systems simultaneously and is typically observed in FCC metals and alloys with medium to high SFE [351–354]. Deformation in wavy glide materials is accompanied by the formation of multi-slip structures such as dislocation cell blocks, promoting homogeneous deformation [6–8, 156, 158, 196].

The occurrence of planar or wavy glide in pure metals and alloys depends on their SFE, with low SFE alloys favoring planar slip. Some authors have also suggested that pronounced short range

clustering (SRC) of solute in some solid solution strengthened alloys can also play a decisive role in controlling the nature of slip by promoting planar slip through a phenomenon known as glide plane softening [355–358]. Apart from solid solution strengthened alloys, it has been shown that some precipitation hardening alloys also exhibit this planar slip behavior [355, 359–362]. However, their overall slip behavior depends greatly on the kind of interaction between the moving dislocations and the finely dispersed particles which act as obstacles against shearing. Gliding dislocations can either shear through or bypass the precipitated particles depending on the coherency of the precipitate/matrix system. It has been debated that coherent and ordered precipitates promote planar slip whereas the comparatively larger non-shearable, incoherent precipitates support wavy glide [131, 359, 361]. Hornbogen and co-workers suggested that planar slip in precipitation hardening alloys results from local work softening on the operative slip plane [363, 364]. This work softening is due to the reduced cross-section of the sheared precipitates on that specific slip plane, ultimately leading to a decrease in the obstacle strength on that individual plane due to continuous shearing of precipitates, thereby promoting planar slip. Poole et al. studied the precipitation and work hardening behavior of an Al-Mg-Si-Cu alloy (AA6111) with special emphasis on the shearable and non-shearable nature of precipitates [131]. The authors showed that dislocations on many parallel slip planes have propagated through the shearable precipitates and further reported an increase in the tendency of localized bands formation as thermal aging progressed, which is contrary to the trend predicted by Hornbogen and Gahr [364]. Several other authors suggested that the tendency of localized banding in precipitation hardening alloys is not associated with the local softening of slip plane due to shearing of coherent precipitates but instead due to the intrinsically low work hardening often observed under such conditions [131, 305, 365].

While the occurrence of planar slip has been observed in some precipitation hardening aluminum alloys, conflicting observations have been reported and there does not seem to be an agreement on the mechanism of their formation. In the present investigation, deformation banding and the formation of planar slip bands is studied during simple shear deformation of a precipitation hardening aluminum alloy. The observed planar slip behavior is analyzed in light of crystallographic texture and microstructure development and is linked with the formation of stacking faults and the inherent difficulty to cross slip.

10.2 Experimental Procedures

An age-hardenable Al-Mg-Si alloy with Fe and Mn additions was used in the present study. The alloy was received as an extruded profile with a nominal wall thickness of 2.0 mm, in a T6 tempered condition. The chemical composition of the alloy is given in Table 10-1. Quasi-static, room temperature simple shear tests were carried out along the extrusion direction to characterize the in-plane simple shear response of the alloy. Detailed information on specimen geometry and test procedure is provided elsewhere [366]. Electron backscatter diffraction (EBSD) measurements were performed to study the microstructure evolution during simple shear deformation. The EBSD measurements were made on the ED-TD shear plane with TD being the transverse direction using

a field-emission Nova NanoSEM™. Transmission electron microscopy (TEM) was performed at 200 keV using FEI's Tecnai Osiris STEM.

Table 10-1: Chemical composition (wt%) of as-received extruded alloy.

Mg	Si	Cu	Fe	Mn	Al
0.92	0.65	0.3	0.25	0.2	Bal.

10.3 Results and Discussion

A representative thin-film high-angle annular dark-field (HAADF) TEM microstructure of as-received material with EDS elemental mapping is shown in Figure 10-1(a). The microstructure shows the presence of several near round shape particles with an approximate size of 150 nm. The EDS mapping results reveal that these 2nd phase particles are of α-Al(FeMn)Si type. Furthermore, the bright field (BF) TEM image (in in Figure 10-1(b)) shows the presence of very fine (~ 4.0 nm in size) needle-shaped and spherical strengthening precipitates. It is apparent from the corresponding EDS mapping results (in Figure 10-1(b)) that most of these Mg-Si based precipitates contain Cu enrichment, highlighting the existence of Q phase (Mg-Si-Cu) precipitates.

Figure 10-2(a) shows the inverse pole figure (IPF) map after simple shear deformation. The average grain size of the material after deformation is approx. 300 μm and the presence of several coarse planar deformation bands have been observed within several grains. These deformation bands form an angle of approx. 45°-50° with the vertical loading axis (i.e. ED). The length of the bands is comparable to the grain size, whereas their lateral width is approx. between 5 μm to 25 μm. The formation of these deformation bands is more apparent in the near $\{101\}[uvw]$ and near $\{111\}[uvw]$ oriented grains as apparent from the IPF map. Unlike the previous observations by several authors where the occurrence of multiple planar slip bands intersecting on different {111} planes was reported [131, 305, 360], the present results in Figure 10-2(a) show the occurrence of deformation banding which is limited to a set of parallel slip directions.

To investigate the effects of grain size on deformation banding, the EBSD data is partitioned to separate grains without and with deformation bands and the results are shown in Figure 10-2(b) and Figure 10-2(c) respectively. It is noticed that grains which are smaller than approx. 100 μm in size do not show deformation banding. On the other hand, not all grains bigger than 100 μm in size show band formation. However, consistent with previously reported results in literature [305, 367], it seems that deformation banding is weakly dependent on grain size, being more widespread in relatively coarser grains. Furthermore, the <111> pole figures, corresponding to grains without and with deformation banding (see Figure 10-2(d) and Figure 10-2(e) respectively), show that there are subtle differences in the location of texture poles and their corresponding peak intensities for the two cases. The evolution of local crystallographic texture is further investigated by analyzing the orientation relationship between the parent grains and the corresponding deformation bands that form within those parent grains. The orientation relationship for two such grains (encircled in Figure 10-2(c)) is shown by the <111> pole figure in in Figure 10-2(f). It is observed

that the poles for regions within the deformation bands show a significant rotation with respect to their parent grains. It is noted that the observed misorientation between parent crystal lattice and the band has a mix of both tilt and twist character (as shown in Figure 10-2(g)) and is accommodated by edge and screw dislocations, respectively. Furthermore, there exists a crystallographic relationship between the planar deformation band and its parent grain. It is observed that irrespective of the parent grain orientation, the orientation mismatch between the parent grain and its corresponding deformation band is fixed as indicated by the <111> pole figure plot in Figure 10-2(h). This misorientation is approx. 40˚ as represented by the angle/axis misorientation results in Figure 10-2(i).

The effects of grain orientation on the observed banding behavior have been examined by calculating the Schmid factor for the primary {111}<110> slip systems and the results are shown in Figure 10-3(a). It is observed that irrespective of the grain size, grains with a Schmid factor of greater than approx. 0.3 show a larger propensity towards formation of planar slip bands. It is further noticed that for those grains showing presence of planar slip bands, the Schmid factor within the band is relatively higher than the parent grain as shown by regions encircled in black in Figure 10-3(a). This suggests that the higher resolved shear stress within the band has led to strong dislocation channeling within the band, resulting in a region with a relatively high cumulative misorientation across it, as apparent from the IPF map in Figure 10-2(a). This accommodation of deformation reorients the local texture in a manner that further promotes an increase in the Schmid factor within the band. This increase in Schmid factor further promotes strong slip activity within the band. These observations are further supported by the geometrically necessary dislocation (GND) density map in Figure 10-3(b), where a significantly higher GND content is observed for regions within the bands. The dislocation density within the planar bands is, on average, an order of magnitude higher as compared to regions that are away or outside the bands. Based on the experimental results, it is apparent that the simple shear deformation behavior of the investigated alloy is heterogeneous at local (i.e. within grain) as well as global level. Locally, the presence of planar deformation bands within several grains suggests that the deformation within those grains is rather heterogeneous and the large variation in GND content across several grains (as observed in Figure 10-3(b)) further suggests that the shear deformation is also heterogeneous at the global scale.

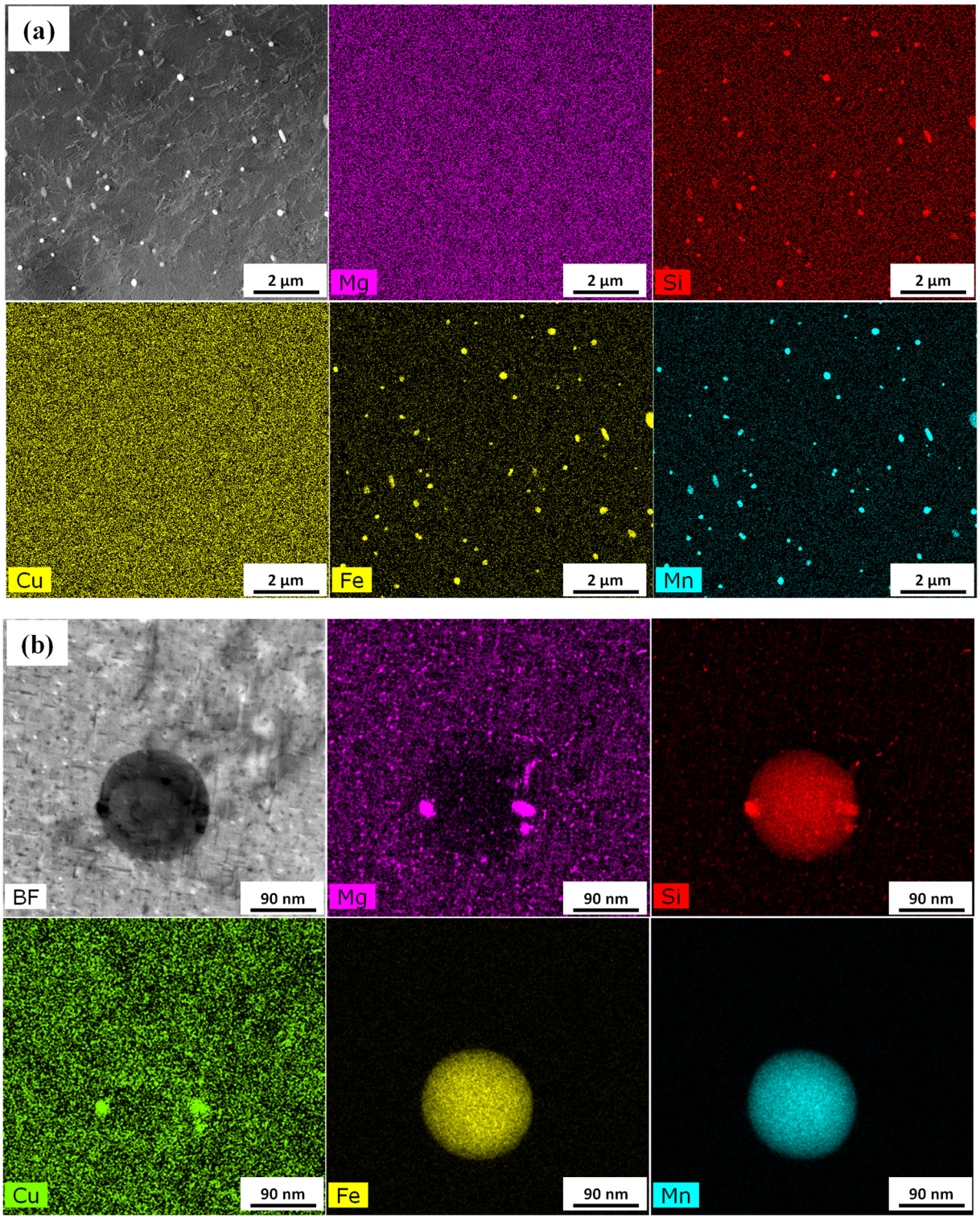

Figure 10-1: (a) HAADF-STEM image and (b) BF-STEM image along with corresponding EDS elemental mapping of the as-received microstructure showing Mg-Si-Cu based precipitates and intermetallic particles.

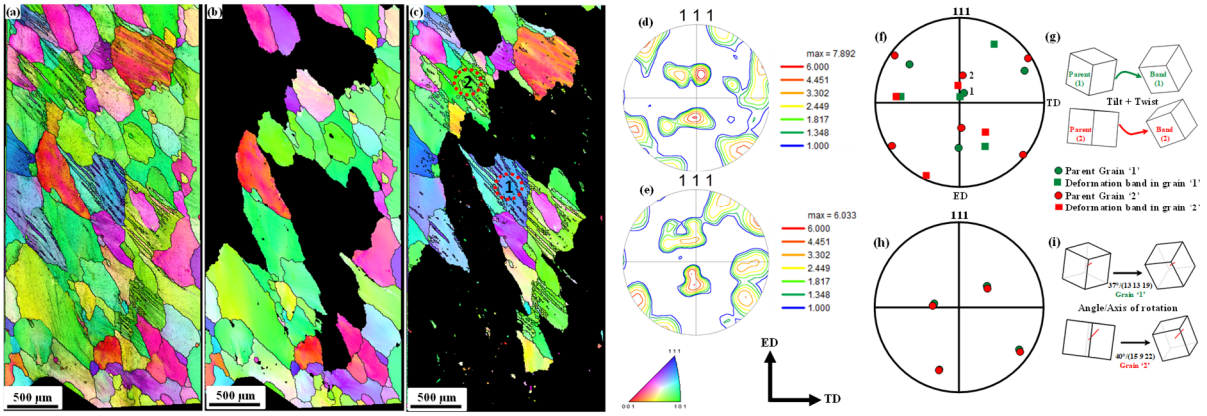

Figure 10-2: (a) Inverse pole figure (IPF) map of the region within the shear zone after simple shear deformation along ED and partition of IPF map and the corresponding <111> pole figures for grains without (b), (d) and with (c), (e) deformation bands. (f) <111> pole figure showing the orientation relationship between the parent grain and the deformation bands within the parent grain for grains '1' and '2' encircled in Figure 10-2(c); (g) Crystal lattice orientation of the parent grain and the deformation band for grains '1' and '2'; (h) <111> pole figure of the misorientation angle between the parent grain and the corresponding deformation bands for grains '1' and '2' plotted with respect to the reference frame of the parent grain; (i) Angle/axis of rotation misorientation relationship between the parent grain and the deformation band for grains '1' and '2'.

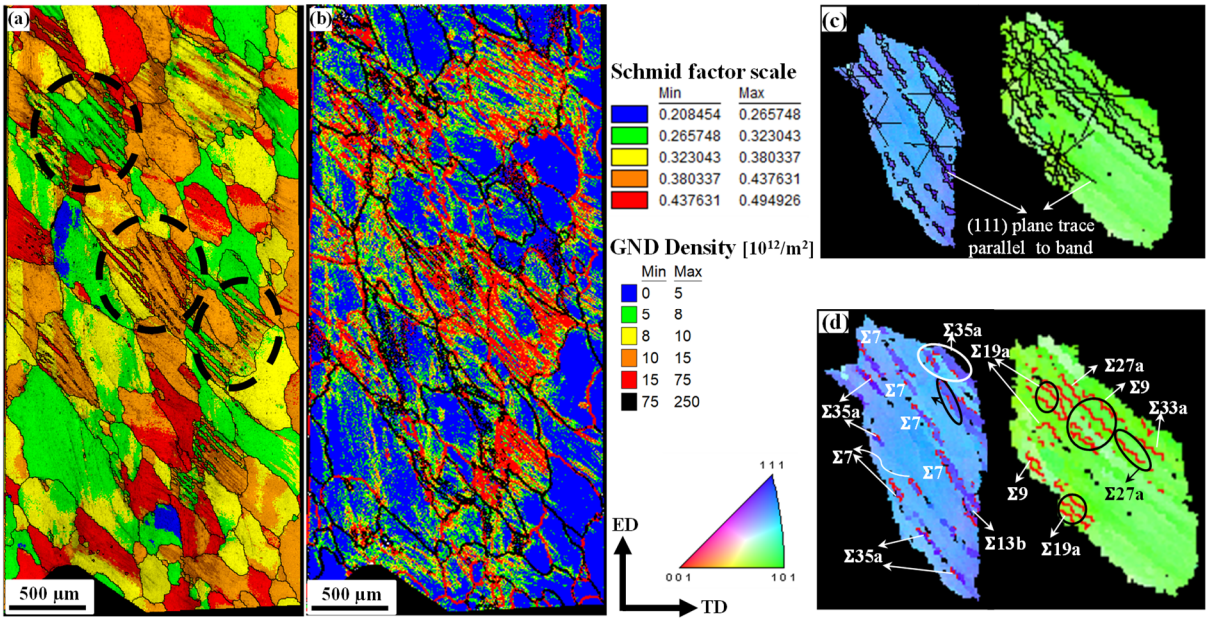

Figure 10-3: (a) Schmid factor map for simple shear loading along the {111}<110> family slip systems; (b) Geometrically necessary dislocations (GND) density map showing dislocation content after shear deformation; (c) Relationship between the (111) Slip plane traces and deformation banding; (d) Lateral growth of planar slip bands and the formation of special coincident site lattice (CSL) boundaries.

Typically, the multi-slip nature and the ease of cross-slip in aluminum alloys lead to significant evolution of dislocation substructure, promoting homogeneous deformation in these alloys [352, 353]. However, it has been established that alloying additions decrease the SFE of aluminum alloys [368–370]. Muzyk and coworkers have shown that the addition of alloying elements such as Mg,

Fe and Mn in Al matrix can bring about significant increase in the tendency for formation of partial dislocations and the SFE of the resulting alloys has been lowered by up to 40% [369]. Furthermore, the presence of numerous stacking faults after equal channel angular pressing has been reported in a precipitation hardening aluminum alloy having comparable composition to the current alloy being studied [371]. In line with these observations, stacking faults were observed after simple shear deformation in the present study, as shown in the bright field TEM image in Figure 10-4(a). The width of these stacking faults is approximated to be 2 nm and their presence indicates the inability of the extended screw dislocations to cross-slip onto other intersecting slip planes, thereby promoting planar slip which is characteristic of heterogeneous plastic deformation [341, 342].

It is well known that gliding dislocation in FCC crystals tend to dissociate into partials known as an extended dislocation and the region between them is a stacking fault (as shown schematically in Figure 10-4(b-c). The separation (or the stacking fault ribbon width W) between the partials is inversely proportional to the SFE of the alloy. An extended screw dislocation is constrained to move in the {111} plane of the fault as it cannot cross slip to an intersecting plane, unless the moving partials recombine into a perfect dislocation. This requires constriction in the stacking fault ribbon which is achieved rather easily in high SFE materials due to lower ribbon widths (see Figure 10-4(b)) thereby allowing cross-slip. On the contrary, the ribbon width for low SFE alloys (as is the case for the present alloy) is relatively much larger which makes it more difficult to produce constrictions in the stacking faults, thereby reducing or preventing the tendency to cross-slip (see Figure 10-4(c)). In this case, the extended dislocation is constrained to move in the same plane and upon persistent deformation, dislocation multiplication would continuously generate more dislocations on the same plane, thereby promoting the observed planar slip behavior. Deformation can continue by further emission of dislocations from the same sources or by new sources activated on neighboring parallel {111} planes. This phenomenon is further supported by the EBSD measurement results, where the slip plane trace analysis shows multiple sets of parallel planar slip bands aligned with the trace of {111} slip planes as shown in Figure 10-3(c). Apart from affecting the cross-slip behavior, the lower SFE also increases the strength of the obstacles given by the forest dislocations, thereby increasing the levels of latent hardening [372, 373]. It is suggested that the stacking faults might prevent the glide of other dislocations on slip planes crossing the faulted planes due to the inherent difficulty faced by the dislocations on the second set of slip planes cutting through the faulted region on the first slip system, thus further promoting planar slip behavior. However, as mentioned in the introduction, the presence of shearable precipitates can also facilitate this planar slip behavior in precipitation hardened aluminum alloys [355, 359].

In the present study, it is further observed that the longitudinal growth of the planar slip bands is limited by the high angle grain boundaries which act as strong barriers to further propagation and their lateral growth is influenced by the formation of special coincident site lattice (CSL) boundaries as shown in Figure 10-3(d). These boundaries are identified as type Σ7, Σ9, Σ13b, Σ19a, Σ27a, Σ33a and Σ35a, out of which Σ7, Σ13b and Σ19a boundaries usually exhibit relatively higher

mobility [374]. The CSL boundaries are typically associated with low boundary energy and can lead to stable structures. In the current study, the observed CSL boundaries are straight or planar in nature and are formed discontinuously in specific orientations as the deformation proceeds. This discontinuous formation of boundaries can lead to localization of deformation within the planar boundary regions, further assisting planar slip [375]. Furthermore, it is suggested that the lateral inhibition of planar slip by the newly created CSL boundaries may well be associated with the difficulty of slip transfer across such boundaries due to the inherent boundary misorientation. The interaction of dislocations with CSL boundaries has been studied by several researchers and it has been shown that such boundaries can provide an effective barrier to dislocation passage [376–378]. As the new boundaries are formed during simple shear deformation, further slip activity would cause several of the moving dislocations to terminate at the boundary, leading to the pilling up of dislocations. This piling up of dislocations would significantly increase the GND content across such boundaries as shown in Figure 10-3(b). Furthermore, this slip inhibition also leads to locally misoriented regions across such boundaries, as shown in Figure 10-2(f). In a separate study, the authors have not observed the formation of such CSL boundaries under tensile deformation of the same alloy. In the present study, the formation of these CSL boundaries under simple shear deformation may well be associated with the fact that in shear tests, one can avoid the early localization-necking phenomenon commonly observed in uniaxial tension tests. The formation of these CSL boundaries may also play a significant role in controlling the fracture and recrystallization behavior of the alloy.

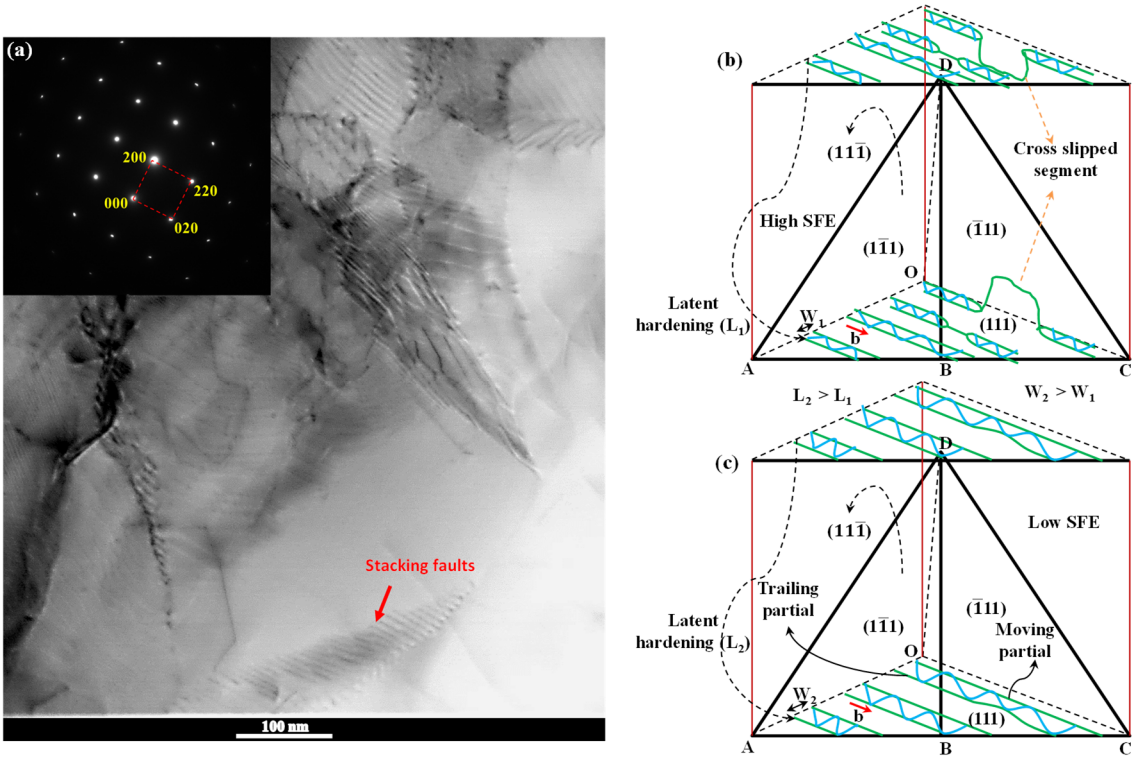

Figure 10-4: (a) Bright field TEM image showing presence of stacking faults after shear deformation; (b) and (c) Schematic tetrahedron showing the effect of SFE on cross slip and latent hardening.

10.4 Chapter Conclusions

A strong propensity to form planar deformation bands is observed in an extruded precipitation hardened aluminum alloy. Multiple sets of deformation bands are formed via dislocation activity on a set of parallel {111} slip planes. The longitudinal and lateral growth of planar slip bands are limited by high angle grain boundaries and special CSL boundaries, respectively. The formation of these deformation bands is more profound in the near {101}[*uvw*] and {111}[*uvw*] oriented grains and the region within the bands show a comparatively higher Schmid factor and GND content. Regardless of the parent grain orientation, these deformation bands are misoriented by approx. 40˚ with respect to the parent grain. Stacking faults are observed after the deformation and the formation of planar slip bands is attributed to the inherent difficulty for an extended screw dislocation to cross-slip to an intersecting {111} plane.

Chapter 11: Conclusions & Future Work

11.1 Key Conclusions

The goal of this work is to enhance the existing experimental understanding and modeling capabilities with respect to strain localization, shear banding and fracture in precipitation hardened aluminum alloys, through the development and coupling of multiscale modeling frameworks with advanced constitutive models for work hardening and failure. In this regard, a new slip level hardening model is proposed that employs the experimentally measured microstructure to incorporate the effects of intragranular backstresses due to the formation of deformation and precipitation induced dislocation cellular substructure. A new failure criterion is proposed that employs the nano-void coalescence theory to predict failure in precipitation hardened aluminum alloys. A new multiscale modeling framework is developed that couples the rather computationally efficient macro-scale component level phenomenological modeling to micro-scale crystal plasticity based finite element modeling that can represent all relevant microstructural physics, to attain a reasonable compromise between accuracy and computational efficiency. As a result of this work, a new understanding of the microstructure – property relationships applicable to age-hardenable aluminum alloys has been gained. Some of the key observations and conclusions based on the work presented in this thesis are summarized next.

11.1.1 Development and Validation of Slip level Hardening Model for Precipitation Hardened Aluminum alloys

- Strain hardening in precipitation hardened AA6063 shows the presence of precipitation induced dislocation cell substructure within the microstructure after cyclic simple shear deformation of AA6063.
- The substructure starts as pinned dislocation tangles with some regions having relatively high dislocation content while others being virtually dislocation free. With persistent deformation the substructure evolves into a well defined equiaxed cell/subgrain structure with majority of dislocations being trapped at the subgrain cell wall boundaries.
- The substructure induces intragranular backstresses due to blockage of dislocation passage leading to kinematic hardening – Bauschinger effect at the macroscopic scale.
- Strain softening is observed prior to failure during forward simple shear deformation. The softening behavior is associated with texture evolution that promotes continuous rotation of texture components during simple shear deformation.
- A crystal plasticity based backstress hardening model is proposed to account for the intragranular backstresses which arise from the formation of dislocation cell substructure in the microstructure.
- The backstress hardening is introduced at slip system level and consequently it induces a latent hardening effect which manifests as differences in strain localization at macroscopic

scale. The proposed model successfully predicts the experimentally observed strain localization behavior during cyclic simple shear deformation.

- The model successfully predicts the experimentally measured flow behavior during cyclic simple shear and cyclic TCT and CTC loading. More importantly, the new backstress hardening model can reproduce the experimentally observed Bauschinger effect upon loading reversal.
- It is noted that the simulated TCT and CTC results show discrepancies from the experimentally measured behavior within the elasto-plastic transition regime or the so-called short transient regime. These discrepancies may well be associated with the change in the effective elastic modulus with deformation and the proposed model is unable to account for such changes. On the other hand, the model performs significantly better in predicting the long-transient effect or the so-called steady state behavior. This better prediction of the long transient behavior may well be related with the buildup of elastic phase (i.e. cell walls - boundaries) and the associated induced internal stresses with deformation.
- In the present work, the induced backstresses are linked with the formation of cell substructure in which the walls are impenetrable elastic regions within an elasto-plastic core shell structure. However, recent in-situ TEM studies have shown that the cell walls do not exactly behave as impenetrable elastic medium, with dislocations penetrating or inserting on one side of the wall and emerging from the other. Hence a more sophisticated approach of modeling such behavior would be required. Studies have also shown that a structured dislocation microstructure (i.e. cellular substructure) is not a pre-requisite for generation of internal stresses. In fact, similar backstress effects have been observed in materials with non-structured dislocation substructures. In this regard, models based on dislocation density evolution laws may be better suited to account for such induced internal stresses.
- Lastly, to properly predict the flow and the experimentally observed Bauschinger effect in precipitation hardened aluminum alloys, a physically motivated model that can account for the induced internal stresses, must be employed to describe material hardening on a polycrystalline level.

11.1.2 Development and Application of a Multiscale Modeling Framework to predict Strain Localization and Surface Roughness during bending

- A multiscale modeling approach is developed where a macro-scale component level simulation is performed using conventional phenomenological plasticity and the boundary conditions of the region of interest are extracted and applied to the crystal plasticity based finite element model that accounts for the relevant microstructural physics such as grain morphology, texture, dislocation-precipitate interactions etc.

- The proposed approach enhances existing modeling capabilities for better predictability of material response under complex loading paths as simplified assumptions (i.e. such as pure bending) are not required due to availability of actual - realistic boundary conditions.
- The proposed multi-scale approach in conjunction with the backstress hardening model (developed in the previous chapter) are employed to successfully predict the experimentally observed texture evolution, slip band formation within grains, through thickness strain localization and the development of surface roughness during bending of AA6063.
- Based on detailed experimental investigation, it is concluded that the development of surface undulations on the outer tensile surface is not a mere surface effect but is in fact linked with strain localization through thickness of the bend.
- It is concluded that the development of surface roughness along the outer bend surface acts as a precursor to fracture.
- It is concluded that the observed surface ridging phenomenon along the outer tensile surface during bending is promoted by the collective co-deformation of similarly oriented crystals assembled in layers or grain clusters through thickness of the material.
- Lastly, it is established that by eliminating or by reducing the tendency towards clustering of similarly oriented grains within the microstructure, a transition from a ridging to an orange peel type surface topographic behavior can be achieved.

11.1.3 Development and Validation of Failure Criterion for Precipitation Hardened Aluminum Alloys

- A new constitutive approach is proposed to predict failure by extending the existing nano-void theory of ductile failure to precipitation hardened aluminum alloys by incorporating the effects of dynamic microstructure evolution due to the formation of deformation and precipitation induced cellular dislocation substructure.
- The newly proposed failure criterion accounts for the effects of precipitation induced dislocation substructure on point defect generation by incorporating a new evolution law for the effective obstacle strength associated with substructure evolution.
- The new failure criterion is successfully validated against experimental data by predicting tensile failure strains for three AA6xxx series age-hardened aluminum alloys with very different starting microstructures and processing history.
- The versatility of the proposed constitutive approach is demonstrated by coupling the failure criterion with stress-strain data generated through crystal plasticity simulations, to predict failure strain for arbitrary loading – stress triaxiality conditions.
- It is noted that the point defect generation - vacancy concentrations reported in the present work are significantly higher than equilibrium vacancy concentrations. The deformation induced point defect generation reported in the present work for precipitation hardened

aluminum alloys are an order of magnitude higher than previously reported results by Saimoto and co-workers for pure and solid solution strengthened aluminum alloys.

11.1.4 Relationship between Microstructure, Plastic Deformation and Fracture behavior of Precipitation Hardened Aluminum alloys

- The comprehensive experimental study investigates the relationship between microstructure, the nature of plastic deformation, surface topography development, shear banding, grain boundary decohesion, macro-crack initiation and propagation during bending of 1 mm thick sheets of monolithic AA6016 and cladded AA6016X alloys.
- It is concluded that the bendability of monolithic AA6016 alloy is limited by the formation of severe surface undulations and surface cracking, which is associated with the heterogenous nature of slip concentrating into coarse slip bands and intense shear banding originating from surface low cusps in the form of mutually orthogonal transgranular bands.
- It is concluded that the fracture behavior of AA6016 is dominantly transgranular in nature with micro-cracks originating from low cusp regions along the outer tensile surface and propagating along the intensely sheared planes within shear bands.
- It is further concluded that grains with S texture component are prone to shear banding and failure during bending and the contrary is true for Cube oriented grains.
- It is concluded that intergranular micro-void nucleation and crack propagation is favored in areas with high grain boundary misorientations and intense slip band impingements along boundaries, perhaps due to the reduction in local cohesive strength of such boundaries.
- It is shown that the significant bending strains in AA6016X are accommodated homogeneously through a grain subdivision process within the clad layers. It is this homogeneous accommodation of strain, which is responsible for the low surface roughness and extremely high bendability of the alloy.
- Lastly, it is concluded that the bendability of an AA6xxx series precipitation hardened aluminum alloy can be improved drastically by cladding it with a non-age hardenable AA8xxx series aluminum alloy through a properly conducted thermomechanical roll bonding process.

11.1.5 Multiscale Modeling of Strain localization, Shear Banding and Fracture

- The developed multiscale modeling approach in conjunction with the newly developed hardening and failure models for age-hardenable aluminum alloys are used to predict the experimentally observed shear banding and fracture behavior of AA6016 and AA6016X alloys during bending.
- The simulated results successfully predict the experimentally observed shear banding and transgranular fracture behavior.

- It is numerically shown that that the propagating micro-crack tends to alternate from one shear band to another under the influence of applied loading. It is concluded that the advancing crack tip alternates from a less critical localization condition to a more critical one, as it requires less energy for the creation of new fracture surfaces while still sustaining the imposed plastic deformation.
- It is concluded that Copper and Brass texture components show good resistance to the development of severe surface undulations and shear banding and are therefore excellent candidates for enhancing bendability of rolled sheets materials.
- Goss and rotated Goss components can develop intense shear bands and it is shown that higher volume fraction of these components within the microstructure can also promote intergranular crack propagation.
- S texture component is susceptible to shear band development and offers little to no resistance to crack propagation and thus exhibits by far the worst bending characteristics
- Cube texture component accommodates plastic deformation rather easily and is therefore characterized as high bendability component. However, excess volume fraction or through thickness clustering of Cube oriented grains within the microstructure can induce local strain incompatibilities that can severely degrade the surface roughness characteristics.
- It is numerically shown that the ductile clad layer provides an efficient barrier against development of shear bands within the less ductile inner core by accommodating a substantial portion of the imposed bending strains along the outer tensile edge.
- The developed CPFEM based approach presented herein, can be used as a guiding tool for development of aluminum alloy sheets with enhanced bendability.

11.1.6 Development of Planar Deformation Bands and Coincidence Site Lattice Boundaries in a Precipitation Hardened Aluminum alloy

- A strong propensity to form planar deformation bands on a set of parallel {111} planes is observed in an extruded precipitation hardened aluminum alloy.
- Band formation is more profuse in the near {101}[uvw] and {111} [uvw] oriented grains.
- The lateral growth of these planar deformation bands is limited by the formation of special coincident site lattice (CSL) boundaries.
- Regardless of the parent grain orientation, these deformation bands are misoriented by approx. 40° with respect to the parent grain.
- In the present work, planar band formation is attributed to the inherent difficulty for an extended dislocation to cross-slip to an intersecting {111} plane. It is important to mention that the current TEM observations related to the presence of stacking faults after simple shear deformation are rather very preliminary in nature and require further investigation. As such, the formation of stacking faults and the associated difficulty to cross-slip can be viewed as a candidate mechanism for formation of planar deformation bands. Other more likely mechanisms include pronounced short range clustering of solute and precipitate shearing, promoting slip localization.

- The formation of planar deformation bands, the deformation induced CSL boundaries and the associated heterogeneous plastic deformation may all play a significant role in controlling the fracture behavior of the studied age-hardenable aluminum alloy.

11.2 Future Work

The coupled framework, including the multiscale modeling approach, the constitutive work hardening model and the failure criterion presented in this thesis provide an excellent tool for computer-aided engineering, virtual material characterization and analysis of microstructure-property relationships. The proposed constitutive model can be extended to include the elevated temperature effects, which require further consideration of thermo-mechanically influenced mechanisms such as dislocation climb and dynamic recovery. Inclusion of thermal effects would enable the model to be applied to warm forming or high-temperature deformation processes such as extrusion and modeling heat affected zones of welded parts. Another important aspect to be considered is the incorporation of high-strain rate effects into the proposed constitutive model. High strain-rates are routinely experienced during automotive crashworthiness testing and high through-put forming operations, therefore an advanced constitutive model that can predict material behavior under elevated temperature and high strain-rate conditions would be invaluable.

The failure criterion proposed in the present work is based on nano-void ductile failure theory where it is assumed that nano-voids form at pre-existing nano-particles that are distributed homogeneously throughout the material matrix. However, for age-hardenable aluminum alloys, preferential or heterogeneous distribution of precipitate particles is typically observed. As such, the extension of the proposed criterion to account for such initial heterogeneity within the starting microstructure would further improve model predictions for materials exhibiting severe microstructural heterogeneity. In addition, in the present work, the versatility of the proposed constitutive model is demonstrated by coupling the failure criterion with stress-strain data generated through crystal plasticity simulations, to predict failure strain for arbitrary loading – stress triaxiality conditions. Such failure strain versus stress-triaxiality data is invaluable as it is routinely used as an input for modeling failure within conventional phenomenological plasticity based finite element (FE) simulations. The next logical step would be to conduct such forming and crashworthiness simulations to further validate the wide-scale applicability of the proposed approach.

Lastly, in Chapter 10 of this thesis, it has been shown that under certain processing and loading conditions, age-hardenable aluminum alloys can show a very heterogeneous deformation behavior, exhibiting the formation of planar deformation bands and deformation induced CSL boundaries. Such deformation characteristics may play a vital role in controlling the work hardening and fracture behavior of age-hardenable aluminum alloys and require further investigation.

References

[1] "US Bureau of Transportation Statistics." [Online]. Available: http://www.rita.dot.gov/bts/sites/rita.dot.gov.bts%0A/files/publications/national_transportation_statistics/index.html. [Accessed: 24-Feb-2017].

[2] S. Esmaeili, "Precipitation hardening behavior of AA6111," University of British Columbia, 2002.

[3] Altek-Mhd, "7000 series aluminum wrought alloys." [Online]. Available: http://altek-mhd.ru/en/articles/overview7k2. [Accessed: 20-Feb-2017].

[4] M. Liu, "Investigation of Quenched-in Vacancies in Pure Aluminium and the Precipitation in Al-Zn-Mg Alloys," p. 63, 2010.

[5] T. Belytschko, "Advanced Finite Elements," *Civil Engineering Department, Northwestern University*. [Online]. Available: http://www.tam.northwestern.edu/tb/D26/. [Accessed: 26-Feb-2017].

[6] H. Mughrabi, "Dislocation wall and cell structures and long-range internal stresses in deformed metal crystals," *Acta Metall.*, vol. 31, no. 9, pp. 1367–1379, 1983.

[7] M. Sauzay, "Analytical modelling of intragranular backstresses due to deformation induced dislocation microstructures," *Int. J. Plast.*, vol. 24, no. 5, pp. 727–745, 2008.

[8] T. Hasegawa, T. Yakou, and S. Karashima, "Deformation behaviour and dislocation structures upon stress reversal in polycrystalline aluminium," *Mater. Sci. Eng.*, vol. 20, pp. 267–276, 1975.

[9] X. Huang and G. Winther, "Dislocation structures. Part I. Grain orientation dependence," *Philos. Mag.*, vol. 87, no. 33, pp. 5189–5214, 2007.

[10] A. H. Cottrell and D. L. Dexter, "Dislocations and plastic flow in crystals," *Am. J. Phys.*, vol. 22, no. 4, pp. 242–243, 1954.

[11] D. Kuhlmann-Wilsdorf and C. Laird, "Dislocation behavior in fatigue II. Friction stress and back stress as inferred from an analysis of hysteresis loops," *Mater. Sci. Eng.*, vol. 37, no. 2, pp. 111–120, 1979.

[12] T. Ungar, H. Mughrabi, M. Wilkens, and A. Hilscher, "Long-range internal stresses and asymmetric X-ray line-broadening in tensile-deformed [001]-oriented copper single crystals: the correction of an erratum," *Philos. Mag. A*, vol. 64, no. 2, pp. 495–496, 1991.

[13] M. Huang, Z. Li, and J. Tong, "The influence of dislocation climb on the mechanical behavior of polycrystals and grain size effect at elevated temperature," *Int. J. Plast.*, vol. 61, pp. 112–127, Oct. 2014.

[14] D. Raabe, "Multiscale Modeling of Materials." [Online]. Available: http://www.dierk-raabe.com/multiscale-modeling/. [Accessed: 26-Feb-2017].

[15] D. R. Askeland, P. P. Fulay, and W. J. Wright, *The science and engineering of materials*. 2011.

[16] D. Hull and D. Bacon, *Book: Introduction to dislocations*, Fifth Edit. 1984.

[17] D. Hull and D. J. Bacon, *Introduction to dislocations*. Butterworth-Heinemann, 2011.

[18] H. Mughrabi, "Deformation-induced long-range internal stresses and lattice plane misorientations and the role of geometrically necessary dislocations," *Acta Mater.*, vol. 54, no. 13, pp. 3417–3427, 2006.

[19] P. Lukáš, M. Klesnil, and J. Krejčí, "Dislocations and persistent slip bands in fatigued copper single crystals," *Czechoslov. J. Phys.*, vol. 19, no. 3, pp. 335–336, 1969.

[20] M. Gerland, R. Alain, B. Ait Saadi, and J. Mendez, "Low cycle fatigue behaviour in vacuum of a 316L-type austenitic stainless steel between 20 and 600°C—Part II: Dislocation structure evolution and correlation with cyclic behaviour," *Mater. Sci. Eng. A*, vol. 229, no. 1–2, pp. 68–86, 1997.

[21] H. Mughrabi, "Cyclic plasticity and fatigue of metals," *J. Phys. IV*, vol. 3, pp. 659–668, 1993.

[22] J. Zhang and Y. Jiang, "An experimental study of the formation of typical dislocation patterns in polycrystalline copper under cyclic shear," *Acta Mater.*, vol. 55, no. 5, pp. 1831–1842, 2007.

[23] H.-J. (Hans J. Bunge and P. R. Morris, *Texture analysis in materials science : mathematical methods*. .

[24] U. F. Kocks, C. N. Tomé, and H.-R. Wenk, *Texture and anisotropy: preferred orientations in polycrystals and their effect on materials properties*. Cambridge university press, 2000.

[25] A. Von Hehl and K. Peter, "Aluminum and aluminum alloys," in *Structural Materials and Processes in Transportation*, 2013, pp. 49–99.

[26] P. Cavaliere, E. Cerri, and P. Leo, "Effect of heat treatments on mechanical properties and fracture behavior of a thixocast A356 aluminum alloy," *J. Mater. Sci.*, vol. 39, no. 5, pp. 1653–1658, 2004.

[27] T. Pardoen, D. Dumont, A. Deschamps, and Y. Brechet, "Grain boundary versus transgranular ductile failure," *J. Mech. Phys. Solids*, vol. 51, no. 4, pp. 637–665, 2003.

[28] A. Deschamps and Y. Brechet, "Influence of predeformation and agEing of an Al–Zn–Mg alloy—II. Modeling of precipitation kinetics and yield stress," *Acta Mater.*, vol. 47, no. 1, pp. 293–305, Dec. 1998.

[29] H. Jiang and R. G. Faulkner, "Modelling of grain boundary segregation, precipitation and precipitate-free zones of high strength aluminium alloys—II. Application of the models," *Acta Mater.*, vol. 44, no. 5, pp. 1865–1871, 1996.

[30] I. Westermann, O. S. Hopperstad, K. Marthinsen, and B. Holmedal, "Ageing and work-

hardening behaviour of a commercial AA7108 aluminium alloy," *Mater. Sci. Eng. A*, vol. 524, no. 1–2, pp. 151–157, 2009.

[31] J. M. Silcock, "The effect of quenching on the formation of g.p. zones and θ′ in al cu-alloys," *Philos. Mag.*, vol. 4, no. 46, pp. 1187–1194, Oct. 1959.

[32] C. García-Cordovilla and E. Louis, "Calorimetric Studies of Al-Cu Alloys: Quench Sensitivity and Sample Preparation," *Metall. Trans. A*, vol. 15, no. 2, pp. 389–391, 1984.

[33] T.-R. Chen, G.-J. Peng, and J. C. Huang, "Low quench sensitivity of superplastic 8090 AI-Li thin sheets," *Metall. Mater. Trans. A*, vol. 27, no. 10, pp. 2923–2933, 1996.

[34] D. S. Thompson, "Metallurgical factors affecting high strength aluminum alloy production," *Metall. Trans. A*, vol. 6, no. 4, pp. 671–683, 1975.

[35] A. Wilm, "Physikalisch-metallurgische Untersuchungen über magnesiumhaltige Aluminiumlegierungen," *Metallurgie*, vol. 8, pp. 225–227, 1911.

[36] H. Merica, P D; Waltenberg, R G; Scott, "Heat treatment and constitution of duralumin," *Trans AIMME*, vol. 64, p. 41, 1920.

[37] A. Guinier, "Structure of Age-Hardened Aluminium-Copper Alloys," *Nature*, vol. 142, pp. 569–570, 1938.

[38] G. D. Preston, "The Diffraction of X-Rays by Age-Hardening Aluminium Copper Alloys," *Proc. R. Soc. London. Ser. A. Math. Phys. Sci.*, vol. 167, no. 931, p. 526 LP-538, Sep. 1938.

[39] P. B. Hirsch, A. Howie, R. B. Nicholson, D. W. Pashley, M. J. Whelan, and L. Marton, "Electron microscopy of Thin Crystals," *Phys. Today*, vol. 19, no. 10, p. 93, 1966.

[40] G. Gottstein, *Physikalische Grundlagen der Materialkunde*. Springer Berlin Heidelberg, 2007.

[41] L. Löchte, A. Gitt, G. Gottstein, and I. Hurtado, "Simulation of the evolution of GP zones in Al–Cu alloys: an extended Cahn–Hilliard approach," *Acta Mater.*, vol. 48, no. 11, pp. 2969–2984, 2000.

[42] S. Pogatscher, H. Antrekowitsch, H. Leitner, T. Ebner, and P. J. Uggowitzer, "Mechanisms controlling the artificial aging of Al–Mg–Si Alloys," *Acta Mater.*, vol. 59, no. 9, pp. 3352–3363, May 2011.

[43] J. Buha, R. N. Lumley, and A. G. Crosky, "Secondary ageing in an aluminium alloy 7050," *Mater. Sci. Eng. A*, vol. 492, no. 1, pp. 1–10, 2008.

[44] J. D. Evensen, N. Ryum, and J. D. Embury, "The intergranular fracture of Al-Mg-Si alloys," *Mater. Sci. Eng.*, vol. 18, no. 2, pp. 221–229, Apr. 1975.

[45] T. L. Anderson and T. L. Anderson, *Fracture mechanics: fundamentals and applications*, 3rd ed. CRC press, 2005.

[46] T. Belytschko and T. Black, "Elastic crack growth in finite elements with minimal

remeshing," *Int. J. Numer. Methods Eng.*, vol. 45, no. 5, pp. 601–620, 1999.

[47] R. A. Gingold and J. J. Monaghan, "Smoothed particle hydrodynamics: theory and application to non-spherical stars," *Mon. Not. R. Astron. Soc.*, vol. 181, no. 3, pp. 375–389, 1977.

[48] T. Belytschko, Y. Y. Lu, and L. Gu, "Element-free Galerkin methods," *Int. J. Numer. Methods Eng.*, vol. 37, no. 2, pp. 229–256, 1994.

[49] L. D. Libersky, P. W. Randles, T. C. Carney, and D. L. Dickinson, "Recent improvements in SPH modeling of hypervelocity impact," *Int. J. Impact Eng.*, vol. 20, no. 6–10, pp. 525–532, 1997.

[50] T. Rabczuk and J. Eibl, "Modelling dynamic failure of concrete with meshfree methods," *Int. J. Impact Eng.*, vol. 32, no. 11, pp. 1878–1897, 2006.

[51] T. Rabczuk, "Computational Methods for Fracture in Brittle and Quasi-Brittle Solids : State-of-the-art Review and Future Perspectives," *ISRN Appl. Math.*, vol. 2013, no. l, pp. 1–61, 2012.

[52] S. A. Silling, "Reformulation of elasticity theory for discontinuities and long-range forces," *J. Mech. Phys. Solids*, vol. 48, no. 1, pp. 175–209, 2000.

[53] S. A. Silling and R. B. Lehoucq, "Peridynamic Theory of Solid Mechanics," in *Advances in Applied Mechanics*, vol. 44, H. Aref and E. van der Giessen, Eds. Elsevier, 2010, pp. 73–168.

[54] D. M. Saylor, J. Fridy, B. S. El-Dasher, K.-Y. Jung, and A. D. Rollett, "Statistically representative three-dimensional microstructures based on orthogonal observation sections," *Metall. Mater. Trans. A*, vol. 35, no. 7, pp. 1969–1979, 2004.

[55] A. Brahme, M. H. Alvi, D. Saylor, J. Fridy, and A. D. Rollett, "3D reconstruction of microstructure in a commercial purity aluminum," *Scr. Mater.*, vol. 55, no. 1 SPEC. ISS., pp. 75–80, 2006.

[56] O. Instruments, "EBSD Explained: From data acquisition to advanced analysis," *Oxford Instruments*, pp. 1–23, 2015.

[57] M. Nemco, "2D and 3D Analysis on the Deformation and Fracture of Commercially Pure Magnesium," McMaster University, 2015.

[58] H. G. F. Wilsdorf, "The ductile fracture of metals: A microstructural viewpoint," *Mater. Sci. Eng.*, vol. 59, no. 1, pp. 1–39, 1983.

[59] W. M. Garrison and N. R. Moody, "Ductile fracture," *J. Phys. Chem. Solids*, vol. 48, no. 11, pp. 1035–1074, 1987.

[60] M. F. Horstemeyer, S. Ramaswamy, and M. Negrete, "Using a micromechanical finite element parametric study to motivate a phenomenological macroscale model for void/crack nucleation in aluminum with a hard second phase," *Mech. Mater.*, vol. 35, no. 7, pp. 675–

687, 2003.

[61] D. François, A. Pineau, and A. Zaoui, *Mechanical Behaviour of Materials: Volume II: Fracture Mechanics and Damage*, 2nd ed., vol. 191. Springer Science & Business Media, 2012.

[62] A. S. Argon, J. Im, and R. Safoglu, "Cavity formation from inclusions in ductile fracture," *Metall. Trans. A*, vol. 6, no. 3, pp. 825–837, 1975.

[63] A. S. Argon, "Formation of Cavities From Nondeformable Second-Phase Particles in Low Temperature Ductile Fracture," *J. Eng. Mater. Technol.*, vol. 98, no. 1, p. 60, 1976.

[64] S. H. Goods and L. M. Brown, "Overview No. 1. The nucleation of cavities by plastic deformation," *Acta Metall.*, vol. 27, no. 1, pp. 1–15, 1979.

[65] R. H. Van Stone, T. B. Cox, J. R. Low Jr, and J. A. Psioda, "Microstructural aspects of fracture by dimpled rupture," *Int. Met. Rev.*, vol. 30, no. 4, pp. 157–180, 1985.

[66] N. Kanetake, M. Nomura, and T. Choh, "Continuous observation of microstructural degradation during tensile loading of particle reinforced aluminium matrix composites," *Mater. Sci. Technol.*, vol. 11, no. 12, pp. 1246–1252, 1995.

[67] D. LASSANCE, D. FABREGUE, F. DELANNAY, and T. PARDOEN, "Micromechanics of room and high temperature fracture in 6xxx Al alloys," *Prog. Mater. Sci.*, vol. 52, no. 1, pp. 62–129, Jan. 2007.

[68] G. Mrówka-Nowotnik, "The effect of intermetallics on the fracture mechanism in AlSi1MgMn alloy," *J. Achiev. Mater. Manuf. Eng.*, vol. 30, no. 1, pp. 35–42, 2008.

[69] L. Babout, Y. Brechet, E. Maire, and R. Fougères, "On the competition between particle fracture and particle decohesion in metal matrix composites," *Acta Mater.*, vol. 52, no. 15, pp. 4517–4525, 2004.

[70] P. F. Thomason, "Ductile fracture of metals," *Pergamon Press plc, Ductile Fract. Met. 1990,* p. 219, 1990.

[71] D. Lassance, F. Scheyvaerts, and T. Pardoen, "Growth and coalescence of penny-shaped voids in metallic alloys," *Eng. Fract. Mech.*, vol. 73, no. 8, pp. 1009–1034, 2006.

[72] F. a. McClintock, "A Criterion for Ductile Fracture by the Growth of Holes," *J. Appl. Mech.*, vol. 35, no. 2, p. 363, 1968.

[73] A. Needleman, "A continuum model for void nucleation by inclusion debonding," *J. Appl. Mech.*, vol. 54, no. 3, p. 525, 1987.

[74] F. M. Beremin, "Cavity formation from inclusions in ductile fracture of A508 steel," *Metall. Trans. A*, vol. 12, no. 5, pp. 723–731, 1981.

[75] L. M. Brown and W. M. Stobbs, "The work-hardening of copper-silica V. equlibrium plastic relaxation by secondary dislocations," *Philos. Mag.*, vol. 34, no. 3, pp. 351–372, 1976.

[76] A. L. Gurson, “Plastic flow and fracture behaviour of ductile materials incorporating void nucleation, growth and interaction,” Brown University,Providence, R.I., 1975.

[77] C. C. Chu and A. Needleman, “Void nucleation effects in biaxially stretched sheets,” *J. Eng. Mater. Technol.*, vol. 102, no. 3, p. 249, 1980.

[78] Z. L. Zhang and E. Niemi, “A new failure criterion for the Gurson-Tvergaard dilational constitutive model,” *Int. J. Fract.*, vol. 70, no. 4, pp. 321–334, 1994.

[79] Z. L. Zhang, C. Thaulow, and J. Ødegård, “Complete Gurson model approach for ductile fracture,” *Eng. Fract. Mech.*, vol. 67, no. 2, pp. 155–168, 2000.

[80] J. Besson, *Continuum Models of Ductile Fracture: A Review*, vol. 19, no. 1. 2009.

[81] J. W. Hancock and A. C. Mackenzie, “On the mechanisms of ductile failure in high-strength steels subjected to multi-axial stress-states,” *J. Mech. Phys. Solids*, vol. 24, no. 2–3, pp. 147–160, 1976.

[82] M. Geni and M. Kikuchi, “Void configuration under constrained deformation in ductile matrix materials,” *Comput. Mater. Sci.*, vol. 16, no. 1, pp. 391–403, 1999.

[83] K. E. Puttick, “Necking and fracture in aluminium crystals,” *Acta Metallurgica*, vol. 11, no. 8. Pergamon, pp. 986–989, 1963.

[84] L. Babout, E. Maire, and R. Fougères, “Damage initiation in model metallic materials: X-ray tomography and modelling,” *Acta Mater.*, vol. 52, no. 8, pp. 2475–2487, 2004.

[85] E. Maire, C. Bordreuil, L. Babout, and J. C. Boyer, “Damage initiation and growth in metals. Comparison between modelling and tomography experiments,” *J. Mech. Phys. Solids*, vol. 53, no. 11, pp. 2411–2434, 2005.

[86] J. R. Rice and D. M. Tracey, “On the ductile enlargement of voids in triaxial stress fields,” *J. Mech. Phys. Solids*, vol. 17, no. 3, pp. 201–217, 1969.

[87] G. Le Roy, J. D. Embury, G. Edwards, and M. F. Ashby, “A model of ductile fracture based on the nucleation and growth of voids,” *Acta Metall.*, vol. 29, no. 8, pp. 1509–1522, 1981.

[88] B. Budiansky, J. W. Hutchinson, and S. Slutsky, “Void Growth and Collapse in Viscous Solids,” in *Mechanics of Solids*, 1982, pp. 13–45.

[89] Y. Huang, “Accurate Dilatation Rates for Spherical Voids in Triaxial Stress Fields,” *J. Appl. Mech.*, vol. 58, no. 4, pp. 1084–1086, Dec. 1991.

[90] A. L. Gurson, “Continuum Theory of Ductile Rupture by Void Nucleation and Growth: Part I- Yield criteria and Flow Rules for Porous Ductile Media,” *J. Eng. Mater. Technol.*, vol. 99, no. 76, pp. 2–15, 1977.

[91] V. Tvergaard and A. Needleman, “Analysis of the cup-cone fracture in a round tensile bar,” *Acta Metall.*, vol. 32, no. 1, pp. 157–169, 1984.

[92] G. Rousselier, “Ductile fracture models and their potential in local approach of fracture,”

Nucl. Eng. Des., vol. 105, no. 1, pp. 97–111, 1987.

[93] K. . Zhang, J. . Bai, and D. François, "Numerical analysis of the influence of the Lode parameter on void growth," *Int. J. Solids Struct.*, vol. 38, no. 32, pp. 5847–5856, 2001.

[94] Y. Bai and T. Wierzbicki, "A new model of metal plasticity and fracture with pressure and Lode dependence," *Int. J. Plast.*, vol. 24, no. 6, pp. 1071–1096, 2008.

[95] Y. Bai and T. Wierzbicki, "Application of extended Mohr-Coulomb criterion to ductile fracture," *Int. J. Fract.*, vol. 161, no. 1, pp. 1–20, 2010.

[96] T. B. Cox and J. R. J. Low, "An investigation of the plastic fracture of AISI 4340 and 18 Nickel-200 grade maraging steels," *Metall. Trans. B*, vol. 5, no. 6, pp. 1457–1470, 1974.

[97] I. Barsoum and J. Faleskog, "Rupture mechanisms in combined tension and shear-Micromechanics," *Int. J. Solids Struct.*, vol. 44, no. 17, pp. 5481–5498, 2007.

[98] D. Fabrègue and T. Pardoen, "A constitutive model for elastoplastic solids containing primary and secondary voids," *J. Mech. Phys. Solids*, vol. 56, no. 3, pp. 719–741, 2008.

[99] D. Lassance, D. Fabrègue, F. Delannay, and T. Pardoen, "Micromechanics of room and high temperature fracture in 6xxx Al alloys," *Progress in Materials Science*, vol. 52, no. 1. pp. 62–129, 2007.

[100] A. Weck and D. S. Wilkinson, "Experimental investigation of void coalescence in metallic sheets containing laser drilled holes," *Acta Mater.*, vol. 56, no. 8, pp. 1774–1784, 2008.

[101] T. Pardoen and F. Delannay, "The coalescence of voids in prestrained notched round copper bars," *Fatigue Fract. Eng. Mater. Struct.*, vol. 21, no. 12, pp. 1459–1472, 1998.

[102] L. M. Brown and J. D. Embury, "The Initiation and growth of voids at second phase particles," in *Proceedings of the third international conference on Strength of Metals and Alloys*, 1973, vol. 1, no. 3, pp. 164–169.

[103] X. Gao, T. Wang, and J. Kim, "On ductile fracture initiation toughness: Effects of void volume fraction, void shape and void distribution," *Int. J. Solids Struct.*, vol. 42, no. 18–19, pp. 5097–5117, 2005.

[104] J. Kim, G. Zhang, and X. Gao, "Modeling of ductile fracture: Application of the mechanism-based concepts," *Int. J. Solids Struct.*, vol. 44, no. 6, pp. 1844–1862, Mar. 2007.

[105] A. Needleman and V. Tvergaard, "An analysis of ductile rupture in notched bars," *J. Mech. Phys. Solids*, vol. 32, no. 6, pp. 461–490, 1984.

[106] P. F. Thomason, "Three-dimensional models for the plastic limit-loads at incipient failure of the intervoid matrix in ductile porous solids," *Acta Metall.*, vol. 33, no. 6, pp. 1079–1085, 1985.

[107] A. A. Benzerga and J.-B. Leblond, "Ductile Fracture by Void Growth to Coalescence," in *Advances in Applied Mechanics*, vol. 44, 2010, pp. 169–305.

[108] M. F. Horstemeyer, J. Lathrop, A. M. Gokhale, and M. Dighe, “Modeling stress state dependent damage evolution in a cast Al–Si–Mg aluminum alloy,” *Theor. Appl. Fract. Mech.*, vol. 33, no. 1, pp. 31–47, 2000.

[109] A. A. Benzerga, J. Besson, and A. Pineau, “Anisotropic ductile fracture: Part II: theory,” *Acta Mater.*, vol. 52, no. 15, pp. 4639–4650, 2004.

[110] M. E. Torki, A. A. Benzerga, and J.-B. Leblond, “On Void Coalescence Under Combined Tension and Shear,” *J. Appl. Mech.*, vol. 82, no. 7, pp. 71005–71015, Jul. 2015.

[111] A. Pineau, A. A. Benzerga, and T. Pardoen, “Failure of metals I: Brittle and ductile fracture,” *Acta Mater.*, vol. 107, pp. 424–483, 2016.

[112] L. Morin, J.-B. Leblond, A. A. Benzerga, and D. Kondo, “A unified criterion for the growth and coalescence of microvoids,” *J. Mech. Phys. Solids*, vol. 97, pp. 19–36, 2016.

[113] B. Kondori and A. A. Benzerga, “Modeling damage accumulation to fracture in a magnesium-rare earth alloy,” *Acta Mater.*, vol. 124, pp. 225–236, 2017.

[114] D. A. Ryder and A. C. Smale, “Fracture of Solids,” *Interscience, New York, 1963) p*, vol. 237, 1963.

[115] P. N. T. Unwin and G. C. Smith, “The microstructure and mechanical properties of Al-6 percent Zn-3 percent Mg,” *J Inst Met.*, vol. 97, no. 10, pp. 299–310, 1969.

[116] A. J. Sedriks, P. W. Slattery, and E. N. Pugh, “Deformation within precipitate-free zones in an aged Al-Zn-Mg alloy,” *ASM TRANS QUART*, vol. 62, no. 3, pp. 815–818, 1969.

[117] M. Raghavan, “Microanalysis of precipitate free zones (PFZ) in Al-Zn-Mg and Cu-Ni-Nb alloys,” *Metall. Trans. A*, vol. 11, no. 6, pp. 993–999, 1980.

[118] J. D. Embury and E. Nes, “On the tensile fracture of aluminium alloys,” *Zeitschrift f{ü}r Met.*, vol. 65, pp. 45–55, 1974.

[119] I. Kirman, “The relation between microstructure and toughness in 7075 aluminum alloy,” *Metall. Trans.*, vol. 2, no. 7, pp. 1761–1770, 1971.

[120] H. C. Burghard, “The influence of precipitate morphology on microvoid growth and coalescence in tensile fractures,” *Metall. Trans.*, vol. 5, no. 9, pp. 2083–2094, 1974.

[121] B. Liscic, H. M. Tensi, L. C. F. Canale, and G. E. Totten, *Quenching theory and technology*. CRC Press, 2010.

[122] A. H. Geisler, “Phase transformations in solids,” *New York*, vol. 387, 1951.

[123] G. Lütjering, A. Gysler, C. A. Pampillo, H. Biloni, and D. E. Embury, “Aluminum, Transformation Technology and Application,” in *Proceedings of International Symposium at Puert Madryn, Chubut, Argentina, August*, 1980, p. 171.

[124] E. Hornbogen and M. Gräf, “Fracture toughness of precipitation hardened alloys containing narrow soft zones at grain boundaries,” *Acta Metall.*, vol. 25, no. 8, pp. 877–881, 1977.

[125] M. Kikuchi, K. Shiozawa, and J. R. Weertman, “Void nucleation in astroloy: theory and experiments,” *Acta Metall.*, vol. 29, no. 10, pp. 1747–1758, 1981.

[126] A. K. Vasudévan and R. D. Doherty, “Grain boundary ductile fracture in precipitation hardened aluminum alloys,” *Acta Metall.*, vol. 35, no. 6, pp. 1193–1219, 1987.

[127] N. F. Mott, “Bakerian Lecture. Dislocations, Plastic Flow and Creep,” *Proc. R. Soc. London A Math. Phys. Eng. Sci.*, vol. 220, no. 1140, pp. 1–14, 1953.

[128] N. Ryum, “Ageing and plastic deformation of an Al-Mg-Zn alloy,” *Acta Metall.*, vol. 17, no. 7, pp. 821–830, 1969.

[129] P. Sainfort, P. Guyot, C. Baker, P. J. Gregson, S. J. Harris, and C. J. Peel, “Aluminum-Lithium Alloys III,” *Inst. Met. London, 1986) p*, vol. 420, 1986.

[130] I. R. Dover and J. D. Embury, “The influence of microstructural features on the formability of aluminium alloys,” in *Materials forum*, 1986, vol. 9, no. 4, pp. 188–201.

[131] W. J. Poole, X. Wang, D. J. Lloyd, and J. D. Embury, “The shearable–non-shearable transition in Al–Mg–Si–Cu precipitation hardening alloys: implications on the distribution of slip, work hardening and fracture,” *Philos. Mag.*, vol. 85, no. 26–27, pp. 3113–3135, Sep. 2005.

[132] A. N. STROH, “The formation of cracks as a result of plastic flow,” *Proc. R. Soc. A Math. Phys. Sci.*, vol. 223, no. 1154, pp. 404–414, 1954.

[133] E. Pouillier, A. F. Gourgues, D. Tanguy, and E. P. Busso, “A study of intergranular fracture in an aluminium alloy due to hydrogen embrittlement,” *Int. J. Plast.*, vol. 34, pp. 139–153, 2012.

[134] J. R. Rice, “Inelastic constitutive relations for solids: An internal-variable theory and its application to metal plasticity,” *J. Mech. Phys. Solids*, vol. 19, no. 6, pp. 433–455, 1971.

[135] D. Peirce, R. J. Asaro, and A. Needleman, “An analysis of nonuniform and localized deformation in ductile single crystals,” *Acta Metall.*, vol. 30, no. 6, pp. 1087–1119, Jun. 1982.

[136] D. Peirce, R. J. Asaro, and A. Needleman, “Material rate dependence and localized deformation in crystalline solids,” *Acta Metall.*, vol. 31, no. 12, pp. 1951–1976, 1983.

[137] Y. W. Chang and R. J. Asaro, “An experimental study of shear localization in aluminum-copper single crystals,” *Acta Metall.*, vol. 29, no. 1, pp. 241–257, 1981.

[138] R. J. Asaro, “Crystal Plasticity,” *J. Appl. Mech.*, vol. 50, no. 4b, pp. 921–934, Dec. 1983.

[139] S. B. Brown, K. H. Kim, and L. Anand, “An internal variable constitutive model for hot working of metals,” *Int. J. Plast.*, vol. 5, no. 2, pp. 95–130, 1989.

[140] J. L. Bassani and T.-Y. Wu, “Latent Hardening in Single Crystals II. Analytical Characterization and Predictions,” *Proc. R. Soc. A Math. Phys. Eng. Sci.*, vol. 435, no. 1893, pp. 21–41, 1991.

[141] A. Arsenlis and D. M. Parks, “Modeling the evolution of crystallographic dislocation density in crystal plasticity,” *J. Mech. Phys. Solids*, vol. 50, no. 9, pp. 1979–2009, 2002.

[142] A. Arsenlis, D. M. Parks, R. Becker, and V. V Bulatov, “On the evolution of crystallographic dislocation density in non-homogeneously deforming crystals,” *J. Mech. Phys. Solids*, vol. 52, no. 6, pp. 1213–1246, 2004.

[143] K.-S. Cheong and E. P. Busso, “Discrete dislocation density modelling of single phase {FCC} polycrystal aggregates,” *Acta Mater.*, vol. 52, no. 19, pp. 5665–5675, 2004.

[144] A. Ma and F. Roters, “A constitutive model for fcc single crystals based on dislocation densities and its application to uniaxial compression of aluminium single crystals,” *Acta Mater.*, vol. 52, no. 12, pp. 3603–3612, 2004.

[145] A. Ma, F. Roters, and D. Raabe, “A dislocation density based constitutive model for crystal plasticity {FEM} including geometrically necessary dislocations,” *Acta Mater.*, vol. 54, no. 8, pp. 2169–2179, 2006.

[146] A. Ma, F. Roters, and D. Raabe, “On the consideration of interactions between dislocations and grain boundaries in crystal plasticity finite element modeling – Theory, experiments, and simulations,” *Acta Mater.*, vol. 54, no. 8, pp. 2181–2194, 2006.

[147] S. Saimoto and P. Van Houtte, “Constitutive relation based on Taylor slip analysis to replicate work-hardening evolution,” *Acta Mater.*, vol. 59, no. 2, pp. 602–612, 2011.

[148] A. P. Brahme, K. Inal, R. K. Mishra, and S. Saimoto, “A new strain hardening model for rate-dependent crystal plasticity,” *Comput. Mater. Sci.*, vol. 50, no. 10, pp. 2898–2908, 2011.

[149] P. Lukáš, M. Klesnil, and J. Krejčí, “Dislocations and Persistent Slip Bands in Copper Single Crystals Fatigued at Low Stress Amplitude,” *Phys. status solidi*, vol. 27, no. 2, pp. 545–558, 1968.

[150] H. Mughrabi, “The long-range internal stress field in the dislocation wall structure of persistent slip bands,” *Phys. status solidi*, vol. 104, no. 1, pp. 107–120, 1987.

[151] M. Gerland, J. Mendez, P. Violan, and B. A. Saadi, “Evolution of dislocation structures and cyclic behaviour of a 316L-type austenitic stainless steel cycled in vacuo at room temperature,” *Mater. Sci. Eng. A*, vol. 118, pp. 83–95, 1989.

[152] J. Polák, *Cyclic plasticity and low cycle fatigue life of metals*. Elsevier, 1991.

[153] H. Mughrabi, T. Ungár, W. Kienle, and M. Wilkens, “Long-range internal stresses and asymmetric X-ray line-broadening in tensile-deformed [001]-orientated copper single crystals,” *Philos. Mag. A*, vol. 53, no. 6, pp. 793–813, 1986.

[154] A. S. Nowick and E. S. Machlin, “Dislocation Theory as Applied by N.A.C.A. to the Creep of Metals,” *J. Appl. Phys.*, vol. 18, no. 1, pp. 79–87, 1947.

[155] L. Li, L. Shen, and G. Proust, “A texture-based representative volume element crystal

plasticity model for predicting Bauschinger effect during cyclic loading," *Mater. Sci. Eng. A*, vol. 608, pp. 174–183, 2014.

[156] L. E. Levine, P. Geantil, B. C. Larson, J. Z. Tischler, M. E. Kassner, W. Liu, M. R. Stoudt, and F. Tavazza, "Disordered long-range internal stresses in deformed copper and the mechanisms underlying plastic deformation," *Acta Mater.*, vol. 59, no. 14, pp. 5803–5811, 2011.

[157] D. Zhu, H. Zhang, and D. Y. Li, "Effects of nano-scale grain boundaries in Cu on its Bauschinger's effect and response to cyclic deformation," *Mater. Sci. Eng. A*, vol. 583, pp. 140–150, 2013.

[158] H. Kato, K. Sasaki, and T. Mori, "Four-point bending test of the Bauschinger effect in prestrained IF steel thin sheet," *Mater. Sci. Eng. A*, vol. 642, pp. 150–156, 2015.

[159] B. Chen, P. E. J. Flewitt, D. J. Smith, and C. P. Jones, "An improved method to identify grain boundary creep cavitation in 316H austenitic stainless steel," *Ultramicroscopy*, vol. 111, no. 5, pp. 309–313, 2011.

[160] M. Berveiller and A. Zaoui, "An extension of the self-consistent scheme to plastically-flowing polycrystals," *J. Mech. Phys. Solids*, vol. 26, no. 5, pp. 325–344, 1978.

[161] X. Lemoine, M. Berveiller, and D. Muller, "Texture of Microstructures in BCC Metals for Various Loading Paths," in *Textures of Materials - ICOTOM 10*, 1994, vol. 157, pp. 1821–1826.

[162] L. Langlois and M. Berveiller, "Overall softening and anisotropy related with the formation and evolution of dislocation cell structures," *Int. J. Plast.*, vol. 19, no. 5, pp. 599–624, 2003.

[163] J. D. Eshelby, "The determination of the elastic field of an ellipsoidal inclusion, and related problems," in *Proceedings of the Royal Society of London A: Mathematical, Physical and Engineering Sciences*, 1957, vol. 241, no. 1226, pp. 376–396.

[164] A. P. Brahme, K. Inal, R. K. Mishra, and S. Saimoto, "The backstress effect of evolving deformation boundaries in FCC polycrystals," *Int. J. Plast.*, vol. 27, no. 8, pp. 1252–1266, 2011.

[165] G. Z. Voyiadjis and P. I. Kattan, "Phenomenological evolution equations for the backstress and spin tensors," *Acta Mech.*, vol. 88, no. 1–2, pp. 91–111, 1991.

[166] A. S. Khan and P. Cheng, "An anisotropic elastic-plastic constitutive model for single and polycrystalline metals. I-theoretical developments," *Int. J. Plast.*, vol. 12, no. 2, pp. 147–162, 1996.

[167] R. D. McGinty and D. L. McDowell, "Multiscale Polycrystal Plasticity," *J. Eng. Mater. Technol.*, vol. 121, no. 2, pp. 203–209, Apr. 1999.

[168] F. Yoshida and T. Uemori, "A model of large-strain cyclic plasticity describing the Bauschinger effect and workhardening stagnation," *Int. J. Plast.*, vol. 18, no. 5, pp. 661–686, 2002.

[169] C. H. Goh, R. W. Neu, and D. L. McDowell, "Crystallographic plasticity in fretting of Ti-6AL-4V," *Int. J. Plast.*, vol. 19, no. 10, pp. 1627–1650, 2003.

[170] J. a. Wollmershauser, B. Clausen, and S. R. Agnew, "A slip system-based kinematic hardening model application to in situ neutron diffraction of cyclic deformation of austenitic stainless steel," *Int. J. Fatigue*, vol. 36, no. 1, pp. 181–193, Mar. 2012.

[171] R. H. Wagoner, H. Lim, and M.-G. Lee, "Advanced Issues in springback," *Int. J. Plast.*, vol. 45, pp. 3–20, 2013.

[172] M.-G. Lee, D. Kim, C. Kim, M. L. Wenner, and K. Chung, "Spring-back evaluation of automotive sheets based on isotropic–kinematic hardening laws and non-quadratic anisotropic yield functions, part III: applications," *Int. J. Plast.*, vol. 21, no. 5, pp. 915–953, 2005.

[173] M. Banu, M. Takamura, T. Hama, O. Naidim, C. Teodosiu, and A. Makinouchi, "Simulation of springback and wrinkling in stamping of a dual phase steel rail-shaped part," *J. Mater. Process. Technol.*, vol. 173, no. 2, pp. 178–184, 2006.

[174] I. N. Vladimirov, M. P. Pietryga, and S. Reese, "Anisotropic finite elastoplasticity with nonlinear kinematic and isotropic hardening and application to sheet metal forming," *Int. J. Plast.*, vol. 26, no. 5, pp. 659–687, 2010.

[175] D. Steglich, W. Brocks, J. Bohlen, and F. Barlat, "Modelling direction-dependent hardening in magnesium sheet forming simulations," *Int. J. Mater. Form.*, vol. 4, no. 2, pp. 243–253, Mar. 2011.

[176] W. Muhammad, M. Mohammadi, J. Kang, R. K. Mishra, and K. Inal, "An elasto-plastic constitutive model for evolving asymmetric/anisotropic hardening behavior of AZ31B and ZEK100 magnesium alloy sheets considering monotonic and reverse loading paths," *Int. J. Plast.*, vol. 70, pp. 30–59, 2015.

[177] D. Bardel, M. Perez, D. Nelias, S. Dancette, P. Chaudet, and V. Massardier, "Cyclic behaviour of a 6061 aluminium alloy: Coupling precipitation and elastoplastic modelling," *Acta Mater.*, vol. 83, pp. 256–268, 2015.

[178] B. Peeters, S. R. Kalidindi, P. Van Houtte, and E. Aernoudt, "A crystal plasticity based work-hardening/softening model for b.c.c. metals under changing strain paths," *Acta Mater.*, vol. 48, no. 9, pp. 2123–2133, 2000.

[179] C. J. Bayley, W. A. M. Brekelmans, and M. G. D. Geers, "A comparison of dislocation induced back stress formulations in strain gradient crystal plasticity," *Int. J. Solids Struct.*, vol. 43, no. 24, pp. 7268–7286, 2006.

[180] K. Kitayama, C. N. Tomé, E. F. Rauch, J. J. Gracio, and F. Barlat, "A crystallographic dislocation model for describing hardening of polycrystals during strain path changes. Application to low carbon steels," *Int. J. Plast.*, vol. 46, pp. 54–69, 2013.

[181] W. Wen, M. Borodachenkova, C. N. Tomé, G. Vincze, E. F. Rauch, F. Barlat, and J. J. Grácio, "Mechanical behavior of Mg subjected to strain path changes: Experiments and

modeling," *Int. J. Plast.*, vol. 73, pp. 171–183, 2015.

[182] B. Peeters, M. Seefeldt, C. Teodosiu, S. R. Kalidindi, P. Van Houtte, and E. Aernoudt, "Work-hardening/softening behaviour of b.c.c. polycrystals during changing strain paths: I. An integrated model based on substructure and texture evolution, and its prediction of the stress–strain behaviour of an IF steel during two-stage strain paths," *Acta Mater.*, vol. 49, no. 9, pp. 1607–1619, 2001.

[183] M. Knezevic, R. a. Lebensohn, O. Cazacu, B. Revil-Baudard, G. Proust, S. C. Vogel, and M. E. Nixon, "Modeling bending of α-titanium with embedded polycrystal plasticity in implicit finite elements," *Mater. Sci. Eng. A*, vol. 564, pp. 116–126, 2013.

[184] M. Zecevic, R. J. McCabe, and M. Knezevic, "Spectral database solutions to elasto-viscoplasticity within finite elements: Application to a cobalt-based FCC superalloy," *Int. J. Plast.*, 2015.

[185] M. Zecevic, Y. P. Korkolis, T. Kuwabara, and M. Knezevic, "Dual-phase steel sheets under cyclic tension–compression to large strains: Experiments and crystal plasticity modeling," *J. Mech. Phys. Solids*, vol. 96, pp. 65–87, 2016.

[186] W. Wen, M. Borodachenkova, C. N. Tomé, G. Vincze, E. F. Rauch, F. Barlat, and J. J. Grácio, "Mechanical behavior of low carbon steel subjected to strain path changes: Experiments and modeling," *Acta Mater.*, vol. 111, pp. 305–314, 2016.

[187] S. M. A. Khan, H. M. Zbib, and D. A. Hughes, "Modeling planar dislocation boundaries using multi-scale dislocation dynamics plasticity," *Int. J. Plast.*, vol. 20, no. 6, pp. 1059–1092, 2004.

[188] Z. L. Liu, X. M. Liu, Z. Zhuang, and X. C. You, "A multi-scale computational model of crystal plasticity at submicron-to-nanometer scales," *Int. J. Plast.*, vol. 25, no. 8, pp. 1436–1455, 2009.

[189] C. Zhou and R. LeSar, "Dislocation dynamics simulations of the Bauschinger effect in metallic thin films," *Comput. Mater. Sci.*, vol. 54, pp. 350–355, 2012.

[190] G. G. Yapici, I. J. Beyerlein, I. Karaman, and C. N. Tomé, "Tension–compression asymmetry in severely deformed pure copper," *Acta Mater.*, vol. 55, no. 14, pp. 4603–4613, 2007.

[191] H. L. Kim, W. K. Bang, and Y. W. Chang, "Effect of initial texture on deformation behavior of AZ31 magnesium alloy sheets under biaxial loading," *Mater. Sci. Eng. A*, vol. 552, pp. 245–251, Aug. 2012.

[192] R. J. Asaro and J. R. Rice, "Strain localization in ductile single crystals," *J. Mech. Phys. Solids*, vol. 25, no. 5, pp. 309–338, Oct. 1977.

[193] R. J. Asaro and A. Needleman, "Overview no. 42 Texture development and strain hardening in rate dependent polycrystals," *Acta Metall.*, vol. 33, no. 6, pp. 923–953, Jun. 1985.

[194] J. H. Kim, D. Kim, Y.-S. Lee, M.-G. Lee, K. Chung, H.-Y. Kim, and R. H. Wagoner, "A

temperature-dependent elasto-plastic constitutive model for magnesium alloy AZ31 sheets," *Int. J. Plast.*, vol. 50, pp. 66–93, Nov. 2013.

[195] J. Kang, D. S. Wilkinson, P. D. Wu, M. Bruhis, M. Jain, J. D. Embury, and R. K. Mishra, "Constitutive Behavior of AA5754 Sheet Materials at Large Strains," *J. Eng. Mater. Technol.*, vol. 130, no. 3, p. 031004, 2008.

[196] W. Muhammad, A. Brahme, J. Kang, R. Mishra, and K. Inal, "Large Strain Cyclic Simple Shear Behavior of Aluminum Extrusions: An Experimental and Numerical Study," in *Light Metals 2016*, E. Williams, Ed. 2016, pp. 169–174.

[197] J. Kang and K. Gong, "Determination of Fracture Behavior of AA6060 Aluminum Alloy Extrusion Using Digital Image Correlation{\copyright} Her Majesty the Queen in Right of Canada, as represented by the Minister of Natural Resources, 2015.," in *Evaluation of Existing and New Sensor Technologies for Fatigue, Fracture and Mechanical Testing*, ASTM International, 2015.

[198] GOM mbH User's Manual; Version 6, *Aramis-Deformation Measurement Using the Grating Method*. Braunschweig, Germany, 2011.

[199] J. Rossiter, A. Brahme, M. H. Simha, K. Inal, and R. Mishra, "A new crystal plasticity scheme for explicit time integration codes to simulate deformation in 3D microstructures: Effects of strain path, strain rate and thermal softening on localized deformation in the aluminum alloy 5754 during simple shear," *Int. J. Plast.*, vol. 26, no. 12, pp. 1702–1725, Dec. 2010.

[200] V. M. Segal, "Materials processing by simple shear," *Mater. Sci. Eng. A*, vol. 197, no. 2, pp. 157–164, 1995.

[201] S. Ferrasse, K. T. Hartwig, R. E. Goforth, and V. M. Segal, "Microstructure and properties of copper and aluminum alloy 3003 heavily worked by equal channel angular extrusion," *Metall. Mater. Trans. A*, vol. 28, no. 4, pp. 1047–1057, 1997.

[202] M. Richert, Q. Liu, and N. Hansen, "Microstructural evolution over a large strain range in aluminium deformed by cyclic-extrusion–compression," *Mater. Sci. Eng. A*, vol. 260, no. 1–2, pp. 275–283, 1999.

[203] D. A. Hughes and N. Hansen, "High angle boundaries formed by grain subdivision mechanisms," *Acta Mater.*, vol. 45, no. 9, pp. 3871–3886, 1997.

[204] A. Azimi, S. Tutunchilar, G. Faraji, and M. K. B. Givi, "Mechanical properties and microstructural evolution during multi-pass ECAR of Al 1100--O alloy," *Mater. Des.*, vol. 42, pp. 388–394, 2012.

[205] N. Van Thuong, H. Zuhailawati, A. A. Seman, T. D. Huy, and B. K. Dhindaw, "Microstructural evolution and wear characteristics of equal channel angular pressing processed semi-solid-cast hypoeutectic aluminum alloys," *Mater. Des.*, vol. 67, pp. 448–456, 2015.

[206] S. Esmaeili, X. Wang, D. J. Lloyd, and W. J. Poole, "On the Precipitation-Hardening

Behavior of the Al-Mg-Si-Cu Alloy AA6111," vol. 34, no. March, 2003.

[207] R. Z. Valiev, A. V Korznikov, and R. R. Mulyukov, "Structure and properties of ultrafine-grained materials produced by severe plastic deformation," *Mater. Sci. Eng. A*, vol. 168, no. 2, pp. 141–148, 1993.

[208] R. Z. Valiev, E. V Kozlov, Y. F. Ivanov, J. Lian, A. A. Nazarov, and B. Baudelet, "Deformation behaviour of ultra-fine-grained copper," *Acta Metall. Mater.*, vol. 42, no. 7, pp. 2467–2475, 1994.

[209] P. D. Wu, K. W. Neale, and E. Van der Giessen, "Simulation of the behaviour of FCC polycrystals during reversed torsion," *Int. J. Plast.*, vol. 12, no. 9, pp. 1199–1219, Jan. 1996.

[210] K. Inal, P. D. Wu, and K. W. Neale, "Finite element analysis of localization in FCC polycrystalline sheets under plane stress tension," *Int. J. Solids Struct.*, vol. 39, no. 13–14, pp. 3469–3486, Jun. 2002.

[211] D. L. Holt, "Dislocation cell formation in metals," *J. Appl. Phys.*, vol. 41, no. 8, pp. 3197–3201, 1970.

[212] M. R. Staker and D. L. Holt, "The dislocation cell size and dislocation density in copper deformed at temperatures between 25 and 700 C," *Acta Metall.*, vol. 20, no. 4, pp. 569–579, 1972.

[213] L. E. Murr and D. Kuhlmann-Wilsdorf, "Experimental and theoretical observations on the relationship between dislocation cell size, dislocation density, residual hardness, peak pressure and pulse duration in shock-loaded nickel," *Acta Metall.*, vol. 26, no. 5, pp. 847–857, 1978.

[214] K. Inal, K. W. Neale, P. D. Wu, and S. R. MacEwen, "Numerical simulation of large deformation polycrystalline plasticity," 2000.

[215] P. D. Wu, S. R. MacEwen, D. J. Lloyd, and K. W. Neale, "A mesoscopic approach for predicting sheet metal formability," *Model. Simul. Mater. Sci. Eng.*, vol. 12, no. 3, p. 511, 2004.

[216] S. Saimoto, "Dynamic dislocation–defect analysis," *Philos. Mag.*, vol. 86, no. 27, pp. 4213–4233, 2006.

[217] S. Saimoto and B. J. Diak, "Point defect generation, nano-void formation and growth. I. Validation," *Philos. Mag.*, vol. 92, no. 15, pp. 1890–1914, May 2012.

[218] K. Inal, P. D. Wu, and K. W. Neale, "Instability and localized deformation in polycrystalline solids under plane-strain tension," *Int. J. Solids Struct.*, vol. 39, no. 4, pp. 983–1002, 2002.

[219] M. Dao and M. Li, "A micromechanics study on strain-localization-induced fracture initiation in bending using crystal plasticity models," *Philos. Mag. A*, vol. 81, no. 8, pp. 1997–2020, 2001.

[220] S. Ikawa, M. Asano, M. Kuroda, and K. Yoshida, "Effects of crystal orientation on

bendability of aluminum alloy sheet," *Mater. Sci. Eng. A*, vol. 528, no. 12, pp. 4050–4054, May 2011.

[221] D. J. Lloyd, D. Evans, C. Pelow, P. Nolan, and M. Jain, "Bending in aluminium alloys AA 6111 and AA 5754 using the cantilever bend test," *Mater. Sci. Technol.*, vol. 18, no. 6, pp. 621–628, Jun. 2002.

[222] Y. Shi, H. Jin, P. D. Wu, D. J. Lloyd, and D. Embury, "Failure analysis of fusion clad alloy system AA3003/AA6xxx sheet under bending," *Mater. Sci. Eng. A*, vol. 610, pp. 263–272, Jul. 2014.

[223] J. Sarkar, T. R. G. Kutty, K. T. Conlon, D. S. Wilkinson, J. D. Embury, and D. J. Lloyd, "Tensile and bending properties of AA5754 aluminum alloys," *Mater. Sci. Eng. A*, vol. 316, no. 1–2, pp. 52–59, Nov. 2001.

[224] W. B. Lievers, A. K. Pilkey, and D. J. Lloyd, "The influence of iron content on the bendability of AA6111 sheet," *Mater. Sci. Eng. A*, vol. 361, no. 1, pp. 312–320, 2003.

[225] R. Akeret, "Failure mechanisms in the bending of aluminum sheets and limits of bendability," *Aluminium*, vol. 54, no. 2, pp. 117–123, 1978.

[226] C. Soyarslan, M. Malekipour Gharbi, and A. E. Tekkaya, "A combined experimental–numerical investigation of ductile fracture in bending of a class of ferritic–martensitic steel," *Int. J. Solids Struct.*, vol. 49, no. 13, pp. 1608–1626, Jun. 2012.

[227] D. J. Lloyd, "Bending in aluminum automotive alloys," *Proc. from Mater. Solut. Conf. Adv. Metall. Alum. Alloy.*, pp. 160–166, 2001.

[228] N. Triantafyllidis, A. Needleman, and V. Tvergaard, "On the development of shear bands in pure bending," *Int. J. Solids Struct.*, vol. 18, no. 2, pp. 121–138, 1982.

[229] J. Hutchinson and V. Tvergaard, "Shear band formation in plane strain," *Int. J. Solids Struct.*, vol. 17, no. 5, pp. 451–470, 1981.

[230] M. Kuroda and V. Tvergaard, "Shear band development in anisotropic bent specimens," *Eur. J. Mech. - A/Solids*, vol. 23, no. 5, pp. 811–821, Sep. 2004.

[231] A. Davidkov, R. H. Petrov, P. De Smet, B. Schepers, and L. A. I. Kestens, "Microstructure controlled bending response in AA6016 Al alloys," *Mater. Sci. Eng. A*, vol. 528, no. 22–23, pp. 7068–7076, Aug. 2011.

[232] D. Raabe, M. Sachtleber, H. Weiland, G. Scheele, and Z. Zhao, "Grain-scale micromechanics of polycrystal surfaces during plastic straining," *Acta Mater.*, vol. 51, no. 6, pp. 1539–1560, 2003.

[233] A. J. Beaudoin, J. D. Bryant, and D. A. Korzekwa, "Analysis of ridging in aluminum auto body sheet metal," *Metall. Mater. Trans. a-Physical Metall. Mater. Sci.*, vol. 29, no. 9, pp. 2323–2332, 1998.

[234] O. Engler and J. Hirsch, "Texture control by thermomechanical processing of AA6xxx Al-

Mg-Si sheet alloys for automotive applications - a review," *Mater. Sci. Eng. A*, vol. 336, no. 1–2, pp. 249–262, 2002.

[235] K. Osakada and M. Oyane, "On the Roughening of Free Surface in Deformation Processes," *Bull. JSME*, vol. 14, no. 68, pp. 171–177, 1971.

[236] D. V. Wilson, W. T. Roberts, and P. M. B. Rodrigues, "Effects of grain anisotropy on limit strains in biaxial stretching: part ii. sheets of cubic metals and alloys with well-developed preferred orientations," *Metall. Trans. A*, vol. 12, no. 9, pp. 1603–1611, Sep. 1981.

[237] T. Mizuno and H. Mulki, "Changes in surface texture of zinc-coated steel sheets under plastic deformation," *Wear*, vol. 198, no. 1–2, pp. 176–184, Oct. 1996.

[238] M. Jain, D. J. Lloyd, and S. R. MacEwen, "Hardening laws, surface roughness and biaxial tensile limit strains of sheet aluminium alloys," *Int. J. Mech. Sci.*, vol. 38, no. 2, pp. 219–232, Feb. 1996.

[239] R. Mahmudi and M. Mehdizadeh, "Surface roughening during uniaxial and equi-biaxial stretching of 70-30 brass sheets," *J. Mater. Process. Technol.*, vol. 80, pp. 707–712, 1998.

[240] R. Becker, "Effects of strain localization on surface roughening during sheet forming," *Acta Mater.*, vol. 46, no. 4, pp. 1385–1401, Feb. 1998.

[241] M. R. Stoudt and J. B. Hubbard, "Analysis of deformation-induced surface morphologies in steel sheet," *Acta Mater.*, vol. 53, no. 16, pp. 4293–4304, 2005.

[242] T. J. Turner and M. P. Miller, "Modeling the Influence of Material Structure on Deformation Induced Surface Roughening in AA7050 Thick Plate," *J. Eng. Mater. Technol.*, vol. 129, no. 3, p. 367, 2007.

[243] P. D. Wu and D. J. Lloyd, "Analysis of surface roughening in AA6111 automotive sheet," *Acta Mater.*, vol. 52, no. 7, pp. 1785–1798, 2004.

[244] N. . Wittridge and R. . Knutsen, "A microtexture based analysis of the surface roughening behaviour of an aluminium alloy during tensile deformation," *Mater. Sci. Eng. A*, vol. 269, no. 1, pp. 205–216, 1999.

[245] G. J. Baczynski, R. Guzzo, M. D. Ball, and D. J. Lloyd, "Development of roping in an aluminum automotive alloy AA6111," *Acta Mater.*, vol. 48, no. 13, pp. 3361–3376, 2000.

[246] R. Becker, "Analysis of shear localization during bending of a polycrystalline sheet.," *J. Appl. Mech.*, 1992.

[247] V. Tvergaard, "Ductile shear fracture at the surface of a bent specimen," *Mech. Mater.*, vol. 6, no. 1, pp. 53–69, Mar. 1987.

[248] X. H. Hu, M. Jain, P. D. Wu, D. S. Wilkinson, and R. K. Mishra, "A macro–micro-multi-level modeling scheme to study the effect of particle distribution on wrap-bendability of AA5754 sheet alloys," *J. Mater. Process. Technol.*, vol. 210, no. 9, pp. 1232–1242, Jun. 2010.

[249] J. Rossiter, A. Brahme, K. Inal, and R. Mishra, “Numerical analyses of surface roughness during bending of FCC single crystals and polycrystals,” *Int. J. Plast.*, vol. 46, pp. 82–93, Jul. 2013.

[250] M. Kuroda and V. Tvergaard, “Effects of texture on shear band formation in plane strain tension/compression and bending,” *Int. J. Plast.*, vol. 23, no. 2, pp. 244–272, Feb. 2007.

[251] Y. Shi, P. Z. Zhao, H. Jin, P. D. Wu, and D. J. Lloyd, “Analysis of Surface Roughening in AA6111 Automotive Sheet Under Pure Bending,” *Metall. Mater. Trans. A Phys. Metall. Mater. Sci.*, vol. 47, no. 2, pp. 949–960, 2016.

[252] J. Sarkar, T. R. . Kutty, D. . Wilkinson, J. . Embury, and D. . Lloyd, “Tensile properties and bendability of T4 treated AA6111 aluminum alloys,” *Mater. Sci. Eng. A*, vol. 369, no. 1–2, pp. 258–266, Mar. 2004.

[253] P. Castany, F. Diologent, A. Rossoll, J.-F. Despois, C. Bezençon, and A. Mortensen, “Influence of quench rate and microstructure on bendability of AA6016 aluminum alloys,” *Mater. Sci. Eng. A*, vol. 559, pp. 558–565, Jan. 2013.

[254] J. Datsko and C. T. Yang, “Correlation of Bendability of Materials With Their Tensile Properties,” *J. Eng. Ind.*, vol. 82, no. 4, p. 309, 1960.

[255] L. Mattei, D. Daniel, G. Guiglionda, H. Klöcker, and J. Driver, “Strain localization and damage mechanisms during bending of AA6016 sheet,” *Mater. Sci. Eng. A*, vol. 559, pp. 812–821, Jan. 2013.

[256] Y. Shi, P. D. Wu, D. J. Lloyd, and D. Embury, “Numerical study of surface roughening in blow-formed aluminum bottle with crystal plasticity,” *Mater. Sci. Eng. A*, vol. 638, pp. 97–105, 2015.

[257] M. R. Stoudt, J. B. Hubbard, J. E. Carsley, and S. E. Hartfield-Wünsch, “Characterizing the Hemming Performance of Automotive Aluminum Alloys With High-Resolution Topographic Imaging,” *J. Eng. Mater. Technol.*, vol. 136, no. 3, p. 031001, Apr. 2014.

[258] B. C. Meyer, G. Tempus, H. Doyen, D. Emanowski, T. Hirsch, and P. Mayr, “Dispersoid-free zones in the heat-affected zone of aluminum alloy welds,” *Metall. Mater. Trans. A*, vol. 31, no. 5, pp. 1453–1459, May 2000.

[259] P. Schwellinger, “On the mechanism of ductile intergranular fracture in AL□Mg□SI alloys,” *Scr. Metall.*, vol. 12, no. 10, pp. 899–901, Oct. 1978.

[260] Y. Zhou and K. . Neale, “Predictions of forming limit diagrams using a rate-sensitive crystal plasticity model,” *Int. J. Mech. Sci.*, vol. 37, no. 1, pp. 1–20, Jan. 1995.

[261] J. Savoie, M. Jain, A. R. Carr, P. D. Wu, K. W. Neale, Y. Zhou, and J. J. Jonas, “Predictions of forming limit diagrams using crystal plasticity models,” *Mater. Sci. Eng. A*, vol. 257, no. 1, pp. 128–133, Nov. 1998.

[262] L. S. Tóth, J. Hirsch, and P. Van Houtte, “On the role of texture development in the forming limits of sheet metals,” *Int. J. Mech. Sci.*, vol. 38, no. 10, pp. 1117–1126, Oct. 1996.

[263] J. D. Bryant, A. J. Beaudoin, and R. T. VanDyke, “The Effect of Crystallographic Texture on the Formability of AA 2036 Autobody Sheet,” in *SAE Technical Paper 940161*, 1994, pp. 1–11.

[264] W. Muhammad, A. P. Brahme, J. Kang, R. K. Mishra, and K. Inal, “Experimental and numerical investigation of texture evolution and the effects of intragranular backstresses in aluminum alloys subjected to large strain cyclic deformation,” *Int. J. Plast.*, vol. 93, pp. 137–163, Jun. 2017.

[265] S. R. Agnew and Ö. Duygulu, “Plastic anisotropy and the role of non-basal slip in magnesium alloy AZ31B,” *Int. J. Plast.*, vol. 21, no. 6, pp. 1161–1193, Jun. 2005.

[266] P. D. Wu, K. W. Neale, E. Van Der Giessen, M. Jain, S. R. MacEwen, and A. Makinde, “Crystal plasticity forming limit diagram analysis of rolled aluminum sheets,” *Metall. Mater. Trans. A*, vol. 29, no. 2, pp. 527–535, Feb. 1998.

[267] V. (Valerie) Randle, *Introduction to Texture Analysis : Macrotexture, Microtexture and Orientation Mapping.* CRC Press, 2000.

[268] X. Lou, M. Li, R. Boger, S. Agnew, and R. Wagoner, “Hardening evolution of AZ31B Mg sheet,” *Int. J. Plast.*, vol. 23, no. 1, pp. 44–86, Jan. 2007.

[269] Y. Chino, X. Huang, K. Suzuki, K. Sassa, and M. Mabuchi, “Influence of Zn concentration on stretch formability at room temperature of Mg–Zn–Ce alloy,” *Mater. Sci. Eng. A*, vol. 528, no. 2, pp. 566–572, 2010.

[270] K. Inal, P. D. Wu, and K. W. Neale, “Finite element analysis of localization in FCC polycrystalline sheets under plane stress tension,” *Int. J. Solids Struct.*, vol. 39, no. 13, pp. 3469–3486, 2002.

[271] A. P. Brahme, “Generating non-homogenous synthetic microstructures for single phase materials,” *Under Prep.*, 2017.

[272] G. Winther, L. Margulies, S. Schmidt, and H. F. Poulsen, “Lattice rotations of individual bulk grains Part II: Correlation with initial orientation and model comparison,” *Acta Mater.*, vol. 52, no. 10, pp. 2863–2872, 2004.

[273] R. A. Lebensohn, R. Brenner, O. Castelnau, and A. D. Rollett, “Orientation image-based micromechanical modelling of subgrain texture evolution in polycrystalline copper,” *Acta Mater.*, vol. 56, no. 15, pp. 3914–3926, 2008.

[274] L. Mattei, D. Daniel, G. Guiglionda, N. Moulin, H. Klöcker, and J. Driver, “Grain scale modeling of the bendability of AA6xxx Al alloy sheet,” *Mater. Sci. Eng. A*, vol. 583, pp. 96–104, Oct. 2013.

[275] X. Wang, S. Esmaeili, and D. J. Lloyd, “The Sequence of Precipitation in the Al-Mg-Si-Cu Alloy AA6111,” vol. 37, no. September, pp. 2691–2699, 2006.

[276] L. P. Troeger and E. A. Starke, “Microstructural and mechanical characterization of a superplastic 6xxx aluminum alloy,” *Mater. Sci. Eng. A*, vol. 277, no. 1, pp. 102–113, 2000.

[277] D. Steele, D. Evans, P. Nolan, and D. J. Lloyd, "Quantification of grain boundary precipitation and the influence of quench rate in 6XXX aluminum alloys," *Mater. Charact.*, vol. 58, no. 1, pp. 40–45, 2007.

[278] J. M. Dowling and J. W. Martin, "The influence of MN additions on the deformation behaviour of an Al-Mg-Si alloy," *Acta Metall.*, vol. 24, no. 12, pp. 1147–1153, Dec. 1976.

[279] D. Teirlinck, F. Zok, J. D. Embury, and M. F. Ashby, "Fracture mechanism maps in stress space," *Acta Metall.*, vol. 36, no. 5, pp. 1213–1228, 1988.

[280] E. Maire, S. Zhou, J. Adrien, and M. Dimichiel, "Damage quantification in aluminium alloys using in situ tensile tests in X-ray tomography," *Eng. Fract. Mech.*, vol. 78, no. 15, pp. 2679–2690, 2011.

[281] H. Agarwal, a. . Gokhale, S. Graham, and M. . Horstemeyer, "Void growth in 6061-aluminum alloy under triaxial stress state," *Mater. Sci. Eng. A*, vol. 341, no. 1–2, pp. 35–42, Jan. 2003.

[282] A. A. Benzerga, "Micromechanics of coalescence in ductile fracture," *J. Mech. Phys. Solids*, vol. 50, no. 6, pp. 1331–1362, 2002.

[283] J. Gammage, D. Wilkinson, Y. Brechet, and D. Embury, "A model for damage coalescence in heterogeneous multi-phase materials," *Acta Mater.*, vol. 52, no. 18, pp. 5255–5263, 2004.

[284] V. Tvergaard and A. Needleman, "Effects of nonlocal damage in porous plastic solids," *Int. J. Solids Struct.*, vol. 32, no. 8, pp. 1063–1077, 1995.

[285] V. Tvergaard and A. Needleman, "Nonlocal effects on localization in a void-sheet," *Int. J. Solids Struct.*, vol. 34, no. 18, pp. 2221–2238, 1997.

[286] T. Pardoen and J. W. Hutchinson, "An extended model for void growth and coalescence," *J. Mech. Phys. Solids*, vol. 48, no. 12, pp. 2467–2512, 2000.

[287] F. R. Brotzen and A. Seeger, "Diffusion near dislocations, dislocation arrays and tensile cracks," *Acta Metall.*, vol. 37, no. 11, pp. 2985–2992, 1989.

[288] L. Westfall, B. J. Diak, M. A. Singh, and S. Saimoto, "Dynamic Dislocation-Defect Analysis and SAXS Study of Nanovoid Formation in Aluminum Alloys," *J. Eng. Mater. Technol.*, vol. 130, no. 2, pp. 21011–21017, Mar. 2008.

[289] S. Saimoto, B. J. Diak, and D. J. Lloyd, "Point defect generation, nano-void formation and growth. II. Criterion for ductile failure," *Philos. Mag.*, vol. 92, no. 15, pp. 1915–1936, May 2012.

[290] P. B. Hirsch, "Extended jogs in dislocations in face-centred cubic metals," *Philos. Mag. A J. Theor. Exp. Appl. Phys.*, vol. 7, no. 73, pp. 67–93, 1962.

[291] J. Friedel, "On the linear work hardening mate of face-centred cubic single crystals," *Philos. Mag.*, vol. 46, no. 382, pp. 1169–1186, 1955.

[292] J. D. Baird, B. Gale, and N. P. Allen, "Attractive dislocation intersections and work

hardening in metals," *Philos. Trans. R. Soc. London. Ser. A, Math. Phys. Sci.*, vol. 257, no. 1087, pp. 553–590, 1965.

[293] A. S. Argon, "Patterning in crystal plasticity of FCC metals," *Scr. Mater.*, vol. 47, no. 10, pp. 683–687, 2002.

[294] L. Kubin, T. Hoc, and B. Devincre, "Dynamic recovery and its orientation dependence in face-centered cubic crystals," *Acta Mater.*, vol. 57, no. 8, pp. 2567–2575, 2009.

[295] L. M. Brown, "Unifying concepts in dislocation plasticity," *Philos. Mag.*, vol. 85, no. 26–27, pp. 2989–3001, 2005.

[296] S. Saimoto, J. I. Cooley, B. J. Diak, H. Jin, and R. K. Mishra, "Recovery studies of cold rolled aluminum sheet using X-ray line broadening and activation volume determinations," *Acta Mater.*, vol. 57, no. 16, pp. 4822–4834, 2009.

[297] S. Saimoto, J. Cooley, H. Larsen, and C. Scholler, "Kinetic analysis of dynamic point defect pinning in aluminium initiated by strain rate changes," *Philos. Mag.*, vol. 89, no. 10, pp. 853–868, Apr. 2009.

[298] G. Liu, S. Scudino, R. Li, U. Kühn, J. Sun, and J. Eckert, "Coupling effect of primary voids and secondary voids on the ductile fracture of heat-treatable aluminum alloys," *Mech. Mater.*, vol. 43, no. 10, pp. 556–566, 2011.

[299] D. J. Lloyd, "The scaling of the tensile ductile fracture strain with yield strength in Al alloys," *Scr. Mater.*, vol. 48, no. 4, pp. 341–344, 2003.

[300] I. Westermann, K. O. Pedersen, T. Furu, T. Børvik, and O. S. Hopperstad, "Effects of particles and solutes on strength, work-hardening and ductile fracture of aluminium alloys," *Mech. Mater.*, vol. 79, pp. 58–72, 2014.

[301] K. O. Pedersen, I. Westermann, T. Furu, T. Børvik, and O. S. Hopperstad, "Influence of microstructure on work-hardening and ductile fracture of aluminium alloys," *Mater. Des.*, vol. 70, pp. 31–44, 2015.

[302] G. I. Taylor, "The mechanism of plastic deformation of crystals. Part I:Theoretical," *Proc. R. Soc. London. Ser. A*, vol. 145, no. 855, pp. 362–387, 1934.

[303] D. Kuhlmann-Wilsdorf, "The theory of dislocation-based crystal plasticity," *Philos. Mag. A*, vol. 79, no. 4, pp. 955–1008, 1999.

[304] J. J. Bhattacharyya, B. Bittmann, and S. R. Agnew, "The effect of precipitate-induced backstresses on plastic anisotropy: Demonstrated by modeling the behavior of aluminum alloy, 7085," *Int. J. Plast.*, 2018.

[305] L. M. Cheng, W. J. Poole, J. D. Embury, and D. J. Lloyd, "The influence of precipitation on the work-hardening behavior of the aluminum alloys AA6111 and AA7030," *Metall. Mater. Trans. A*, vol. 34, no. 11, pp. 2473–2481, 2003.

[306] M. F. Horstemeyer and D. L. McDowell, "Modeling effects of dislocation substructure in

polycrystal elastoviscoplasticity," *Mech. Mater.*, vol. 27, no. 3, pp. 145–163, 1998.

[307] M. Richert, Q. Liu, and N. Hansen, "Microstructural evolution over a large strain range in aluminium deformed by cyclic-extrusion–compression," *Mater. Sci. Eng. A*, vol. 260, no. 1, pp. 275–283, 1999.

[308] G. J. Baczynski, R. Guzzo, M. D. Ball, and D. J. Lloyd, "Development of roping in an aluminum automotive alloy AA6111," *Acta Mater.*, vol. 48, no. 13, pp. 3361–3376, 2000.

[309] M. Asano, T. Minoda, Y. Ozeki, and H. Yoshida, "Effect of Copper Content on the Bendability of Al-Mg-Si Alloy Sheet," *Mater. Sci. Forum*, vol. 519–521, pp. 771–776, 2006.

[310] S. M. Hirth, G. J. Marshall, S. A. Court, and D. J. Lloyd, "Effects of Si on the aging behaviour and formability of aluminium alloys based on AA6016," *Mater. Sci. Eng. A*, vol. 319–321, pp. 452–456, 2001.

[311] Z. Fan, X. Lei, L. Wang, X. Yang, and R. E. Sanders, "Influence of quenching rate and aging on bendability of AA6016 sheet," *Mater. Sci. Eng. A*, vol. 730, pp. 317–327, 2018.

[312] Y. Shi, P. Z. Zhao, H. Jin, P. D. Wu, and D. J. Lloyd, "Analysis of Surface Roughening in AA6111 Automotive Sheet Under Pure Bending," *Metall. Mater. Trans. A*, vol. 47, no. 2, pp. 949–960, Feb. 2016.

[313] W. Muhammad, U. Ali, A. P. Brahme, J. Kang, R. K. Mishra, and K. Inal, "Experimental analyses and numerical modeling of texture evolution and the development of surface roughness during bending of an extruded aluminum alloy using a multiscale modeling framework," *Int. J. Plast.*, pp. 1–29, Sep. 2017.

[314] D. . Wilson, A. . Mirshams, and W. . Roberts, "An experimental study of the effect of sheet thickness and grain size on limit-strains in biaxial stretching," *Int. J. Mech. Sci.*, vol. 25, no. 12, pp. 859–870, Jan. 1983.

[315] P. D. Wu, D. J. Lloyd, A. Bosland, H. Jin, and S. R. MacEwen, "Analysis of roping in AA6111 automotive sheet," *Acta Mater.*, vol. 51, no. 7, pp. 1945–1957, 2003.

[316] P. Schwellinger, "On the mechanism of ductile intergranular fracture in ALMgSI alloys," *Scr. Metall.*, vol. 12, no. 10, pp. 899–901, 1978.

[317] D. J. Lloyd, M. Gallerneault, and R. B. Wagstaff, "The deformation of clad aluminum sheet produced by direct chill casting," *Metall. Mater. Trans. A Phys. Metall. Mater. Sci.*, vol. 41, no. 8, pp. 2093–2103, 2010.

[318] H. Jin, R. B. Wagstaff, D. J. Lloyd, J. D. Embury, X. Ren, and M. Gallerneault, *The bendability of AA1200/AA2124 laminate sheets produced via Fusion^{TM} technology*. 2011.

[319] H. Jin and D. J. Lloyd, "Improvement of bendability in Fusion AA3003/AA6xxx sheets with different clad thickness after artificial aging," *Mater. Sci. Technol.*, vol. 29, no. 12, pp. 1447–1452, Dec. 2013.

[320] F. J. Humphreys, “The nucleation of recrystallization at second phase particles in deformed aluminium,” *Acta Metall.*, vol. 25, no. 11, pp. 1323–1344, 1977.

[321] O. Engler, “On the origin of the R orientation in the recrystallization textures of aluminum alloys,” *Metall. Mater. Trans. A*, vol. 30, no. 6, pp. 1517–1527, 1999.

[322] R. D. Doherty, “Recrystallization and texture,” *Prog. Mater. Sci.*, vol. 42, no. 1, pp. 39–58, 1997.

[323] A. Davidkov, M. K. Jain, R. H. Petrov, D. S. Wilkinson, and R. K. Mishra, “Strain localization and damage development during bending of Al–Mg alloy sheets,” *Mater. Sci. Eng. A*, vol. 550, pp. 395–407, Jul. 2012.

[324] L. Mattei, D. Daniel, G. Guiglionda, N. Moulin, H. Klöcker, and J. Driver, “Grain scale modeling of the bendability of AA6xxx Al alloy sheet,” *Mater. Sci. Eng. A*, vol. 583, pp. 96–104, Oct. 2013.

[325] H. Jin, R. B. Wagstaff, D. J. Lloyd, J. D. Embury, X. Ren, and M. Gallerneault, “The Bendability of AA1200 / AA2124 Laminate Sheets Produced via Fusion TM Technology,” pp. 1–6, 2010.

[326] S. Esmaeili, D. J. Lloyd, and W. J. Poole, “Modeling of precipitation hardening for the naturally aged Al-Mg-Si-Cu alloy AA6111,” *Acta Mater.*, vol. 51, no. 12, pp. 3467–3481, Jul. 2003.

[327] X. Peng, M. Guo, X. Wang, L. Cui, J. Zhang, and L. Zhuang, “Influence of particles with different sizes on microstructure, texture and mechanical properties of Al-Mg-Si-Cu series alloys,” *Acta Metall. Sin.*, vol. 51, no. 2, pp. 169–177, 2015.

[328] J. Hirsch, “Aluminium Alloys for Automotive Application,” *Mater. Sci. Forum*, vol. 242, pp. 33–50, 1997.

[329] K. Odusote, A. A. Adeleke, and P. A. Ajayi, “Mechanical properties and microstructure of precipitation-hardened Al-Cu-Zn alloy,” *Int. J. Automot. Mech. Eng.*, vol. 12, no. 1, pp. 3033–3042, 2015.

[330] F. Ozturk, A. Sisman, S. Toros, S. Kilic, and R. C. Picu, “Influence of aging treatment on mechanical properties of 6061 aluminum alloy,” *Mater. Des.*, vol. 21, no. 2, pp. 972–975, 2010.

[331] O. Engler, C. Schäfer, and O. R. Myhr, “Effect of natural ageing and pre-straining on strength and anisotropy in aluminium alloy AA 6016,” *Mater. Sci. Eng. A*, 2015.

[332] J. Yanagimoto, T. Oya, S. Kawanishi, N. Tiesler, and T. Koseki, “Enhancement of bending formability of brittle sheet metal in multilayer metallic sheets,” *CIRP Ann. - Manuf. Technol.*, vol. 59, no. 1, pp. 287–290, 2010.

[333] I. Westermann, K. E. Snilsberg, Z. Sharifi, O. S. Hopperstad, K. Marthinsen, and B. Holmedal, “Three-Point Bending of Heat-Treatable Aluminum Alloys: Influence of Microstructure and Texture on Bendability and Fracture Behavior,” *Metall. Mater. Trans.*

A, vol. 42, no. 11, pp. 3386–3398, Jul. 2011.

[334] G. Lin, S. J. Hu, and W. Cai, "Evaluation of Formability in Bending/Hemming of Aluminum Alloys Using Plane-Strain Tensile Tests," *J. Manuf. Sci. Eng.*, vol. 131, no. 5, p. 051009, 2009.

[335] W. B. Lievers, A. K. Pilkey, and M. J. Worswick, "The co-operative role of voids and shear bands in strain localization during bending," *Mech. Mater.*, vol. 35, no. 7, pp. 661–674, Jul. 2003.

[336] M. Kuroda and V. Tvergaard, "Effects of texture on shear band formation in plane strain tension/compression and bending," *Int. J. Plast.*, 2007.

[337] W. Muhammad, J. Kang, A. P. Brahme, U. Ali, J. Hirsch, H.-J. Brinkman, O. Engler, R. K. Mishra, and K. Inal, "Bendability enhancement of an age-hardenable aluminum alloy: Part I — Relationship between microstructure, plastic deformation and fracture," *Mater. Sci. Eng. A*, p. Under review, 2019.

[338] K. Cheong, K. Omer, C. Butcher, R. George, and J. Dykeman, "Evaluation of the VDA 238-100 Tight Radius Bending Test using Digital Image Correlation Strain Measurement," *J. Phys. Conf. Ser.*, vol. 896, no. 1, 2017.

[339] R. Becker, "An Analysis of Shear Localization During Bending of a Polycrystalllne Sheet," 2014.

[340] R. Becker, "Effects of strain localization on surface roughening during sheet forming," *Acta Mater.*, vol. 46, no. 4, pp. 1385–1401, 1998.

[341] C. Laird, S. Stanzl, R. de la Veaux, and L. Buchinger, "The cyclic stress—strain response and dislocation structures of Cu-16 at.%Al alloy II: Polycrystalline behavior," *Mater. Sci. Eng.*, vol. 80, no. 2, pp. 143–154, 1986.

[342] A. Rohatgi, K. S. Vecchio, and G. T. Gray, "The influence of stacking fault energy on the mechanical behavior of Cu and Cu-Al alloys: Deformation twinning, work hardening, and dynamic recovery," *Metall. Mater. Trans. A*, vol. 32, no. 1, pp. 135–145, 2001.

[343] P. Lukáš, L. Kunz, and J. Krejčí, "Fatigue behaviour of single crystals of a Cu-22%Zn alloy," *Mater. Sci. Eng. A*, vol. 158, no. 2, pp. 177–183, 1992.

[344] L. Xiao and Z.-B. Kuang, "Biaxial path dependence of macroscopic response and microscopic dislocation substructure in type 302 stainless steel," *Acta Mater.*, vol. 44, no. 8, pp. 3059–3067, 1996.

[345] E. El-Danaf, S. R. Kalidindi, and R. D. Doherty, "Influence of grain size and stacking-fault energy on deformation twinning in fcc metals," *Metall. Mater. Trans. A*, vol. 30, no. 5, pp. 1223–1233, May 1999.

[346] I. Gutierrez-Urrutia and D. Raabe, "Dislocation and twin substructure evolution during strain hardening of an Fe–22wt.% Mn–0.6wt.% C TWIP steel observed by electron channeling contrast imaging," *Acta Mater.*, vol. 59, no. 16, pp. 6449–6462, 2011.

[347] I. P. Jones and W. B. Hutchinson, “Stress-state dependence of slip in Titanium-6Al-4V and other H.C.P. metals,” *Acta Metall.*, vol. 29, no. 6, pp. 951–968, 1981.

[348] Z. Wang, “Cyclic deformation response of planar-slip materials and a new criterion for the wavy-to-planar-slip transition,” *Philos. Mag.*, vol. 84, no. 3–5, pp. 351–379, 2004.

[349] S.-H. Doong, D. F. Socie, and I. M. Robertson, “Dislocation Substructures and Nonproportional Hardening,” *J. Eng. Mater. Technol.*, vol. 112, no. 4, pp. 456–464, Oct. 1990.

[350] H. Abdel-Raouf, A. Plumtree, and T. H. Topper, “Temperature and strain rate dependence of cyclic deformation response and damage accumulation in ofhc copper and 304 stainless steel,” *Metall. Trans.*, vol. 5, no. 1, p. 267, Jan. 1974.

[351] A. S. Malin and M. Hatherly, “Microstructure of cold-rolled copper,” *Met. Sci.*, vol. 13, no. 8, pp. 463–472, 1979.

[352] B. Bay, N. Hansen, D. A. Hughes, and D. Kuhlmann-Wilsdorf, “Evolution of f.c.c. deformation structures in polyslip,” *Acta Metall. Mater.*, vol. 40, no. 2, pp. 205–219, 1992.

[353] D. A. Hughes, “Microstructural evolution in a non-cell forming metal: AlMg,” *Acta Metall. Mater.*, vol. 41, no. 5, pp. 1421–1430, 1993.

[354] R. A. Jago and N. Hansen, “Grain size effects in the deformation of polycrystalline iron,” *Acta Metall.*, vol. 34, no. 9, pp. 1711–1720, 1986.

[355] V. Gerold and H. P. Karnthaler, “On the origin of planar slip in f.c.c. alloys,” *Acta Metall.*, vol. 37, no. 8, pp. 2177–2183, 1989.

[356] T. Steffens, C. Schwink, A. Korner, and H. P. Karnthaler, “Transmission electron microscopy study of the stacking-fault energy and dislocation structure in CuMn alloys,” *Philos. Mag. A*, vol. 56, no. 2, pp. 161–173, Aug. 1987.

[357] L. Xiao and Y. Umakoshi, “Cyclic deformation behaviour and dislocation structure of Ti-5 at.% Al single crystals oriented for double prism slip,” *Philos. Mag. A*, vol. 82, no. 12, pp. 2379–2396, 2002.

[358] S. Heino and B. Karlsson, “Cyclic deformation and fatigue behaviour of 7Mo–0.5N superaustenitic stainless steel—slip characteristics and development of dislocation structures,” *Acta Mater.*, vol. 49, no. 2, pp. 353–363, 2001.

[359] A. A. Csontos and E. A. Starke, “The effect of inhomogeneous plastic deformation on the ductility and fracture behavior of age hardenable aluminum alloys,” *Int. J. Plast.*, vol. 21, no. 6, pp. 1097–1118, 2005.

[360] L. Xiao, D. L. Chen, and M. C. Chaturvedi, “Shearing of γ″ precipitates and formation of planar slip bands in Inconel 718 during cyclic deformation,” *Scr. Mater.*, vol. 52, no. 7, pp. 603–607, 2005.

[361] H. F. Merrick, “Effect of heat treatment on the structure and properties of extruded P/M

alloy 718," *Metall. Trans. A*, vol. 7, no. 4, pp. 505–514, Apr. 1976.

[362] D. W. Worthem, I. M. Robertson, F. A. Leckie, D. F. Socie, and C. J. Altstetter, "Inhomogeneous deformation in INCONEL 718 during monotonic and cyclic loadings," *Metall. Trans. A*, vol. 21, no. 12, pp. 3215–3220, Dec. 1990.

[363] H. Gleiter and E. Hornbogen, "Beobachtung der Wechselwirkung von Versetzungen mit kohärenten geordneten Zonen (II)," *Phys. status solidi*, vol. 12, no. 1, pp. 251–264, 1965.

[364] E. Hornbogen and Z. K. Gahr, "Distribution of Plastic Strain in Alloys Containing Small Particles," *Metallography*, vol. 202, pp. 181–202, 1975.

[365] U. F. Kocks, "Superposition of Alloy Hardening, Strain Hardening, and Dynamic Recovery*," in *Strength of Metals and Alloys*, P. HAASEN, V. GEROLD, and G. KOSTORZ, Eds. Pergamon, 1979, pp. 1661–1680.

[366] W. Muhammad, J. Kang, R. K. Mishra, and K. Inal, "A Simple Approach to Performing Large Strain Cyclic Simple Shear Tests: Methodology and Experimental Results," *J. Test. Eval.*, vol. 46, no. 6, Nov. 2018.

[367] C. S. Lee and B. J. Duggan, "Deformation banding and copper-type rolling textures," *Acta Metall. Mater.*, vol. 41, no. 9, pp. 2691–2699, 1993.

[368] P. C. J. Gallagher, "The influence of alloying, temperature, and related effects on the stacking fault energy," *Metall. Trans.*, vol. 1, no. 9, pp. 2429–2461, 1970.

[369] M. Muzyk, Z. Pakiela, and K. J. Kurzydlowski, "Ab initio calculations of the generalized stacking fault energy in aluminium alloys," *Scr. Mater.*, vol. 64, no. 9, pp. 916–918, 2011.

[370] J. W. Christian and P. R. Swann, "Stacking faults in Metals and Alloys," in *Alloying Behaviour and Effects in Concentrated Solid Solutions. Metallurgical Society Conferences, edited by TB MASSALSKI*, 1965, vol. 29, p. 105.

[371] M. Liu, H. J. Roven, Y. Yu, and J. C. Werenskiold, "Deformation structures in 6082 aluminium alloy after severe plastic deformation by equal-channel angular pressing," *Mater. Sci. Eng. A*, vol. 483–484, no. 1–2 C, pp. 59–63, 2008.

[372] A. M. Cuitiño, "Effect of temperature and stacking fault energy on the hardening of FCC crystals," *Mater. Sci. Eng. A*, vol. 216, no. 1–2, pp. 104–116, 1996.

[373] Y. Z. Tian, L. J. Zhao, S. Chen, A. Shibata, Z. F. Zhang, and N. Tsuji, "Significant contribution of stacking faults to the strain hardening behavior of Cu-15%Al alloy with different grain sizes," *Sci. Rep.*, vol. 5, no. October, pp. 2–10, 2015.

[374] F. J. Humphreys and M. Hatherly, "The Mobility and Migration of Boundaries," *Recryst. Relat. Annealing Phenom.*, pp. 121–167, 2004.

[375] G. E. Lloyd, A. B. Farmer, and D. Mainprice, "Misorientation analysis and the formation and orientation of subgrain and grain boundaries," *Tectonophysics*, vol. 279, no. 1–4, pp. 55–78, 1997.

[376] Z. F. Zhang and Z. G. Wang, “Dependence of intergranular fatigue cracking on the interactions of persistent slip bands with grain boundaries,” *Acta Mater.*, vol. 51, no. 2, pp. 347–364, 2003.

[377] S. D. Antolovich and R. W. Armstrong, “Plastic strain localization in metals: Origins and consequences,” *Prog. Mater. Sci.*, vol. 59, no. 1, pp. 1–160, 2014.

[378] S. Kobayashi, T. Inomata, H. Kobayashi, S. Tsurekawa, and T. Watanabe, “Effects of grain boundary- and triple junction-character on intergranular fatigue crack nucleation in polycrystalline aluminum,” *J. Mater. Sci.*, vol. 43, no. 11, pp. 3792–3799, 2008.